U N A M

T E S I S P A R A O B T E N E R E L G R A D O A C A D É M I C O
D E D O C T O R E N C I E N C I A S (A S T R O N O M Í A)

Midiendo Regiones de Formación Estelar Cercanas con el VLBA: de la Distancia a la Dinámica

R O S A M . T O R R E S

Directores
Dr. Laurent Loinard, CRyA - UNAM
Dra. Amy J. Mioduszewski, DSOC - NRAO

U N I V E R S I D A D N A C I O N A L A U T Ó N O M A D E M É X I C O
C e n t r o d e R a d i o a s t r o n o m í a y A s t r o f í s i c a
N a t i o n a l R a d i o A s t r o n o m y O b s e r v a t o r y

Morelia, Michoacán, México 2009

U N A M

THESIS FOR THE PHD. IN ASTRONOMY

Measuring Nearby Star Forming Regions with the VLBA: from the Distance to the Dynamics

ROSA M. TORRES

Advisors

Dr. Laurent Loinard, Centro de Radioastronomía y Astrofísica, UNAM
Apartado Postal 72–3 (Xangari), 58089 Morelia, Mich., México

Dr. Amy J. Mioduszewski, Domenici Science Operations Center, NRAO
1003 Lopezville Road, 87801 Socorro, NM, USA

UNIVERSIDAD NACIONAL AUTÓNOMA DE MÉXICO
Centro de Radioastronomía y Astrofísica
National Radio Astronomy Observatory

September 2009

Agradecimientos

Mi más profunda gratitud a Laurent Loinard por haberme propuesto el tema de esta tesis, por confiar en que no echaría a perder el proyecto y por el esfuerzo dedicado durante los últimos años.

Agradezco a los directores de la tesis, Laurent Loinard y Amy Mioduszewski, y a los sinodales Luis Felipe Rodríguez, Paola D'Alessio y Mark Reid por su atenta y rápida leída de este manuscrito y por los valiosos comentarios que lo han enriquecido.

El trabajo de presentado aquí no habría sido posible sin el apoyo, dedicación y paciencia de Amy Mioduszewski, quien durante los últimos tres años, me explicó pacientemente todo lo que ahora sé sobre VLBI, además revisó cuidadosamente cada uno de los pasos durante la reducción de datos y me ha motivado a seguir adelante.

Agradezco a la UNAM y al CRyA por las facilidades brindadas durante la maestría y doctorado, a DGAPA-UNAM por el complemento de beca que me otorgó en maestría, al CONACyT por las becas de maestría y doctorado, y al NRAO por hacer posible las estancias de trabajo en Socorro. De igual manera agradezco al Posgrado en Astronomía de la UNAM, al CRyA y a los proyectos CONACyT y PAPIIT por el apoyo económico proporcionado para asistir a escuelas y congresos durante estos cuatro años.

Doy las gracias a mis profesores de la maestría quienes apoyaron mi formación académica, a los investigadores que aunque no me dieron clases siempre estuvieron dispuestos a ayudarme con mis dudas, al personal administrativo y de cómputo del CRyA por su ayuda brindada día con día y al personal del Posgrado en Astronomía por el tiempo invertido en trámites de la maestría y doctorado.

De la misma manera agradezco a todo el personal del NRAO, quienes de alguna u otra manera ayudaron a que mis estancias en Socorro fueran buenas. En especial agradezco a Kumar, Emmanuel, Mary, Lorant, Vivek, Urvashi, Sanjay, Veronica, Maurilio, Adam, Nissim, Esteban, Wei-Hao, Masaya, Aya, Malcolm y Brigette, por el buen café después del lunch, por las BBQ los fines de semana y por llevarme al Bosque del Apache.

Gracias a mis compañeros del posgrado. A Ramiro y Daniel por contestar todas mis preguntas, por apostar a que sí pasaba el de admisión y los gen-

erales. A Gaby, Edgar y Alfonso por las desveladas, por el trabajo en equipo, por la compañía y por todo lo que nos divertimos en la maestría. A Roberto por sus consejos y por buena gente. A todos los que se fueron agregando en el camino (Alfredo, Alma, Álvaro, Aurora, Bernardo, Charly, Chente, Chuy, el Hippie, Karla, Eréndira) por su compañía, por las fiestas, porque me caen bien. A Gabiota y Roberta por no cuestionarme, por quedarse conmigo y apoyarme en las decisiones que tomé, por soñar juntos y por las tardes gastadas planeando lo que haremos cuando seamos doctores.

A Roberto Vázquez por descubrirme, por creer en mi, por fracasar tratando de acercarme a la astronomía óptica y por su invaluable amistad. A Yolanda por permitirme desarrollar en la parte de divulgación. A Ramiro por ser mi ejemplo a seguir desde los propedéuticos y por ser tan chido el tiempo que compartimos oficina. A Yolanda, Luis Felipe, Paola y Javier por ayudarnos a salir adelante estos últimos meses. A mis astrónomas favoritas: Amy, Yolanda y Paola, por todo su cariño, por acercarme a sus familias y porque las quiero un montón. A Gusana por seguir al otro lado de la línea. A Paty por derecho de antigüedad. A Nena porque siempre está cuando la necesito. A Moni por las noches de estrellas. A Gabiota, porque estos años hubieran sido imposibles sin su amistad.

A Mamá, Abuelita, Abuelito, Lore y César porque los adoro y me aceptan con todas mis virtudes y todos mis defectos. A mis tres amores: Kike, Tella y Mimí, por superar juntos todo lo que vivimos y porque además de hermanos son mis grandes amigos. Agradezco de manera especial a mi familia por su amor incondicional (y condicional a veces), por no dejar que desaparezca la esperanza, por enseñarme que la felicidad se consigue con pasión, mucho trabajo y tenacidad. Les agradezco a cada uno de ellos por darme su ejemplo, bueno o malo, que finalmente me ha enseñado cómo *quiero* y cómo *no quiero* ser.

Y a Rami porque es lo mejor que me pasó en el posgrado. Por reencontrarme después de tres largos años y darle un rumbo a mi vida. Por quedarse conmigo, por los planes para el postdoc, por hacerme sonreír todos los días, por nuestras vidas juntos y porque lo amo.

Rosy

Morelia, Michoacán, México
Septiembre del 2009

To Ramiro

Contents

Resumen

Introducción

El problema de la determinación de distancias en el Universo siempre ha jugado un papel central en la astronomía. A través del tiempo se han ido desarrollando diferentes métodos para estimar la distancia a los cuerpos celestes. La gran mayoría de estos métodos son indirectos y, para objetos fuera del Sistema Solar, solamente hay una técnica disponible que es cien por ciento directa, sin suposiciones y puramente geométrica: la paralaje trigonométrica. A la fecha, muchas de las mediciones de la paralaje trigonométrica han sido basadas en observaciones ópticas o del cercano infrarrojo, en las cuales la precisión astrométrica está limitada a 1 milisegundo de arco. Como consecuencia, la determinación de la paralaje en el óptico e infrarrojo cercano está limitada a la Vecindad Solar ($d \lesssim 500$ pc).

De hecho, a finales de los 90s nuestro conocimiento de la distribución de las estrellas en la Vecindad Solar ha sido dramáticamente mejorado gracias al satélite Hipparcos, que midió la paralaje trigonométrica a miles de estrellas dentro de algunos cientos de parcecs alrededor del Sol con una precisión de $\sim$ 5–10% (Perryman et al. 1997; van Leeuwen 2007). Trabajando a longitudes de onda del óptico, Hipparcos representó una mejora para estrellas brillantes aisladas y fue comparativamente pobre para aquellas en regiones de formación estelar. Esto se debe a que las estrellas jóvenes se encuentran embebidas en su nube madre, lo cuál las hace ópticamente débiles o tienden a estar rodeadas de nebulosidades. Las barras de error típicas de Hipparcos para la distancia a estrellas cercanas de pre-secuencia principal por lo regular exceden 100 pc (resultando en precisiones típicas del 30% o peores para la distancia). Consecuentemente, mientras el satélite Hipparcos nos permitió penetrar en el entendimiento de la distribución local de estrellas de secuencia principal, no mejoró mucho nuestro conocimiento sobre la distancia a regiones de formación estelar cercanas (Bertout et al. 1999).

Entonces en el 2005, cuando empecé a trabajar en los datos que presentamos en éste manuscrito, las mejores estimaciones para la distancia a regiones

de formación estelar cercanas seguían siendo basadas en métodos indirectos. Podría decirse que la situación más favorable era para el complejo de Tauro, al cuál se le estimaba una distancia promedio de 140 ± 10 pc (Kenyon et al. 1994). Sin embargo, aún no estaba claro qué tan profundo era el complejo y si existían gradientes significantes en la distancia a lo largo de la región. La situación para Ophiuchus era un poco más incierta. Tradicionalmente se ha estimado una distancia de 165 ± 20 pc (Chini 1981) y recientemente se había sugerido que está más cerca, a 120–125 pc (de Geus et al. 1989; Knude & Hog 1998). Sin embargo muchos autores aún prefieren el antiguo valor o uno intermedio de 140 pc (e.g. Mamajek 2007). La precisión en la distancia para otros sitios de formación estelar cercanos menos estudiados (Perseo, Serpens, Monoceros, Orion, etc.) era más o menos similar o peor, no mejor que un 20%.

Había entonces una necesidad urgente de mejorar el estado insatisfactorio del asunto. Primero, porque las grandes incertidumbres en la distancia limitan la determinación precisa de las propiedades de las estrellas jóvenes como la masa o la luminosidad. Esto a su vez limita fuertemente la comparación de modelos teóricos de evolución de estrellas de pre-secuencia principal con los datos observacionales. Adicionalmente, la determinación de la estructura interna y la cinemática de las regiones de formación estelar cercanas (las cuales pueden ser obtenidas a partir de mediciones astrométricas precisas) proveen información valiosa sobre la historia de la formación estelar dentro de cada región y sobre los procesos de formación estelar mismos. Finalmente, los sitios de formación estelar no están distribuidos aleatoriamente dentro de la Vía Láctea. En particular, muchas de las regiones de formación estelar en la Vecindad Solar parecen estar aproximadamente alineadas en una estructura toroidal llamada el Cinturón de Gould. Entender el origen de dicha estructura es relevante en el contexto de Astronomía Galáctica y requiere una determinación precisa de su geometría. La información necesaria se puede obtener a partir de la determinación precisa de la distancia y la profundidad de cada una de las regiones que forman el Cinturón de Gould.

Debido a que las observaciones en el óptico e infrarrojo cercano son afectadas por el obscurecimiento por polvo, uno debe moverse a longitudes de onda más grandes para progresar en la determinación de la paralaje para estrellas jóvenes. Recientemente, la calidad de la astrometría proveniente de datos del mediano y lejano infrarrojo, así como de observaciones submilimétricas, sigue

siendo pobre. El dominio del radio (particularmente a 1 cm $\lesssim \lambda \lesssim$ 10 cm) provee, por mucho, la mejor posibilidad porque los grandes interferómetros de radio pueden proporcionar astrometría extremadamente precisa (mejor que una décima de milisegundo de arco).

Metas

Esta tesis es parte de una gran cadena de esfuerzos para determinar la distancia y estructura a todas las regiones de formación estelar alrededor de algunos cientos de parcecs del Sol usando observaciones de radio interferometría. Específicamente, las metas principales de esta tesis pueden resumirse como sigue:

(1) Encontrar la distancia promedio a las dos regiones de formación estelar cercanas de baja masa más estudiadas (Tauro y Ophiuchus) con precisiones de uno o dos órdenes de magnitud mejores que los valores presentes. La estrategia básica para lograr ésta meta fue obtener, durante el curso de uno o dos años, imágenes multi época con radio interferómetros de algunas estrellas jóvenes en cada región. La posición de cada estrella a cada época y la paralaje de cada estrella puede ser medida muy precisamente a través de una calibración de datos cuidadosa. Una vez que conocemos la distancia a cada una de las estrellas individuales, simplemente tomamos la media para estimar la distancia promedio de cada región.

(2) Explorar la estructura y la dinámica de estas regiones de formación estelar. En particular, la determinación de la distancia a algunas estrellas dentro de cada complejo nos permite estimar la profundidad y obtener una aproximación de la forma de cada región. Adicionalmente, los movimientos propios (que son medidos simultáneamente con la paralaje trigonométrica) combinados con mediciones de velocidades radiales tomados de la literatura, proveen algunas pistas de la cinemática interna de cada región, la cual puede ser analizada en términos de modelos dinámicos.

(3) Estudiar las estrellas por sí mismas. En particular, a través de la combinación de temperatura efectiva y luminosidad bolométrica de la literatura (reescaladas a las distancias propias de las fuentes), hemos

sido capaces de refinar la localización en el diagrama HR de las estrellas jóvenes estudiadas en ésta tesis. Esto, sucesivamente, nos permite refinar la determinación de las edades y poner restricciones en los modelos evolutivos de pre-secuencia principal. También algunas estrellas en nuestra muestra han resultado ser sistemas binarios muy cercanos. En algunos de estos casos nuestras observaciones nos permiten refinar la determinación de las órbitas y de las masas de los componentes. Esto provee fuertes restricciones sobre las propiedades intrínsecas de las estrellas.

Observaciones

Nuestra muestra contiene un total de siete objetos estelares jóvenes: cinco en el complejo de Tauro (T Tau Sb, HDE 283572, Hubble 4, HP Tau/G2 y V773 Tau A), y dos en la región de Ophiuchus (S1 y DoAr 21). Seis de estos siete objetos son estrellas de pre-secuencia principal de baja a intermedia masa ($M \lesssim 3\ M_{\odot}$). La séptima fuente (S1 en Ophiuchus) es una estrella joven de secuencia principal tipo B. Todos los siete objetos han sido previamente bien identificados como fuentes brillantes de radio no térmicas, detectados usando interferómetros de línea de base muy larga (VLBI por sus siglas en inglés).

Para cada fuente, hemos obtenido series de observaciones en el continuo a 3.6 cm (8.42 GHz) usando el *arreglo de linea de base muy larga* (VLBA por sus siglas en inglés). El número de observaciones en cada serie, así como la frecuencia con la cuál fueron obtenidas, fue ajustado de acuerdo a cada fuente. Para todas las observaciones usamos referencia de fase, método a través del cual se combina la observación del objetivo científico en cuestión y un calibrador compacto localizado a unos pocos grados de la fuente. La resolución angular típica de nuestras imágenes finales fue de 1 a 2 milisegundos de arco, y la precisión astrométrica típica de cada observación fue de 0.05 a 0.1 milisegundos de arco para las fuentes en Tauro, y de 0.2 a 0.6 milisegundos de arco en Ophiuchus. La pobre precisión en las observaciones de Ophiuchus se debe a la baja declinación de esta región ($\delta = -24^{\circ}$ contra $\delta = +20^{\circ}$ para Tauro) y a la binaridad no modelada de las fuentes (ver abajo).

Resultados principales

Distancias

Para T Tau Sb fueron obtenidas 12 observaciones que resultaron en una paralaje de 6.82 ± 0.03 milisegundos de arco, correspondiente a una distancia de $d = 146.7 \pm 0.6$ pc (Loinard et al. 2005, 2007). Para Hubble 4 y HDE 283572 fueron suficientes series de seis observaciones para precisar las paralajes en 7.53 ± 0.03 milisegundos de arco ($d = 132.8 \pm 0.5$ pc) y 7.78 ± 0.04 milisegundos de arco ($d = 128.5 \pm 0.6$ pc), respectivamente (Torres et al. 2007). Para HP Tau/G2 se obtuvieron nueve observaciones que dieron la paralaje de 6.20 ± 0.03 milisegundos de arco, correspondiente a $d = 161.2 \pm 0.9$ pc (Torres et al. 2009a). Finalmente, para V773 Tau A se hicieron 19 observaciones que nos permitieron medir una paralaje de 7.57 ± 0.20 milisegundos de arco, correspondiente a $d = 132.0 \pm 3.5$ pc (Torres et al. 2009b).

Dos de estos cinco objetos tienen paralaje trigonométrica medida por Hipparcos (Bertout et al. 1999): T Tau Sb con 5.66 ± 1.58 milisegundos de arco y HDE 283572 con 7.81 ± 1.30 milisegundos de arco. Nuestros resultados son consistentes con estos valores, pero uno o dos órdenes de magnitud más precisos. Además, la paralaje trigonométrica de Hubble 4 y HDE 283572 ha sido estimada por Bertout & Genova (2006) usando un método de punto convergente modificado. Sus resultados (8.12 ± 1.50 milisegundos de arco para Hubble 4 y 7.64 ± 1.05 milisegundos de arco para HDE 283572) también son consistentes con los nuestros, pero con un orden de magnitud menos precisos que los nuestros. Anteriormente ha sido determinada la distancia a V773 Tau A ($d = 148.4 \pm 5.3$ pc; Lestrade et al. 1999) usando técnicas de VLBI. Nuestros resultados son marginalmente consistentes con los anteriores y argumentamos que la discrepancia se debe al hecho de que Lestrade et al. (1999) no modeló la binaridad de la fuente en su análisis (se sabe que dicha fuente es una binaria espectroscópica con un periodo orbital de 51 días y semieje mayor de unos cuantos milisegundos de arco). Adicionalmente obtuvimos una estimación independiente de la distancia a V773 Tau A modelando la órbita física de la binaria (usando una combinación de mediciones en el óptico para velocidades radiales, observaciones del interferómetro Keck y nuestros propios datos obtenidos con el VLBA –ver abajo). La distancia obtenida con éste método alternativo es de 134.5 ± 3.2 pc, consistente con el valor obtenido a partir de nuestras mediciones de paralaje, pero nuevamente

marginalmente consistente con el valor a partir de VLBI por Lestrade et al. (1999). La distancia promedio resultante para el complejo de Tauro es de alrededor de 139 pc, consistente con determinaciones previas. Sin embargo, el complejo parece tener 30 pc de profundidad, lo cuál discutiremos en un momento.

Para S1 y DoAr 21 se obtuvieron seis y siete observaciones respectivamente. Las paralajes resultantes son 8.55 ± 0.50 y 8.20 ± 0.37 milisegundos de arco respectivamente. Las cuáles corresponden a $d = 116.9^{+7.2}_{-6.4}$ pc para S1 y $d = 121.9^{+5.8}_{-5.3}$ pc para DoAr 21 (Loinard et al. 2008). Note que la incertidumbre en la distancias para ambas estrellas en Ophiuchus son significativamente más grandes que aquellas obtenidas para las estrellas en Tauro. Como se mencionó anteriormente, esto es una consecuencia de la baja declinación en Ophiuchus relativa a Tauro, y debido a la binaridad no modelada en las dos fuentes de Ophiuchus. La media de estas dos paralajes es 8.33 ± 0.30 milisegundos de arco, correspondiente a una distancia de $120.0^{+4.5}_{-4.2}$ pc. Debido a que S1 y DoAr 21 son miembros del núcleo de Ophiuchus, dicha distancia debe representar una buena estimación de la distancia a ésta región de formación estelar. Lo anterior es consistente con varias de las recientes determinaciones (p. ej. Knude & Hog 1999; de Geus et al. 1989; Lombardi et al. 2008).

Multiplicidad

Para todas las fuentes de nuestra muestra, las trayectorias observadas sobre el plano del cielo pueden ser descritas como la combinación del movimiento elíptico de la Tierra alrededor del Sol y del movimiento propio de la estrella. Si la fuente es soltera, esperaríamos un movimiento propio lineal y uniforme. Sin embargo, si la fuente es miembro de un sistema múltiple, el movimiento propio observado será la combinación del movimiento propio uniforme del baricentro del sistema y el movimiento orbital acelerado. Tres de nuestras fuentes (Hubble 4, HDE 283572 y DoAr 21) anteriormente habían sido reportadas como solteras, pero las otras cuatro como sistemas múltiples. En uno de estos cuatro casos (HP Tau/G2), el periodo orbital esperado es de algunos miles de años, por lo tanto, la correspondiente aceleración es muy pequeña como para ser detectada con nuestras observaciones. A consecuencia de esto, esperábamos un movimiento propio uniforme de la fuente, como si se tratara de una fuente soltera. Por otro lado, el periodo orbital de T Tau Sb es de

unas cuantas décadas, pequeño pero no insignificante comparado con el lapso de tiempo de nuestras observaciones. En este caso pensamos que era suficiente incluir un término de movimiento acelerado en el ajuste astrométrico. Finalmente, en los dos últimos casos (V773 Tau A en Tauro y S1 en Ophiuchus) esperábamos un periodo orbital más corto que el lapso de tiempo de nuestras observaciones. En tales situaciones uno debería, en principio, caracterizar por completo el movimiento orbital antes de poder realizar un ajuste astrométrico completo. Esto fue lo que hicimos para V773 Tau A, pero no para S1 porque suponíamos que S1 era mucho más masiva que su compañera, y como consecuencia, esperábamos una amplitud pequeña de su movimiento reflejo.

En resumen, para Hubble 4, HDE 283572 y DoAr 21 esperábamos movimientos propios uniformes porque creíamos que las tres fuentes eran solteras. Vale la pena mencionar que el movimiento propio de HP Tau/G2 también debería ser uniforme a nuestro nivel de precisión. Para S1 esperábamos el movimiento propio uniforme pero con un pequeño residuo periódico debido a la compañera. Finalmente, para T Tau Sb esperábamos obtener un buen ajuste con un movimiento propio uniformemente acelerado, mientras que para V773 Tau A estábamos conscientes de que se requería una solución orbital completa.

Cuatro de nuestras fuentes se encontraron de a cuerdo a nuestras expectativas:

- Encontramos a V773 Tau A como una fuente de radio doble resuelta. La órbita física del sistema se construyó a partir de la combinación de nuestros datos del VLBA, mediciones en el óptico de las velocidades radiales y datos del interferómetro Keck (Torres et al. 2009b). Este ajuste nos permitió refinar la determinación de las masas de las dos estrellas en el sistema y deducir la posición del baricentro del sistema a cada época. Realizando un nuevo ajuste astrométrico para éstas posiciones anteriores (asumiendo movimiento propio uniforme del baricentro) nos dio la misma distancia obtenida con el método anterior.

- Para describir una adecuada trayectoria de T Tau Sb, asumimos un ajuste con movimiento propio uniformemente acelerado. En este caso, nuestras observaciones no fueron suficientes para determinar la órbita

del sistema, pero proveen información consistente y complementaria con datos existentes del cercano infrarrojo.

- Como se esperaba, el movimiento propio de HDE 283572 se encontró lineal y uniforme.

- Se pudo obtener un ajuste adecuado para S1 asumiendo el movimiento propio como uniforme, pero se encontraron residuos aproximadamente periódicos (en ascensión recta y en declinación) con un periodo de alrededor de 0.7 años. Esto es del orden de magnitud correcto si se interpreta como el movimiento reflejo de S1 debido a su compañera (Loinard et al. 2008, Richichi et al. 1994).

Las otras tres fuentes no se encontraron como se esperaba. Para Hubble 4 y HP Tau/G2 (donde se esperaban movimientos propios uniformes), encontramos residuos significantes en declinación (pero no en ascensión recta). Hasta el momento no es claro si los residuos son consecuencia de una compañera que no vemos, debido a estructura en las magnetósferas de las estrellas, o debido a errores residuales de calibración en la fase. Finalmente, DoAr 21 se encontró muy parecida a S1: con movimiento propio uniforme que provee un buen ajuste, pero con residuos aproximadamente periódicos (en este caso de alrededor de 1.2 años), y la fuente se encontró doble por lo menos en una de nuestras imágenes. Concluimos que DoAr 21 probablemente pertenece a un sistema binario.

Entonces, por lo menos 4 de las 7 fuentes en nuestra muestra (57%) son sistemas binarios muy cercanos con separaciones entre unos pocos milisegundos de arco y unas cuantas decenas de milisegundos de arco. Esto representa una fracción de binaridad mucho más grande que aquella para estrellas de secuencia principal con el mismo rango de separación. Nosotros argumentamos que probablemente hay un fuerte efecto de selección. Los sistemas considerados en ésta tesis fueron seleccionados porque eran conocidos previamente como emisores no térmicos con técnicas de VLBI. Entonces, la alta tasa de binaridad probablemente nos indica que las binarias muy cercanas tienen mayor emisión en radio que las binarias con separaciones más grandes o que las estrellas solteras. Esta idea se refuerza con las observaciones de V773 Tau A donde confirmamos que el flujo emitido depende fuertemente de la separación entre las dos estrellas (el flujo incrementa cerca del periastro y

es muy débil al apoastro). Se cree que la emisión no térmica se crea durante los eventos de reconexión en las magnetósferas activas de las estrellas. Los eventos de reconexión *entre* las estrellas (además de los producidos dentro de las magnetósferas individuales) de un sistema binario muy cercano, podrían explicar naturalmente el flujo de radio tan alto en V773 Tau A.

Estructura tridimensional

La extensión espacial total de Tauro en el cielo es de aproximadamente 10°, correspondiente a un tamaño físico de alrededor de 25 pc. Nuestras observaciones muestran que la profundidad del complejo es de un tamaño similar debido a que HP Tau/G2 está aproximadamente 30 pc más lejos que Hubble 4, HDE 283572 o V773 Tau A. Esto tiene una consecuencia importante: aunque la distancia promedio a la asociación de Tauro fuera determinada con una precisión infinita, se estarían cometiendo errores del rango de 10–20% si uno usara indiscriminadamente dicha distancia promedio para cualquier fuente en Tauro. Para reducir ésta sistemática fuente de error, necesitaríamos establecer la estructura tridimensional de toda la asociación de Tauro, lo cuál se lograría con más observaciones similares a las que presentamos aquí, y así nos acercaríamos más a la meta. Sin embargo, las observaciones de las cinco estrellas presentadas en esta tesis nos dan algunas pistas de cómo debería de ser la estructura tridimensional de Tauro. Hubble 4, HDE 283572 y V773 Tau A, que se encontraron a aproximadamente 130 pc y con una cinemática parecida (Torres et al. 2007, 2009b), están localizadas en la misma porción de Tauro, cerca de Lynds 1495. T Tau Sb está localizado en la parte Sur de Tauro, cerca de Lynds 1551, su velocidad tangencial es claramente diferente a la que presentan Hubble 4, HDE 283572 y V773 Tau A, y además parece estar un poco más lejos de nosotros. Finalmente, HP Tau/G2 está localizada cerca del borde Este (Galáctico)de Tauro y es la más lejana de las cinco fuentes consideradas aquí. Aunque se necesitan observaciones adicionales para dar una conclusión definitiva, nuestros datos sugieren que la región alrededor de Lynds 1495 corresponde al lado más cercano del complejo de Tauro, a aproximadamente 130 pc, mientras que el lado Este de Tauro corresponde a la parte más lejana a 160 pc. La región alrededor de Lynds 1551 y T Tau Sb parecen estar a una distancia intermedia de alrededor 147 pc.

Es bien sabido que Tauro presenta estructura filamentaria. Los dos filamentos principales están aproximadamente paralelos uno del otro y tienen un eje

de proporción de 7:1. Nuestras observaciones sugieren que estas estructuras filamentarias están orientadas casi a lo largo de la línea de visión, p. ej. aproximadamente a lo largo del eje centro–anticentro Galáctico. Esta orientación peculiar podría explicar la baja eficiencia de formación estelar en Tauro comparada con otras regiones de formación estelar cercanas (Ballesteros-Paredes et al. 2009).

Ophiuchus está compuesto de un núcleo compacto de sólo 2 pc de tamaño, y estructuras filamentarias (llamadas "streamers") que se extienden (en proyección) alrededor de 10 pc. El núcleo de Ophiuchus es suficientemente compacto que no esperamos resolver estructuras a lo largo de la línea de visión, y nuestras observaciones muestran que dicho núcleo se encuentra a una distancia de 120 pc. Podría haber gradientes en distancia de algunos cuantos parcecs a lo largo de los streamers. De hecho, hemos notado que Schaefer et al. (2008) determinó la órbita física del sistema binario Haro 1-14C y dedujo una distancia de 111 ± 19 pc, consistente con nuestra determinación. Haro 1-14C está localizado en el streamer norte (asociado con las nubes obscuras L1709/L1704), entonces el resultado de Schaefer et al. (2008) sugiere que ese streamer está un poco más cerca de nosotros que el núcleo. De hecho, esto es consistente con resultados recientes de Lombardi et al. (2008). Por otro lado, usando el sistema VLBI japonés (VERA), Imai et al. (2007) determinaron la paralaje a la protoestrella IRAS 16293–2422 que se encuentra embebida en el streamer Sur de Ophiuchus (en L1689N). Ellos obtuvieron una distancia de 178^{+18}_{-37} pc, la cuál es más consistente con el antiguo valor de 165 pc usado para Ophiuchus. Aún incluyendo los streamers, es improbable que Ophiuchus tenga 60 pc de profundidad debido a que Ophiuchus tiene apenas unos 10 pc de tamaño en proyección. Entonces, si los resultados de Imai et al. (2007) son confirmados, estos indicarían la existencia de varias regiones de formación estelar a lo largo de la línea de visión que no están relacionadas. Se necesitan más observaciones, algunas de las cuales ya han sido recolectadas y parcialmente analizadas, para llegar a un acuerdo.

Perspectivas

Los resultados presentados en ésta tesis nos han permitido refinar la determinación de la distancia a las dos más importantes regiones de formación estelar cercanas y comenzar a examinar la estructura tridimensional de Tauro. Además nos proporcionan un gran número de temas que podrían ser abordados con nuevos datos y sugiere algunos de los siguientes estudios.

- Como hemos mencionado, el radio flujo de V773 Tau A depende de la fase de la órbita, siendo más alto al periastro y más débil al apoastro. En muchas de nuestras observaciones, la fuente se resuelve en dos componentes asociadas con las dos estrellas del sistema. No obstante, nuestras observaciones han mostrado que cerca del periastro la posición de las radio fuentes están significativamente desplazadas de la posición de las estrellas asociadas. Esto nos da evidencia adicional de que la emisión no térmica en el sistema es afectada por la presencia de la compañera. En una propuesta recientemente aceptada, solicitamos tiempo para observar V773 Tau A cerca del periastro con el High Sensitivity Array (arreglo interferométrico compuesto por el VLBA, el radiotelescopio de Green Bank, el VLA y el disco de Arecibo en Puerto Rico). Estas observaciones nos permitirán examinar la evolución espacial de la binaria cuando está cerca del periastro en un periodo de seis horas. Esto debería decirnos mucho a cerca del origen de la variabilidad de la fuente.

- Para decidir si están o no relacionadas varias regiones de formación estelar existentes en Ophiuchus a lo largo de la linea de visión, hemos estado observando algunas nuevas fuentes en la dirección del complejo: VSSG 14 en la subregión Oph–B y ROX 39 en la región entre L1686 y L1689.

- Otras regiones de formación estelar (p. ej. Serpens o Perseo) han estado siendo estudiadas con mucho detalle a muchas otras longitudes de onda, pero no tienen una buena determinación de la distancia. Se sabe que existen algunas fuentes no térmicas en dichas regiones, entonces observaciones multiépoca con el VLBA permitirían mejorar significativamente la determinación de sus distancias. Ya hemos obtenido algunas de las observaciones para Serpens, mientras que para Perseo serán parte de una propuesta futura.

Summary

Introduction

The problem of the determination of distances in the Universe has always played a central role in astronomy, and many different methods have been devised to obtain distance estimates to celestial sources. The vast majority of these methods are indirect, and –for objects outside of the Solar System– there is only one direct, assumption-free, purely geometrical technique available: the determination of the trigonometric parallax. Most parallax measurements to date have been based on optical or near-infrared observations, whose astrometric accuracy is limited to about 1 milli-arcsecond. As a consequence, optical and near-infrared parallax determinations are largely limited to the Solar Neighborhood ($d \lesssim 500$ pc).

Indeed, our knowledge of the distribution of stars in the Solar Neighborhood dramatically improved at the end of the 1990s thanks to the Hipparcos satellite mission. Hipparcos measured the trigonometric parallax of thousands of stars within several hundred parsecs of the Sun with a precision better than $\sim$ 5–10% (Perryman et al. 1997; van Leeuwen 2007). Working at optical wavelengths, it performed best for optically bright isolated stars, and did comparatively poorly in star-forming regions. This is because young stars tend to be surrounded by nebulosities, and –being still enshrouded in their parental cloud– they are usually optically rather faint. Indeed, the typical Hipparcos error bars for the distances to individual nearby pre-main sequence stars usually exceeded 100 pc (resulting in typical distance accuracies of 30% or worse). Consequently, the Hipparcos satellite, while allowing a breakthrough in our understanding of the local distribution of main sequence stars, did little to improve our knowledge of the distance to nearby star-forming regions (Bertout et al. 1999).

Thus, in 2005 when I started working on the data that will be presented in this manuscript, the best estimates for the distances to the nearest star-forming regions remained those based on indirect methods. Arguably the

most favorable situation was that of the Taurus complex which was assumed to be at an average distance of 140 ± 10 pc (Kenyon et al. 1994). It remained unclear, however, how deep the complex was, and if significant distance gradients existed across the region. The situation for Ophiuchus was a bit more uncertain. Traditionally assumed to be at 165 ± 20 pc (Chini 1981), it had recently been suggested to be somewhat nearer: at 120–125 pc (de Geus et al. 1989; Knude & Hog 1998). Many authors, however, still preferred the older value, or an intermediate one of about 140 pc (e.g. Mamajek 2007). The accuracy for other, less studied, nearby sites of star formation (Perseus, Serpens, Monoceros, Orion, etc.) was similar or worse, and it is fair to say that the distances to nearby star-forming regions were, on average, not known to better than 20%.

There was an urgent need to improve this unsatisfactory state of affair. First because the large distance uncertainties precluded accurate determinations of such basic properties of young stars as their mass or luminosity. This, in turn, strongly limited the precision with which theoretical pre-main sequence evolutionary models could be constrained by observational data. In addition, the determination of the internal structure and kinematics of star-forming regions (which can be obtained from accurate astrometric measurements) provides valuable information on the history of star-formation within each regions, and on the star-forming process itself. Finally, sites of star-formation are not randomly distributed within the Milky Way. In particular, most of the star-forming regions in the Solar Neighborhood appear to delineate a roughly toroidal structure called the Gould Belt. Understanding the origin of such a structure is relevant in the context of Galactic Astronomy, and requires an accurate determination of its exact geometry. Precise determinations of the distance and depth of each of the regions forming the Gould Belt would directly provide the required constraints.

Since optical and near-infrared observations are affected by dust obscuration, one must turn to longer wavelengths to make progress in the determination of the parallax of young stars. Currently, the astrometry quality provided by mid- and far-infrared data as well as by sub-millimeter observations remains poor. The radio domain (particularly at 1 cm $\lesssim \lambda \lesssim$ 10 cm) provides, by far, the best prospect because large radio-interferometers can deliver extremely accurate astrometry (better than a tenth of a milli-arcsecond).

Goals

This thesis inserts itself in a large ongoing effort to determine the distance and structure of all star-forming regions within several hundred parsecs of the Sun using radio-interferometric observations. Specifically, the main goals of the thesis can be summarized as follows:

(1) Find the mean distance to the two best-studied nearby regions of low-mass star-formation (Taurus and Ophiuchus) with accuracies (a few percent or better) one to two orders of magnitude better than the present values. The basic strategy to achieve this goal was to obtain multi-epoch radio-interferometric images of several young stars in each region over the course of one to two years. Through careful data calibration, the position of each star at each epoch, and the parallax of each star could be measured very accurately. Once the distances to the individual stars were known, we simply took their weighted mean to estimate the average distance of each region.

(2) Explore the structure and dynamics of these star forming regions. In particular, the determination of the distance to several stars within each complex allowed us to estimate the depth and to obtain a rough approximation of the shape of each region. In addition, the proper motions (which are measured simultaneously with the trigonometric parallaxes) combined with radial velocity measurements taken from the literature provide some hints on the internal kinematics of each region, which can be analyzed in terms of dynamical models.

(3) Study the stars themselves. In particular, we were able to refine the location in the HR diagram of the young stars studied in this thesis by combining effective temperature and bolometric luminosities (re-scaled to the proper distances) taken from the literature. This, in turns, allowed us to refine age determinations, and to put constraints on pre-main sequence evolutionary models. Also, several stars in our sample turned out to be tight binary systems. In some of these cases, our observations allowed us to refine the determination of their orbital paths, and of the mass of the individual components. This provided further constrains on the intrinsic properties of the stars.

Observations

Our sample contains a total of seven young stellar objects: five in the Taurus complex (T Tau Sb, HDE 283572, Hubble 4, HP Tau/G2, and V773 Tau A), and two in the Ophiuchus region (S1 and DoAr 21). Six of these seven objects are low- to intermediate-mass ($M \lesssim 3\ M_\odot$) pre-main sequence stars. The seventh source (S1 in Ophiuchus) is a young main sequence B star. All 7 objects were previously known to be fairly bright non-thermal radio sources, detectable using Very Long Baseline Interferometers.

For each source, we obtained a series of 3.6 cm (8.42 GHz) continuum observations using the *Very Long Baseline Array* (VLBA) of the National Radio Astronomy Observatory (NRAO). The number of observations in each series as well as the cadence at which they were obtained were adjusted to each source. Phase-referencing –whereby observations of the scientific target and a compact calibrator located within a few degrees of the source are intertwined– was used for all the observations. The typical angular resolution of our final images is 1 to 2 milli-arcsecond, and the typical astrometric accuracy of each observation is 0.05 to 0.1 milli-arcseconds for the sources in Taurus, and 0.2 to 0.6 milli-arcseconds in Ophiuchus. The poorer performance in Ophiuchus is related to the lower declination of this region ($\delta = -24^\circ$ against $\delta = +20^\circ$ for Taurus), and to the unmodeled binarity of the sources (see below).

Main results

Distances

For T Tau Sb, 12 observations were obtained, with a resulting parallax of 6.82 ± 0.03 mas, corresponding to a distance $d = 146.7 \pm 0.6$ pc (Loinard et al. 2005, 2007). For Hubble 4 and HDE 283572, series of six observations were sufficient to constrain the parallaxes to 7.53 ± 0.03 mas ($d = 132.8 \pm 0.5$ pc) and 7.78 ± 0.04 mas ($d = 128.5 \pm 0.6$ pc), respectively (Torres et al. 2007). Nine observations of HP Tau/G2 were obtained, and yielded a parallax of 6.20 ± 0.03 mas, corresponding to $d = 161.2 \pm 0.9$ pc (Torres et al. 2009a). Finally, for V773 Tau A, 19 observations were obtained, and allowed us to measure a parallax of 7.57 ± 0.20 mas, corresponding to $d = 132.0 \pm 3.5$ pc (Torres et al. 2009b).

Two of these five objects have measured Hipparcos parallaxes (Bertout et al. 1999): T Tau Sb with 5.66 ± 1.58 mas, and HDE 283572 with 7.81 ± 1.30 mas. Our results are consistent with these values, but one to two orders of magnitude more accurate. Also, the parallax of both Hubble 4 and HDE 283572 were estimated by Bertout & Genova (2006) using a modified convergent point method. Their results (8.12 ± 1.50 mas for Hubble 4 and 7.64 ± 1.05 mas for HDE 283572) are also consistent with our results, but again more than one order of magnitude less accurate. The distance to V773 Tau A had been obtained using Very Long Baseline Interferometer (VLBI) observations before ($d = 148.4 \pm 5.3$ pc; Lestrade et al. 1999). Our result is only marginally consistent with this earlier figure, and we argue that the discrepancy is due to the fact that Lestrade et al. (1999) did not model the binarity of the source in their analysis (this source is a know spectroscopic binary with an orbital period of 51 days and a semi-major axis of a few mas). Indeed, we obtained a mostly independent estimate of the distance to V773 Tau A by modeling the physical orbit of the binary (using a combination of optical radial velocity measurements, Keck Interferometer observations, and our own VLBA data –see below). The distance obtained by this alternative method is 134.5 ± 3.2 pc, in excellent agreement with the value obtained from our parallax measurement, but again only marginally consistent with the older VLBI value. The resulting mean distance to the Taurus complex is about 139 pc, in excellent agreement with previous determination. The complex, however, appears to be at least 30 pc deep, as will be discussed in a moment.

Six observations of S1 and seven of DoAr 21 were obtained. The resulting parallaxes are 8.55 ± 0.50 mas and 8.20 ± 0.37 mas, respectively. This corresponds to $d = 116.9^{+7.2}_{-6.4}$ pc for S1 and $d = 121.9^{+5.8}_{-5.3}$ pc for DoAr 21 (Loinard et al. 2008). Note that the uncertainties on the distances to the stars in Ophiuchus are significantly larger than those for the stars in Taurus. As mentioned earlier, this is a consequence of the lower declination of Ophiuchus relative to Taurus, and of the unmodeled binarity of both sources in Ophiuchus. The weighted mean of these two parallaxes is 8.33 ± 0.30 mas, corresponding to a distance $120.0^{+4.5}_{-4.2}$ pc. Since both S1 and DoAr 21 are members of the Ophiuchus core, this figure must represent a good estimate of the distance to this star-forming region. Note that it is in excellent agreement with several recent determination (e.g. Knude & Hog 1999; de Geus et al. 1989; Lombardi et al. 2008).

Multiplicity

The observed trajectories on the plane of the sky for all the stars in our sample can be described as combinations of a parallactic ellipse and a proper motion. If the source is single, the proper motion is expected to be linear and uniform. If the source is a member of a multiple system, however, the observed proper motion will be the combination of the uniform proper motion of the barycenter of the system and the accelerated orbital motion. Three of our sources (Hubble 4, HDE 283572, and DoAr 21) were believed to be single, but the other four were previously known to be members of multiple systems. In one case (HP Tau/G2), the orbital period is expected to be several thousand years, and the corresponding acceleration is too small to be detectable with our observations. As a consequence, the proper motion of the source is expected to be uniform as if it were single. For T Tau Sb, on the other hand, the orbital period is a few decades, small but not negligible compared with our observing time span. In this situation, it is sufficient to include a uniform acceleration term in the astrometric fit. Finally, in the last two cases (V773 Tau A in Taurus, and S1 in Ophiuchus), the orbital period is expected to be shorter than the time spans covered by our observations. In such situations, one should in principle fully characterize the orbital motion before a full astrometric fit can be performed. This was done in V773 Tau A, but not in S1 because S1 itself is expected to be much more massive than its companion. As a consequence, the amplitude of its reflex motion is anticipated to be small.

In summary, we expected to proper motions of Hubble 4, HDE 283572, and DoAr 21 to be uniform because all three of these source were believed to be single. We anticipated that the proper motion of HP Tau/G2 would also be uniform at our level of precision. For S1, we expected the proper motion to be uniform but with a small periodic residual due to its known companion. Finally, for T Tau Sb we expected to obtain a good fit with a uniformly accelerated proper motion, whereas we were aware that a complete orbital solution would have to be sought for V773 Tau A.

Four of the sources were found to behave according to our expectations:

- V773 Tau A was found to be a resolved double radio source. The physical orbit of the system was constrained by combining optical radial velocity measurements, Keck Interferometer data, and our own VLBA

data (Torres et al. 2009b). This fit allowed us to refine the determination of the masses of the two stars in the system, and to deduce the position of the barycenter of the system at each epoch. An astrometric fit to these positions (assuming a uniform proper motion for the barycenter) yielded the distance quoted earlier.

- A fit assuming a uniformly accelerated proper motion appeared to provide an adequate description of the trajectory of T Tau Sb. In this case, our observations are not sufficient to constrain the orbit of the system, but they provide information consistent with, and complementary of, existing near infrared data.

- As expected, the proper motion of HDE 283572 was found to be linear and uniform.

- Assuming the proper motion of S1 to be uniform appears to provide an adequate fit, but with roughly periodic residuals (in both right ascension and declination) with a period of about 0.7 years. This is of the correct order of magnitude to be interpreted as the reflex motion of S1 due to its known companion (Loinard et al. 2008, Richichi et al. 1994).

The other three sources did not behave as expected. For both Hubble 4 and HP Tau/G2 (where the proper motions were expected to be uniform) we find significant residuals in declination (but not in right ascension). It is unclear at the moment whether these residuals are the consequence of an unseen companion, of structure in the magnetospheres of the stars, or of residual phase errors in our calibration. Finally, DoAr 21 was found to behave much like S1: a uniform proper motion provides a good fit but with roughly periodic residuals (with a period of about 1.2 years in this case), and the source was found to be double in at least one of our images. We conclude that DoAr 21 is likely to belong to a binary system.

Thus, at least 4 of the 7 sources in our sample (57%) turn out to be tight binary systems with separations between a few and a few tens of milliarcseconds. This represents a binarity fraction much larger than that of main sequence stars for the same separation range. We argue that a strong selection effect is likely to be at work. The systems considered in this thesis were selected because they were known to be non-thermal emitters previously

detected with VLBI techniques. The high binary rate may, therefore, indicate that tight binaries are more likely to emit non-thermal radio emission than looser binaries or single stars. This idea is reinforced by the observations of V773 Tau A where we confirm that the emitted flux depends strongly on the separation between the two stars (the flux is strongest near the periastron of the system, and weakest near apoastron). Non-thermal emission is believed to be created during reconnection events in the active magnetospheres of the stars. Reconnection events *between* the stars (in addition to those within the individual magnetospheres) in tight binary systems might naturally explain the higher radio flux of V773 Tau A.

Three dimensional structure

The total spatial extent of Taurus on the sky is about 10°, corresponding to a physical size of about 25 pc. Our observations show that the depth of the complex is similar since HP Tau/G2 is about 30 pc farther than Hubble 4, HDE 283572 or V773 Tau A. This has an important consequence: even if the mean distance of the Taurus association were known to infinite accuracy, one would still make errors as large as 10–20% by using the mean distance indiscriminately for all sources in Taurus. To reduce this systematic source of error, one needs to establish the three-dimensional structure of the Taurus association, and observations similar to those presented here currently represent the most promising avenue toward that goal. Indeed, the observations of the five stars presented here already provide some hints of what the three-dimensional structure of Taurus might be. Hubble 4, HDE 283572, and V773 Tau A which were found to be at about 130 pc and to share a similar kinematics (Torres et al. 2007, 2009b), are also located in the same portion of Taurus, near Lynds 1495. T Tau Sb is located in the southern part of Taurus near Lynds 1551, its tangential velocity is clearly different from that of Hubble 4, HDE 283572, and V773 Tau A, and it appears to be somewhat farther from us. Finally, HP Tau/G2 is located near the (Galactic) eastern edge of Taurus, and is the farthest of the five sources considered here. Although additional observations are needed to draw definite conclusions, our data, therefore, suggest that the region around Lynds 1495 corresponds to the near side of the Taurus complex at about 130 pc, while the eastern side of Taurus corresponds to the far side at 160 pc. The region around Lynds 1551 and T Tau Sb appears to be at an intermediate distance of about 147 pc.

Taurus has long been known to present a filamentary structure. The two main filaments are roughly parallel to one another, and have an axis ratio of about 7:1. Our observations suggest that these filaments are oriented nearly along the line of sight, i.e. roughly along the Galactic center–anticenter axis. This peculiar orientation might indeed explain the low star-forming efficiency of Taurus compared with other nearby star-forming regions (Ballesteros-Paredes et al. 2009).

Ophiuchus is composed of a compact core, only about 2 pc across, and filamentary structures (called "streamers") extending (in projection) to about 10 pc. The Ophiuchus core is sufficiently compact that we do not expect to resolve any structure along the line of sight, and our observations show that it is at a distance of 120 pc. There could potentially be distance gradients of several parsecs across the streamers. We note, however, that Schaefer et al. (2008) determined the physical orbit of the binary system Haro 1-14C, and deduced a distance of 111 ± 19 pc, in good agreement with our determination. Haro 1-14C is located in the northern streamer (associated with the darks clouds L1709/L1704), so the result of Schaefer et al. (2008) suggests that streamer is, if anything, somewhat closer that the core. This is, indeed, in agreement with recent results of Lombardi et al. (2008). On the other hand, Imai et al. (2007) used the Japanese VLBI system (VERA) to determine the parallax to the very young protostar IRAS 16293–2422 deeply embedded in the southern Ophiuchus streamer (in L1689N). They obtain a distance of 178^{+18}_{-37} pc, which would be more consistent with the older value of 165 pc. Even including the streamers, Ophiuchus is only 10 pc across in projection, so it is unlikely to be 60 pc deep. Thus, if the results of Imai et al. (2007) are confirmed, they would indicate the existence of several unrelated star-forming regions along the line of sight. More observations –some of which have already been collected and partially analyzed– will be necessary to settle this issue.

Perspectives

The results presented in this thesis have allowed us to refine the determination of the distance to two important regions of nearby star-formation, and to start examining the three-dimensional structure of Taurus. They also raised a number of issues that could be tackled with new data, and suggested several follow-up studies.

- As we mentioned, the radio flux of V773 Tau A depends on the orbit phase, being highest at periastron and weakest at apoastron. In most of our observations, it is resolved into two components associated with the two stars in the system. Our observations have shown, however, that near periastron, the position of the radio source is significantly displaced from the position of the associated star. This is additional evidence that the non-thermal emission in the system is affected by the presence of the companion. In a recently accepted proposal, we requested time to observe V773 Tau A near periastron with the High Sensitivity Array (a composite VLBI array comprised of the VLBA, the Green Bank Telescope, and the VLA plus the Arecibo dish in Puerto Rico). These observations will allow us to examine the spatial evolution of this interacting binary when it is near periastron over a six hour period. This ought to shed light on the origin of the variability of the source.

- To decide whether or not several unrelated star-forming regions exist along the line of sight to Ophiuchus, we have also been observing several new sources in the direction of the complex: VSSG 14 in the Oph–B sub-region, and ROX 39 in the region between L1686 and L1689.

- Several other nearby star-forming regions (e.g. Serpens or Perseus) have been studied in detail at many wavelengths but have poorly determined distances. Non-thermal sources are known to exist in these regions, so multi-epoch VLBA observations would allow significant improvements in the determination of their distances. The corresponding observations of Serpens, are indeed already being obtained, whereas Perseus will be the subject of forthcoming proposals.

Measuring Nearby Star Forming Regions with the VLBA: from the Distance to the Dynamics

1 Introduction

This thesis will describe how multi-epoch VLBA observations can be used to measure the distance to nearby young stars to extremely high accuracy. This first chapter is intended as a broad introduction to the subject. We start with a very brief description of astrometry (Sect. 1.1), and explain why high accuracy astrometry of young stars is important (Sect. 1.2). We then move on to describe the two star-forming regions on which we will concentrate: Taurus and Ophiuchus (Sect. 1.3 and 1.4). In Sect. 1.5, we explain why VLBI instruments are ideal to obtain high accuracy astrometric observations of young stars. This leads us to state the specific goals of this thesis (Sect. 1.6). Finally, in Sect. 1.7, we describe the main characteristics of the young stars that will be studied in the rest of the manuscript.

1.1 Astrometry

Astrometry is the branch of astronomy concerned with making precise measurements of the positions of celestial bodies, and of their movements on the celestial sphere. For objects outside of the Solar System, the observed

Table 1.1. Parallax and proper motions as a function of the distance.

Distance [pc]	1	2	5	10	20	50	100	200	500	1000	2000	5000	10000
π [mas]	1000	500	200	100	50	20	10	5	2	1	0.5	0.2	0.1
μ [mas yr^{-1}] †	2000	1000	400	200	100	40	20	10	4	2	1	0.4	0.2

†Proper motions calculated for $v = 10$ km s^{-1}.

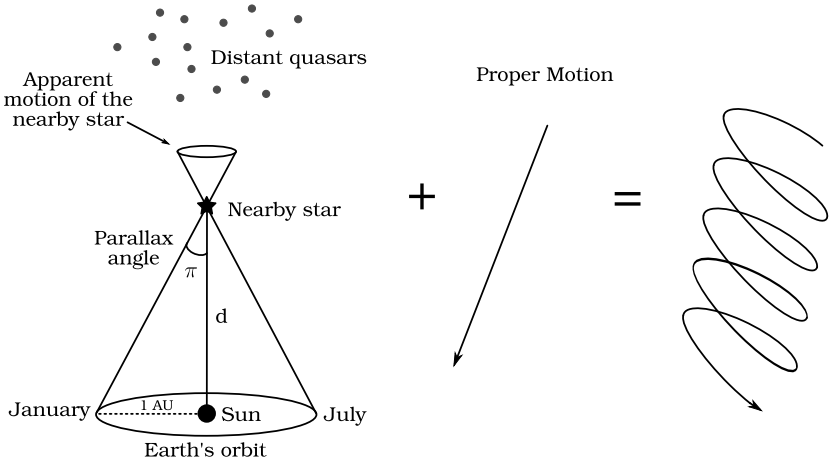

Figure 1.1 Parallax and proper motion.

displacements will result from two contributions. First, the true relative motion between the source and the Sun: the *proper motion*. In most cases, the proper motion can be assumed to be linear and uniform, but in some specific situations (for instance if a star is a member of a multiple system), the proper motion can be non-uniform. The second contribution is the apparent change in the position of the source due to the annual rotation of the Earth about the Sun. The semi-major axis of the elliptical path resulting from this effect is called the *trigonometric parallax* (π), and provides a direct estimate of the distance d to the object (see Fig. 1.1). The value in milli-arcsecond (mas) of the trigonometric parallax as a function of distance are indicated in Tab. 1.1, together with the value of the proper motion in mas yr^{-1} for an object with a rather modest transverse speed of 10 km s^{-1}.

Table 1.2. Distances to Taurus and Ophiuchus star-forming regions.

Region	Distance [pc]	Author
Taurus	135 ± 10	Racine (1968)
	140 ± 20	Elias (1978)
	140 ± 10	Kenyon et al. (1994)
	139^{+10}_{-9}	Bertout et al. (1999)
	140^{+40}_{-12}	Bertout & Genova (2006)
Ophiuchus	145 ± 10	Racine (1968)
	160 ± 20	Elias (1978)
	165 ± 20	Chini (1981)
	125 ± 25	de Geus et al. (1989)
	$120 - 150$	Knude & Hog (1998)
	135 ± 8	Mamajek (2007)
	119 ± 6	Lombardi et al. (2008)

1.2 Motivation

Astrometric observations of young stellar objects can provide a wealth of important information on their properties. First and foremost, an accurate trigonometric parallax measurement is a pre-requisite to the derivation, from observational data, of their most important characteristics (luminosity, age, mass, etc.). Unfortunately, even in the current post-Hipparcos era, the distance to even the nearest star-forming regions (Taurus, Ophiuchus, Perseus, etc.) is rarely known to better than 20 to 30% (e.g. Knude & Hog 1998, Bertout et al. 1999). At this level of accuracy, the luminosity of any given star cannot be assessed to better than 50%. As a consequence, the accuracy with which young stars can be positioned on an HR diagram is rather limited, and the comparison between observations and detailed theoretical models can only be approximate. This unsatisfactory state of affairs is largely the result of the fact that young stars are still embedded in their opaque parental cloud. They are, therefore, dim in the visible bands that were observed by Hipparcos.

The proper motions of young stars are also important because they can be used to characterize the overall dynamics of star-forming regions and the orbital paths of young multiple systems. This last point is particularly important because the mass of the individual stars which can be obtained from Kepler's law provides strong constraints for pre-main sequence evolutionary

models (e.g. Hillenbrand & White 2004).

Much of what we know about the formation of stars has been derived from the observation and modeling of a few nearby regions (Taurus, Ophiuchus, Perseus, Orion, Serpens, etc.). Thus, a significant improvement in the determination of the distance to these few regions would represent a major step forward. In this thesis, we will concentrate on the two nearest regions of low-mass star formation: Taurus and Ophiuchus.

1.3 Taurus

The Taurus star-forming region has been intensively studied, starting with the historical observations of T Tauri and its surroundings by Hind in the 1850s. It contains a few 10^4 $M_\odot$ in molecular gas (e.g. Goldsmith et al. 2008), mostly distributed along three filamentary structures. At smaller scales, these filaments break up into dense clumps and cores with individual masses of 1–100 $M_\odot$. These dense regions are associated with optically visible dark nebulae, cataloged by Barnard or Lynds.

The Taurus region contains a large number of pre-main sequence stars (nearly 400 according to the recent review by Kenyon et al. 2008). Numerous surveys conducted in the last several decades at optical, infrared, radio, and (more recently) X-ray frequencies have revealed the existence of three populations of young stars (e.g. Lada 1987). The embedded (optically invisible) population is believed to be the youngest and is only found in association with dense molecular gas. The two somewhat older populations (the Classical and Weak Line T Tauri stars –WTTS and CTTS) are more dispersed across the cloud, but still follow closely the contours of the molecular gas.

Most young stars in Taurus are grouped into small clusters of a few tens of objects (e.g. Gómez et al. 1993). The most prominent such groups in the central portion of Taurus are associated with the dark clouds L1495, B18, and B22. Another prominent group located to the south of the complex (and containing the famous young star T Tauri) is associated with the dark cloud L1551 (see Kenyon et al. 2008 for a recent review).

Many pre-main sequence stars in Taurus are in binary or multiple systems (see Kenyon et al. 2008). Indeed, the fraction of binaries among pre-main sequence stars in Taurus is similar to or slightly larger than the corresponding figure for field main sequence stars. Most of these binaries are pairs of either

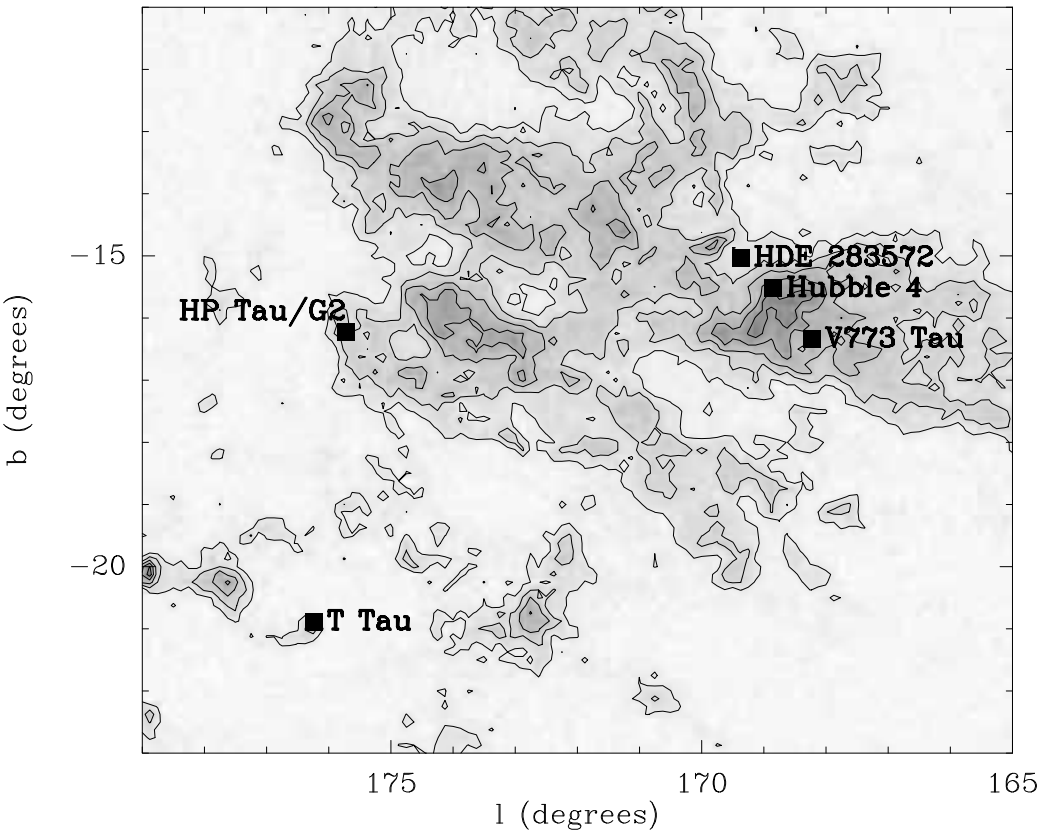

Figure 1.2 ^{12}CO map of Taurus from Dame et al. (2001). The positions of the five stars studied in this thesis are shown as black squares.

two WTTS, or two CTTS, but there are a number of mixed pairs, containing two stars in seemingly different evolutionary stages. We shall see an example of such a system in this thesis (V773 Tau).

The mean distance to Taurus has been determined by a number of authors using various methods. In the last few decades, there has been a consensus for a value of about 140 pc (see Tab. 1.2). However, the extent of Taurus on the plane of the sky is about 25 pc, so it likely to also be about 10–30 pc deep. Moreover, given its filamentary structure, the Taurus complex is unlikely to be "round", and systematic distance differences may well exist within the complex.

1.4 Ophiuchus

Ophiuchus is one of the most active regions of star formation within a few hundred parsecs of the Sun (e.g. Lada & Lada 2003). It comprises a main core associated with the dark cloud L1688, and lower density filaments (called "streamers") associated with the clouds L1704 and L1689 (Fig. 1.3). The core contains over 300 young stellar objects (Wilking et al. 2008). The youngest, more embedded population has a mean age of about 0.3 Myr whereas the more diffusely distributed population is a few million years old. The star formation in Ophiuchus is somewhat more clustered than in Taurus, and more massive stars are being formed in Ophiuchus than in Taurus. Indeed, one the stars that will be included in this thesis (S1) is a B star of about 6 $M_{\odot}$.

The Ophiuchus cloud has played an important role in the development of our understanding of star formation, and remains an important benchmark for this field of research. As for Taurus, detailed multi-wavelengths observations are available (see the review by Wilking et al. 2008).

Traditionally assumed to be at 165 ± 20 pc (Chini 1981), Ophiuchus has recently been suggested to be somewhat closer. For example, de Geus et al.

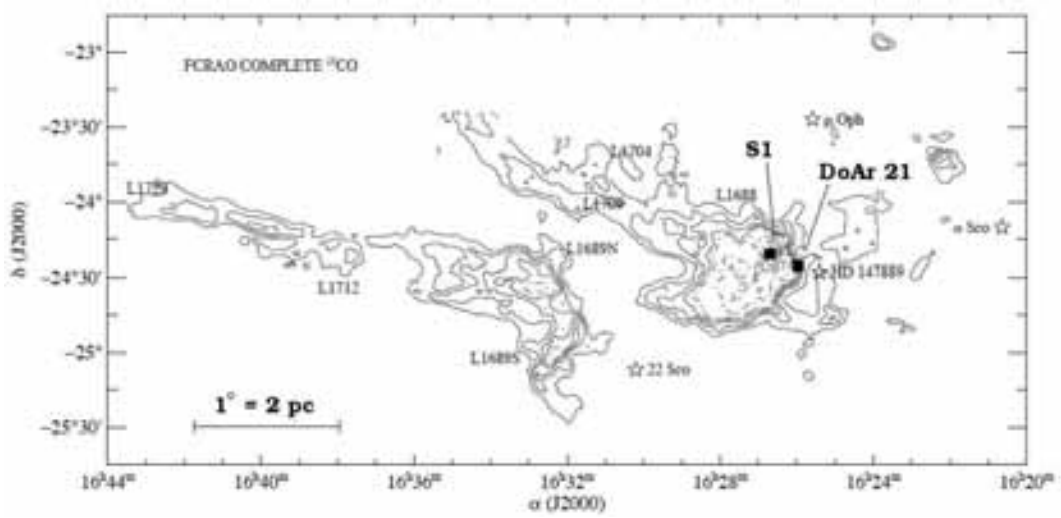

Figure 1.3 ^{13}CO map of Ophiuchus from Ridge et al. (2006). The main dark clouds are indicated, and the positions of the two stars studied in this thesis are shown as black squares.

(1989) found a mean photometric distance of 125 ± 25 pc. Knude & Hog (1998), who examined the reddening of stars in the direction of Ophiuchus as a function of their Hipparcos distances, also found a clear extinction jump at 120 pc. Using a similar method, Lombardi et al. (2008) also find a distance of about 120 pc for the Ophiuchus core. Finally, Mamajek (2007) identified reflection nebulae within 5° of the center of Ophiuchus, and obtained the trigonometric parallax of the illuminating stars from the Hipparcos catalog. From the average of these Hipparcos parallaxes, he obtains a mean distance to Ophiuchus of 135 ± 8 pc. While the core of Ophiuchus is fairly compact (about 1°, or 2 pc), the total extent of the streamers on the plane of the sky is about 5 degrees (≡ 10 pc; Fig. 1.3). It is therefore possible that distance gradients might exist across the streamers.

1.5 VLBI parallax measurements

Since observations of young stars in the visible range are limited by the effect of dust extinction, one must turn to a more favorable wavelength regime in order to obtain high quality astrometric data. Radio observations, particularly using large interferometers is currently the best prospect because the interstellar medium is largely transparent at these wavelengths, and because the astrometry delivered by radio-interferometers is extremely accurate and calibrated against fixed distant quasars. Of course, only those young stars associated with radio sources are potential targets. Moreover, radio-interferometers effectively filter out any emission more extended than a certain limiting angular size, so only compact sources will be detectable.

Low-mass young stars often generate non-thermal continuum emission produced by the interaction of free electrons with the intense magnetic fields that tend to exist near their surfaces (e.g. Feigelson & Montmerle 1999; see Chap. 2). Since the magnetic field strength decreases quickly with the distance to the stellar surface (as r^{-3} in the magnetic dipole approximation), the emission is strongly concentrated to the inner few stellar radii. If the magnetic field intensity and the electron energy are sufficient, the resulting compact radio emission can be detected with Very Long Baseline Interferometers (VLBI –e.g. André et al. 1992). The relatively recent possibility of accurately calibrating the phase of VLBI observations of faint, compact radio sources using nearby quasars makes it possible to measure the absolute position of these objects (or, more precisely, the angular offset between

them and the calibrating quasar) to better than a tenth of a milli-arcsecond. This level of precision is sufficient to constrain the trigonometric parallax of sources within a few hundred parsecs of the Sun (in particular of nearby young stars) with a precision better than a few percent using multi-epoch VLBI observations (see Tab. 1.1).

1.6 Goals

Taking advantage of the very accurate astrometry attainable with the *Very Long Baseline Array* (VLBA) of the National Radio Astronomy Observatory (NRAO), we initiated a large project aimed at accurately measuring the trigonometric parallax of a significant sample of magnetically active young stars in nearby star-forming regions (Taurus, Ophiuchus, Perseus, Cepheus, and Serpens) using the VLBA with accuracies one to two orders of magnitude better than the present values.

The specific goal of this thesis is to use multi-epoch radio-interferometric VLBA observations of seven young stellar objects in Taurus and Ophiuchus in order to measure their displacement over the celestial sphere, and deduce their trigonometric parallax and proper motion with a level of precision that currently cannot be attained at any other wavelength.

1.7 Sources

We chose from the literature a list of seven young stellar objects: five in the Taurus complex (T Tau, Hubble 4, HDE 283572, HP Tau/G2 and V773 Tau A; Fig. 1.2), and two in the Ophiuchus complex (S1 and DoAr 21; Fig. 1.3). Those sources are low- to intermediate-mass ($M \lesssim 3\ M_\odot$) pre-main sequence stars (with the exception of S1 which is a main sequence B star). All seven sources were previously known to be non-thermal radio emitters, and had been detected with VLBI techniques in the past.

T Tau— T Tau was initially identified as a single optical star, with unusual variability and peculiar emission lines (Barnard 1895, Joy 1945, and references therein). Early infrared observations then revealed the existence of a heavily obscured companion (hereafter T Tau S) located about $0\farcs7$ to the south of the visible star (Dyck et al. 1982) and most likely gravitationally bound to it (Ghez et al. 1991). Recently, this infrared companion was itself

found to contain two sources (T Tau Sa and T Tau Sb; Koresko 2000 and Kohler et al. 2000) in rapid relative motion (Duchêne et al. 2002; Furlan et al. 2003). Thus, T Tau is now acknowledged to be at least a triple stellar system. At radio wavelengths, T Tau has long been known to be a double source (Schwartz et al. 1986). The northern radio component is associated with the optical star and mostly traces the base of its thermal jet (e.g., Johnston et al. 2003), whereas the southern radio source is related to the infrared companion and is thought to be the superposition of a compact component of magnetic origin and an extended halo, presumably related to stellar winds (Johnston et al. 2003; Loinard et al. 2003).

The non-thermal mechanisms at the origin of the compact radio emission in T Tau S require the presence of an underlying, magnetically active star (Skinner 1993). Specifically, the emission is expected to be either gyrosynchrotron radiation associated with reconnection flares in the stellar magnetosphere and at the star-disk interface or coherently amplified cyclotron emission from magnetized accretion funnels connecting the disk to the star (Dulk 1985; Feigelson & Montmerle 1999; Smith et al. 2003). In all cases, the emission is produced within less than about 10 stellar radii (roughly 30 $R_\odot$) of the star itself. Indeed, 3.6 cm VLBA observations revealed the existence, near the expected position of T Tau Sb, of a source with an angular size less than about 15 $R_\odot$ (Smith et al. 2003). Because it is so small, any structural changes in this compact radio component would occur on such small scales that the effects on the astrometry would be very limited. Thus, observations focusing on it should accurately trace the path of the underlying pre-main sequence star.

Hubble 4 and HDE 283572— Hubble 4 (V1023 Tau, HBC 374, IRAS 0415+2813) is a K7 naked T Tauri star with an effective temperature of 4060 K (Briceño et al. 2002). It has long been known to have a particularly active magnetosphere that produces non-thermal radio emission characterized by significant variability, large circular polarization and a nearly flat spectral index (Skinner 1993). It was detected in VLBI experiments, with a flux of a few mJy by Phillips et al. (1991), and is also an X-ray source (Güdel et al. 2007). The superficial magnetic field of Hubble 4 has been estimated to be about 2.5 kG using Zeeman-sensitive Ti I lines (Johns-Krull et al. 2004). HDE 283572 (V987 Tau, HIP 20388), on the other hand, is a somewhat hotter ($T_{\rm eff}$ = 5770 K –Kenyon & Hartmann 1995) G5 naked T Tauri star. Early observations with the Einstein satellite showed that it has a fairly bright

X-ray counterpart (Walter et al. 1987). It was initially detected as a radio source by O'Neal et al. (1990), and in VLBI observations by Phillips et al. (1991) with a flux of about 1 mJy.

HP Tau/G2— The well-known variable star HP Tau (IRAS 04328+2248) was discovered by Cohen & Kuhi (1979) to be surrounded by a small group of young stars (called HP Tau/G1, HP Tau/G2, and HP Tau/G3). HP Tau/G1 is located about 20″ north of HP Tau, whereas HP Tau/G2 and HP Tau/G3 are about 15″ to its south-east (see the finding charts in Fig. 22 of Cohen & Kuhi 1979). HP Tau/G2 and HP Tau/G3 are believed to form a gravitationally bound system with a separation of about 10″. Recently, HP Tau/G3 was itself found to be a tight binary (Richichi et al. 1994), so the HP Tau/G2 - HP Tau/G3 system appears to be a hierarchical triple system. HP Tau/G2 is a weak-line T Tauri star of spectral type G0, with an effective temperature of 6030 K (Briceño et al. 2002). It is somewhat obscured ($A_V \sim 2.1$ mag) and has a bolometric luminosity of 6.5 $L_\odot$ (Briceño et al. 2002; Kenyon & Hartmann 1995). This corresponds to an age of about 10.5 Myr and a mass of 1.58 $M_\odot$ (Briceño et al. 2002). The first radio detection of HP Tau/G2 was reported by Bieging et al. (1984) who found a 5 GHz flux of 5–7 mJy. A few years later, however, the flux had fallen to only about 0.3 mJy (Cohen & Bieging 1986). Such strong variability is suggestive of non-thermal processes (e.g. Feigelson & Montmerle 1999). The successful detection of HP Tau/G2 in VLBI experiments (at levels of 1 to 3 mJy) by Phillips et al. (1991) confirmed the non-thermal origin of the radio emission.

V773 Tau— The young stellar system V773 Tau (HD 283447, HBC 367, HIP 19762, IRAS 04111+2804) is located in the surroundings of the dark cloud Lynds 1495 in Taurus. V773 Tau has been known to be a multiple system since it was almost simultaneously found to be a double-line spectroscopic binary (V773 Tau A) with an orbital period of about 51 days (Welty 1995), and to have a companion at about 150 mas (V773 Tau B; Ghez et al. 1993, Leinert et al. 1993). More recently, Duchêne et al. (2003) identified a fourth component in the system (V773 Tau C), showing that V773 Tau is (at least) a quadruple system. This fourth component belongs to the still poorly understood class of "infrared companions" (young stellar sources, fairly bright in the infrared but invisible at optical wavelengths, which have been discovered around a small number of T Tauri stars). It is interesting to point out that the four (almost certainly coeval) stars in V773 Tau belong to three different spectral classes: both members of the spectroscopic binary

are WTTS, the optical companion is a CTTS, and the fourth member is (as mentioned above) an infrared companion. Such a variety of apparently distinct evolutionary stages in a single system likely reflects the effect of binarity on the evolution of young stars.

The relative orbital motion between the spectroscopic binary and the two companions has been monitored by Duchêne et al. (2003), and the orbit between the two members of the spectroscopic binary has recently been investigated in detail by Boden et al. (2007) who combined (optical) Radial Velocity measurements, Keck Interferometer data, and radio VLBI images. Using these data, Boden et al. (2007) constructed a preliminary physical orbit for the spectroscopic binary system, which yields masses of 1.54 and 1.33 $M_\odot$ for the primary and the secondary, respectively. The distance to the system obtained from these data is 136.2 ± 3.7 pc. There is also a direct trigonometric parallax measurement based on multi-epoch VLBI observations for this source (Lestrade et al. 1999). This VLBI-based distance measurement ($d = 148.4^{+5.7}_{-5.3}$ pc) is roughly consistent (at the 2–3 σ level) with the value obtained from the orbital fit.

V773 Tau A has long been known to be a strong radio source (Kutner et al. 1986). Indeed, it was the strongest source in the 5 GHz VLA survey of WTTS in the Taurus-Auriga molecular cloud complex by O'Neal et al. (1990). The two companions V773 Tau B and C, on the other hand, are not known to be radio sources. From detailed multi-frequency observations, Feigelson et al. (1994) concluded that the radiation was most likely of non-thermal origin. This was confirmed by Phillips et al. (1991) who obtained VLBI observations, and resolved the radio emission into a clear double source, most likely corresponding to the two components of the spectroscopic binary. More recently, Massi et al. (2002, 2006) showed that the radio emission exhibits periodic variations with a period corresponding to the 51 day orbital period of the spectroscopic binary. This variability is due to an increase in the flaring activity near periastron and likely reflect interactions between the magnetospheres of the two stars when they get close to one another. Finally, Boden et al. (2007) and Massi et al. (2008) also resolved the radio emission from V773 Tau A into two components, which they associate with the two stars in the spectroscopic binary.

S1 and DoAr 21— The star S1 (IRAS 16235-2416, ROX 14, YLW 36) of spectral type B4, and $M \sim 6$ $M_\odot$, is among the brightest red and near-infrared objects in Ophiuchus (Grasdalen et al. 1973). It is also the brightest

far-infrared member of the cluster (Fazio et al. 1976), a very bright X-ray source (ROX 14 –Montmerle et al. 1983), and the brightest steady radio stellar object in Ophiuchus (Leous et al. 1991). S1 is fairly heavily obscured ($A_V \sim 10$), and there is clear evidence for an interaction between S1 and the dense gas associated with Oph-A sub-region, and traced by DCO^+ emission (Loren et al. 1990). Moreover, the age of the H II region excited by S1 is estimated to be about 5,000 yr (André et al. 1988). DoAr 21 (V2246 Oph, Haro 1-6, HBC 637, ROX 8, YLW 26) is a somewhat less massive star (~ 2.2 $M_\odot$) of spectral type K1. Like S1, it is fairly obscured ($A_V \sim 6-7$), and probably younger than 10^6 yr. It is associated with a bright X-ray source (ROX 8 –Montmerle et al. 1983), and with a strongly variable radio source (Feigelson & Montmerle 1985). Although it has long been classified as a naked T Tauri star (e.g. André et al. 1990), it was recently found to show a substantial infrared excess at 25 μm (Jensen et al. 2009) suggestive of a circumstellar disk. As mentioned above, both S1 and DoAr 21 are fairly strong radio sources. Indeed, both have been detected at 6 cm in previous VLBI experiments: S1 with a flux density of 6–9 mJy (André et al. 1991), and DoAr 21 with a flux density of nearly 10 mJy (Phillips et al. 1991).

1.8 Conclusions

In this chapter, we justified why VLBI parallax measurements of young stars in nearby star-forming regions are important. We also described briefly the structure of the two regions (Taurus and Ophiuchus) on which we will focus in this thesis, and presented the main characteristics of the seven young stars that were observed as part of this work. In the next chapter, we will examine in more detail the processes at work to generate the non-thermal radiation emitted by young stars.

2

Emission Processes of Radio Waves

In Chapter 1, we mentioned that all seven sources presented in this thesis produce non-thermal radio emission. This kind of emission in young stellar objects is due to electrons spiraling in a magnetic field, as will be described in this chapter. Our treatment is based primarily on the book by Rybicki & Lightman (1986), and the articles of Dulk (1985), Robinson & Melrose (1984), and Petrosian & McTiernan (1983).

2.1 Electromagnetic waves

An electromagnetic wave is a transversal wave composed of an electric and magnetic field oscillating together. The fields are oriented perpendicular to each other, and the wave travels in a direction perpendicular to both fields. Electromagnetic waves can be characterized by any of three properties: wavelength λ, frequency ν, and energy E of the individual photons. The

relationships between wavelength, frequency, and energy are:

$$\lambda = \frac{c}{\nu} = \frac{hc}{E} \tag{2.1}$$

where c is the speed of light, and h is the Planck constant.

The polarization is a property of electromagnetic waves that describes the orientation of their electric fields, that may be oriented in a single direction (linear polarization) or rotate (circular and elliptical polarization). For circular polarization the electric field vector describes a helix along the direction of wave propagation, and may be referred to as right or left, depending on the direction in which the electric field vector rotates.

In the most general sense, an electromagnetic wave is generated by accelerating charges. In the next sections we will describe the relevant processes at radio wavelengths.

2.2 Radiation at radio wavelengths

Much of the radiation emitted as radio waves by astrophysical objects is due to individual electrons accelerated by collisions with ions or by spiraling in a magnetic field. In this case the radiation is the result of a random process of collisions and it is incoherent.

In some cases there could exist an efficient process where the energy of the electrons is converted into some natural wave mode of the plasma (e.g. electron-cyclotron or Langmuir waves). These waves are in the radio-frequency domain because the characteristic frequencies of plasma are typically $\lesssim 10^{10}$ Hz, and they are:
the electron plasma frequency

$$\nu_{\rm p} = \left[\frac{n_e e^2}{\pi m_e}\right]^{1/2} \simeq 9000\ n_e^{1/2} \tag{2.2}$$

and the electron-cyclotron frequency

$$\nu_{\rm B} = \frac{eB}{2\pi m_e c} \simeq 2.8 \times 10^6\ B \tag{2.3}$$

where n_e is the electron density, e the electric charge, m_e the electron mass, B the magnetic field, and c is the speed of light.

It is possible to have resonances between particles and waves with these characteristic frequencies (Eqs. 2.2 and 2.3). These can rapidly extract any free energy that might exist in the electron distribution. Plasmas with free energy can only exist when the electron-electron and electron-ion collision frequencies are neither as high as the resonance frequencies nor so high as to restore the plasma quickly to equilibrium and thus quench the instabilities. This is the major reason that amplified radiation (maser) is generally confined to radio frequencies. The resistive instabilities could amplify a particular wave mode and lead to coherent emission as in the case of an electron-cyclotron maser.

2.3 Radiative transfer

The equation of radiative transfer is usually written in terms of the specific intensity I_ν:

$$\frac{dI_\nu}{d\tau_\nu} = -I_\nu + S_\nu \tag{2.4}$$

where τ_ν is the optical depth and S_ν is the source function defined as the ratio of the emission coefficient to the absorption coefficient:

$$S_\nu = \frac{\eta_\nu}{\kappa_\nu}. \tag{2.5}$$

From Eq. 2.4 we see that if $I_\nu > S_\nu$ then $\frac{dI_\nu}{d\tau_\nu} < 0$, and I_ν tends to decrease. If $I_\nu < S_\nu$ then I_ν tends to increase. Thus the source function is the quantity that the specific intensity tries to approach, and does approach if given sufficient optical depth. In this respect the transfer equation describes a "relaxation" process.

A black body is an idealized object that absorbs all electromagnetic radiation that falls on it. No electromagnetic radiation passes through it and none is reflected. Because no electromagnetic radiation is reflected or transmitted, the object appears black when it is cold. The thermal radiation from a black body is called blackbody radiation.

Two important properties of I_ν in that case, are that (1) it depends only on the temperature, and (2) it is isotropic. Therefore we have the relation

$$I_\nu(T) \equiv B_\nu(T) \tag{2.6}$$

where the function $B_\nu(T)$ is called the Planck function.

If we consider that the material of the object is emitting at temperature T, so that its emission depends solely on its temperature and internal properties, then we have the relation

$$S_\nu = B_\nu(T) \tag{2.7}$$

and the emissivity η_ν can be related to the absorption coefficient κ_ν and temperature by the Kirchoff law:

$$\eta_\nu = \kappa_\nu B(T) \tag{2.8}$$

the transfer equation for thermal radiation is, then

$$\frac{dI_\nu}{d\tau_\nu} = -I_\nu + B_\nu(T). \tag{2.9}$$

Note that for blackbody radiation $I_\nu = B_\nu$, whereas for thermal radiation $S_\nu = B_\nu$. Thermal radiation becomes blackbody radiation only for optically thick media.

The Planck function represents the emitted power per unit area of emitting surface, per unit solid angle, and per unit frequency. It can be expressed as a function of frequency, and is written as

$$B_\nu(T) = \frac{2h\nu^3/c^2}{\mathrm{e}^{(h\nu/kT)-1}}. \tag{2.10}$$

Eq. 2.10 is called the Planck law, and describes the spectral radiance of electromagnetic radiation at all wavelengths from a black body at temperature T.

For $h\nu \ll kT$ the exponential in Eq. 2.10 can be expanded and we have the Rayleigh–Jeans law:

$$I_\nu^{\mathrm{RJ}}(T) = \frac{2\nu^2}{c^2} kT \tag{2.11}$$

that applies at low frequencies. In particular, it almost always applies in the radio region.

One way to characterize brightness at a certain frequency is to give the temperature of the blackbody having the same brightness at that frequency. That is, for any value I_ν we define the brightness temperature $T_\mathrm{b}(\nu)$ by

$$I_\nu = B_\nu(T_\mathrm{b}). \tag{2.12}$$

The effective temperature T_eff of a source is derived from the total amount of flux, integrated over all frequencies, radiated at the source. We obtain T_eff by equating the actual flux F to the flux of a blackbody at temperature T_eff:

$$F = \int cos\theta \; I_\nu \; d\nu d\Omega \equiv \sigma \; T_\mathrm{eff}^4. \tag{2.13}$$

In radio astronomy, where the Rayleigh–Jeans law is applicable, it is convenient to change variables from I_ν to brightness temperature T_b. So that for $h\nu \ll kT$ we have

$$I_\nu = \frac{2\nu^2}{c^2} k \; T_\mathrm{b}. \tag{2.14}$$

It is also convenient to replace the source function S_ν by the effective temperature T_eff of the radiating electrons, using the Kirchoff law:

$$S_\nu = \frac{2\nu^2}{c^2} k \; T_\mathrm{eff}. \tag{2.15}$$

I_ν can be written as a combination of the orthogonal polarizations as

$$I_\nu^\mathrm{tot} = I_\nu^\mathrm{p1} + I_\nu^\mathrm{p2} \tag{2.16}$$

in this case, there will be no factor of 2 in the equations for I_ν and S_ν.

Eqs. 2.14 and 2.15 allow us to write Eq. 2.4 for radiative transfer in the form:

$$\frac{dT_\mathrm{b}}{d\tau_\nu} = -T_\mathrm{b} + T_\mathrm{eff} \tag{2.17}$$

or, if we use the geometry of Fig. 2.1, we can write:

$$T_\mathrm{b} = \int_0^{\tau_\nu} T_\mathrm{eff} \; \mathrm{e}^{-t_\nu} \; dt_\nu + T_\mathrm{bo} \; \mathrm{e}^{-\tau_\nu} \tag{2.18}$$

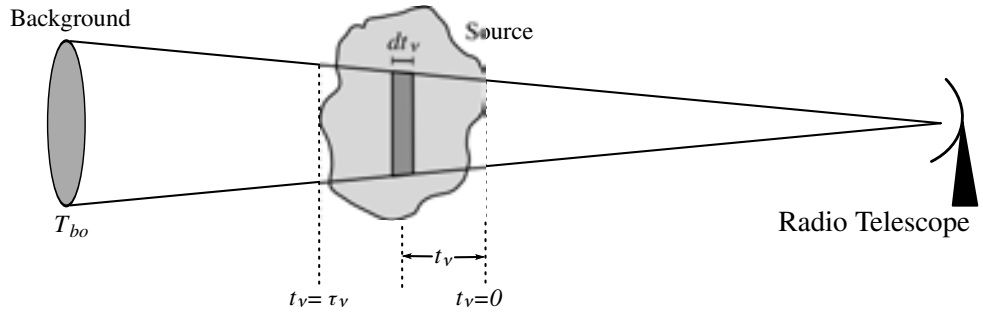

Figure 2.1 A source of optical depth τ_ν located in front of a background of brightness temperature $T_{\rm bo}$.

In the special case of an isolated source with constant $T_{\rm eff}$, Eq. 2.18 reduces to

$$T_{\rm b} = T_{\rm eff}[1 - e^{-\tau_\nu}] \tag{2.19}$$

$$T_{\rm b} = \begin{cases} T_{\rm eff} & \text{if} \quad \tau_\nu \gg 1 \\ T_{\rm eff}\ \tau_\nu = \dfrac{c^2}{\nu^2}\dfrac{\eta_\nu L}{k} & \text{if} \quad \tau_\nu \ll 1 \end{cases} \tag{2.20}$$

where L is the size of the source along the line of sight.

For incoherent radiation, Eq. 2.20 shows that the radiation cannot attain a value of $T_{\rm b}$ higher than $T_{\rm eff}$, where $T_{\rm eff}$ is related to the average energy of the emitting particles:

$$\langle E \rangle = kT_{\rm eff} \tag{2.21}$$

$T_{\rm eff}$ and $T_{\rm b}$ of incoherent emission are usually limited to about 10^9 to 10^{10} K. Higher values imply a coherent mechanism, such as maser or plasma radiation.

The flux density J_ν of a radio source is related to the brightness temperature by

$$J_\nu = \frac{\nu^2}{c^2} k \int T_{\rm b}\ d\Omega, \tag{2.22}$$

where $d\Omega$ is a differential solid angle and the integral is over the projected area of the source.

The circular polarization reflects the direction of the magnetic field in the source. The degree of circular polarization r_c is given by

$$r_c = \frac{T_{b-} - T_{b+}}{T_{b-} + T_{b+}} \tag{2.23}$$

where T_b is the brightness temperature, and the two signs, (+) and (−), correspond to two different directions of rotation of electric field. The (−) sign is related to the right-hand-side circular polarization of electromagnetic wave, when the direction of the electric field rotation coincides with the direction of an electron gyration in the magnetic field. In optics, such a wave is usually referred to as the extraordinary wave. The (+) sign is related to the left-hand-side circular polarization of electromagnetic wave, that in optics is usually referred to as the ordinary wave.

Eq. 2.23 will be valid when we have no significant variations in the magnetic field strength, the effective temperature or the angle between the line of sight and the magnetic field across the region.

Finally, a very useful quantity is the frequency of peak flux density $\nu_{\rm peak}$ in a spectrum that changes from a positive to a negative slope (see Fig. 2.2).

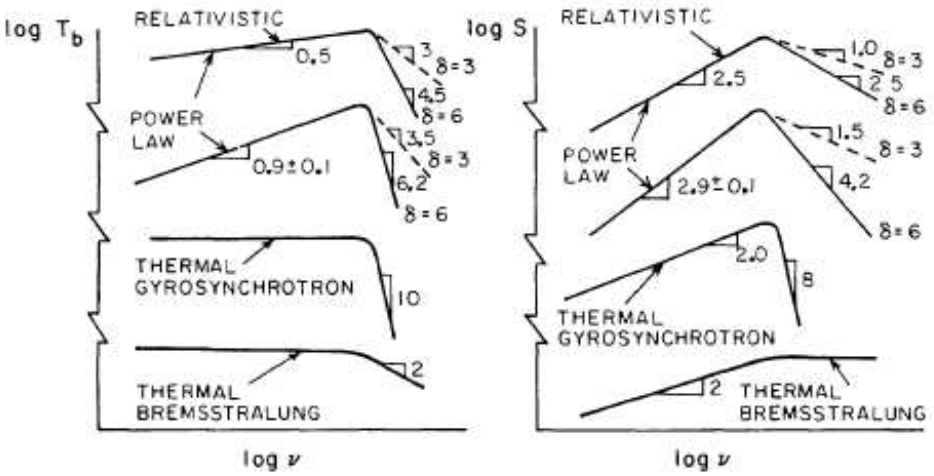

Figure 2.2 Spectra of brightness temperature and flux density for gyrosynchrotron radiation from Dulk (1985).

The peak occurs at that frequency where

$$\tau_\nu = \kappa_\nu L \approx 1. \tag{2.24}$$

For gyrosynchrotron emission, $\nu_{\rm peak}$ depends very strongly on the magnetic field strength and the average electron energy, but very weakly on electron numbers or path lengths.

2.4 Continuous radiation from radio sources

Radio sources can be classified into two categories: those which radiate by thermal mechanisms and the others, which radiate by non-thermal processes. In principle many different radiation mechanisms could be responsible for non-thermal emission, but in practice one single mechanism seems to dominate: synchrotron emission.

With the exception of thermal line emission of atoms and molecules, and thermal emission from solid bodies, radio emission always arises from free electrons, and since free electrons can exchange energy by arbitrary amounts, no definite energy jumps will occur: thus we are dealing with a continuous spectrum.

2.5 Acceleration due to particle gyration

When a plasma contains a magnetic field, accelerations due to particle collisions can often be negligible in comparison with those due to gyration around the field lines (see Fig. 2.3). There are three possible cases of emission: *cyclotron* for non-relativistic particles (Lorentz factor γ =1), *gyrosynchrotron* for mildly relativistic particles ($\gamma \lesssim 2$ or 3), and *synchrotron* for highly relativistic particles ($\gamma \gg 1$).

In the case of cyclotron emission, *thermal electron* distributions are of most interest because the average energy of electrons is low, leading to frequent collisions and generally to *Maxwellian* distributions. Emission is concentrated at low harmonics ($s \lesssim 10$) and at the fundamental frequency $\omega = \Omega_{\rm e}$, where $\Omega_{\rm e}$ is the electron cyclotron frequency. Radiation at the fundamental frequency ($s = 1$) is directed mainly along the magnetic field, and radiation at low harmonics is mainly at moderate angles.

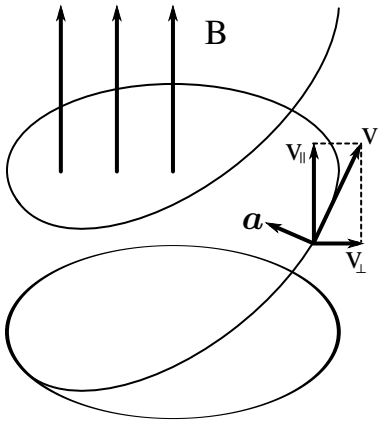

Figure 2.3 Helical motion of a particle in a uniform magnetic field.

In the opposite limit of synchrotron radiation, electron collisions are rare, a *non-Maxwellian tail* is generally dominant, and the energy distribution of the electrons is usually well described by a *power-law*. Emission is distributed over a broad continuum at high harmonics near $s \approx (\gamma\ sin\theta)^3$, i.e. near frequency $\omega \approx \Omega_e \gamma^2\ sin\theta$. Emission is directed very strongly in the direction of the instantaneous electron motion, which leads, for approximately isotropic distributions, to a peak of radiation perpendicular to the field.

In the intermediate case of gyrosynchrotron radiation, both *thermal* and *power-law* distributions are of interest, emission at harmonics $10 \lesssim s \lesssim 100$ is of major importance, and the emission from approximately isotropic electrons has a broad maximum perpendicular to the field.

2.6 Gyrosynchrotron emission from thermal electrons

For temperatures in the range from 10^7 to 10^9 K, emission and absorption are usually important in the range of harmonics from 10 to 100. Thus, one cannot use only the leading terms of a power-series expansion of the Bessel functions (as for non-relativistic electrons) or the Airy integral approximation (as for relativistic electrons). Analytical expressions had been derived for the radiation, and here we will give a simple expression from Dulk et al. (1979)

that is valid in the ranges $10^8 \lesssim T \lesssim 10^9$ K and $10 \lesssim s \lesssim 100$:

$$\frac{\kappa_\nu B}{N} \approx 50\ T^7\ [sin\theta]^6\ \left[\frac{B}{\nu}\right]^{10} \tag{2.25}$$

where κ_ν is the absorption coefficient, N is the number of electrons per cubic centimeter, and θ is the angle between the line of sight and magnetic field.

The source function, the degree of circular polarization for small optical depth, and the frequency of maximum flux density for a homogeneous source are given by:

$$S_\nu = \frac{\eta_\nu}{\kappa_\nu} \approx 1.2 \times 10^{-24}\ T\ \left[\frac{B\nu}{\nu_{\rm B}}\right]^2 \tag{2.26}$$

$$r_{\rm c} \approx 13.1\ T^{-0.138} 10^{0.231 cos\theta - 0.219 cos^2\theta}\ \left[\frac{\nu}{\nu_{\rm B}}\right]^{-0.782+0.545 cos\theta} \qquad (\tau_\nu \ll 1) \tag{2.27}$$

$$\nu_{\rm peak} \approx \begin{cases} 1.4\ \left[\frac{N\ L}{B}\right]^{0.1}\ [sin\theta]^{0.6}\ T^{0.7}\ B & (10^8 < T < 10^9\ {\rm K}) \\ 475\ \left[\frac{N\ L}{B}\right]^{0.05}\ [sin\theta]^{0.6}\ T^{0.5}\ B & (10^7 < T < 10^8\ {\rm K}) \end{cases} \tag{2.28}$$

2.7 Gyrosynchrotron emission from power-law electrons

We now consider an electron population that is isotropic in pitch angle and has a power law energy distribution:

$$n(E) = KE^{-\delta} \tag{2.29}$$

where K is related to N, the number of electrons per cubic centimeter with $E > E_0$, by

$$K = (\delta - 1)\ E_0^{\delta - 1}\ N. \tag{2.30}$$

Electrons with energy less than 50 to 100 keV contribute very little to the radiation, and for normalization we assume $E_0 = 10$ keV $= 1.6 \times 10^{-8}$ erg.

Empirical expressions (from Dulk & Marsh 1982) for the quantities, valid over the range $2 \lesssim \delta \lesssim 7$, $\theta \gtrsim 20°$, and $10 \lesssim \nu/\nu_{\rm B} \lesssim 100$ is given by:

$$\frac{\kappa_\nu B}{N} \approx 1.4 \times 10^{-9} 10^{-0.22\delta} \left[sin\theta\right]^{-0.9+0.72\delta} \left[\frac{\nu}{\nu_{\rm B}}\right]^{-1.30-0.98\delta} \tag{2.31}$$

The emissivity, degree of circular polarization, effective temperature, and the frequency of maximum flux density are given by:

$$\frac{\eta_\nu}{BN} \approx 3.3 \times 10^{-24} 10^{-0.52\delta} \left[sin\theta\right]^{-0.43+0.65\delta} \left[\frac{\nu}{\nu_{\rm B}}\right]^{1.22-0.90\delta} \tag{2.32}$$

$$r_c \approx 1.26\ 10^{0.035\delta} 10^{-0.071 cos\theta} \left[\frac{\nu}{\nu_{\rm B}}\right]^{0.782+0.545 cos\theta} \qquad (\tau_\nu \ll 1) \tag{2.33}$$

$$T_{\rm eff} \approx 2.2 \times 10^{9} 10^{-0.31\delta} \left[sin\theta\right]^{-0.36-0.06\delta} \left[\frac{\nu}{\nu_{\rm B}}\right]^{0.50+0.085\delta} \tag{2.34}$$

$$\nu_{\rm peak} \approx 2.72 \times 10^{3} 10^{0.27\delta} \left[sin\theta\right]^{0.41+0.03\delta} \left[N\ L\right]^{0.32-0.03\delta} \times B^{0.68+0.03\delta}. \tag{2.35}$$

2.8 Conclusions

In this chapter we briefly reviewed the possible cases of emission due to particle gyration around magnetic fields: cyclotron, gyrosynchrotron, and synchrotron radiation. In the case (appropriate for young stars) of mildly relativistic electrons, gyrosynchrotron emission is produced. Depending on the situation, the electrons can have a *thermal* or a *power-law* energy distribution.

3
Interferometry

Having examined the processes that generate non-thermal radiation in young stars, we now move on to describe the instruments used to detect this kind of emission. Treatment is based mostly on the books by Wilson et al. (2009) and Thompson et al. (2001).

3.1 The interferometer

The angular resolution of a radio telescope is $\delta \sim \frac{\lambda}{D}$ where λ is the wavelength of the radiation received, and D is the diameter of the telescope. In order to improve this angular resolution, for a given wavelength, the diameter D of the telescope must be increased. Obviously, there are practical limits on how large a telescope can be built. In the radio domain, this limit is in the range of 100–300 m depending on the technical and financial means available.

Therefore, radio astronomers have increased the effective resolving power of their instruments by joining together the outputs of several small telescopes separated by a maximum distance D. The basic principle behind such an *interferometer* may become clear from considering Fig. 3.1 where we compare the electric field patterns produced be a filled aperture telescope of uniform illumination, with that of a reflector in which only the outer edge of the

aperture is illuminated. This figure shows that the resolving powers of the main beams of these two configurations are comparable. The main difference is in the side lobe level; in the second case this level is of the same order as the main beam, whereas it is much lower in the first situation. An image formed by such a two-element instrument therefore will differ considerably from that of a conventional full aperture. It will be corrupted by contributions of a large number of side lobes. As we shall see, there are techniques to remove (or at least minimize) those effects.

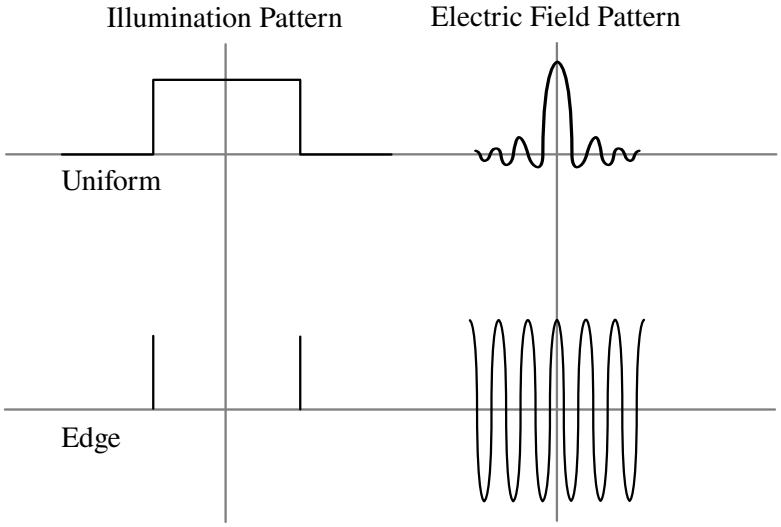

Figure 3.1 Comparison of aperture illumination and resulting electric field pattern. The upper panel shows a uniformly illuminated full aperture, the lower one, an instrument in which only the outer edge is illuminated.

3.2 The mutual coherence function

Suppose that we have a plane monochromatic wave propagating through space. If we know the intensity of the electromagnetic field at a position P_1, it is possible to calculate the field intensity at another position P_2 for all times. In this case the wave is said to be fully *coherent*. Now, if we have an arbitrary polychromatic wave, the field and the time variation at P_1 has no relation to the field at P_2, and this is the case of an *incoherent* wave.

A measure of coherence is given by the mutual coherence function of the

(complex) wave field $U(P_1, t_1)$ and $U(P_2, t_2)$:

$$\begin{aligned}\Gamma(P_1, P_2, \tau) &= \lim_{T\to\infty}\frac{1}{2T}\int_{-T}^{T} U(P_1, t)U^*(P_2, t+\tau)\ dt \\ &= \langle U(P_1, t)U^*(P_2, t+\tau)\rangle\end{aligned} \tag{3.1}$$

where the brackets are used to indicate time averaging.

For a plane monochromatic wave field propagating in the z direction, Γ is easily computed. Using a complex representation, $U(P, t) = U_0 e^{\mathrm{i}(kz-\omega t)}$, where $P = (x, y, z)$, $k = 2\pi/\lambda = \text{const}$, $\omega = 2\pi\nu = \text{const}$, we get

$$\Gamma(P_1, P_2, \tau) = \mid U_0 \mid \mathrm{e}^{\mathrm{i}[k(z_1-z_2)+\omega\tau]}, \tag{3.2}$$

where τ is the time delay. The mutual coherence function of the travelling monochromatic wave field is thus periodic with a constant amplitude and a wavelength equal to that of the original wave field. The coherence function does not propagate; it is a standing wave with a phase such that, for $\tau = 0$, $\Gamma = \Gamma_{max}$ for $z_1 = z_2$. It is often useful to normalize Eq. 3.1 by referring it to a wave field of intensity I. Thus

$$\gamma(P_1, P_2, \tau) = \frac{\Gamma(P_1, P_2, \tau)}{\sqrt{I(P_1)I(P_2)}}. \tag{3.3}$$

For this complex coherence, we always have

$$\mid \gamma(P_1, P_2, \tau) \mid \leqq 1. \tag{3.4}$$

3.3 The coherence function of extended sources

A wave field that is only slightly more complex than a monochromatic plane wave is formed by the (incoherent) superposition of two such wave fields with identical wavelengths but propagating in different directions:

$$\begin{aligned}U_a &= U_{0a}\ \mathrm{e}^{\mathrm{i}(k\mathbf{s}_a\cdot\mathbf{x}-\omega t)}, \\ U_b &= U_{0b}\ \mathrm{e}^{\mathrm{i}(k\mathbf{s}_b\cdot\mathbf{x}-\omega t)}.\end{aligned} \tag{3.5}$$

where $\mathbf{s}_a$ and $\mathbf{s}_b$ are unit vectors describing the propagation direction, and both $k = 2\pi/\lambda$ and $\omega = 2\pi\nu$ are assumed to be equal for both waves. The

total wave field is then formed by $U = U_a + U_b$ and the mutual coherence function (Eq. 3.1) is

$$\begin{aligned}\langle U(P_1,t_1)U^*(P_2,t_2)\rangle = &\langle U_a(P_1,t_1)U_a^*(P_2,t_2)\rangle \\ &+ \langle U_b(P_1,t_1)U_b^*(P_2,t_2)\rangle \\ &+ \langle U_a(P_1,t_1)U_b^*(P_2,t_2)\rangle \\ &+ \langle U_b(P_1,t_1)U_a^*(P_2,t_2)\rangle\,.\end{aligned} \tag{3.6}$$

If we now assume the two wave fields U_a and U_b to be incoherent, we accept the field strengths U_a and U_b to be uncorrelated even when taken at the same point so that

$$\langle U_a(P_1,t_1)U_b^*(P_2,t_2)\rangle = \langle U_b(P_1,t_1)U_a^*(P_2,t_2)\rangle \equiv 0. \tag{3.7}$$

Such incoherence is not possible for strictly monochromatic waves of identical polarization consisting of a wave train of infinite duration and length. Eq. 3.7 is true only if the wave is made up of sections of finite duration between which arbitrary phase jumps occur. In such a situation, the waves are not strictly monochomatric but have a finite, although small bandwidth. Substituting Eq. 3.7 into Eq. 3.6 we obtain

$$\begin{aligned}\Gamma(P_1,P_2,\tau) &= \langle U(P_1,t)U^*(P_2,t+\tau)\rangle \\ &= \langle U_a(P_1,t)U_a^*(P_2,t+\tau)\rangle + \langle U_b(P_1,t)U_b^*(P_2,t+\tau)\rangle\end{aligned} \tag{3.8}$$

or using Eq. 3.5

$$\Gamma(P_1,P_2,\tau) = \mid U_{0a} \mid^2 \mathrm{e}^{\mathrm{i}(k\mathbf{s}_a\cdot\mathbf{u}+\omega t)} + \mid U_{0b} \mid^2 \mathrm{e}^{\mathrm{i}(k\mathbf{s}_b\cdot\mathbf{u}+\omega t)} \tag{3.9}$$

where $\mathbf{u} = \mathbf{x}_1 - \mathbf{x}_2$.

Thus only the difference of the two positions P_1 and P_2 enter into the problem. For the case of two waves of equal amplitude, $\mid U_{0a} \mid = \mid U_{0b} \mid = \mid U_0 \mid$, Eq. 3.9 can be simplified using the identities $\mathbf{s}_a = 1/2(\mathbf{s}_a + \mathbf{s}_b) + 1/2(\mathbf{s}_a - \mathbf{s}_b)$, $\mathbf{s}_b = 1/2(\mathbf{s}_a + \mathbf{s}_b) - 1/2(\mathbf{s}_a - \mathbf{s}_b)$, resulting in

$$\Gamma(\mathbf{u},\tau) = 2 \mid U_0 \mid^2 cos\left(\frac{k}{2}(\mathbf{s}_a - \mathbf{s}_b)\cdot\mathbf{u}\right)\mathrm{e}^{\mathrm{i}\left(\frac{k}{2}(\mathbf{s}_a+\mathbf{s}_b)\cdot\mathbf{u}+\omega\tau\right)}, \tag{3.10}$$

or, if normalized,

$$\gamma(\mathbf{u},\tau) = cos\left(\frac{k}{2}(\mathbf{s}_a - \mathbf{s}_b)\cdot\mathbf{u}\right)\mathrm{e}^{\mathrm{i}\left(\frac{k}{2}(\mathbf{s}_a+\mathbf{s}_b)\cdot\mathbf{u}+\omega\tau\right)}. \tag{3.11}$$

For two waves propagating in directions that differ only slightly, $\mid \mathbf{s}_a - \mathbf{s}_b \mid /2$ is a small quantity, while $(\mathbf{s}_a + \mathbf{s}_b)/2$ differs only little from either $\mathbf{s}_a$ or $\mathbf{s}_b$. The normalized coherence function therefore is similar to that of a single plane wave, but with an amplitude that varies slowly with position. We will have a complete loss of coherence for

$$\frac{k}{2}(\mathbf{s}_a - \mathbf{s}_b) \cdot \mathbf{u} = (2n+1)\frac{\pi}{2}, \qquad n = 0, 1, 2, ... \tag{3.12}$$

This principle of superposition of simple monochromatic plane waves can be extended to an arbitrary number of plane waves, and the result will be a simple generalization of Eq. 3.9 if we assume these fields to be mutually incoherent. The signals at P_1 and P_2 are then the sum of the components $U_n(P,t)$,

$$U(P,t) = \sum_n U_n(P,t), \tag{3.13}$$

and, if the different waves are incoherent, then $\langle U_m(P_1,t)U_n^*(P_2,t+\tau)\rangle = 0$ for all $m \neq n$, while $\langle U_n(P_1,t)U_n^*(P_2,t+\tau)\rangle = \mid U_{0n} \mid^2 \mathrm{e}^{\mathrm{i}(\mathrm{k}\mathbf{s}_\mathrm{n}\cdot\mathrm{u}+\omega\tau)}$, so that

$$\Gamma(\mathbf{u},\tau) = \langle U(P_1,t)U^*(P_2,t+\tau)\rangle = \sum_n \mid U_n \mid^2 \mathrm{e}^{\mathrm{i}(k\mathbf{s}_n\cdot\mathbf{u}+\omega\tau)}. \tag{3.14}$$

Or, if we go to the limit $n \to \infty$

$$\Gamma(\mathbf{u},\tau) = \int\int I(\mathbf{s})\mathrm{e}^{\mathrm{i}(k\mathbf{s}\cdot\mathbf{u}+\omega\tau)}\, d\mathbf{s}, \tag{3.15}$$

where

$$I(\mathbf{s}) = \int\int U(\mathbf{s}+\sigma)U^*(\mathbf{s}+\sigma)\, d\sigma \tag{3.16}$$

is the total intensity at the position P if the integral is taken over the angular extent of those positions $\mathbf{s}+\sigma$ that contribute to the radiation field propagating into the direction $\mathbf{u}$. The generalization of Eq. 3.13 is

$$U(\mathbf{x},t) = \int\int U(\mathbf{s})\mathrm{e}^{\mathrm{i}(k\mathbf{s}\cdot\mathbf{x}-\omega t)}\, d\mathbf{s}. \tag{3.17}$$

Eq. 3.15 is the monochromatic version of the van Cittert-Zernike theorem. This theorem specifies how the mutual coherence function of an arbitrary monochromatic wave field, built up from plane waves, is related to the intensity distribution.

Provided that $\Gamma(\mathbf{u}, \tau)$ can be measured and Eq. 3.15 can be solved for $I(\mathbf{s})$, we can measure the total intensity. The possible angular resolution with which $I(\mathbf{s})$ can be determined depends on the size of the telescope used. For Eq. 3.15 the difference in the positions where measurements are made, $\mid \mathbf{u} \mid$ is introduced. Since it is possible to measure $\Gamma(\mathbf{u}, \tau)$ for values of $\mid \mathbf{u} \mid$ much larger than the largest single telescope diameters possible, the resolution with which $I(\mathbf{s})$ can be measured from the inversion of Eq. 3.15 is much greater than that which can be achieved by using single-dish telescopes.

3.4 Two-element interferometers

The simplest way to measure the coherence function is by using a two-element interferometer. Let two telescopes T_1 and T_2 be separated by the distance $\mathbf{B}$, both telescopes being sensitive only to radiation of the same state of polarization (see Fig. 3.2).

An electromagnetic wave induces the voltage $U_1 \propto E\ \mathrm{e}^{\mathrm{i}\omega t}$ at the output of antenna T_1 while at T_2 we obtain $U_2 \propto E\ \mathrm{e}^{\mathrm{i}\omega(t-\tau)}$, where τ is the geometric delay caused by the relative orientation of the interferometer baseline $\mathbf{B}$ and the direction of the wave propagation. At the correlator, the signals are injected to a multiplying device followed by a low-pass filter such that the output is proportional to

$$R(\tau) \propto \frac{1}{2} E^2 \mathrm{e}^{\mathrm{i}\omega\tau} \tag{3.18}$$

The output of the correlator and integrator varies periodically with the delay time, and is the mutual coherence function of the received wave. If the relative orientation of interferometer baseline and the wave propagation direction remain fixed, the delay time remains constant, and so does $R(\tau)$. But if the wave propagation direction is slowly changing due to the rotation of the earth, the delay time will vary, and we will measure interference fringes as a function of time.

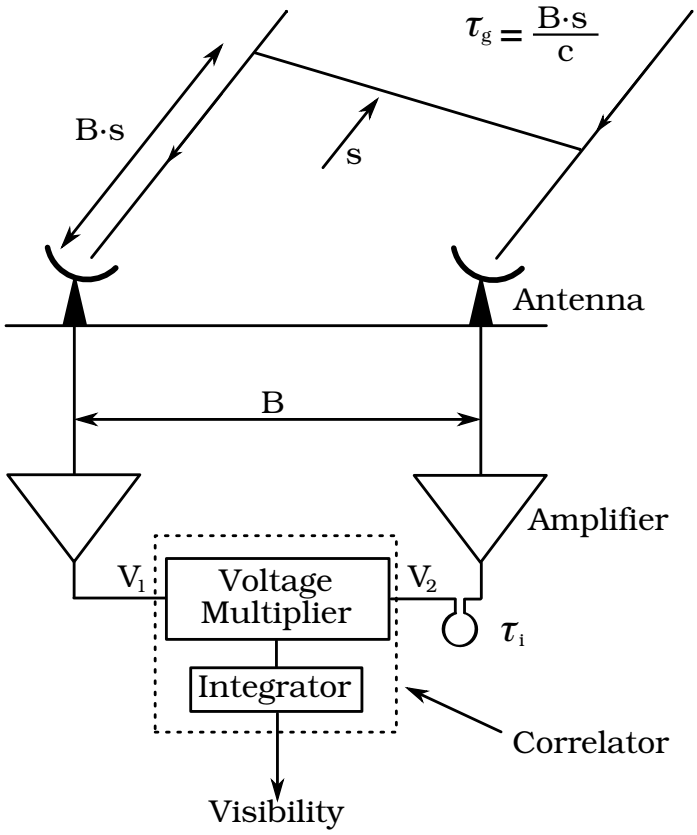

Figure 3.2 Schematic diagram of a two-element interferometer.

The basic constituents of a two-element interferometer are shown in Fig. 3.2. If the radio brightness distribution is given by $I_\nu(\mathbf{s})$, the power received per bandwidth $d\nu$ from the source element $d\Omega$ is $A(\mathbf{s})I_\nu(\mathbf{s})d\Omega d\nu$, where $A(\mathbf{s})$ is the effective collecting area in the direction $\mathbf{s}$; we will assume the same $A(\mathbf{s})$ for each of the antennas. The amplifiers introduce a constant gain factor which we will omit for simplicity.

The output of the correlator for radiation from the direction $\mathbf{s}$ is

$$r_{12} = A(\mathbf{s})I_\nu(\mathbf{s})\mathrm{e}^{\mathrm{i}\omega\tau}\ d\mathbf{s}\ d\nu \tag{3.19}$$

where τ is the difference between the geometrical τ_g and instrumental τ_i delays. If $\mathbf{B}$ is the baseline vector between the two antennas

$$\tau = \tau_g - \tau_i = \frac{1}{c}\mathbf{B}\cdot\mathbf{s} - \tau_i \tag{3.20}$$

and the total response is obtained by integrating over the source S

$$R(\mathbf{B}) = \int\int_S A(\mathbf{s}) I_\nu(\mathbf{s}) \mathrm{e}^{\left[\mathrm{i}2\pi\nu\left(\frac{1}{c}\mathbf{B}\cdot\mathbf{s}-\tau_i\right)\right]}\, d\mathbf{s}\, d\nu. \tag{3.21}$$

This function is closely related to the mutual coherence function of the source but, due to the power pattern $A(\mathbf{s})$ of the individual antennas, it is not identical to $\Gamma(\mathbf{B}, \tau)$. For parabolic antennas it is usually assumed that $A(\mathbf{s}) = 0$ outside the main beam area so that Eq. 3.21 is integrated only over this region.

The reduction in the error caused by finite bandwidth can be estimated by assuming that the expression in Eq. 3.21 is averaged over a range of frequencies $\Delta\nu = \nu_1 - \nu_2$. Then, for an average over frequencies, there will be an additional factor $sin(\Delta\nu\tau)/2\pi\Delta\nu\tau$ in $R(\mathbf{B})$. This will reduce the response if $\Delta\nu$ is large compared to the time delay τ. For typical bandwidths of 100 MHz, the offset from the zero delay must be $\ll 10^{-8}$ s and this adjustment of delays is referred to as a *fringe stopping*. This causes the response of $R(\mathbf{B})$ to loose a component. To recover the full information in the complex $R(\mathbf{B})$, an extra delay of a quarter wavelength relative to the input of the correlator is inserted, so that the sine and cosine response in Eq. 3.21 can be measured.

3.5 Aperture synthesis

Aperture synthesis is a method of solving Eq. 3.21 for $I_\nu(\mathbf{s})$ by measuring $R(\mathbf{B})$ at suitable values of $\mathbf{B}$. To do this effectively, a convenient coordinate system has to be introduced for the two vectorial quantities $\mathbf{s}$ and $\mathbf{B}$. The image center can be chosen at the position of zero phase. This geometry can be introduced using a unit vector $\mathbf{s} = \mathbf{s}_0 + \sigma$, where $\mathbf{s}_0$ is a conveniently chosen position close to the center of the region investigated, and $\mid \sigma \mid = 1$. Thus, substituting the unit vector in $R(\mathbf{B})$, Eq. 3.21 can be written as

$$R(\mathbf{B}) = \mathrm{e}^{\mathrm{i}\omega\left(\frac{1}{c}\mathbf{B}\cdot\mathbf{s}_0-\tau_i\right)} \int\int_S A(\sigma) I(\sigma) \mathrm{e}^{\mathrm{i}\frac{\omega}{c}\mathbf{B}\cdot\sigma}\, d\sigma. \tag{3.22}$$

The exponential factor extracted from the integral is describing a plane wave which defines the phase of $R(\mathbf{B})$ for the image center. The integral is called the visibility function V of the intensity distribution $I(\sigma)$,

$$V(\mathbf{B}) = \int\int_S A(\sigma) I(\sigma)\ \mathrm{e}^{\mathrm{i}\frac{\omega}{c}\mathbf{B}\cdot\sigma}\, d\sigma. \tag{3.23}$$

Since all phases are adjusted to produce a zero delay at the image center the visibility is referred to this position.

We will choose a coordinate system such that $\omega/2\pi c\ \mathbf{B} = (u, v, w)$, and $(\omega \pm \delta\omega)/2\pi c = (f/c)(1 \pm \Delta f/f)$, where u,v,w are measured in units of wavelength $\lambda = 2\pi c/\omega$ and the direction (0,0,1) is parallel to $\mathbf{s}_0$, u points in the local east direction while v points north; the vector $\sigma = (x, y, z)$ is defined such that x and y are the direction cosines with respect to the u and v axes. Then the xy plane represents a projection of the celestial sphere onto a tangent plane with the tangent point (and origin) at $\mathbf{s}_0$. In these coordinates the visibility function V becomes

$$V(u,v,w) = \int_{-\infty}^{\infty}\int_{-\infty}^{\infty} A(x,y)I(x,y) \times \mathrm{e}^{\mathrm{i}2\pi\left(ux,vy,w\sqrt{1-x^2-y^2}\right)} \frac{dx\ dy}{\sqrt{1-x^2-y^2}}. \tag{3.24}$$

The integration limits have been formally extended to $\pm\infty$ by demanding that $A(x, y) = 0$ for $x^2 + y^2 > l^2$; where l is the full width of the primary telescope beams. Interestingly, Eq. 3.24 closely resembles a two dimensional Fourier integral; this would be identical if the term $w\sqrt{1-x^2-y^2}$ could be extracted from under the integral sign. If only a small region of the sky is to be mapped, then $\sqrt{1-x^2-y^2} \cong \text{const} \cong 1$ and Eq. 3.24 becomes

$$V(u,v,w)\mathrm{e}^{\mathrm{i}2\pi\omega} = \int_{-\infty}^{\infty}\int_{-\infty}^{\infty} A(x,y)I(x,y)\mathrm{e}^{\mathrm{i}2\pi(ux,vy)}\ dx\ dy. \tag{3.25}$$

The factor $\mathrm{e}^{\mathrm{i}2\pi\omega}$ is the approximate conversion required to change the observed phase of V to the value that would be measured with antennas in the uv plane: $V(u, v, w)\mathrm{e}^{\mathrm{i}2\pi\omega} \cong V(u, v, 0)$. Substituting this into Eq. 3.25 and performing the inverse Fourier transform we obtain

$$I'(x,y) = A(x,y)I(x,y) = \int_{-\infty}^{\infty} V(u,v,0)\mathrm{e}^{\mathrm{i}2\pi(ux,vy)}\ du\ dv. \tag{3.26}$$

where $I'(x, y)$ is the intensity $I(x, y)$ as modified by the primary beam shape $A(x, y)$. One can easily correct $I'(x, y)$ by dividing it, point for point, by $A(x, y)$. The input $V(u, v)$ is modified by a linear transfer function, which produces the output image I'.

3.6 Interferometer sensitivity

The random noise limit to an interferometer system is calculated following the method used for a single telescope. The *rms* fluctuations in antenna temperature are

$$\Delta T_{\rm A} = \frac{M\ T_{\rm sys}}{\sqrt{t\ \Delta\nu}}, \tag{3.27}$$

where M is a factor of order unity used to account for extra noise from analog to digital conversions, digital clipping, etc. Applying the definition of flux density given in Chapter 2 in terms of antenna temperature for a two-element system, we find:

$$\Delta S_\nu = 2\ k\ \frac{T_{\rm sys}\ {\rm e}^\tau}{A_{\rm e}\sqrt{2}}, \tag{3.28}$$

where τ is the atmospheric opacity and $A_{\rm e}$ is the effective collecting area of a single telescope of diameter D. The extra factor of $\sqrt{2}$ arises from the use of two antennas each of collecting area $A_{\rm e}$, and the fact that the correlation of two noisy signals leads to a decrease in the noise by a factor of $\sqrt{2}$. We denote the system noise corrected for atmospheric absorption by $T'_{\rm sys} = T_{\rm sys}\ {\rm e}^\tau$ in order to simplify the following equations. For an array of n identical telescopes, there are $N = n(n-1)/2$ simultaneous pair-wise correlations. Then the *rms* variation in flux density is

$$\Delta S_\nu = \frac{2\ M\ k\ T'_{\rm sys}}{A_{\rm e}\sqrt{2\ N\ t\ \Delta\nu}}. \tag{3.29}$$

This relation can be recast in the form of brightness temperature fluctuations using the Eq. 2.11:

$$S = 2\ k\ \frac{T_{\rm b}\ \Omega_{\rm b}}{\lambda^2}. \tag{3.30}$$

Then the *rms* brightness temperature, due to random noise, in aperture synthesis image is

$$\Delta T_{\rm b} = \frac{2\ M\ k\ \lambda^2\ T'_{\rm sys}}{A_{\rm e}\ \Omega_{\rm b}\sqrt{2\ N\ t\ \Delta\nu}}. \tag{3.31}$$

A few qualitative comments in regard to the last equation should be made. With shorter wavelengths, the *rms* temperature fluctuations are lower. Thus, for the same collecting area and system noise, a millimeter image is more sensitive than an image made at centimeter wavelengths. With a larger main beam solid angle, these fluctuations will also decrease, if the effective collecting area remains the same. For this reason, smoothing an image will result in a lower *rms* noise in an image. It is frequently noted that multi-element interferometers are capable of producing images faster than single dishes. This is due to the fact that there are n receivers in an interferometer system.

For a Gaussian beam, $\Omega_{\rm mb} = 1.133\ \theta^2$, we can then relate the *rms* temperature fluctuations to observed properties of a synthesis image. Thus, inserting numerical values in Eqs. 3.29 and 3.31, we have

$$\begin{aligned} \Delta S_\nu &= 1.02\ \frac{f\ T'_{\rm sys}}{A_{\rm e}\sqrt{N\ t\ \Delta\nu}}, \\ \Delta T_{\rm b} &= 13.58\ \frac{f\ T'_{\rm sys}}{A_{\rm e}\sqrt{N\ t\ \Delta\nu}}\ \frac{\lambda^2}{\theta^2}, \end{aligned} \tag{3.32}$$

where λ is expressed in mm, θ in arcsec, and $\Delta\nu$ in kHz.

The limitations of the interferometer systems are two-fold. The sensitivity in Kelvins of the system is usually worse than for a single telescope. From Eq. 2.11, since the sensitivity in Jansky is fixed by the antenna collecting area and the receiver noise, the only parameters which can be varied are the wavelength and the angular resolution. And as can be easily seen, the increase in angular resolution is made at the expense of temperature sensitivity. This is not such a great problem for the high-brightness radio sources, which radiate by non-thermal processes, such as synchrotron radiation, but would be for thermal sources, for which the maximum brightness temperatures is about 2×10^4 K for regions of photo ionized gas surrounding massive stars.

Compared with single telescopes, interferometers have the great advantage that uncertainties such as pointing and beam size depend on electronics and fundamentally on timing. Such timing uncertainties can be made very small compared to all other uncertainties. In contrast, the single dish measurements are critically dependent on mechanical deformations of the telescope. In summary, the single dish results are easier to obtain, but source positions and sizes on the arc second scales are difficult to estimate. The interferometer

system has a much greater degree of complexity, but allows one to measure such details. The single dish system responds to the source irrespective of the relation of source to beam size; the correlation interferometer will respond to source structures smaller than the beam corresponding to the minimum separation between the antennas.

One of the most important advantages of an interferometer over a single dish is that with a single dish one needs to subtract an off-source value. This can be corrupted by short term variations in atmospheric emission/absorption or things that affect telescope gain such as pointing. However, the interferometer "switches" at the natural fringe rate, which for VLBI is typically kHz, and this cancels these effects.

The method of aperture synthesis is based on sampling the visibility function $V(u, v, 0)$ with separate telescopes distributed in the (u, v) plane. Many configurations are possible, because all that is needed is a reasonably dense covering of the (u, v) plane. If one calculates the rms noise in a synthesis image obtained by simple Fourier transforming the (u, v) data, one usually finds a corrupted image with a noise level frequently many times higher than that given by ΔS_ν or ΔT_b. The reason is that the phases are affected by atmospheric or instrumental influences, but another cause of higher rms noise is that the (u, v) plane is usually incompletely sampled and instrumental effects are present, such as stripe-like features in the final image. Yet another systematic effect is the presence of grating rings around more intense sources. It has been found that these effects can be eliminated by software techniques.

3.7 Very long baseline interferometers

For a given wavelength the angular resolving power of an interferometer depends only on the length of the interferometer baselines B. But the need to provide a phase-stable links (optical fibers) between individual antennas and the correlator set limits on $\mid B \mid$ to ~ 200 km. Over longer paths, it becomes more difficult to guarantee the phase stability, since transient irregularities in the transmission path will have detrimental effects, so several systems are limited to baselines of a few hundred kilometers.

The development of atomic clocks with extremely phase-stable oscillators opened up the possibility of avoiding altogether the transmission of a phase-stable local oscillator signal. The measurements are made independently

at the individual antennas of the interferometer. The data are recorder on storage media together with precise time marks. These data are correlated later. Currently the data are recorder on hard disks that are shipped to a central correlator location. The antenna outputs contain accurate records of the time variation of the electrical field strengths that the appropriately time-averaged product obtained by multiplying the digitized signal gives the mutual correlation function directly.

Local oscillators with extreme phase stability are needed at each station for two reasons. The disks which are normally used usually permit the recording of signals in a band reaching from zero to at most a hundred MHz; the signal therefore must be mixed down to this band, and for this a phase-stable local oscillator is needed, since all phase jumps of the oscillator affect the IF signal. The second use of the phase stability is to provide the extremely precise time marks needed to align the signals from two stations. Again phase jumps would destroy the coherence, that is the correlation of signals from the source. For the local oscillators, different systems have been used with varying success, ranging from rubidium clocks, free-running quartz oscillators and, most successfully, hydrogen masers. With present day hydrogen maser technologies, it is possible to have frequency and phase stability that allows measurements for many minutes. At longer centimeter wavelengths, the maximum time over which the visibility function can be coherently integrated, that is, where we can determine the amplitude and phase of the visibility function is not limited by the best currently commercially available maser clocks. At wavelengths or 1 cm or shorter, the atmosphere is the limit.

Today, in VLBI only digital data recording is used. The media from different observatories are processed on special purpose digital correlators that align the signals in time, account for local oscillator offsets and geometric delays, clock rate offsets and differential Doppler shifts arising from Earth rotation and then generate a correlation function for each pair of observation sites. Amplitudes and phases of these correlation functions are directly comparable to the complex visibilities of a conventional connected element interferometer. The delay time between the two independent telescopes can vary rapidly. In the past, one could not determine the instrumental phases from measurements of a calibration source, so one had to use *fringe fitting* to allow the accumulation of data over much longer times. The correlator delivers an amplitude as a function of time for a delay range larger than any uncertainty. In the Fourier transform domain the time axis becomes frequency (*residual*

fringe frequency or *fringe rate*) and then the maximum should appear as a peak in this two-dimensional distribution. The coordinates of the *peak*, the *fringe rate* and the *lag* are the required parameters. For strong sources this maximum can be determined directly, but for weaker sources more sophisticated techniques are needed, and will be described in some detail in Chapter 4 and Appendix A. Once these parameters are determined, further reduction procedures are basically identical to those used for the analysis of conventional synthesis array data. To remove the remaining errors , one solves and corrects for residual delays and fringe rate offsets. This is an additional step, *fringe fitting*, is necessary for VLBI reductions. There are several reasons for the phase variation; (1) random delays in the atmospheric propagation properties at the individual sites and (2) phase changes in the electronics and the independent clocks. For these reasons, without fringe fitting the correlation will be only fairly short for a given source.

3.8 Conclusions

In this chapter, we have described in some detail how interferometers work. As we mentioned in Chapter 1, VLBI instruments are ideal for astrometry work because phase-referencing to an extragalactic source with accurately-known position, can be performed. A detailed description of the interferometer that we used to collect the observations presented in this thesis (the Very Long Baseline Array) is given in Appendix A. We are now ready to describe the observations and the calibration made in this thesis.

4
Observations

In this chapter we will describe the observations, the data reduction, and calibration that form the basis of this thesis.

4.1 Summary of observations

We made use of a total of 67 observations obtained with the VLBA. This represents about 382 hours of telescope time. As mentioned earlier, five stars in Taurus and two in Ophiuchus were considered. Tab. 4.1 lists the sources and the corresponding position of the phase centers (i.e. the center of the synthesized field, rather than source position).

All 67 observations were made at 3.6 cm (8.42 GHz), in phase-referenced mode. We used a bit rate of 256 Mb/s rather than 128 Mb/s for several reasons. First, we wanted to schedule when the sources are at high elevation to give us the best chance of successful phase transfer between the calibrators and the targets –this was particularly important for the sources in Ophiuchus. Also, we need as much sensitivity as possible to obtain the astrometric accuracy need to reach our scientific goals.

Since our goal was to measure the annual parallax, each source was observed at least every several months over a few years. In the case of T Tau Sb, we also

Table 4.1. Sources in the thesis.

SFR	Source	$\alpha_{\rm phase}$	$\delta_{\rm phase}$
Taurus	T Tau Sb	$04^{\rm h}21^{\rm m}59\overset{\rm s}{.}426$	$19°32'05\overset{''}{.}730$
	Hubble 4	$04^{\rm h}18^{\rm m}47\overset{\rm s}{.}033$	$28°20'07\overset{''}{.}398$
	HDE 283572	$04^{\rm h}21^{\rm m}58\overset{\rm s}{.}847$	$28°18'06\overset{''}{.}502$
	HP Tau/G2	$04^{\rm h}35^{\rm m}54\overset{\rm s}{.}161$	$22°54'13\overset{''}{.}492$
	V773 Tau A	$04^{\rm h}14^{\rm m}12\overset{\rm s}{.}922$	$28°12'12\overset{''}{.}180$
Ophiuchus	S1	$16^{\rm h}26^{\rm m}34\overset{\rm s}{.}174$	$-24°23'28\overset{''}{.}428$
	DoAr 21	$16^{\rm h}26^{\rm m}03\overset{\rm s}{.}019$	$-24°23'36\overset{''}{.}340$

re-reduced an observation gathered in 1999, and obtained a single additional pointing in 2008, to help characterize the orbital path of the system. For V773 Tau A, we also obtained 13 additional observations spread over about 80 days, which were needed to help determine the physical orbit of the system. Tab. 4.2 contains a summary of these observations, and is divided in seven blocks where each block corresponds to one source. The epoch, mean UT date, and mean Julian Date, are listed in cols. [2], [3] and [4]. The number of antennas, and the total hours of telescope time used in the source and calibrators, are given explicitly in cols. [5] and [6]. Finally, the noise in each resulting image is given in col. [7].

Each observation consisted in a series of cycles with two minutes spent on source and one minute spent on the main phase-referencing quasar. Because the VLBI astrometric accuracy can be improved if more than one reference calibrator is observed, during most observations, secondary quasars were also observed every 24 minutes. Since all seven stars observed are weak targets, then all of the calibrators are used to determine the phase correction at the target source. A simple example of the observing schedule used in the thesis is:

p–T–p–T–p–T–p–T–p–T–p–T–p–T–p–T–p–T–p–**1**–**2**–**3**–p–T–p–T–p–T–
p–T–p–T–p–T–p–T–p–T–p–T–p–**1**–**2**–**3**–p–T–p–T–p–T–p–T–p–T–p–T–
p–T–p–T–p–**1**–**2**–**3**–p–T–p–T–p–T–p–T–p–T–p–T–p–T–p–T–p–T–p–**1**...

where **p** is the primary calibrator, **T** is the target, and **1**, **2**, **3** are the secondary calibrators. Note that one out of every nine **T** observations is

replaced by **1**–**2**–**3** observations.

Tab. 4.3 contains all primary and secondary calibrators used for each source in the project. All calibrators are very compact extragalactic sources whose absolute positions are known to better than a few milli-arcseconds (see cols. [4] and [6] of Tab. 4.3), and are located in the vicinity of the target (the separation between target and calibrator is given in col. [7] of Tab. 4.3). Also, in Fig. 4.1 is shown the calibration configuration for the astronomical targets HDE 283572 and Hubble 4.

The data were edited and calibrated using the Astronomical Image Processing System ($\mathcal{AIPS}$ –Greisen 2003) following the procedures described in the next sections.

4.2 Basic data reduction

In this section we explain all the steps that we followed for the initial data reduction. It follows closely the standard VLBA procedure for phase-referenced observations (Appendix C, $\mathcal{AIPS}$ *CookBook*).

(1) Ionospheric corrections were applied with the VLBATECR procedure which automatically downloads the needed Global Positioning System (GPS) models of the electron content in the Earth atmosphere, and correct the dispersive delays caused by the ionosphere with the task TECOR. This procedure is recommended for all experiments at 8 GHz and lower frequencies, in particular for phase-referencing.

(2) The VLBA correlator must use measurements of the Earth Orientation Parameters (EOPs). It uses the best available estimate at the time of the correlation, but better measurements usually become available several weeks after correlation. It is recommended that all phase-referencing experiments be corrected to these newer EOPs measurements. The procedure VLBAEOPS automatically downloads a file from the US Naval Observatory database and correct the EOPs using CLCOR.

(3) To calibrate visibility amplitudes, we use the procedure VLBACALA which runs several tasks in sequence. The task ACCOR uses the autocorrelation to correct the sampler voltage offsets, and creates a solution table SN which is then smoothed with SNSMO in order to remove any

outlying points. This smoothed SN table is applied to the highest calibration table CL using CLCAL, and a new CL table is created. The task APCAL is then run on the highest TY (system temperature) and GC (gain curve) tables to apply the amplitude calibration, and a new SN table is created. Finally, CLCAL is run to apply the last SN table to the CL table created before.

(4) The RCP and LCP feeds on alt-az antennas will rotate in position angle with respect to the source during the course of the observation. Since this rotation is a simple geometric effect, it can be corrected by adjusting the phases without looking at the data. This correction is important in phase-referencing experiments, because the parallactic angle difference between calibrator and target is different at different stations. This leads to an extra phase error which must be corrected. We used the procedure VLBAPANG that uses TACOP to copy the highest CL table and then runs CLCOR to correct the parallactic angles.

(5) Instrumental delay residuals are caused by the passage of the signal through the electronics of the VLBA baseband converters. We applied the procedure VLBAMPCL that uses the fringes on a strong source to compute the delays and phase residuals for each antenna and IF. This procedure runs FRING to find the corrections and then CLCAL to apply them.

(6) At this point we remove global frequency- and time-dependent phase errors using FRING. For phase-referencing experiments, one could run CALIB instead to FRING, but fringe fitting is recommended because it solves for rates while CALIB does not. FRINGE produces a new SN table which is then smoothed with SNSMO to remove outlying points. Finally, the SN table is used to run CLCAL once for each source. In this last step, we used the 2PT linear vector interpolation method. Note that at this point, FRINGE assumed the calibrator is a point source at the phase center.

(7) In this last step, we apply the calibration to the visibility data and make single-source data set using SPLIT. A set of images were produced using IMAGR. As an example, in Fig. 4.3 we shown the images produced for target, primary and secondary calibrators in the first epoch of HDE 283572 (22/Sep/04; see Tab. 4.2).

4.3 Self-calibration

Even after global fringe fitting, transferring the phases from the calibrator to the target, the phases on the target can still vary with time. Most of these variations are due to inadequate removal of antenna-based atmospheric phases, but some variations also can be caused by an inadequate model of the source structure during fringe fitting (e.g. it is unlikely that the calibrator is a perfect point source). If the calibrator is sufficiently strong, it is possible to reduce these phase fluctuations by looping through cycles of Fourier transform imaging and deconvolution, combined with phase self-calibration in a time interval shorter than the time scale for the variations that one want to remove (Cornwell 1995; Walker 1995; Cornwell & Fomalont 1999). The resulting images can be deconvolved to rid them of substantial sidelobes arising from relatively sparse sampling of the (u, v) plane (Cornwell, Braun, & Briggs 1999).

The first step is to use a point-source model to make the first image of the main calibrator by using the task IMAGR (see second map in Fig. 4.3). It is a good idea to use the task CCMRG in the resulting image to reduce the number of components in the model. This improves the speed of the calibration and make the first negative component be a real negative rather than a minor correction to previous positive components. The resulting clean image can then be used as a model of the source in the following iteration of CALIB to correct only phases. CALIB compares the input (u, v) data set with the predictions of the source model in order to compute a set of antenna-based phase corrections as a function of time which would bring the data into better agreement with the current model. CALIB produces a new improved data set, and will catalog the gain corrections as an SN extension to the input (u, v) data file. If the corrections are believable, we run IMAGR to produce a new clean image. The next step is to use the new clean image as a model in CALIB to produce a new improved data set. The whole process is repeated a few times, and results in an improved image. During these first iterations, we only seek improved phase corrections. During a second set of self-calibration iterations, we also determine improved amplitude corrections. When the new iterations provide little improvement in the image quality, we stop and the last image is kept as our best model for the calibrator.

A different phase calibrator model was produced for each epoch for each source to account for possible small changes in the main calibrator structure

from epoch to epoch. In Fig. 4.4 are shown the main calibrator models used at all six epochs for HDE 283572. Using an image model for the calibrator rather than assuming a point source improved the position accuracy by a few tens of μas.

4.4 Re-fringe fit main phase calibrator

In the images obtained after the self-calibration iterations, the main phase calibrator for almost all epochs was found to be slightly extended or with some source structure (see Fig. 4.4). To take this into account, we followed the extra steps listed below.

(1) The global fringe fitting (FRINGE, SNSMO and CLCAL in step 6 of Sect. 4.2) was repeated using the image of the main phase calibrator (obtained in Sect. 4.3) as a model instead of assuming it to be a point source.

(2) After phases have been corrected with FRING, an improvement of the *a priori* antenna amplitude gains (step 3 in Sect. 4.2) can be obtained using the observations of the main phase calibrator. To achieve that, we ran CALIB instead to FRING to produce a new SN table which was then smoothed with SNSMO. The corrections were transferred to the target and secondary calibrators using CLCAL.

(3) This last step is the same as step 7 of Sect. 4.2: apply the calibration to the visibility data and make single-source data set using SPLIT. The single-source data sets are ready for imaging. In Fig. 4.5 are shown the images produced in this step for the target, primary and secondary calibrators in the first epoch of HDE 283572 (22/Sep/04; see Tab. 4.2). Compare Fig. 4.3 with Fig. 4.5 and note that in the last one, the peak flux is highest, and the r.m.s. is lowest.

4.5 Phase referencing using more than one calibrator

The astrometry precision of VLBA observations depends critically on the quality of the phase calibration. Systematic errors, unremoved by the standard calibration procedures described above, usually dominate the phase

calibration error budget, and limit the astrometric precision achieved to several times the value expected theoretically (Fomalont 1999, Pradel et al. 2006). At the frequency of the present observations, the main sources of systematic errors are inaccuracies in the troposphere model used, as well as clock, antenna and *a priori* source position errors. These effects combine to produce a systematic phase difference between the calibrator and the target, causing position shifts. One effective strategy to measure and correct these systematic errors consists of including observations of more than one phase calibrator chosen to surround the target (Fomalont, 2005). This allows phase gradients around the source due to errors in the troposphere model or related to uncertainties in the cataloged position of the calibrators, to be measured and corrected. This strategy was applied to most of our observations using several secondary calibrators (e.g. see the calibrator configuration for our observations of HDE 283572 and Hubble 4 in Fig. 4.1), and resulted in significant improvements in the final phase calibration and image quality.

The task ATMCA in $\mathcal{AIPS}$ has been written to combine the data from several calibrators to improve the image quality and position accuracy of the target source. This task only requires calibrator data in the vicinity of

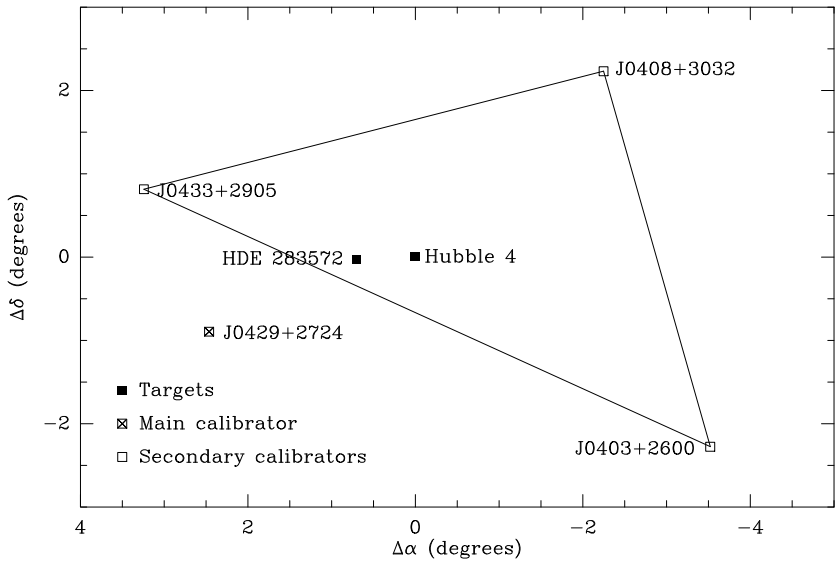

Figure 4.1 Relative position of the astronomical targets HDE 283572 and Hubble 4, the main calibrator J0429+2724, and the secondary calibrators J0433+2905,J0408+3032, J0403+2600.

the target. In Fig. 4.1 the phase differences between each pair of calibrators are sufficient to determine the two-dimensional phase gradient, from which an estimate of the phase at the target position can be obtained. This configuration gives a robust solution. Thus, our observing schedules included observation of secondary calibrators every 24 minutes (see Sect. 4.1).

Several steps have to be taken before running ATMCA. Since most calibrators

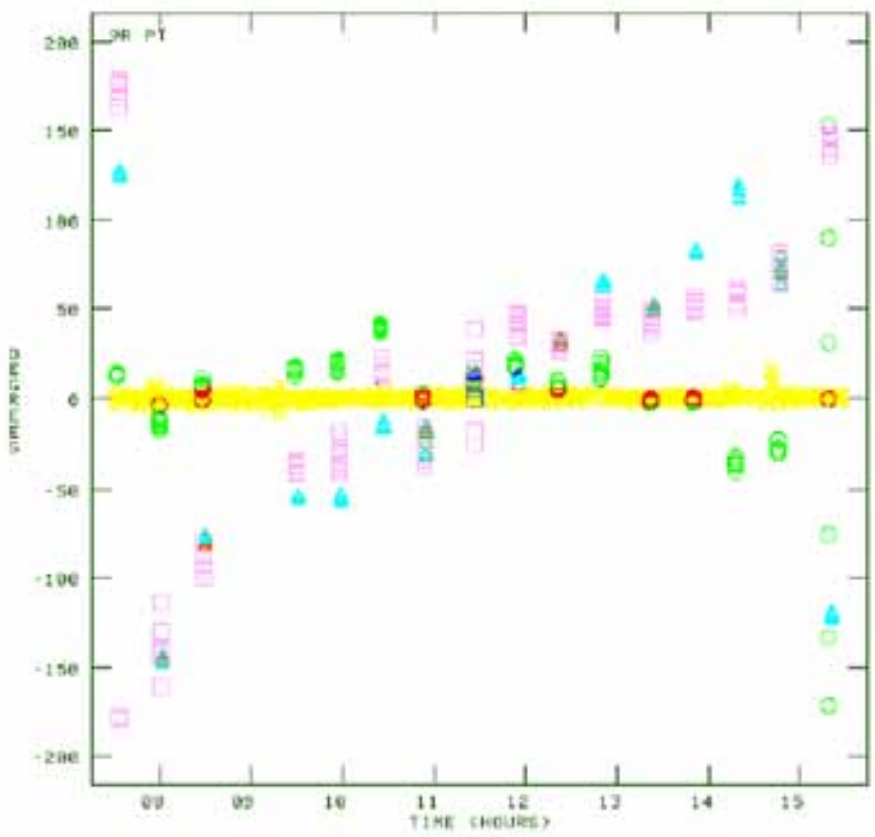

Figure 4.2 The plot shows the residual phases for the calibrators that was input to ATMCA for HDE 283572 at the first epoch (22/Sep/04; see Tab. 4.2). The yellow crosses are for main phase calibrator J0429+2724, the green circles, pink squares, and light blue triangles are for the secondary calibrators J0433+2905, J0408+3032, and J0403+2600, respectively.

are not point sources, self-calibration loops for each secondary calibrator are necessary. From the resulting self-calibrated images, we measure the offsets between the observed and the cataloged calibrator positions (i.e. the offset between the observed position of the calibrators, and their respective phase centers). The task CLCOR is then used to correct for these offsets, and "move" the calibrators to the phase centers. SPLAT was used to obtain data sets averaged in frequency. Finally, we run CALIB on all of the calibrators to produce an SN table with the residual phases for all calibrators. Fig. 4.2 is an example of the residual phases (in antenna 9=PT with all IFs and Stokes RR) for all four calibrators used in HDE 283572 at the first epoch (22/Sep/04). Note the residuals for secondary calibrators at the begin and at the end of observation.

The input to ATMCA is that SN table containing the time variable residual antenna-based phases, sampled in the direction to the calibrators. The phase origin is defined by the main calibrator. The goal of ATMCA is to determine the phase gradient in the sky which is consistent with the phases sampled by the secondary calibrators, and then to apply this gradient to the phase of all sources. The images produced after ATMCA for HDE 283572, primary and secondary calibrators at the first epoch (22/Sep/04) is shown in Fig. 4.6.

4.6 Improvements

In order to give an estimate of the magnitude of the improvements following the calibration method presented in this chapter, we include images (Fig. 4.8 and 4.7) for target and phase calibrator after each step produced for HDE 283572 at the first epoch (22/Sep/04; see Tab. 4.2). Also, in Tab. 4.4 we give intensities and positions after each step, to compare the improvements in calibration.

Table 4.2. Observations.

Source	Epoch	Mean Date		Antennas[a]	$t_{\rm obs}$[c]	rms
		UT	JD		[hr]	[mJy/beam]
T Tau Sb	1	2003 Sep 24 11:33	2452906.981	VLBA	5	0.074
	2	2003 Nov 18 08:02	2452961.834	VLBA	5	0.066
	3	2004 Jan 15 04:09	2453019.672	VLBA-MK	5	0.072
	4	2004 Mar 26 23:26	2453091.476	VLBA	5	0.070
	5	2004 May 13 20:17	2453139.345	VLBA-PT	5	0.111
	6	2004 Jul 08 16:37	2453195.192	VLBA	5	0.064
	7	2004 Sep 16 11:59	2453264.999	VLBA	6	0.070
	8	2004 Nov 09 08:27	2453318.852	VLBA-HN	6	0.104
	9	2004 Dec 28 05:14	2453367.718	VLBA	6	0.070
	10	2005 Feb 24 01:26	2453425.559	VLBA	6	0.080
	11	2005 May 09 20:32	2453500.355	VLBA-OV	6	0.106
	12	2005 Jul 08 16:36	2453560.191	VLBA	6	0.075
	13	2008 May 29 19:09	2454616.298	VLBA	5	0.080
	14[b]	1999 Dec 15 06:04	2451527.753	VLBA	11	0.069
Hubble 4	1	2004 Sep 19 11:47	2453267.991	VLBA	9	0.054
	2	2005 Jan 04 04:46	2453374.699	VLBA	9	0.073
	3	2005 Mar 25 23:28	2453455.478	VLBA	9	0.114
	4	2005 Jul 04 16:51	2453556.202	VLBA	9	0.058
	5	2005 Sep 18 11:52	2453631.994	VLBA	9	0.053
	6	2005 Dec 28 05:15	2453732.719	VLBA	9	0.051
HDE 283572	1	2004 Sep 22 11:35	2453270.983	VLBA	9	0.081
	2	2005 Jan 06 04:39	2453376.693	VLBA	9	0.058
	3	2005 Mar 30 23:08	2453460.464	VLBA	9	0.065
	4	2005 Jun 23 17:34	2453545.232	VLBA	9	0.080
	5	2005 Sep 23 11:32	2453636.981	VLBA-NL	9	0.062
	6	2005 Dec 24 05:31	2453728.729	VLBA	9	0.047
HP Tau/G2	1	2005 Sep 07 12:36	2453621.024	VLBA	6	0.06
	2	2005 Nov 16 08:01	2453690.833	VLBA	6	0.07
	3	2006 Jan 23 03:33	2453758.648	VLBA	6	0.07
	4	2006 Mar 31 23:06	2453826.462	VLBA	6	0.07
	5	2006 Jun 10 18:27	2453897.268	VLBA	6	0.08
	6	2006 Sep 08 12:33	2453987.022	VLBA	6	0.06
	7	2007 Jun 04 18:56	2454256.289	VLBA	9	0.07
	8	2007 Sep 03 12:53	2454347.037	VLBA-HN	9	0.06
	9	2007 Dec 04 06:51	2454438.785	VLBA-SC	9	0.05
V773 Tau A	1	2005 Sep 08 12:01	2453622.001	VLBA	2	0.145
	2	2005 Nov 15 07:31	2453689.813	VLBA	2	0.117

Table 4.2 (cont'd)

Source	Epoch	Mean Date		Antennas[a]	t_{obs}[c]	rms
		UT	JD		[hr]	[mJy/beam]
	3	2006 Jan 21 03:11	2453756.632	VLBA	2	0.109
	4	2006 Apr 01 22:31	2453827.438	VLBA-PT	2	0.238
	5	2006 Jun 12 17:48	2453899.242	VLBA	2	0.102
	6	2006 Sep 05 12:14	2453984.010	VLBA	2	0.159
	7	2007 Aug 23 13:06.....	2454336.046	VLBA	5	0.207
	8	2007 Aug 29 12:42.....	2454342.029	VLBA	5	0.148
	9	2007 Sep 05 12:15	2454349.010	VLBA-HN	5	0.117
	10	2007 Sep 11 11:51	2454354.994	VLBA-HN-SC	5	0.110
	11	2007 Sep 16 11:32	2454359.980	VLBA-HN-SC	5	0.122
	12	2007 Sep 21 11:12	2454364.966	VLBA-SC-PT	5	0.106
	13	2007 Sep 27 10:48	2454370.950	VLBA-SC	5	0.135
	14	2007 Oct 03 10:25	2454376.934	VLBA-SC-NL	5	0.148
	15	2007 Oct 09 10:01	2454382.917	VLBA-SC-PT	5	0.256
	16	2007 Oct 17 09:30	2454390.896	VLBA-SC	5	0.405
	17	2007 Oct 23 09:06	2454396.879	VLBA-SC-KP	5	0.267
	18	2007 Oct 27 08:50	2454400.868	VLBA-SC	5	0.159
	19	2007 Nov 17 07:28.....	2454421.811	VLBA-SC-FD	5	0.139
S1	1	2005 Jun 24 05:32	2453545.730	VLBA	4	0.311
	2	2005 Sep 15 00:05	2453628.504	VLBA-LA	4	0.199
	3	2005 Dec 17 17:56.....	2453722.247	VLBA	4	0.196
	4	2006 Mar 15 12:10.....	2453810.007	VLBA-KP	4	0.135
	5	2006 Jun 03 06:56.....	2453889.789	VLBA-KP-HN	4	0.184
	6	2006 Aug 22 01:41.....	2453969.570	VLBA	4	0.209
DoAr 21	1	2005 Sep 08 00:33	2453621.523	VLBA	4	0.144
	2	2005 Nov 16 19:58.....	2453691.332	VLBA	4	0.185
	3	2006 Jan 08 16:30	2453744.187	VLBA	4	0.054
	4	2006 Jan 19 15:46	2453755.157	VLBA	4	0.063
	5	2006 Mar 28 11:19.....	2453822.971	VLBA-MK	4	0.056
	6	2006 Jun 04 06:52.....	2453890.786	VLBA-HN	4	0.073
	7	2006 Aug 24 01:33.....	2453971.565	VLBA	4	0.043

[a]VLBA antennas: MK–Mauna Kea, PT–Pie Town, HN–Hancock, OV–Owens Valley, NL–North Liberty, SC–St. Croix, KP–Kitt Peak, FD–Fort Davis, BR–Brewster, LA–Los Alamos.

[b]Data from VLBA archive, project BB112, 99-Dec-15.

[c]This time include time spent in source and calibrators.

Table 4.3. Calibrators.

Source	Calibrator [J2000]	$\alpha_{\mathrm{J2000.0}}$ [a] [h m s]	σ_α [a] [mas]	$\delta_{\mathrm{J2000.0}}$ [a] [° ′ ″]	σ_δ [a] [mas]	Sep. [deg]
T Tau Sb	J0428+1732 [p]	04:28:35.633683	0.49	+17:32:23.58810	0.77	2.54
	J0412+1856 [s]	04:12:45.944191	0.58	+18:56:37.07668	0.71	2.26
	J0431+1731 [s]	04:31:57.379257	0.73	+17:31:35.77540	1.23	3.10
	J0426+2327 [s]	04:26:55.734792	0.32	+23:27:39.63378	0.59	4.09
Hubble 4	J0429+2724 [p]	04:29:52.960767	0.23	+27:24:37.87633	0.41	2.62
	J0408+3032 [s]	04:08:20.377570	0.36	+30:32:30.48991	0.58	3.17
	J0433+2905 [s]	04:33:37.829861	0.23	+29:05:55.47708	0.40	3.34
	J0403+2600 [s]	04:03:05.586060	0.23	+26:00:01.50283	0.40	4.20
HDE 283572	J0429+2724 [p]	04:29:52.960767	0.23	+27:24:37.87633	0.41	1.96
	J0408+3032 [s]	04:08:20.377570	0.36	+30:32:30.48991	0.58	3.72
	J0433+2905 [s]	04:33:37.829861	0.23	+29:05:55.47708	0.40	2.68
	J0403+2600 [s]	04:03:05.586060	0.23	+26:00:01.50283	0.40	4.79
HP Tau/G2	J0426+2327 [p]	04:26:55.734792	0.32	+23:27:39.63378	0.59	2.14
	J0435+2532 [s]	04:35:34.582945	1.23	+25:32:59.69695	2.12	2.65
	J0449+1754 [s]	04:49:12.511544	0.56	+17:54:31.59559	0.69	5.89
V773 Tau A	J0408+3032 [p]	04:08:20.377570	0.36	+30:32:30.48991	0.58	2.67
	J0403+2600 [s]	04:03:05.586060	0.23	+26:00:01.50283	0.40	3.31
	J0429+2724 [s]	04:29:52.960767	0.23	+27:24:37.87633	0.41	3.55
	J0356+2903 [s]	03:56:08.461936	0.68	+29:03:42.32059	1.46	4.06
S1	J1625-2527 [p]	16:25:46.891640	0.22	-25:27:38.32687	0.40	1.08
	J1617-1941 [s]	16:17:27.093081	0.96	-19:41:32.01350	1.79	5.15
	J1644-1804 [s]	16:44:35.746823	2.37	-18:04:32.45913	5.36	7.58
	J1626-2951 [s]	16:26:06.020836	0.24	-29:51:26.97118	0.41	5.47
DoAr 21	J1625-2527 [p]	16:25:46.891640	0.22	-25:27:38.32687	0.40	1.07
	J1617-1941 [s]	16:17:27.093081	0.96	-19:41:32.01350	1.79	5.11
	J1644-1804 [s]	16:44:35.746823	2.37	-18:04:32.45913	5.36	7.65
	J1626-2951 [s]	16:26:06.020836	0.24	-29:51:26.97118	0.41	5.46

[a]Taken from L. Petrov, solution 2008a_astro (unpublished, available at http://vlbi.gsfc.nasa.gov/solutions/2008a_astro)

[p]Main phase calibrator.

[s]Secondary calibrator.

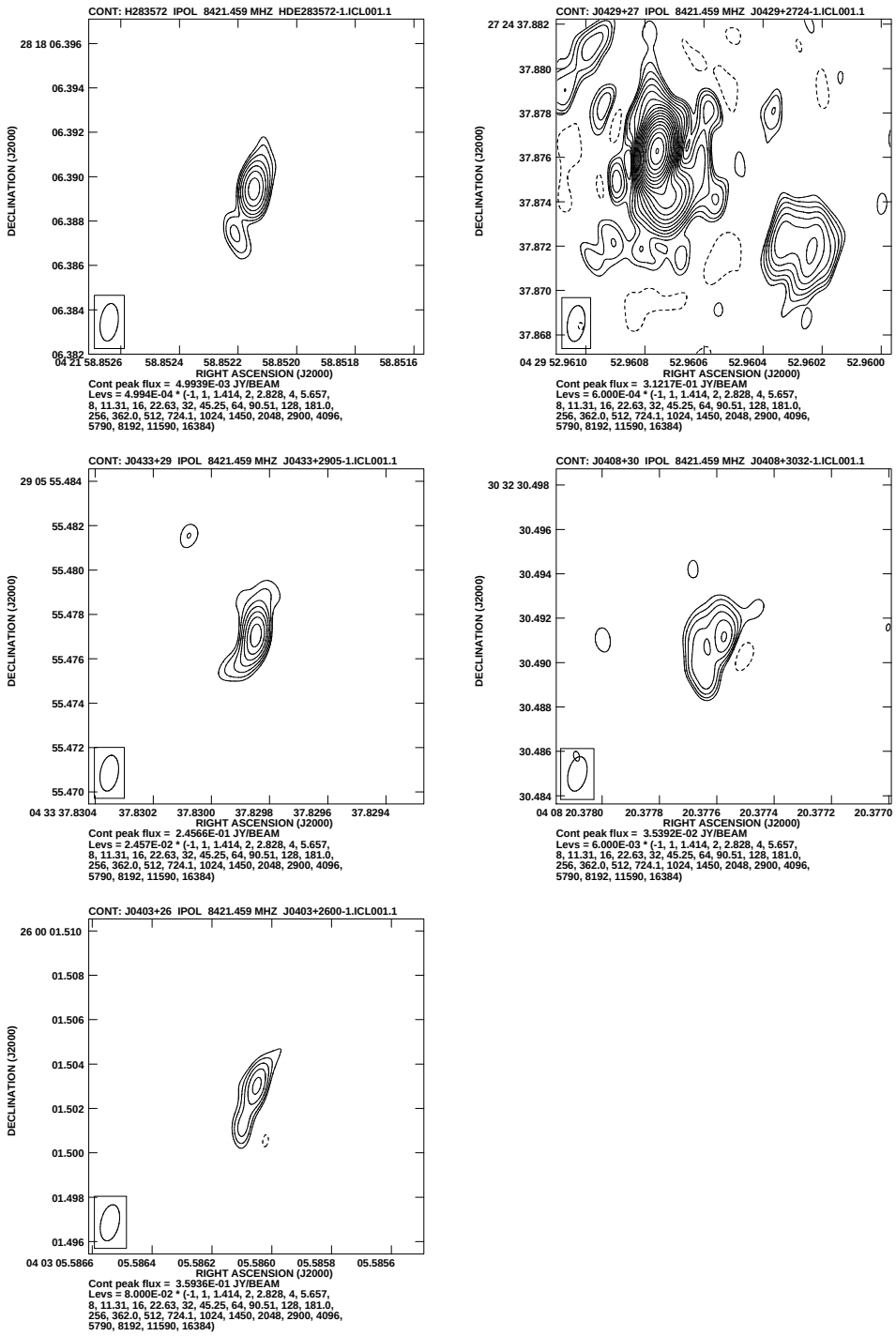

Figure 4.3 Images of the astronomical target HDE 283572, primary calibrator J0429+2724 and secondary calibrators J0433+2905, J0408+3032, J0403+2600 at the first epoch (22/Sep/04; see Tab. 4.2) produced after steps listed in Sect. 4.2.

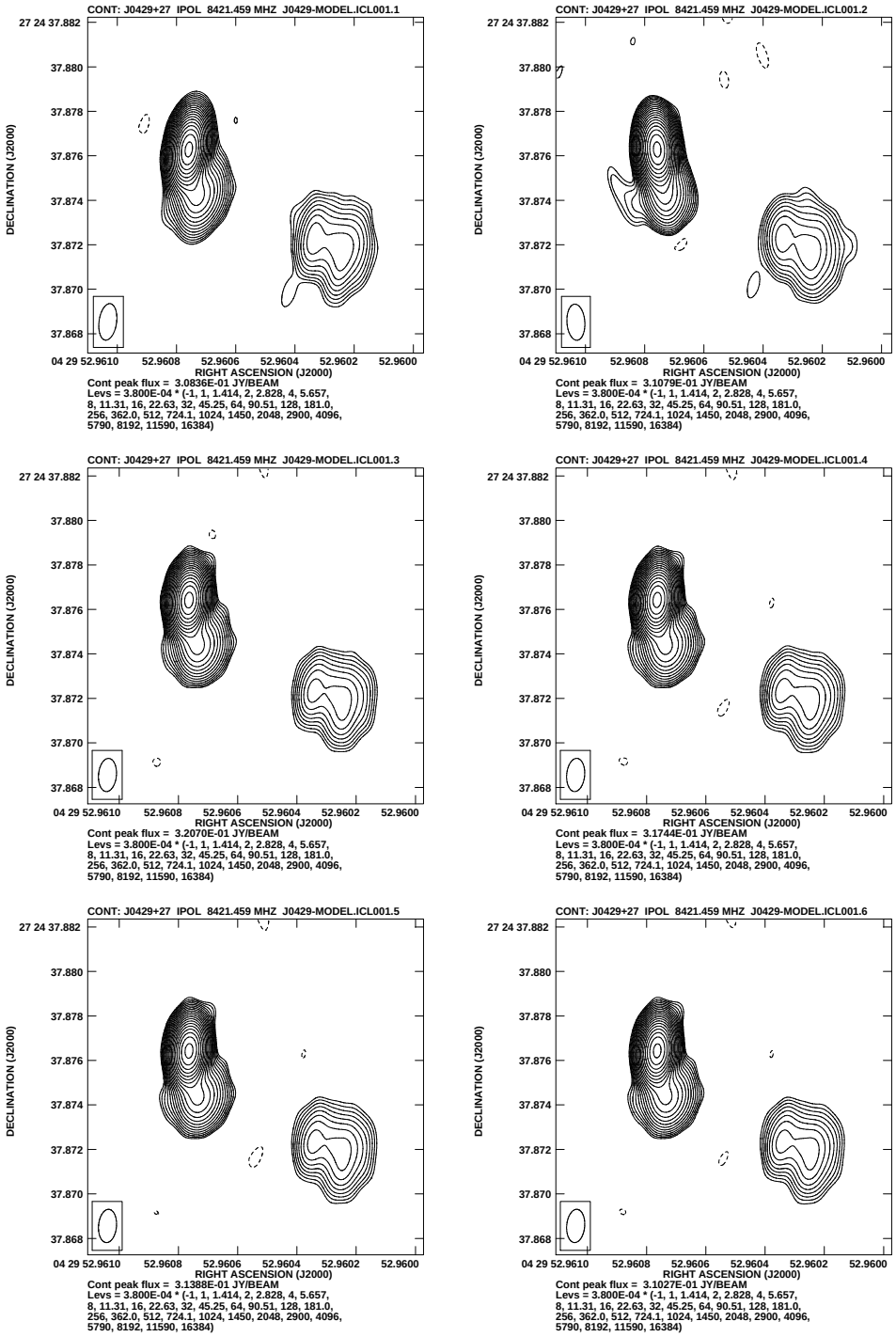

Figure 4.4 Images of the phase calibrator model J0429+2724 used for HDE 283572 at all six epochs (22/Sep/04, 06/Jan/05, 30/Mar/05, 23/Jun/05, 23/Sep/05, 24/Dec/05; see Tab. 4.2). There are produced after the self-calibration iterations, and are plotted with the same contour levels.

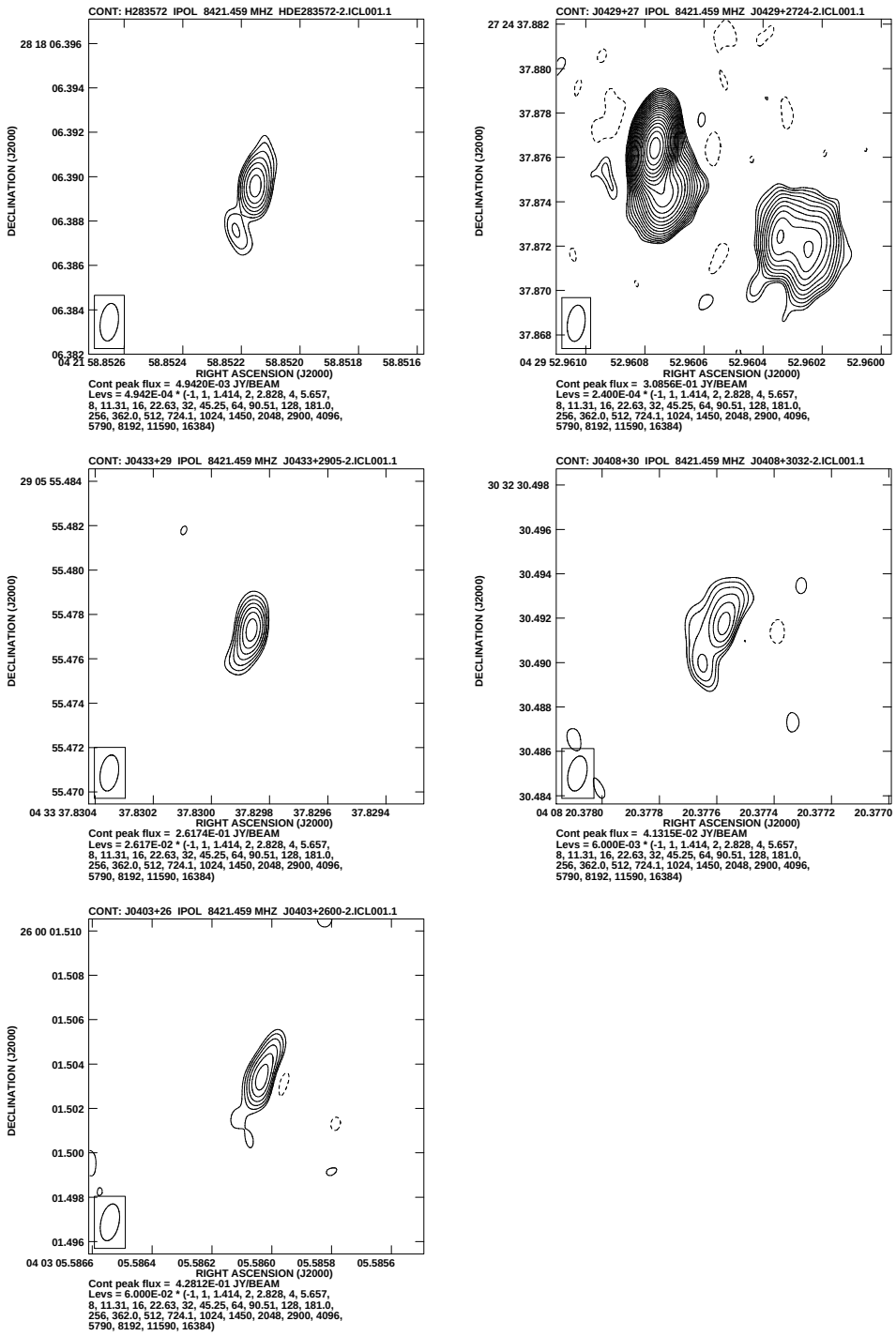

Figure 4.5 Images of the astronomical target HDE 283572, primary calibrator J0429+2724 and secondary calibrators J0433+2905, J0408+3032, J0403+2600 at the first epoch (22/Sep/04; see Tab. 4.2) produced after steps listed in Sect. 4.4.

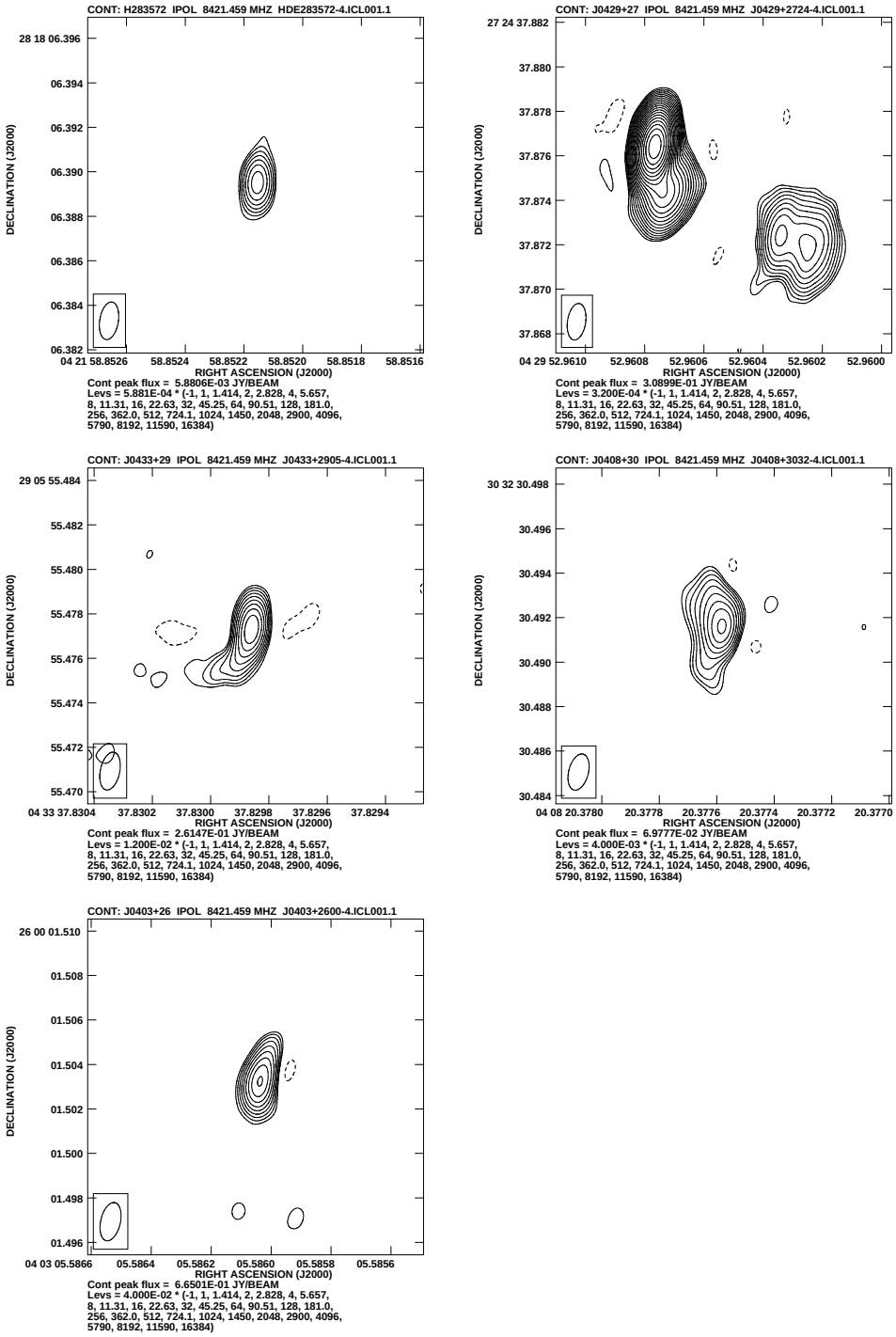

Figure 4.6 Images of the astronomical target HDE 283572, primary calibrator J0429+2724 and secondary calibrators J0433+2905, J0408+3032, J0403+2600 at the first epoch (22/Sep/04; see Tab. 4.2) produced after ATMCA.

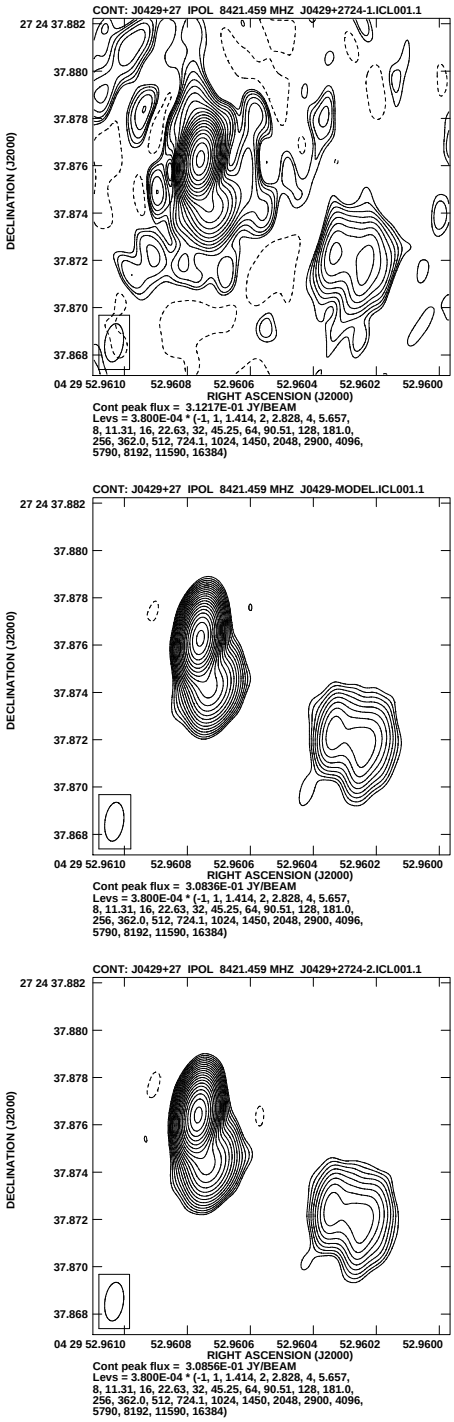

Figure 4.7 Images of the main calibrator J0429+2724 used to reduce data of HDE 283572 at the first epoch (22/Sep/04; see Tab. 4.2). The first map correspond to the image produced after *basic data reduction* (Sect. 4.2) when we assumed the phase calibrator as a punctual source. The second map is the phase calibrator model produced in *self-calibration* (Sect. 4.3; note the structure of the source). And the third map is produced after *re-fringe fit main phase calibrator* (Sect. 4.4) when we used a real phase calibrator. Note that all three images are plotted with the same contour levels.

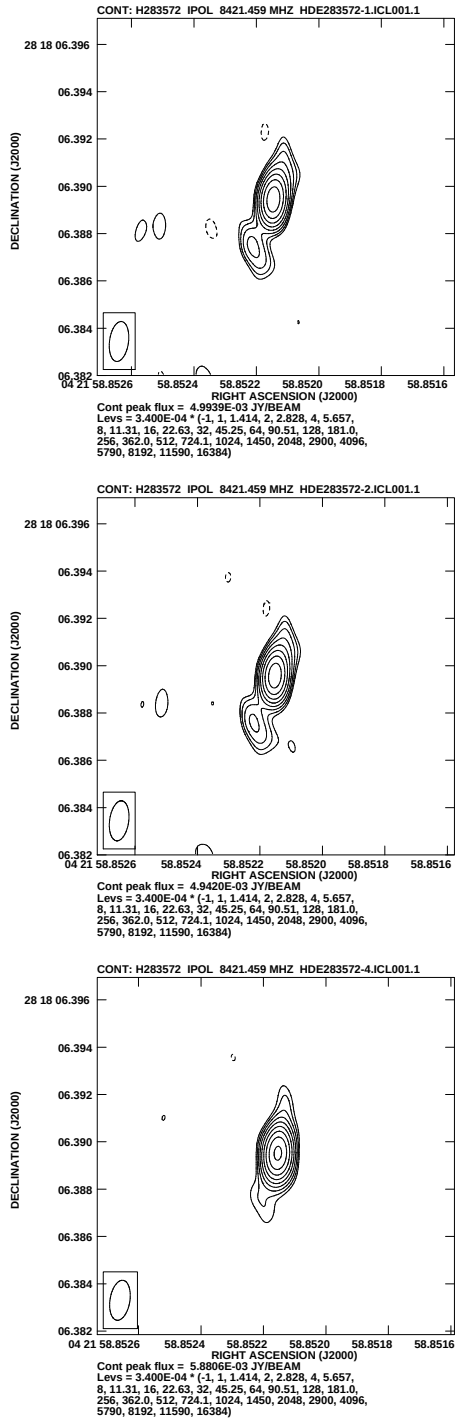

Figure 4.8 Images of the astronomical target HDE 283572 at the first epoch (22/Sep/04; see Tab. 4.2). The first map correspond to the image produced after *basic data reduction* (Sect. 4.2), the second after *re-fringe fit main phase calibrator* (Sect. 4.4), and the third after *phase referencing using more than one calibrator* (Sect. 4.5). Note that all three images are plotted with the same contour levels, and that the peak flux and quality of the image is always better after each step.

Table 4.4. Improvements in intensities and positions of the astronomical target HDE 283572 and the main calibrator J0429+2724 at first epoch (22/Sep/04) after each step in the reduction of data.

Step†	Peak intensity [mJy/beam]	Integral intensity [mJy]	α (J2000.0)	δ (J2000.0)	X-position [pixels]	Y-position [pixels]
HDE 283572			04^h21^m	$28°18'$		
1	4.9091±0.0668	5.9111±0.131	$58\overset{s}{.}85214432\pm0\overset{s}{.}00000040333$	$06''\!.3894682\pm0''\!.0000105262$	1025.256±0.1065	1022.366±0.2105
3	4.8657±0.0654	5.8169±0.128	$58\overset{s}{.}85215084\pm0\overset{s}{.}00000039874$	$06''\!.3896017\pm0''\!.0000103789$	1023.535±0.1053	1025.036±0.2076
4	5.8289±0.0593	6.8963±0.115	$58\overset{s}{.}85215374\pm0\overset{s}{.}00000030889$	$06''\!.3895120\pm0''\!.0000077977$	1022.766±0.0816	1023.241±0.1559
J0429+2724			04^h29^m	$27°24'$		
1	309.33±0.320	329.38±0.578	$52\overset{s}{.}96075807\pm0\overset{s}{.}00000002709$	$37''\!.8762762\pm0''\!.0000007421$	255.981±0.0072	256.924±0.0148
2	305.66±0.112	322.52±0.200	$52\overset{s}{.}96075821\pm0\overset{s}{.}00000000962$	$37''\!.8762719\pm0''\!.0000002637$	255.942±0.0026	256.838±0.0053
3	305.89±0.117	323.78±0.210	$52\overset{s}{.}96076520\pm0\overset{s}{.}00000001001$	$37''\!.8764019\pm0''\!.0000002746$	254.082±0.0027	259.439±0.0055
4	306.36±0.122	323.85±0.219	$52\overset{s}{.}96076520\pm0\overset{s}{.}00000001091$	$37''\!.8764010\pm0''\!.0000002878$	254.080±0.0029	259.420±0.0058

† Step 1=after basic data reduction (Sect. 4.2), 2=after self-calibration (Sect. 4.3), 3=after re-fringe fit main phase calibrator (Sect. 4.4), 4=after phase referencing using more than one calibrator (Sect. 4.5).

5
Results

In this chapter, we will present the main results of the thesis. Sect. 5.1 is about absolute astrometry, and includes parallaxes (and therefore, distances) and proper motions for our seven sources. We use these results to then go on and discuss the kinematics of the sources in Taurus, and the three-dimensional structure of the Taurus and Ophiuchus complexes with the distances. In Sect. 5.2 we briefly discuss the variability of the sources in our sample. The implications for the properties of some stars in the sample are discussed in Sect. 5.3. Finally, the relative astrometry is discussed in Sect. 5.4 which includes orbital fits for T Tau Sa/Sb and V773 Tau Aa/Ab systems.

Once calibrated, the visibilities corresponding to each source at each epoch, were imaged with a pixel size of 50 μas after weights intermediate between natural and uniform (ROBUST = 0 in IMAGR) were applied. 67 continuum images were obtained in the thesis, but here we are showing only 53 contour maps corresponding to: twelve epochs of T Tau Sb (Figs. 5.1 and 5.2), six of Hubble 4 (Fig. 5.3), six of HDE 283572 (Fig. 5.4), six of HP Tau/G2 (Fig. 5.5), all 19 epochs of V773 Tau A system (Figs. 5.6, 5.7, 5.8 and first panel

of Fig. 5.9), two of S1 (panel two and three of Fig. 5.9), and two of DoAr 21 (panel four and five of Fig. 5.9).

From images, we obtained all parameters needed (see Tab. 5.1) to fit for the parallax and proper motions of the sources, as well as for relative motions in multiple systems of our sample. The source absolute positions at each epoch (Cols. [3] and [4] in Tab. 5.1) were determined using a 2D Gaussian fitting procedure (task JMFIT in $\mathcal{AIPS}$). This task provides an estimate of the position error based on the expected theoretical astrometric precision of an interferometer (Condon 1997). Tab. 5.1 also contains the epoch in Col. [1], Julian Day in Col. [2], flux densities in Col. [5], and the corresponding brightness temperature in Col. [6].

Table 5.1. Measured source positions and fluxes.

Epoch	Mean Date [JD]	α (J2000.0)	δ (J2000.0)	f_ν [mJy]	T_b [10^6 K]
T Tau Sb		04^h21^m	$19°32'$		
1	2452906.981522	$59\overset{s}{.}4252942\pm0\overset{s}{.}000001$	$05\overset{''}{.}71762\pm0\overset{''}{.}00004$	1.62±0.14	19.62±1.70
2	2452961.834705	$59\overset{s}{.}4249805\pm0\overset{s}{.}000002$	$05\overset{''}{.}71655\pm0\overset{''}{.}00004$	1.74±0.14	20.06±1.61
3	2453019.672980	$59\overset{s}{.}4245823\pm0\overset{s}{.}000004$	$05\overset{''}{.}71532\pm0\overset{''}{.}00011$	0.92±0.15	6.61±1.08
4	2453091.476395	$59\overset{s}{.}4245420\pm0\overset{s}{.}000002$	$05\overset{''}{.}71533\pm0\overset{''}{.}00005$	1.27±0.14	13.24±1.46
5	2453139.345324	$59\overset{s}{.}4248818\pm0\overset{s}{.}000002$	$05\overset{''}{.}71603\pm0\overset{''}{.}00006$	1.90±0.21	24.36±2.69
6	2453195.192419	$59\overset{s}{.}4253464\pm0\overset{s}{.}000002$	$05\overset{''}{.}71665\pm0\overset{''}{.}00006$	1.25±0.13	14.08±1.46
7	2453264.999583	$59\overset{s}{.}4255476\pm0\overset{s}{.}000002$	$05\overset{''}{.}71660\pm0\overset{''}{.}00004$	1.61±0.14	17.09±1.49
8	2453318.852141	$59\overset{s}{.}4252999\pm0\overset{s}{.}000002$	$05\overset{''}{.}71563\pm0\overset{''}{.}00004$	3.36±0.21	28.89±1.81
9	2453367.718351	$59\overset{s}{.}4249488\pm0\overset{s}{.}000002$	$05\overset{''}{.}71434\pm0\overset{''}{.}00005$	1.26±0.14	14.49±1.61
10	2453425.559664	$59\overset{s}{.}4247667\pm0\overset{s}{.}000002$	$05\overset{''}{.}71383\pm0\overset{''}{.}00004$	2.30±0.16	26.38±1.83
11	2453500.355214	$59\overset{s}{.}4251475\pm0\overset{s}{.}000006$	$05\overset{''}{.}71485\pm0\overset{''}{.}00018$	1.12±0.21	11.17±2.09
12	2453560.191348	$59\overset{s}{.}4256679\pm0\overset{s}{.}000002$	$05\overset{''}{.}71560\pm0\overset{''}{.}00006$	1.41±0.15	14.86±1.58
13	2454616.298136	$59\overset{s}{.}4268831\pm0\overset{s}{.}000011$	$05\overset{''}{.}70677\pm0\overset{''}{.}00018$	1.64±0.24	5.80±0.85
14	2451527.753322	$59\overset{s}{.}4259349\pm0\overset{s}{.}000001$	$05\overset{''}{.}73136\pm0\overset{''}{.}00004$	2.11±0.15	30.85±2.19
Hubble 4		04^h18^m	$28°20'$		
1	2453267.991464	$47\overset{s}{.}0327419\pm0\overset{s}{.}000002$	$07\overset{''}{.}39898\pm0\overset{''}{.}00005$	0.67±0.11	8.60±1.41
2	2453374.699299	$47\overset{s}{.}0319609\pm0\overset{s}{.}000002$	$07\overset{''}{.}38901\pm0\overset{''}{.}00007$	0.76±0.15	10.72±2.12
3	2453455.478107	$47\overset{s}{.}0318775\pm0\overset{s}{.}000001$	$07\overset{''}{.}38139\pm0\overset{''}{.}00002$	4.66±0.23	60.53±2.99
4	2453556.202349	$47\overset{s}{.}0328115\pm0\overset{s}{.}000002$	$07\overset{''}{.}37500\pm0\overset{''}{.}00005$	0.65±0.12	7.58±1.40
5	2453631.994548	$47\overset{s}{.}0330740\pm0\overset{s}{.}000002$	$07\overset{''}{.}37032\pm0\overset{''}{.}00004$	1.25±0.11	13.93±1.23
6	2453732.719045	$47\overset{s}{.}0323418\pm0\overset{s}{.}000001$	$07\overset{''}{.}36057\pm0\overset{''}{.}00003$	1.53±0.10	17.95±1.17
HDE 28357		04^h21^m	$28°18'$		
1	2453270.983223	$58\overset{s}{.}8521561\pm0\overset{s}{.}000001$	$06\overset{''}{.}38942\pm0\overset{''}{.}00001$	7.13±0.16	86.13±1.93
2	2453376.693842	$58\overset{s}{.}8514573\pm0\overset{s}{.}000005$	$06\overset{''}{.}38002\pm0\overset{''}{.}00009$	0.92±0.12	10.67±1.39
3	2453460.464438	$58\overset{s}{.}8514676\pm0\overset{s}{.}000002$	$06\overset{''}{.}37253\pm0\overset{''}{.}00004$	1.71±0.13	18.64±1.42
4	2453545.232390	$58\overset{s}{.}8523648\pm0\overset{s}{.}000001$	$06\overset{''}{.}36785\pm0\overset{''}{.}00001$	4.23±0.16	51.23±1.94
5	2453636.981174	$58\overset{s}{.}8528216\pm0\overset{s}{.}000007$	$06\overset{''}{.}36318\pm0\overset{''}{.}00014$	0.52±0.12	5.71±1.32
6	2453728.729982	$58\overset{s}{.}8522172\pm0\overset{s}{.}000003$	$06\overset{''}{.}35481\pm0\overset{''}{.}00007$	0.51±0.09	6.27±1.11
HP Tau/G2		04^h35^m	$22°54'$		
1	2453621.024774	$54\overset{s}{.}1613574\pm0\overset{s}{.}000003$	$13\overset{''}{.}41131\pm0\overset{''}{.}00009$	0.71±0.12	8.27±1.40
2	2453690.833709	$54\overset{s}{.}1612212\pm0\overset{s}{.}000002$	$13\overset{''}{.}40798\pm0\overset{''}{.}00007$	0.97±0.14	10.70±1.54
3	2453758.648061	$54\overset{s}{.}1609360\pm0\overset{s}{.}000004$	$13\overset{''}{.}40439\pm0\overset{''}{.}00010$	0.99±0.17	7.87±1.35
4	2453826.462390	$54\overset{s}{.}1610940\pm0\overset{s}{.}000003$	$13\overset{''}{.}40161\pm0\overset{''}{.}00010$	0.68±0.15	8.64±1.91
5	2453897.268547	$54\overset{s}{.}1617432\pm0\overset{s}{.}000001$	$13\overset{''}{.}39959\pm0\overset{''}{.}00002$	3.06±0.16	35.24±1.84
6	2453987.022807	$54\overset{s}{.}1623557\pm0\overset{s}{.}000002$	$13\overset{''}{.}39681\pm0\overset{''}{.}00007$	1.08±0.17	13.78±2.17
7	2454256.289010	$54\overset{s}{.}1627018\pm0\overset{s}{.}000004$	$13\overset{''}{.}38267\pm0\overset{''}{.}00013$	0.63±0.13	6.79±1.40

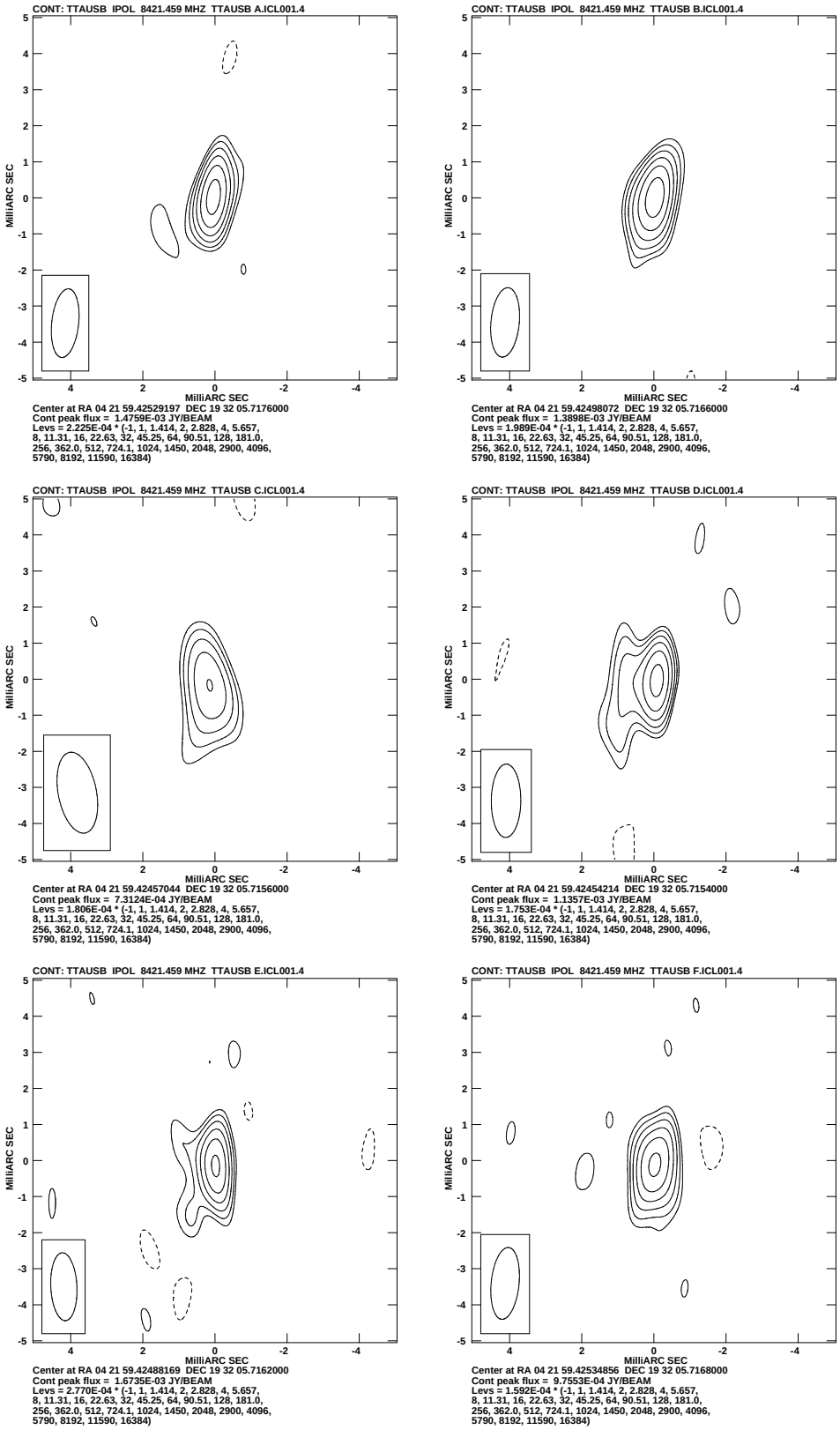

Figure 5.1 VLBA images of T Tau Sb at epochs 1 to 6 listed in Tab. 4.2 and 5.1.

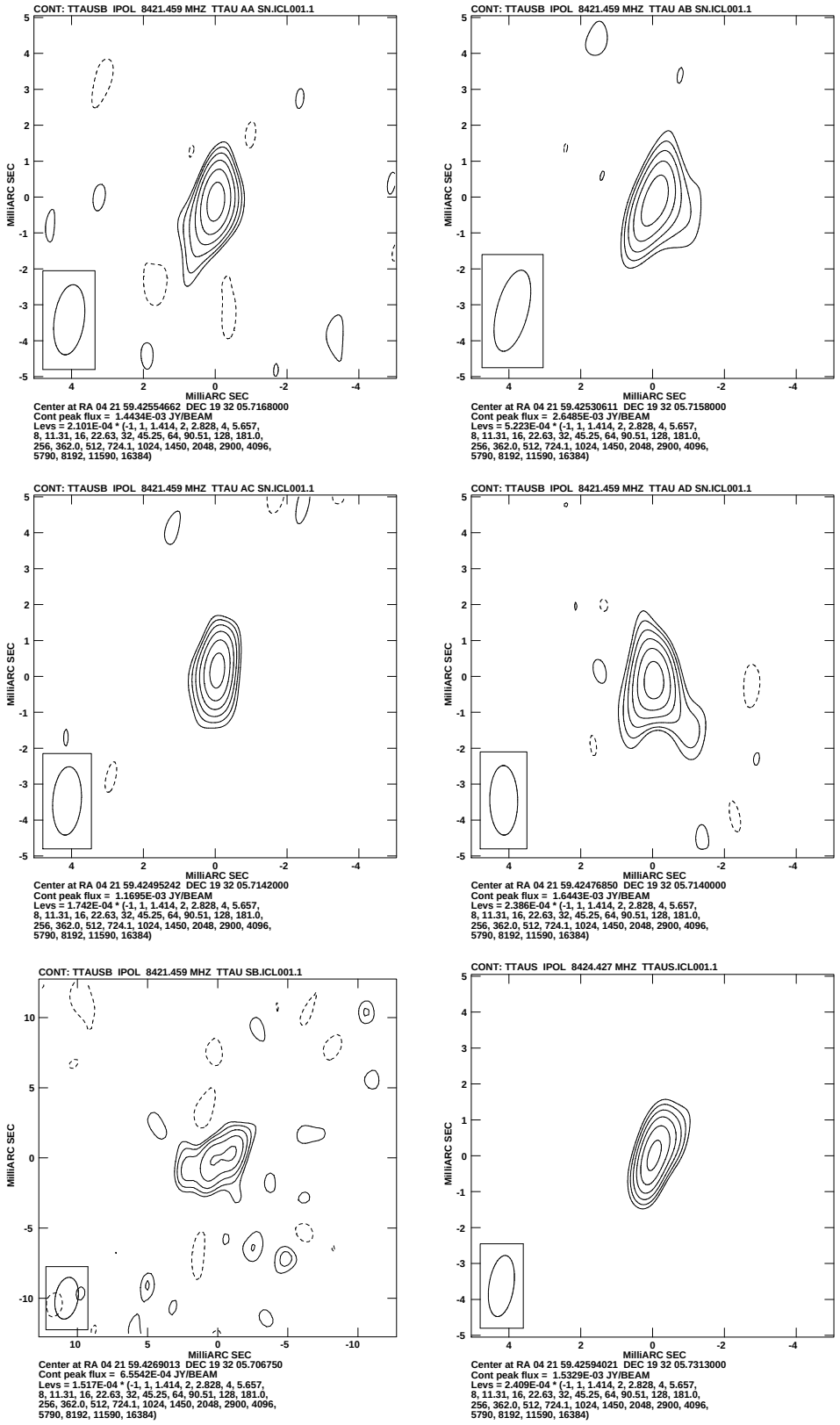

Figure 5.2 VLBA images of T Tau Sb at epochs 7, 8, 9, 10, 13 and 14 listed in Tab. 4.2 and 5.1.

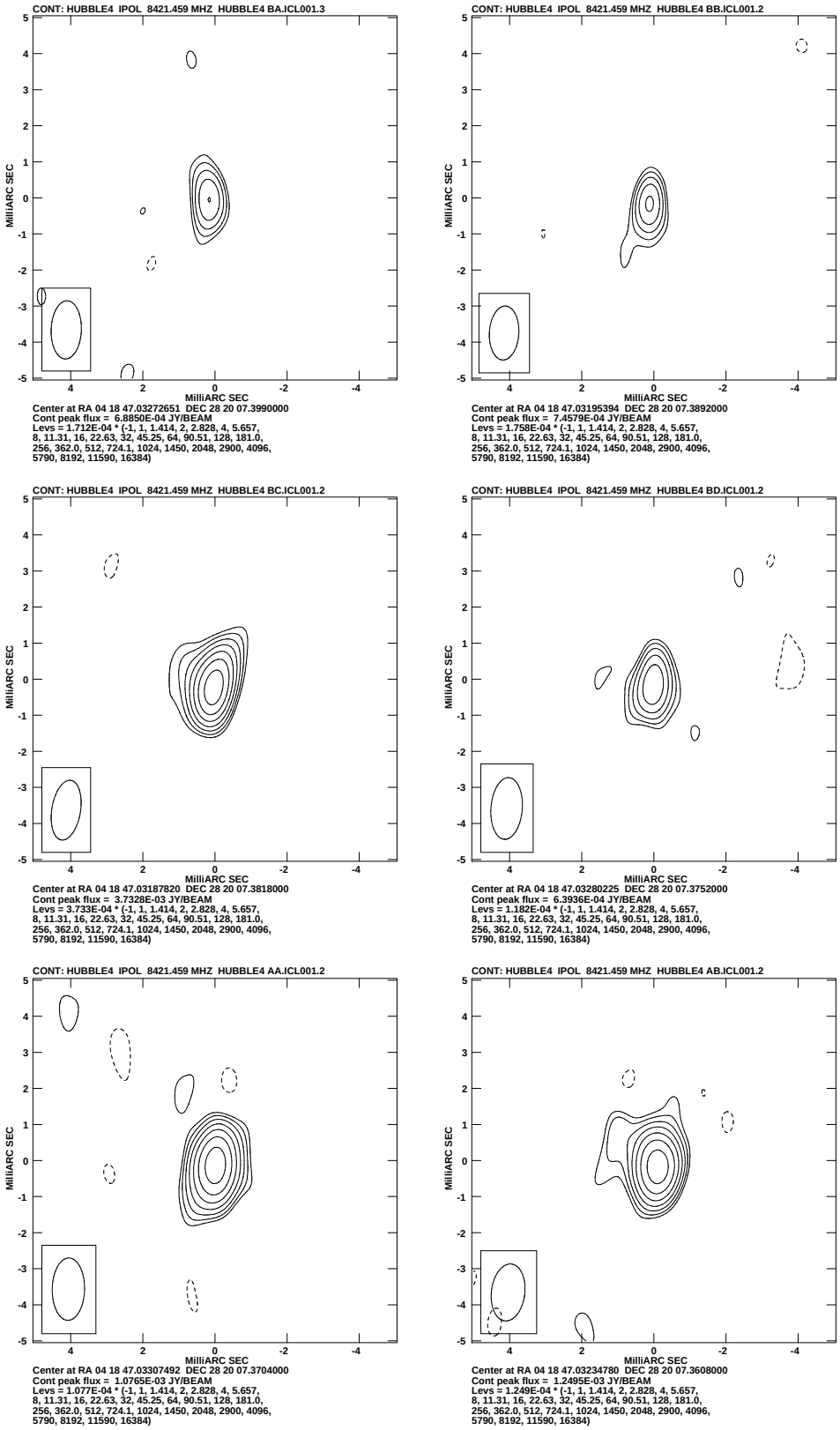

Figure 5.3 VLBA images of Hubble 4 at epochs 1 to 6 listed in Tab. 4.2 and 5.1.

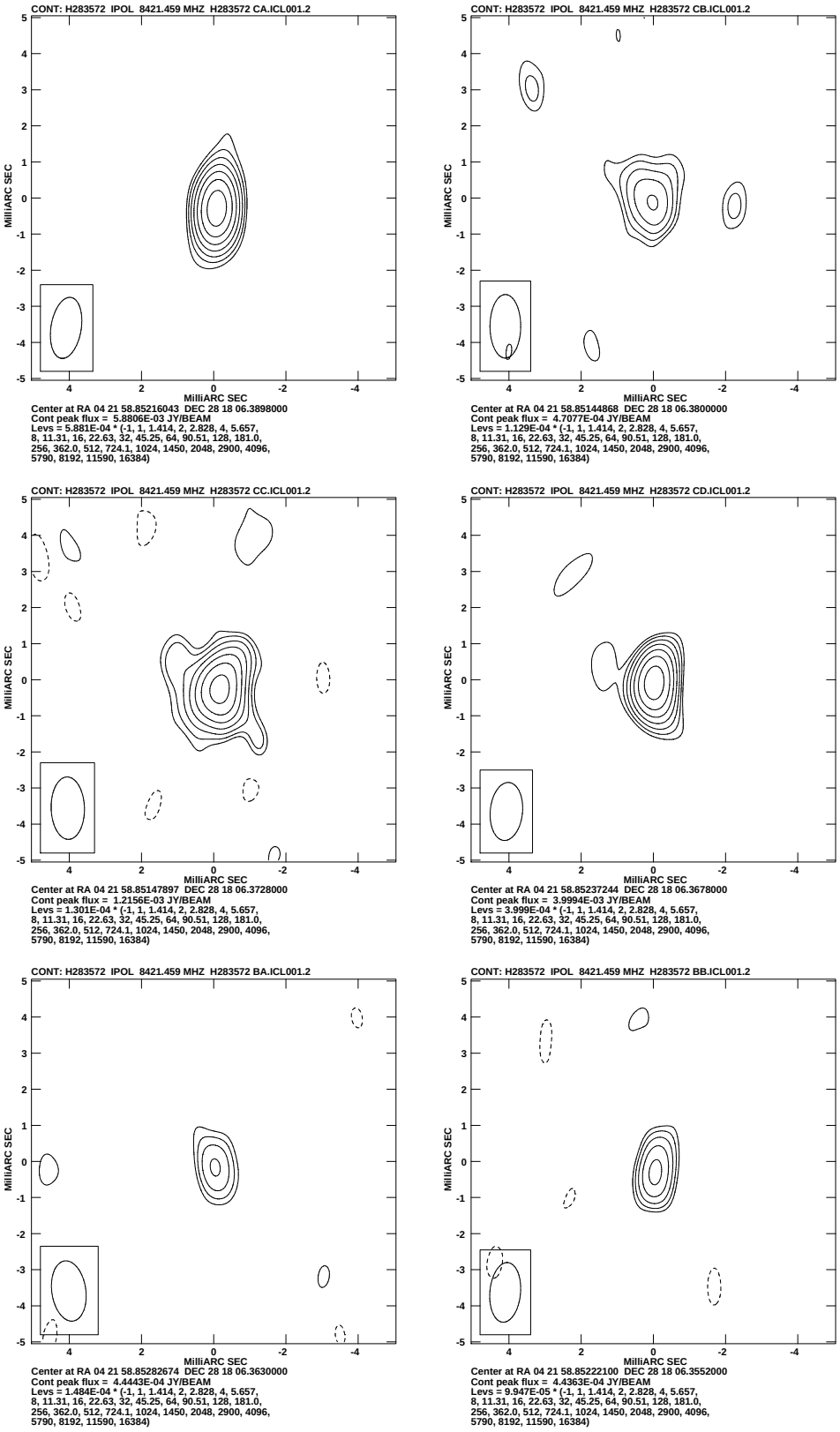

Figure 5.4 VLBA images of HDE 283572 at epochs 1 to 6 listed in Tab. 4.2 and 5.1.

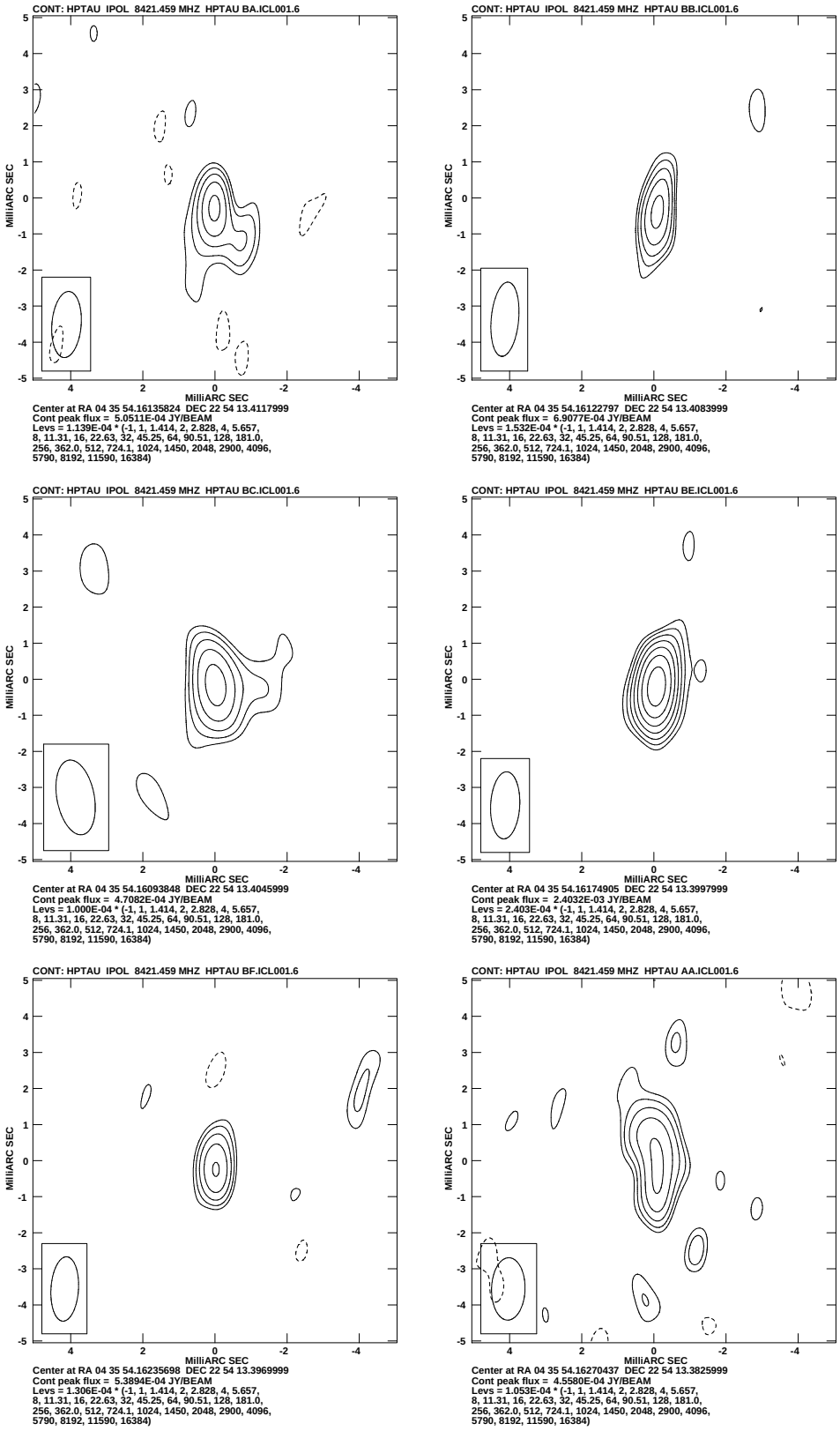

Figure 5.5 VLBA images of HP Tau/G2 at epochs 1, 2, 3, 5, 6 and 7 listed in Tab. 4.2 and 5.1.

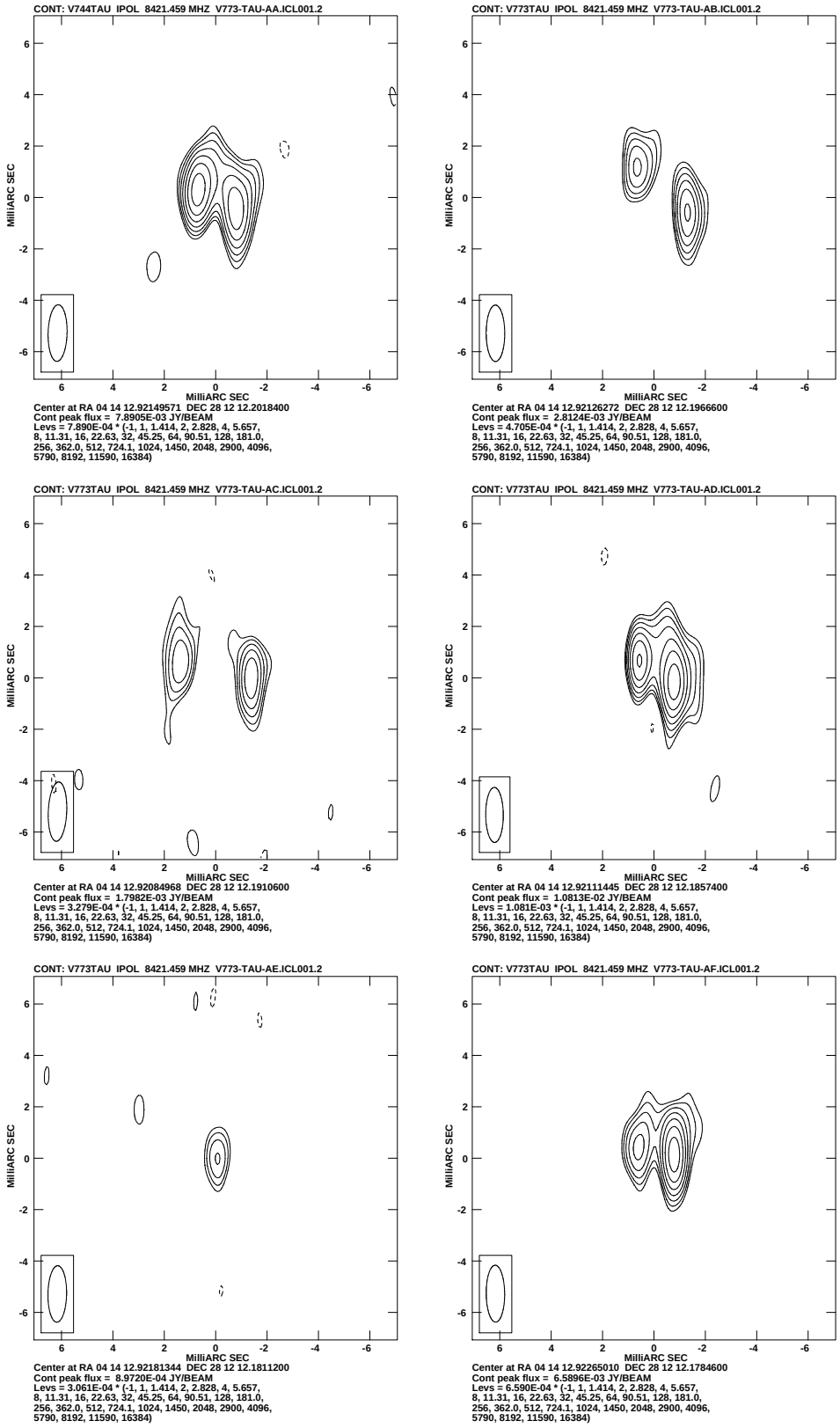

Figure 5.6 VLBA images of V773 Tau A at epochs 1 to 6 listed in Tab. 4.2 and 5.1.

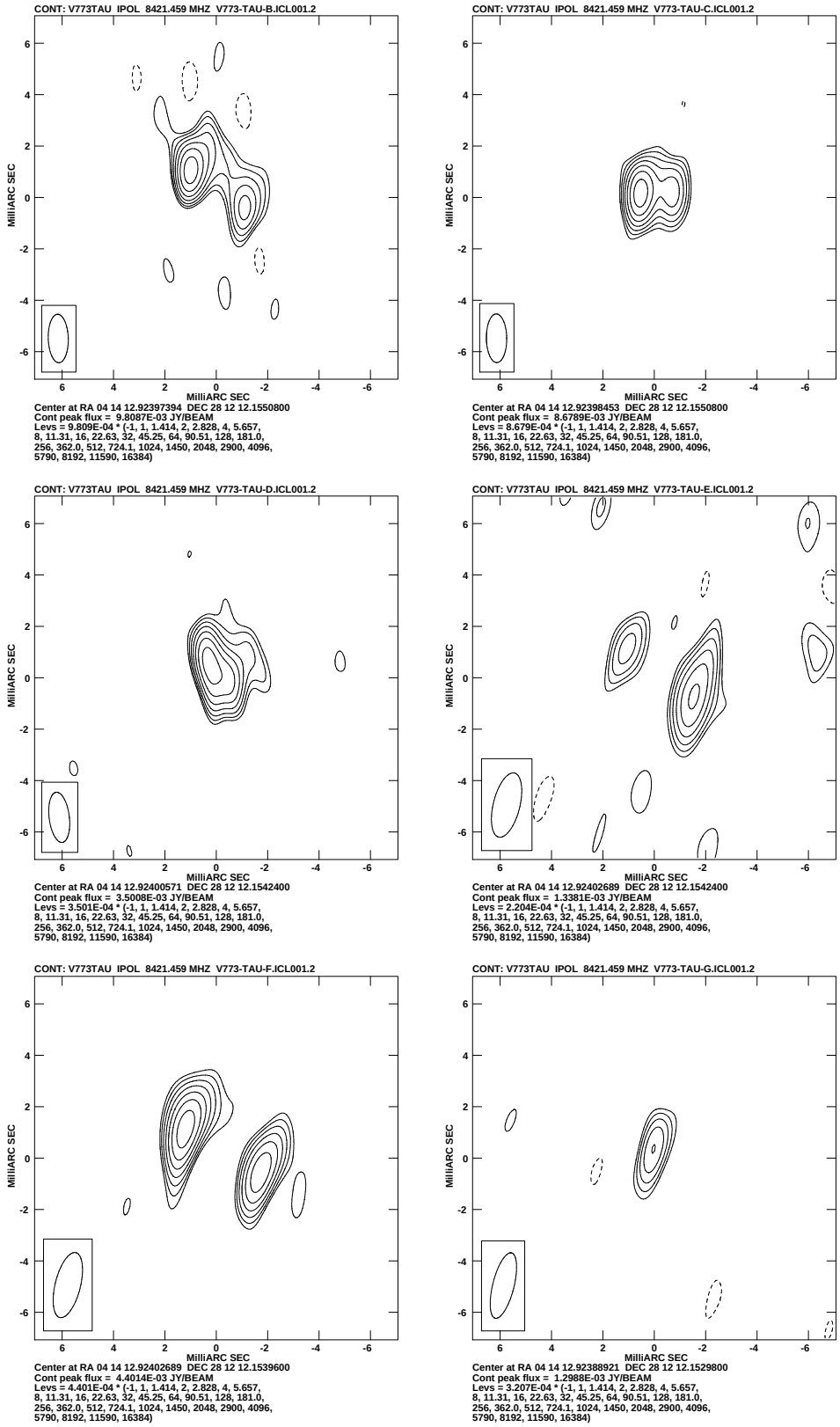

Figure 5.7 VLBA images of V773 Tau A at epochs 7 to 12 listed in Tab. 4.2 and 5.1.

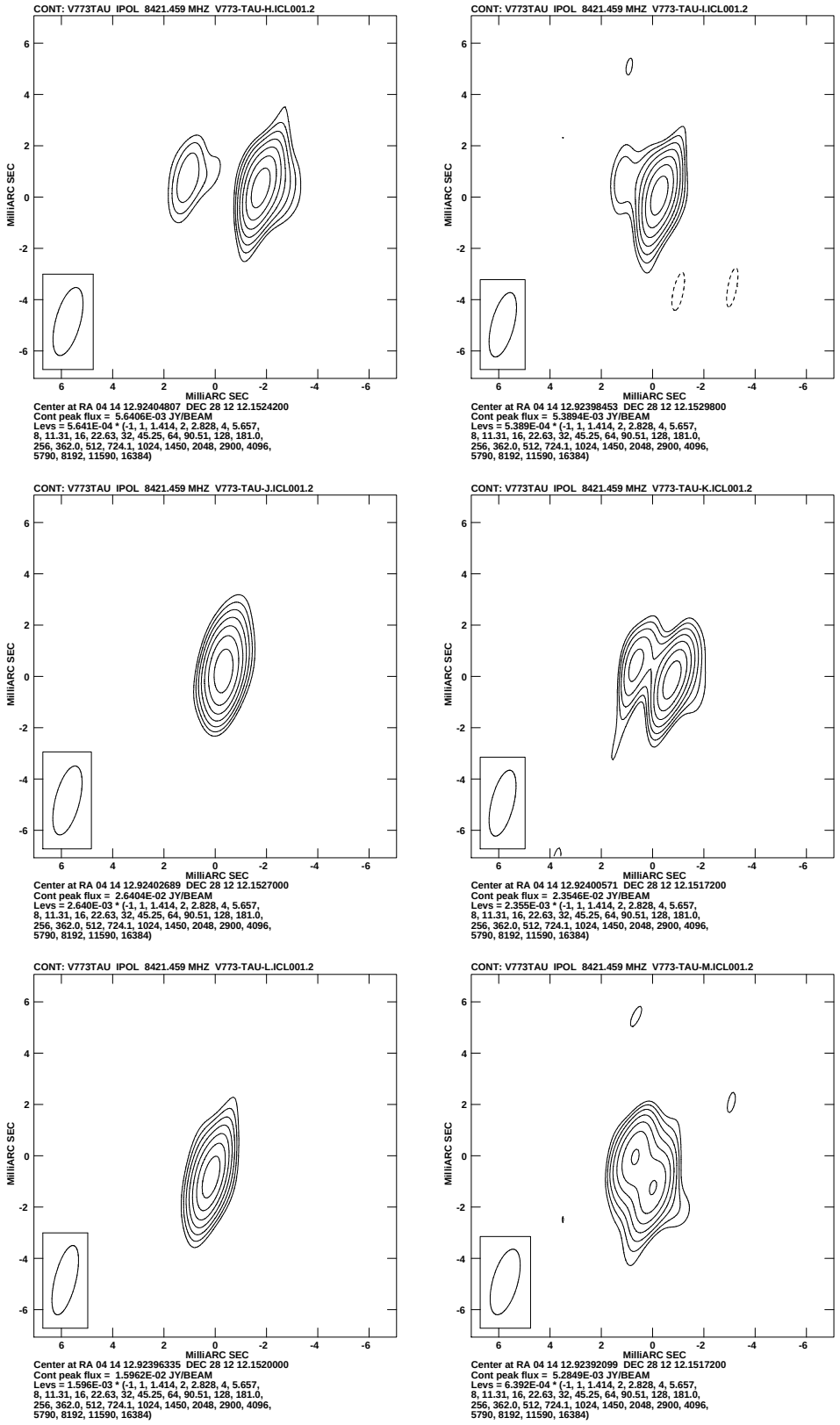

Figure 5.8 VLBA images of V773 Tau A at epochs 13 to 18 listed in Tab. 4.2 and 5.1.

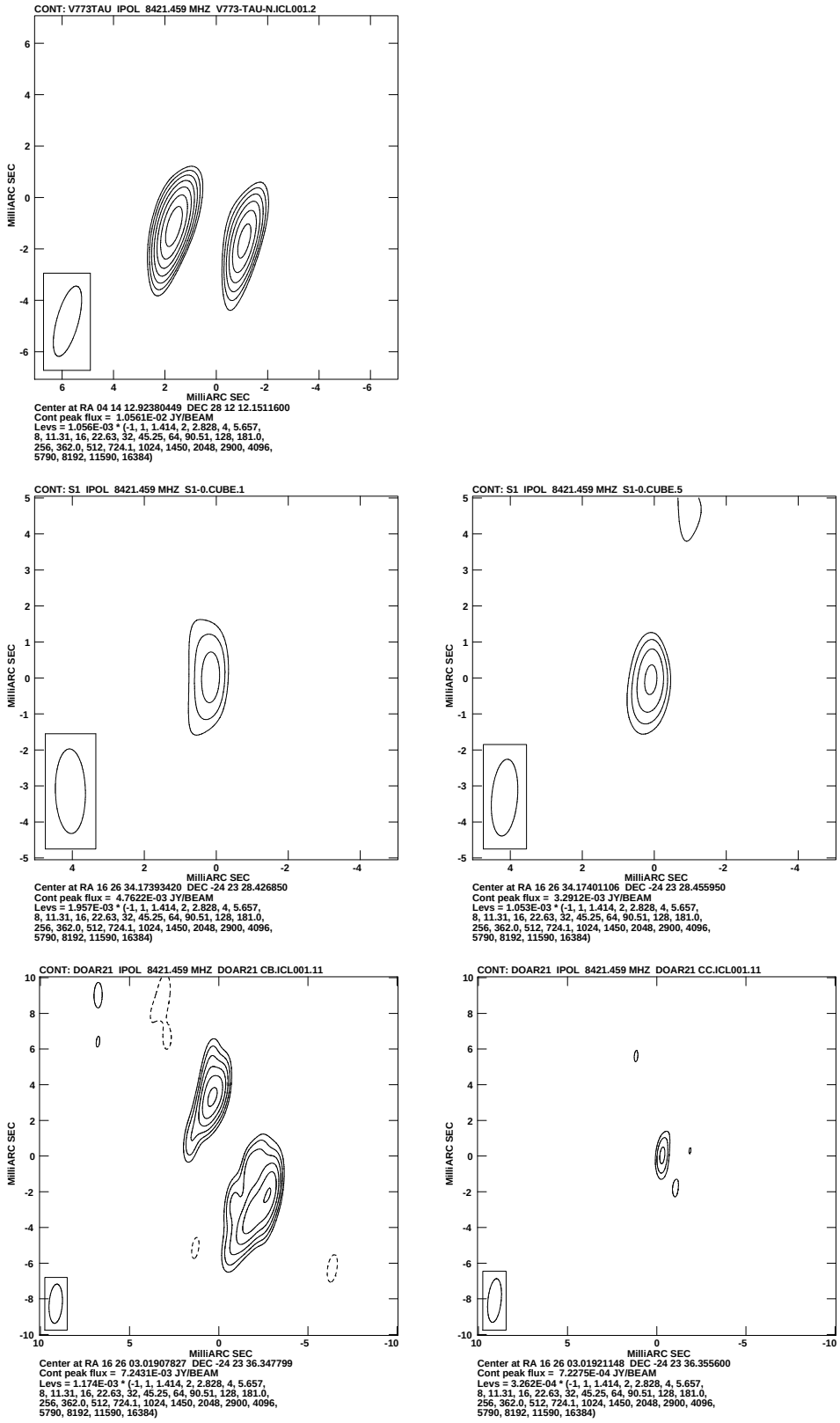

Figure 5.9 VLBA images of V773 Tau A (epoch 19), S1 (epochs 1 and 5), and DoAr 21 (epochs 2 and 4) listed in Tab. 4.2 and 5.1.

Table 5.1 (cont'd)

Epoch	Mean Date [JD]	α (J2000.0)	δ (J2000.0)	f_ν [mJy]	T_b [10^6 K]
8	2454347.037078	$54^s.1633509 \pm 0^s.000003$	$13''.38127 \pm 0''.00008$	0.78±0.12	9.22±1.42
9	2454438.785532	$54^s.1631378 \pm 0^s.000004$	$13''.37605 \pm 0''.00009$	0.76±0.11	5.20±0.75
V773 Tau A †		04^h14^m	$28°12'$		
1	2453622.001337	$12^s.9215438 \pm 0^s.000001$	$12''.20222 \pm 0''.00002$	10.00±0.32	106.59±3.41
		$12^s.9214354 \pm 0^s.000001$	$12''.20152 \pm 0''.00003$	9.22±0.37	98.27±3.94
2	2453689.813594	$12^s.9211625 \pm 0^s.000001$	$12''.19608 \pm 0''.00004$	3.45±0.23	37.97±2.53
		$12^s.9213067 \pm 0^s.000002$	$12''.19793 \pm 0''.00005$	2.46±0.23	27.07±2.53
3	2453756.632731	$12^s.9207455 \pm 0^s.000002$	$12''.19102 \pm 0''.00006$	2.04±0.21	21.28±2.19
		$12^s.9209564 \pm 0^s.000003$	$12''.19180 \pm 0''.00010$	1.90±0.25	19.82±2.61
4	2453827.438617	$12^s.9211553 \pm 0^s.000001$	$12''.18646 \pm 0''.00002$	8.72±0.39	103.98±4.65
		$12^s.9210561 \pm 0^s.000001$	$12''.18575 \pm 0''.00003$	18.38±0.58	219.17±6.92
5	2453899.242297	$12^s.9218088 \pm 0^s.000003$	$12''.18114 \pm 0''.00010$	0.87±0.18	9.53±1.97
6	2453984.010203	$12^s.9226916 \pm 0^s.000002$	$12''.17899 \pm 0''.00005$	3.76±0.32	41.00±3.49
		$12^s.9225899 \pm 0^s.000001$	$12''.17865 \pm 0''.00003$	7.74±0.31	84.41±3.38
7	2454336.046065	$12^s.9240420 \pm 0^s.000001$	$12''.15627 \pm 0''.00002$	13.16±0.50	155.73±5.92
		$12^s.9238934 \pm 0^s.000002$	$12''.15493 \pm 0''.00006$	7.89±0.62	93.37±7.34
8	2454342.029543	$12^s.9240252 \pm 0^s.000001$	$12''.15525 \pm 0''.00001$	9.80±0.29	113.89±3.37
		$12^s.9239338 \pm 0^s.000001$	$12''.15533 \pm 0''.00003$	6.05±0.33	70.31±3.84
9	2454349.010613	$12^s.9240072 \pm 0^s.000002$	$12''.15456 \pm 0''.00003$	7.27±0.34	81.47±3.81
10	2454354.994294	$12^s.9239067 \pm 0^s.000004$	$12''.15360 \pm 0''.00011$	1.84±0.23	11.95±1.49
		$12^s.9241045 \pm 0^s.000007$	$12''.15535 \pm 0''.00015$	0.76±0.20	4.93±1.30
11	2454359.980648	$12^s.9238938 \pm 0^s.000002$	$12''.15346 \pm 0''.00004$	3.45±0.22	23.50±1.50
		$12^s.9241150 \pm 0^s.000001$	$12''.15516 \pm 0''.00003$	5.02±0.23	34.19±1.57
12	2454364.966887	$12^s.9238903 \pm 0^s.000003$	$12''.15329 \pm 0''.00009$	1.39±0.20	11.09±1.60
13	2454370.950388	$12^s.9239105 \pm 0^s.000001$	$12''.15281 \pm 0''.00003$	7.01±0.28	46.41±1.85
		$12^s.9241242 \pm 0^s.000005$	$12''.15324 \pm 0''.00010$	2.16±0.30	14.30±1.99
14	2454376.934236	$12^s.9239656 \pm 0^s.000001$	$12''.15305 \pm 0''.00003$	7.27±0.31	55.56±2.37
15	2454382.917679	$12^s.9240014 \pm 0^s.000001$	$12''.15297 \pm 0''.00001$	36.44±0.51	241.16±3.38
16	2454390.896007	$12^s.9240531 \pm 0^s.000002$	$12''.15221 \pm 0''.00005$	12.27±0.81	93.05±6.14
		$12^s.9239474 \pm 0^s.000001$	$12''.15161 \pm 0''.00002$	28.89±0.85	219.10±6.45
17	2454396.879462	$12^s.9239765 \pm 0^s.000001$	$12''.15119 \pm 0''.00002$	21.96±0.57	165.74±4.30
18	2454400.868432	$12^s.9239199 \pm 0^s.000001$	$12''.15043 \pm 0''.00004$	6.86±0.34	46.48±2.30
		$12^s.9239780 \pm 0^s.000001$	$12''.15179 \pm 0''.00004$	5.31±0.29	35.98±1.97
19	2454421.811366	$12^s.9237229 \pm 0^s.000001$	$12''.14946 \pm 0''.00003$	7.60±0.27	55.67±1.98
		$12^s.9239298 \pm 0^s.000001$	$12''.15003 \pm 0''.00002$	11.49±0.27	84.17±1.98
S1		16^h26^m	$-24°23'$		
1	2453545.730989	$34^s.1739533 \pm 0^s.000002$	$28''.42695 \pm 0''.00006$	7.03±0.56	62.54±4.98
2	2453628.504016	$34^s.1736922 \pm 0^s.000002$	$28''.43209 \pm 0''.00006$	4.56±0.47	46.29±4.77
3	2453722.247609	$34^s.1743677 \pm 0^s.000001$	$28''.44149 \pm 0''.00004$	4.35±0.35	43.63±3.51
4	2453810.007447	$34^s.1746578 \pm 0^s.000002$	$28''.45127 \pm 0''.00005$	5.33±0.41	54.35±4.18
5	2453889.789004	$34^s.1740172 \pm 0^s.000001$	$28''.45594 \pm 0''.00002$	3.29±0.13	37.05±1.46

Table 5.1 (cont'd)

Epoch	Mean Date [JD]	α (J2000.0)	δ (J2000.0)	f_ν [mJy]	T_b [10^6 K]
6	2453969.570572	$34^s.1732962 \pm 0^s.000001$	$28''.46260 \pm 0''.00005$	4.35±0.22	36.53±1.85
DoAr 21		16^h26^m	$-24^\circ23'$		
1	2453621.523501	$03^s.0189304 \pm 0^s.000007$	$36''.34339 \pm 0''.00013$	11.78±1.41	116.03±13.89
2	2453691.332297	$03^s.0191097 \pm 0^s.000002$	$36''.34450 \pm 0''.00005$	20.34±1.42	216.80±15.14
3	2453744.187627	$03^s.0191069 \pm 0^s.000006$	$36''.35580 \pm 0''.00023$	0.39±0.12	2.34± 0.72
4	2453755.157251	$03^s.0191795 \pm 0^s.000003$	$36''.35568 \pm 0''.00013$	0.97±0.19	9.25± 1.81
5	2453822.971950	$03^s.0189625 \pm 0^s.000007$	$36''.36192 \pm 0''.00020$	1.49±0.28	6.18± 1.16
6	2453890.786284	$03^s.0182041 \pm 0^s.000002$	$36''.36376 \pm 0''.00010$	1.92±0.23	16.86± 2.02
7	2453971.565109	$03^s.0169857 \pm 0^s.000004$	$36''.36996 \pm 0''.00016$	1.45±0.32	13.14± 2.90

[†]For 13 epochs we detect a double source, thus we present here the position for both the primary and secondary components, and the flux densities detected for each one.

5.1 Absolute astrometry

The displacement of a source on the celestial sphere is the combination of its trigonometric parallax (π) and its proper motion (μ). In what follows, we will have to consider three different situations in terms of proper motions.

(1) Single Stars

Two of our target stars are apparently single (HDE 283572 and Hubble 4), and one (HP Tau/G2) is a member of a multiple system with an orbital period so much longer than the timespan covered by the observations that the effect of the companions can safely be ignored. Thus, in these three cases, the proper motion can be assumed to be linear and uniform, and the right ascension (α) and the declination (δ) vary as a function of time t as:

$$\begin{aligned} \alpha(t) &= \alpha_0 + (\mu_\alpha \cos\delta)t + \pi f_\alpha(t) \\ \delta(t) &= \delta_0 + \mu_\delta t + \pi f_\delta(t), \end{aligned} \tag{5.1}$$

where α_0 and δ_0 are the coordinates of the source at a given reference epoch, μ_α and μ_δ are the components of the proper motion, and f_α and f_δ are the projections over α and δ, respectively, of the parallactic ellipse.

(2) Binary Systems

One source (T Tau Sb) is a member of a binary system with an orbital period longer than the timespan of our observations but not by a huge factor. While a full Keplerian fit would again, in principle, be needed, we found that including a constant acceleration term provides an adequate description of the trajectory. The fitting functions in this case are of the form:

$$\begin{aligned} \alpha(t) &= \alpha_0 + (\mu_{\alpha 0}\cos\delta)t + \frac{1}{2}(a_\alpha \cos\delta)t^2 + \pi f_\alpha(t) \\ \delta(t) &= \delta_0 + \mu_{\delta 0}t + \frac{1}{2}a_\delta t^2 + \pi f_\delta(t), \end{aligned} \tag{5.2}$$

where $\mu_{\alpha 0}$ and $\mu_{\delta 0}$ are the proper motions at a reference epoch, and a_α and a_δ are the projections of the uniform acceleration.

(3) Tight Binaries

Three of our sources (V773 Tau A, S1 and DoAr 21) are compact binary systems with an orbital period of the order of the timespan covered by the observations. In such a situation, one should fit simultaneously for the uniform proper motion of the center of mass and for the Keplerian orbit of the system. This requires more observations than are needed to fit only for a uniform proper motion. Additional data were collected to adequately constrain the required fits only for V773 Tau, and in this case, the orbital path was fully characterized. For S1 and DoAr 21, we will present preliminary results based on Eqs. 5.1 where the Keplerian motion is not included. We will see momentarily that the main effect of not fitting for the Keplerian orbit is an increase in the final uncertainty on the distance.

The astrometric parameters were determined by least-squares fitting the data points with either Eqs. 5.1 or Eqs. 5.2 using a Singular Value Decomposition (SVD) scheme. To check our results, we also performed two other fits to the data, a linear one based on the associated normal equations, and a non-linear one based on the Levenberg-Marquardt algorithm. They gave results identical to those obtained using the SVD method.

Table 5.2. Astrometric parameters. Reference epochs, source positions at the reference epochs, and number of observations used for each fit.

Source	Reference Epoch ‡	α_0 [at the reference epoch]	δ_0 [at the reference epoch]	No. Obs.
T Tau Sb$^{(a)}$	J2004.627	$04^h21^m59\overset{s}{.}425081\pm0\overset{s}{.}000005$	$19°32'05\overset{''}{.}71566\pm0\overset{''}{.}000030$	12/14
T Tau Sb$^{(b)}$ †.....	J2004.627	$04^h21^m59\overset{s}{.}425065\pm0\overset{s}{.}000002$	$19°32'05\overset{''}{.}71566\pm0\overset{''}{.}000400$	12/14
Hubble 4	J2005.355	$04^h18^m47\overset{s}{.}032414\pm0\overset{s}{.}000001$	$28°20'07\overset{''}{.}37920\pm0\overset{''}{.}000200$	6/6
HDE 2835724	J2005.355	$04^h21^m58\overset{s}{.}852030\pm0\overset{s}{.}000020$	$28°18'06\overset{''}{.}37128\pm0\overset{''}{.}000050$	6/6
HP Tau/G2$^{(a)}$	J2006.810	$04^h35^m54\overset{s}{.}162033\pm0\overset{s}{.}000003$	$22°54'13\overset{''}{.}49345\pm0\overset{''}{.}000020$	9/9
HP Tau/G2$^{(b)}$	J2006.810	$04^h35^m54\overset{s}{.}162030\pm0\overset{s}{.}000002$	$22°54'13\overset{''}{.}49362\pm0\overset{''}{.}000014$	8/9
V773 Tau A$^{(a)}$ ...	J2006.780	$04^h14^m12\overset{s}{.}922271\pm0\overset{s}{.}000010$	$28°12'12\overset{''}{.}17442\pm0\overset{''}{.}000140$	7/19
V773 Tau A$^{(b)}$ ...	J2006.780	$04^h14^m12\overset{s}{.}922269\pm0\overset{s}{.}000009$	$28°12'12\overset{''}{.}17454\pm0\overset{''}{.}000080$	19/19
S1	J2006.061	$16^h26^m34\overset{s}{.}174127\pm0\overset{s}{.}000026$	$-24°23'28\overset{''}{.}44498\pm0\overset{''}{.}000280$	6/6
DoAr 21	J2006.167	$16^h26^m03\overset{s}{.}018535\pm0\overset{s}{.}000020$	$-24°23'36\overset{''}{.}35830\pm0\overset{''}{.}000220$	7/7

‡The reference epoch was taken at the mean of each set of observations.

Table 5.3. Astrometric parameters. Proper motions, parallaxes, and distances.

Source	$\mu_\alpha \cos\delta$ [mas yr^{-1}]	μ_δ [mas yr^{-1}]	π [mas]	d [pc]
T Tau Sb$^{(a)}$	4.00±0.12	−1.18±0.05	6.90±0.09	145.0±2.0
T Tau Sb$^{(b)}$ †.....	4.02±0.03	−1.18±0.05	6.82±0.03	146.7±0.6
Hubble 4	4.30±0.05	−28.90±0.30	7.53±0.03	132.8±0.5
HDE 2835724	8.88±0.06	−26.60±0.10	7.78±0.04	128.5±0.6
HP Tau/G2$^{(a)}$	13.90±0.06	−15.60±0.30	6.19±0.07	161.6±1.7
HP Tau/G2$^{(b)}$	13.85±0.03	−15.40±0.20	6.20±0.03	161.2±0.9
V773 Tau A$^{(a)}$ ...	17.28±0.19	−23.74±0.14	7.53±0.26	132.8±4.5
V773 Tau A$^{(b)}$ ...	17.27±0.14	−23.79±0.09	7.57±0.20	132.0±3.5
S1	−3.88±0.87	−31.55±0.69	8.55±0.50	116.9±7.1
DoAr 21	−26.47±0.92	−28.23±0.73	8.20±0.37	121.9±5.5

†The acelerations terms obtained for this fit were $a_\alpha = 1.53 \pm 0.13$ mas yr^{-2} and $a_\delta = 0.00 \pm 0.19$ mas yr^{-2}.

5.1.1 Parallax and proper motions

T Tau Sb— In order to measure the trigonometric parallax of T Tau Sb, we collected observations roughly every 2 months between 2003 September and 2005 July (first 12 observations listed in Tab. 4.2). Ten of this twelve observations are shown in Fig. 5.1, and in panels 1 to 4 of Fig. 5.2. As time went by, we decide to obtain new observations to fit an orbit to T Tau Sb around T Tau Sa. One additional observation was collected in 2008 May (epoch 13 in Tab. 4.2, panel 5 in Fig. 5.2), and we made use of data from VLBA archive (epoch 14 in Tab. 4.2, panel 6 of Fig. 5.2). The source was detected in all 14 observations. In this section we will explain how we used the first 12 observations to fit for the parallax and proper motions, and the orbit of T Tau S system, where we used all 14 epochs, is explained in Sect. 5.4.

All the measured source positions and fluxes are listed in Tab. 5.1. Since T Tau Sb is a member of a double stellar system (T Tau Sa/Sb) with an orbital period ($\lesssim 20$ yr) longer than the timespan of our observations (~ 2 yr), we performed two astrometric fits: one where we assumed that the proper motion is linear and uniform, and other that includes a constant acceleration.

First astrometric fit— The fit to the data points by Eqs. 5.1 (Fig. 5.10a) yields the astrometric parameters listed in Tabs. 5.2 and 5.3 labelled as T Tau Sb$^{(a)}$. This corresponds to a distance of 145 ± 2 pc. The post-fit r.m.s. however, is not very good (particularly in right ascension: ~ 0.2 mas), as the fit does not pass through many of the observed positions (see Fig. 5.10a). As a matter of fact, 75 μas and 16.5 μs had to be added quadratically to the formal errors listed in Cols. [3] and [4] of Tab. 5.1 to obtain a reduced χ^2 of 1 in both right ascension and declination; the errors on the fitted parameters listed in Tabs. 5.2 and 5.3 include this systematic contribution. These large systematic errors most certainly reflects the fact that the proper motion of T Tau Sb is not uniform because it belongs to a multiple system.

Second astrometric fit— The fit where acceleration terms are included is significantly better (Fig. 5.10b) with a post-fit r.m.s. of 60 μas in right ascension and 90 μas in declination. It yields the parameters listed in Tabs. 5.2 and 5.3 labelled as T Tau Sb$^{(b)}$. To obtain a reduced χ^2 of 1 in both right ascension and declination, one must add quadratically 3.8 μs and 75 μas to the statistical errors listed in Cols. [3] and [4] of Tab. 5.1. The uncertainties on the astrometric parameters (Tabs. 5.2 and 5.3), include this systematic contribu-

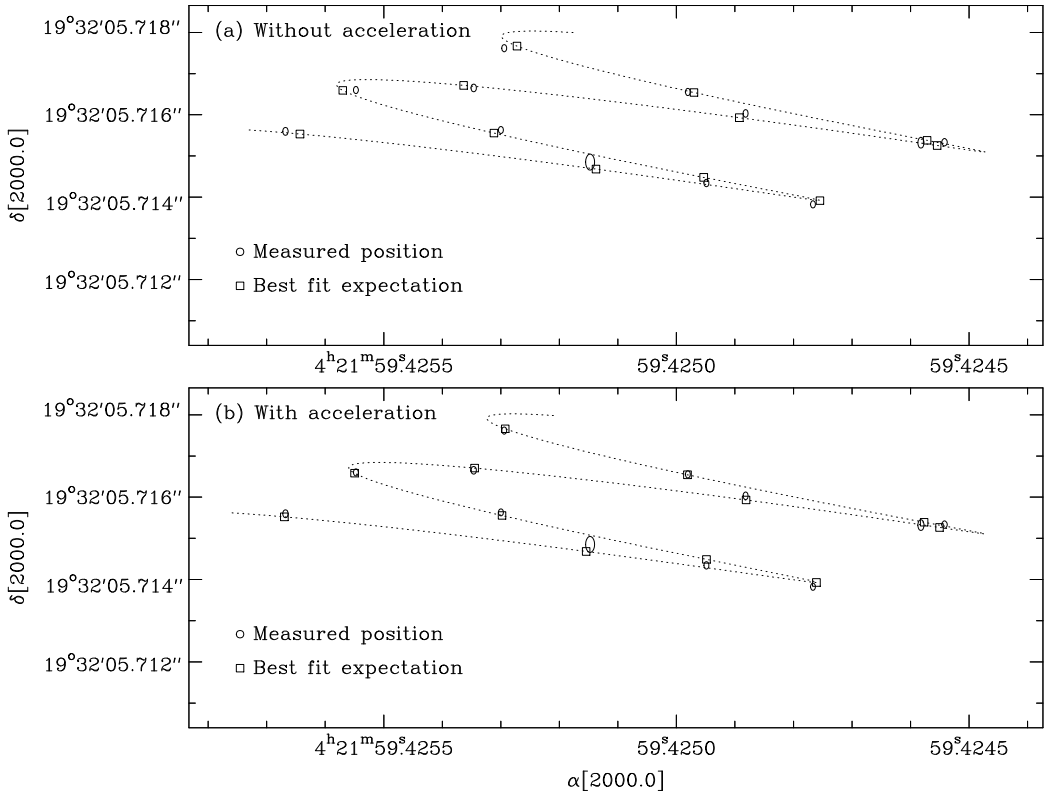

Figure 5.10 Measured positions of T Tau Sb and best fit without (a) and with (b) acceleration terms. The observed positions are shown as ellipses, the size of which represents the magnitude of the errors. Note the very significant improvement when acceleration terms are included.

tion. Note also that the reduced χ^2 for the fit without acceleration terms is almost 8 if the latter systematic errors (rather than those mentioned earlier) are used. The trigonometric parallax obtained when acceleration terms are included, corresponds to a distance of 146.7 ± 0.6 pc, somewhat smaller than, but within 1σ of the distance obtained by *Hipparcos* ($d = 177^{+68}_{-39}$ pc). Note that the relative error of our distance is about 0.4%, against nearly 30% for the *Hipparcos* result, an improvement of almost two orders of magnitude.

Hubble 4 and HDE 283572— We made use of all 6 observations listed in Tab. 4.2 for each source (see contour maps in Fig. 5.3 and 5.4). In Tab. 5.1 we provide the measured source positions and flux densities. Since both sources appear to be isolated, we considered linear and uniform proper motions (Eqs. 5.1). The best fits (Fig. 5.11) give the parameters listed in Tabs. 5.2 and

5.3. The measured parallaxes correspond to distances of 132.8 ± 0.5 pc for Hubble 4, and 128.5 ± 0.6 pc for HDE 283572. The post-fit r.m.s. (dominated by the remaining systematic errors) is quite good for HDE 283572: 60 μas and 90 μas in right ascension and declination, respectively. For Hubble 4, on the other hand, the residual is good in right ascension (40 μas), but large in declination (240 μas). To obtain a reduced χ^2 of one both in right ascension and declination, one must add quadratically 3.1 μs and 340 μas to the formal errors in Cols. [3] and [4] of in Tab. 5.1 for Hubble 4, and 4.3 μs and 115 μas for HDE 283572. All the errors quoted include these systematic contributions.

The origin of the large declination residual for Hubble 4 (which does not affect strongly the parallax determination, because the latter is dominated by the right ascension measurements) is not entirely clear. The fact that the residual is only (or, at least, mostly) detected in declination (Fig. 5.12) would suggest a calibration issue. Indeed, astrometric fitting of phase-referenced VLBI observations is usually worse in declination than in right ascension (e.g. Fig. 1 in Chatterjee et al. 2004) as a result of residual zenith phase delay errors (Reid et al. 1999). We consider this possibility fairly unlikely here, however, because such a problem would have been detected during the multi-source calibration, and because the observations and reduction of Hubble 4 and HDE 283572 (which does not appear to be affected by any calibration issue) were performed following identical protocols and over the same period of time. Another element that argues against a calibration problem is that the large residual is not the result of one particularly discrepant observation: in addition to the fit mentioned above where all 6 observations of Hubble 4 are taken into account, we made 5 fits where we sequentially discarded one of the epochs. All 5 fits gave similar astrometric parameters, and a similarly large declination residual. Thus, we argue that this large residual might be real, rather than related to a calibration problem. At the distance of Hubble 4, 240 μas correspond to 0.032 AU, or about 7 $R_\odot$. Hubble 4 is estimated to have a radius of about 3.4 $R_\odot$ (Johns-Krull et al. 2004), so the amplitude of the residual is just about 2 R_*. Keeping this figure in mind, at least two mechanisms could potentially explain the large declination residual: (i) the magnetosphere of Hubble 4 could be somewhat more extended than its photosphere, and the residuals could reflect variations in the structure of the magnetosphere; (ii) Hubble 4 could have a companion, and the residuals could reflect the corresponding reflex motion. Let us examine the pros and

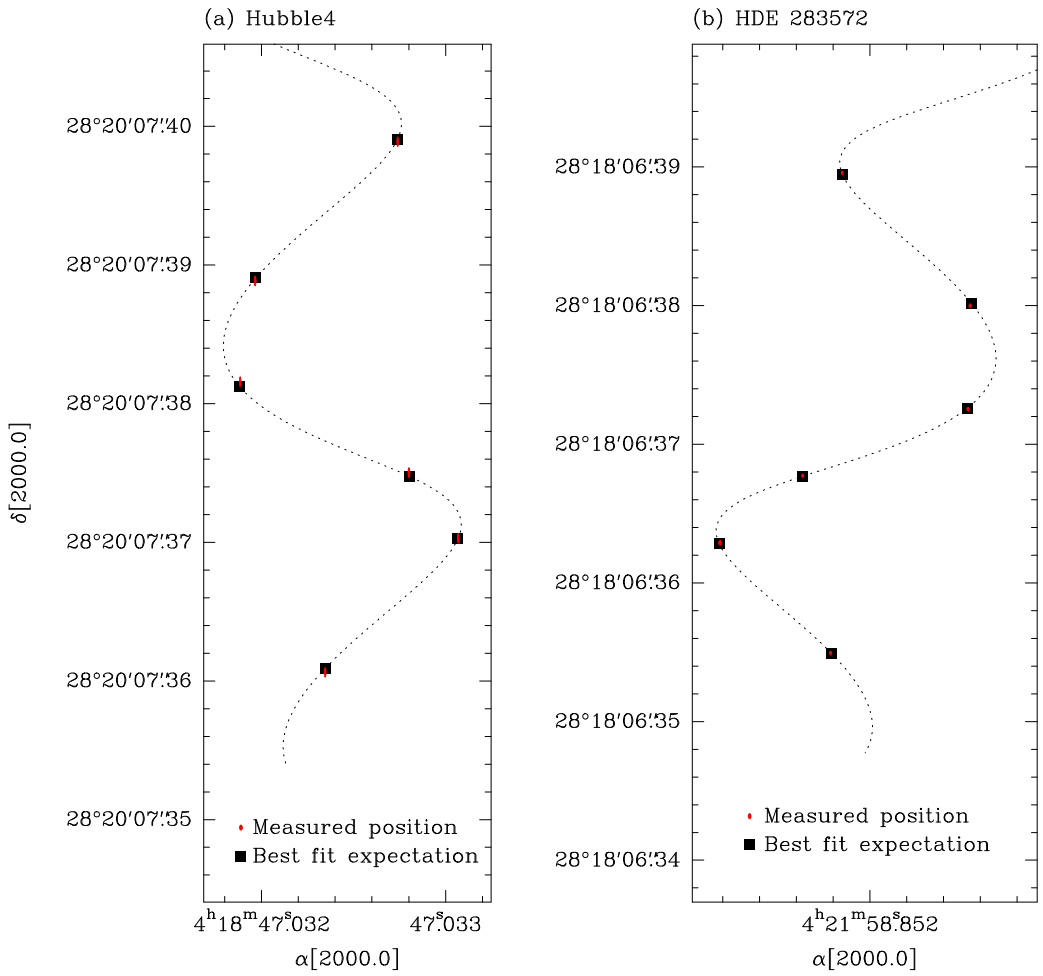

Figure 5.11 Measured positions and best fit for (a) Hubble 4, and (b) HDE 283572. The observed positions are shown as ellipses, the size of which represents the error bars.

cons of these two possibilities.

If the residuals were related to a variable extended magnetosphere, one would expect the emission to be occasionally somewhat extended. Interestingly, Phillips et al. (1991) reported that Hubble 4 was slightly resolved in their VLBI data, and we find it to be resolved also in at least two of our own observations. On the other hand, if the emission were related to variations in the magnetosphere, one would expect to see variations with the periodic-

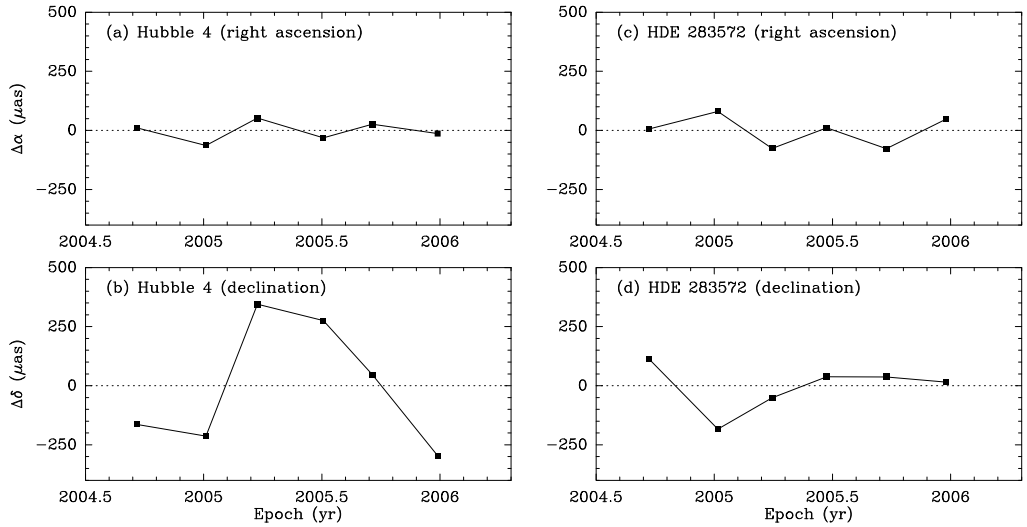

Figure 5.12 Post-fit residuals for Hubble 4 (left) and HDE 283572 (right) in right ascension (top) and declination (bottom).

ity of the rotational period of the star (about $12/\sin i$ days –Johns-Krull et al. 2004). Given that the separation between our successive observations is typically three months, we would expect the residuals to be essentially random. Instead, those residuals seem to show a periodicity of about 1.2 years (see Fig. 5.12). This would be more consistent with our alternative proposal that the residuals be related to the reflex motion of Hubble 4 due to the presence of an unseen companion. The semi-major axis corresponding to a period of 1.2 yr and a mass of 0.7 $M_\odot$ (see below) is just about 1 AU. Since the ratio between the amplitude of the reflex motion and that of the orbital path is the inverse of the ratio between the mass of the primary and that of the companion, the mass of the companion would have to be $0.7(0.032/1) = 0.02$ $M_\odot$. The companion would then have to be a very low-mass star, or a brown dwarf. Note, however, that the residuals are relatively poorly constrained with the existing data, and that additional observations aimed –in particular– at confirming the periodicity in the residuals will be needed to resolve this issue.

HP Tau/G2— We detected the source at all 9 observations listed in Tab. 4.2 (see also contour maps in Fig. 5.5). Since HP Tau/G2 is a member of a triple system, we should in principle describe its proper motion as the combination of the uniform motion of the center of mass and a Keplerian orbit. This is not

necessary, however, because the orbital period of the system must be very much longer than the timespan covered by our observations. If we assume that the total mass of the HP Tau/G2 – HP Tau/G3 system is 2–3 $M_\odot$ and that the current observed separation is a good estimate of the system's semi-major axis, then the orbital period is expected to be 35,000 to 45,000 yr. This is indeed very much longer that the 2 yr covered by our observations, and the acceleration terms can be safely ignored. Thus we made use of Eqs. 5.1 for the astrometric fits. Since the source was elongated in the north-south direction during the seventh observation (see panel 6 in Fig. 5.5), two different fits were made: one where the seventh epoch was included, and one where it was ignored.

First astrometric fit— When the seventh epoch is included, we obtain the astrometric parameters listed in Tabs. 5.2 and 5.3 labelled as HP Tau/G2$^{(a)}$. This corresponds to a distance of 161.6 ± 1.7 pc. The post-fit r.m.s. in this case is 0.12 mas in right ascension and 0.51 mas in declination. To obtain a reduced χ^2 of one in both right ascension and declination, one must add quadratically 8.8 μs and 0.59 mas in right ascension and declination, respectively, to the errors in Cols. [3] and [4] of Tab. 5.1. The uncertainties on the parameters include these systematic contributions. Note that the seventh epoch contributes significantly to the total post-fit r.m.s. since the position corresponding to that observation is farther from the fit (both in right ascension and declination) than that at any other epoch (see Fig. 5.13).

Second astrometric fit— If the seventh observation is ignored, the best fit yields the parameters listed in Tabs. 5.2 and 5.3 labelled as HP Tau/G2$^{(b)}$. All these parameters are consistent within 1σ with those obtained when the seventh observation is included. The corresponding distance in this case is 161.2 ± 0.9 pc, and the post-fit r.m.s. is 0.058 mas in right ascension and 0.33 mas in declination, significantly better than in the previous fit. Indeed, to obtain a reduced χ^2 of one in both right ascension and declination, one must only add quadratically 3.65 μs and 0.38 mas to the formal errors in Cols. [3] and [4] of Tab. 5.1. Again, the uncertainties on the parameters include these systematic contributions.

As mentioned earlier, the source during the seventh epoch was extended, and the astrometry consequently less reliable. Since the fit when this epoch is ignored is clearly much better than that when it is included, we consider the second fit above our best result. It is noteworthy that, whether or not the seventh epoch is included, the post-fit r.m.s. and the systematic error contri-

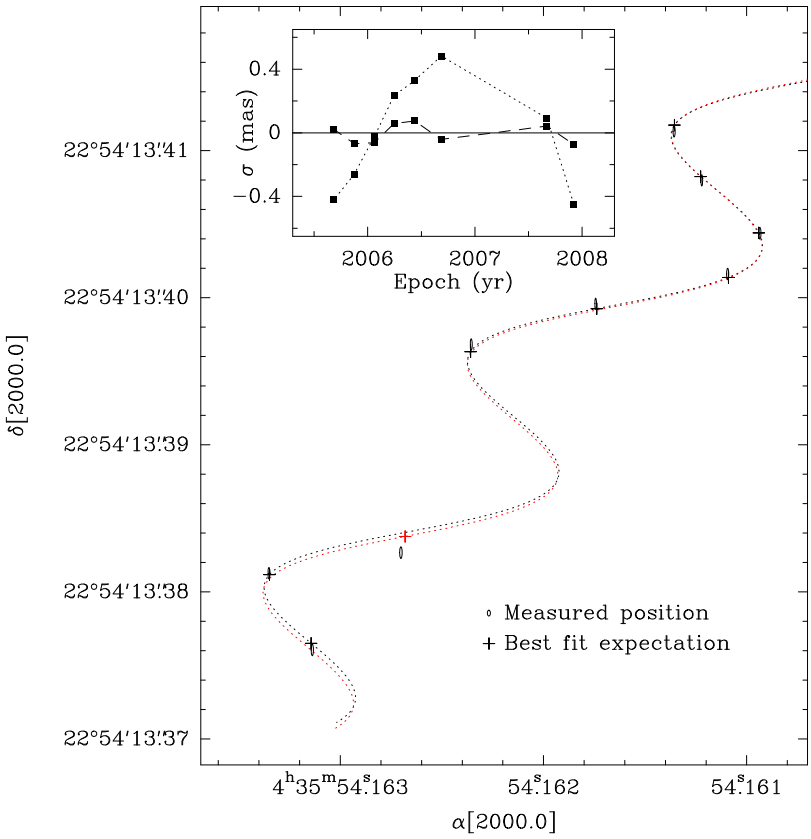

Figure 5.13 Measured positions and best fits for HP Tau/G2. The observed positions are shown as ellipses, the size of which represents the error bars. Two fits are shown: the dotted black line corresponds to the fit where the 7th epoch is ignored, whereas the dotted red line is the fit where it is included. Note that the 7th observation falls significantly to the south of either fit. The inset shows the fit residuals (of the fit without the 7th epoch) in right ascension (dashed line) and declination (dotted line). Note the large residuals in declination.

bution that must be added to the uncertainties quoted in Tab. 5.1, are much larger in declination than in right ascension. Fortunately, this large declination contribution does not strongly affect the distance determination, because the strongest constraints on the parallax come from the right ascension measurements. Interestingly, this is, with Hubble 4, the second source for which we find large systematic declination residuals. In the case of Hubble 4, we argued that the large post-fit declination r.m.s. might trace the reflex motion caused by an unseen companion, because a periodicity of about 1.2 yr could

be discerned in the residuals. In the present source, the case for a periodicity is less clear (Fig. 5.13, inset), but the residuals are clearly not random. Interestingly, the large residuals are in the same north-south direction as the extension of the source seen during our 7th observation. This orientation might, therefore, correspond to a preferred direction of the system along which it tends to vary more strongly. Additional observations will clearly be necessary to settle this issue.

V773 Tau A— The source was detected at all 19 epochs listed in Tab. 4.2, but it was found to be double at 13 epochs, and single for the remaining 6. In Figs. 5.6, 5.7, 5.8, and in panel 1 of Fig. 5.9 are shown all 19 contour maps of the system. The source positions (including both primary and secondary when the source is double) are listed in Tab. 5.1. It is possible to use Eqs. 5.1 for a binary system if we know the position of the barycenter of the system. To deduce the coordinates of the barycenter from the positions listed in Tab. 5.1, we need to take into account the orbital motion of the system. The orbital fit for V773 Tau A is discussed in Sect. 5.4, and we will make reference to this section in the next few paragraphs. We, again, performed two different astrometric fits.

First astrometric fit— The only observations for which obtaining the coordinates of the barycenter of the system can unambiguously be done are those when the source was double. For the corresponding 13 observations (epochs 1, 2, 3, 4, 6, 7, 8, 10, 11, 13, 16, 18, 19; see Tab. 5.8 and also Figs. 5.6, 5.7, 5.8, and 5.9), the preferred strategy would be to combine the *measured* separation between the primary and the secondary (let us call it $\mathbf{r}$), and the masses deduced from the orbital fit. The separation $\mathbf{r}_1$ between the primary to the barycenter is then given by

$$\mathbf{r}_1 = \frac{m_s}{m_s + m_p}\mathbf{r}. \tag{5.3}$$

Here, m_p and m_s are the masses of the primary and secondary, respectively. This strategy works well as long as the separation between the radio sources properly traces the separation between the stars. This is a valid assumption except near periastron (we will come back to this point in Sect. 5.2 when we discuss the variability of V773 Tau A). As a consequence, we initially considered only the seven observations when the source was double and not near periastron (epochs 2, 3, 10, 11, 13, 18, 19; see Tab. 5.8). These observations are sufficiently well spread in time to provide a reasonable characterization of the

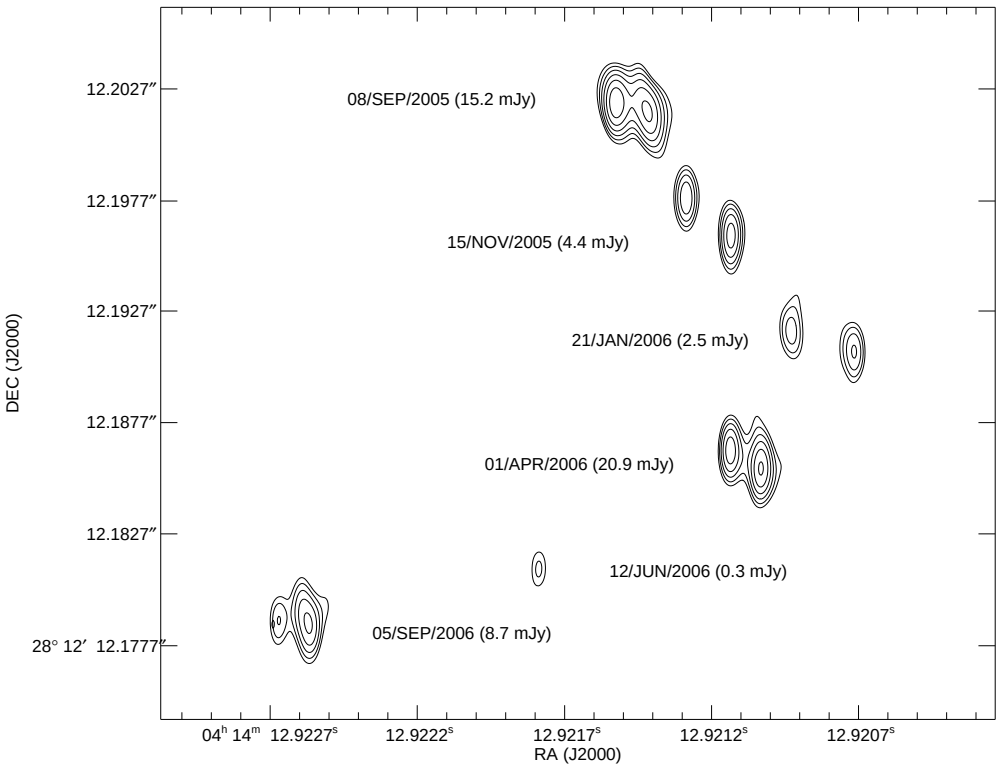

Figure 5.14 3.6 cm VLBA images of V773 Tau A system at six different epochs. The separation between V773 Tau Aa and V773 Tau Ab changes from epoch to epoch, and the flux density changes significantly with separation. The motion seen in the image is real, it is a combination of parallactic, orbital, and proper motion of the center of mass.

trigonometric parallax and proper motion of the barycenter of V773 Tau A. The best fit to these "best seven observations" yields the parameters shown in the Tabs. 5.2 and 5.3 labeled as V773 Tau $A^{(a)}$. The post-fit r.m.s. is 0.26 mas and 0.24 mas in right ascension and declination, respectively. The parallax estimated above corresponds to a distance $d = 132.8^{+4.8}_{-4.5}$.

Second astrometry fit— The astrometric fit obtained above only includes about a third of the VLBA observations available. Although the position of the barycenter of the system is deduced in a somewhat less direct fashion for the other two thirds of the data, it would still be desirable to incorporate them in a global astrometric fit. Moreover, the astrometric behavior of the source is important to help constrain the origin of the radio emission and the

structure of the system at some epochs.

The six observations where the source was found to be double, and which were not included in the last fit, were taken when the system was near periastron (epochs 1, 4, 6, 7, 8, 16; see Tab. 5.8). In such cases, the separation between the radio sources tended to be systematically smaller than the separation between the stars. This likely occurs because of enhanced flaring activity on either of the two stars, or on both of them. If both stars experience this enhanced activity, then the radio sources associated with them are likely to be similarly displaced from their respective star. The best strategy to obtain the position of the barycenter would still be to use Eq. 5.3 using the *measured* separation between the stars for the separation $\mathbf{r}$, because both $\mathbf{r}$ and $\mathbf{r_1}$ are expected to be shrunk by a similar factor. If the enhanced activity only occurs on one of the stars, however, then only for that object will the radio source be offset from the star. A better strategy to derive the position of the barycenter of the system in this case would be to identify the star not affected by enhanced activity, and calculate the separation between that star and the barycenter using the *prediction* of the orbit model presented in Sect. 5.4 (which provides the true separation between the stars) rather than the measured separation between the radio sources. To test for these different possibilities, we ran three tests (all of which include the "best seven observations", in addition to the six resolved observations near periastron: epochs 2, 3, 10, 11, 13, 18, 19, 1, 4, 6, 7, 8, 16). In the first one, we assumed that both stars experienced enhanced activity and that the position of the barycenter should be obtained using the *measured* separation between the radio sources. In the second, we assumed that only the secondary suffered from enhanced activity, and used the measured position of the primary and the separation between the primary and the barycenter predicted by the orbit model to estimate the position of the barycenter. Finally, in the third test, we assumed that only the primary was affected by enhanced activity, and used the position of the secondary and a predicted secondary-barycenter separation. The astrometric parameters obtained from these three tests are very similar to one another, and well within one sigma of the results of the fit presented above (*First astrometric fit* with the "best seven observations"). In terms of post-fit r.m.s., the best result is obtained when the position of the barycenter is deduced from the *measured* separation between the sources. This indicates that both stars experience enhanced activity near periastron, a result that was to be expected since *both* components of the system become

brighter near periastron.

When the radio source associated with V773 Tau A is single, one must again distinguish between two different situations. For two of these observations, the source is weak (~ 1 mJy), and the system was near apoastron (epochs 5, 12; see Tab. 5.8). Both sources are known to become dimmer near apoastron, and one of them has clearly faded below our detection limit in these two cases. It is *a priori* unclear whether the detected source corresponds to the primary or the secondary. To find out, we estimated the position of the barycenter of the system using our orbit model (Sect. 5.4) assuming first that the detected source was the primary and then that it was the secondary. The positions derived assuming that the detected source is the primary fall almost exactly on the astrometry fits, whereas the positions deduced assuming that the detected source is the secondary fall several mas away from the fit. We conclude that in these two cases, the detected source is the primary. For the remaining 4 observations, the source is single, but bright (at least several mJy; epochs 9, 14, 15, 17). All four of these observations were obtained at an orbit phase of about 0.2 before or after periastron (see Tab. 5.8). In this situation, the two stars are located in projection almost exactly north-south of each other, with a projected separation of about 1 mas. Since our resolution in the north-south direction is about 2 mas, we do not expect to resolve the two stars in this situation, but instead to detect a single source slightly elongated in the north-south direction. This is in fact what happens. Indeed, the mean deconvolved FWHM size of the emission for these four epochs is 1.33 mas, 50% larger than the corresponding figure (0.89 mas) when the source is double or single but near apoastron. In this situation, the measured position of the source is likely to provide a good approximation (to within a few tenths of a mas) of the position of the barycenter of the system.

To refine the determination of the parallax and proper motion of V773 Tau A, we performed a final astrometric fit which includes:

- The "best seven observations" used to obtain the *First astrometric fit*.
- The six observations corresponding to double sources near periastron. The position of the barycenter in this case was calculated using Eq. 5.3 and the true separation for $\mathbf{r}$.
- The two observations where the source was single and near apoastron. In this case, we obtained the position of the barycenter using a sepa-

ration between the primary and the barycenter deduced from our orbit model.

- The four epochs at $\Delta\phi \sim 0.2$, for which the position of the barycenter was assumed to be that of the (single) source itself.

The results of this fit are shown in Tabs. 5.2 and 5.3 labeled as V773 Tau $A^{(b)}$, and are very similar to those of our initial fit. All the parameters are well within one sigma of one another. The distance corresponding to this global fit is $132.0^{+3.5}_{-3.4}$, in excellent agreement with the fit to the best seven VLBA observations. We note, finally, that the distance obtained here is only marginally consistent with the the result obtained by Lestrade et al. (1999;

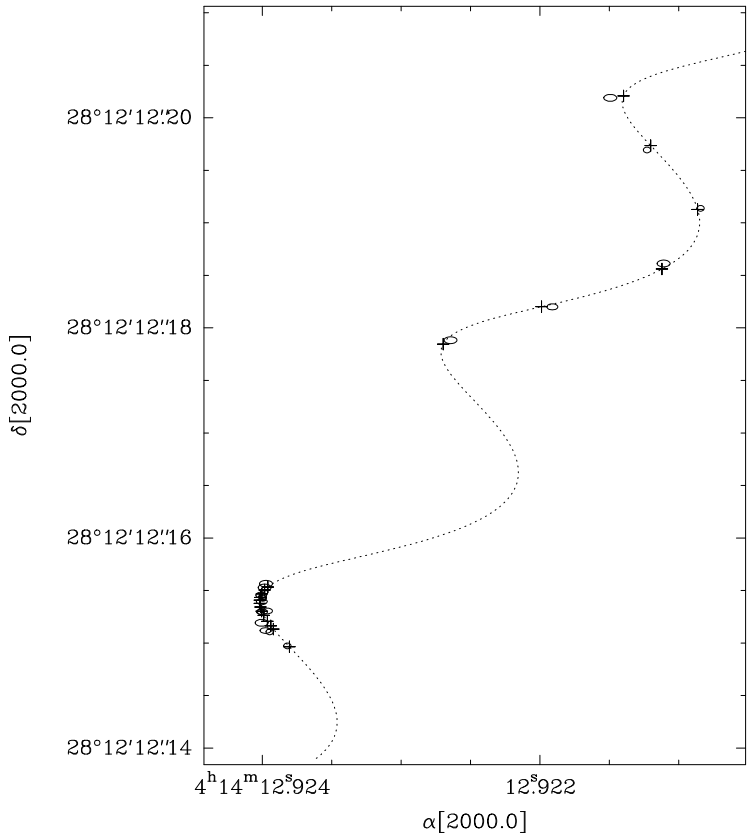

Figure 5.15 Measured positions and best fit for V773 Tau A. The observed positions are shown as ellipses, the size of which represents the error bars.

$d = 148.4 \pm 5.3$ pc). We attribute the discrepancy to the fact that Lestrade did not take into account the binarity of the source in their astrometric fits.

S1 and DoAr 21— We detected the sources in all observations of S1 and DoAr 21 (listed in Tab. 4.2; see contour maps in Fig. 5.9). DoAr 21 was found to be double at several epochs, whereas S1 was always single. The source positions are listed in Tab. 5.1 (when DoAr 21 was a double source, we used the average position of both primary and secondary). We have seen that the extended magnetosphere of S1, and the reflex motions of both S1 and DoAr 21 are likely to produce significant shifts in the positions of the source photocenters. While the effect of an extended magnetosphere might be to produce a random jitter, the reflex orbital motions ought to generate oscillations with a periodicity equal to that of the orbital motions. Six or seven observations, however, are currently insufficient to properly fit full Keplerian orbits. Instead, we represent the possible systematic calibration errors as well as the jitter due to extended magnetospheres and the oscillations due to reflex motions, by a constant error term (the value of which will be determined below) that we add quadratically to the errors given in Cols. [3] and [4] of Tab. 5.1.

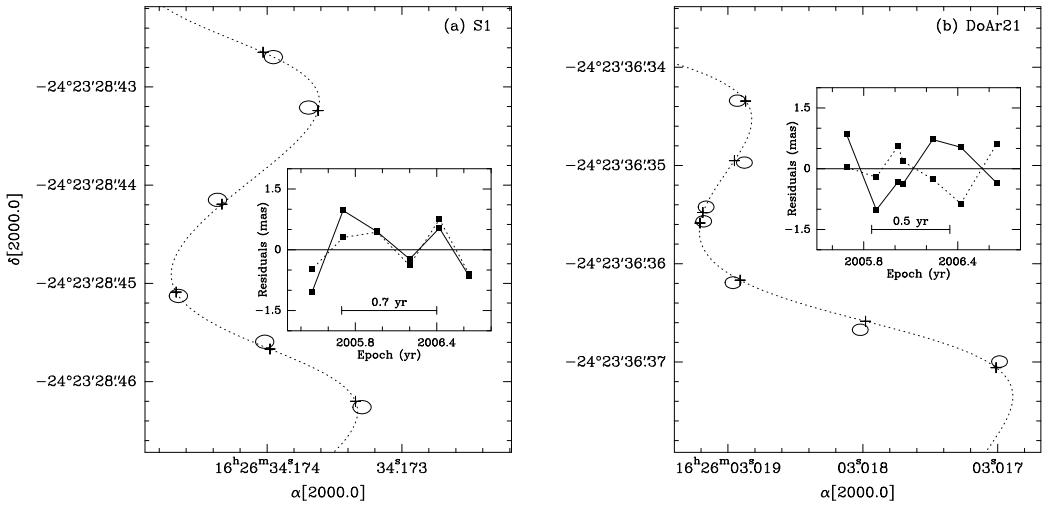

Figure 5.16 Measured positions and best fit for (a) S1, and (b) DoAr 21. The observed positions are shown as ellipses, the size of which represents the magnitude of the errors. The positions at each epoch expected from the best fits are shown as + signs. The insets show the residuals (fit-observation) in right ascension (full line) and declination (dotted line).

The displacements of both S1 and DoAr 21 were assumed to be uniform and linear (Eqs. 5.1), and the best fit for S1 (Fig. 5.16a) and DoAr 21 (Fig. 5.16b) yields the astrometric parameters listed in Tabs. 5.2 and 5.3. To obtain a reduced χ^2 of 1 in both right ascension and declination, one must add quadratically 0.062 ms, 0.67 mas for S1, and 0.053 ms, 0.57 mas for DoAr 21 to the statistical errors listed in Cols. [3] and [4] of Tab. 5.1. These figures include all the unmodeled sources of positional shifts mentioned earlier. Interestingly, the residuals of the fit to the S1 data (inset in Fig. 5.16a) are not random, but seem to show a ~ 0.7 yr periodicity, as expected from the reflex motions. Similarly, the residuals from the fit to DoAr 21 seem to show a periodicity of ~ 1.2 yr (Fig. 5.16b, inset), within the range of expected orbital periods of that system. This suggests that the errors are largely dominated by the unmodeled binarity of both sources, and that additional observations designed to provide a better characterization of the orbits ought to improve significantly the precision on the trigonometric parallax determinations. The distance to S1 deduced from the parallax calculated is $116.9^{+7.2}_{-6.4}$ pc, while the distance deduced for DoAr 21 is $121.9^{+5.8}_{-5.3}$ pc.

5.1.2 Kinematics of the sources in Taurus

For Galactic sources, it is interesting to express the proper motions in Galactic coordinates rather than in the equatorial system naturally delivered by the VLBA. The results for four sources observed in Taurus with the VLBA are given in columns 3 and 4 of Tab. 5.4. Interestingly, the proper motion of HP Tau/G2 is very similar to that of T Tau, but significantly different from those of Hubble 4 and HDE 283572, (which are themselves very similar to each other). HP Tau/G2 and T Tau also happen to both be located on the eastern side of the Taurus complex, whereas Hubble 4 and HDE 283572 are both around Lynds 1495 near the center of the complex (Fig. 5.17).

The fifth star in Taurus, V773 Tau A, is located about a degree south-west of Hubble 4, and the distance are similar to those of Hubble 4 and HDE 283572 (see Tab. 5.3). Thus, we expected the proper motions of V773 Tau A to be like those for Hubble 4 and HDE 283572. However the observed proper motion of V773 Tau A is from the northwest to southeast direction (see Fig. 5.15). We suspect that the peculiar proper motion of V773 Tau A is due to its companions, particularly V773 Tau B. We are currently analyzing this possibility, and here we will take only the other four sources to describe the

Table 5.4. Radial velocities, proper motions, heliocentric, and peculiar velocities in Galactic coordinates for 4 sources in Taurus.

Source	V_r [km s^{-1}]	$\mu_\ell \cos(b)$ [mas yr^{-1}]	μ_b	U	V [km s^{-1}]	W	u	v [km s^{-1}]	w	References[a]
T Tau[b]	19.1±1.2	+17.76±0.03	+0.99±0.04	−19.09	−11.27	−6.30	−9.09	−6.02	+0.87	1,3
Hubble 4	15.0±1.7	+23.94±0.12	−16.74±0.15	−14.96	−12.66	−14.30	−4.96	−7.41	−7.13	1,3
HDE 283572	15.0±1.5	+25.53±0.05	−11.61±0.06	−15.89	−13.07	−10.84	−5.89	−7.82	−3.67	1,2
HP Tau/G2	17.7±1.8	+20.90±0.07	+0.82±0.10	−18.59	−14.65	−4.50	−8.59	−9.40	+2.67	1,2

[a]1=This work; 2=Walter et al. 1988; 3=Hartmann et al. 1986

[b]The radial velocity and proper motions used here are those of T Tau N. The radial velocities for T Tau Sa and T Tau Sb are available in Duchêne et al. (2002) and are very similar.

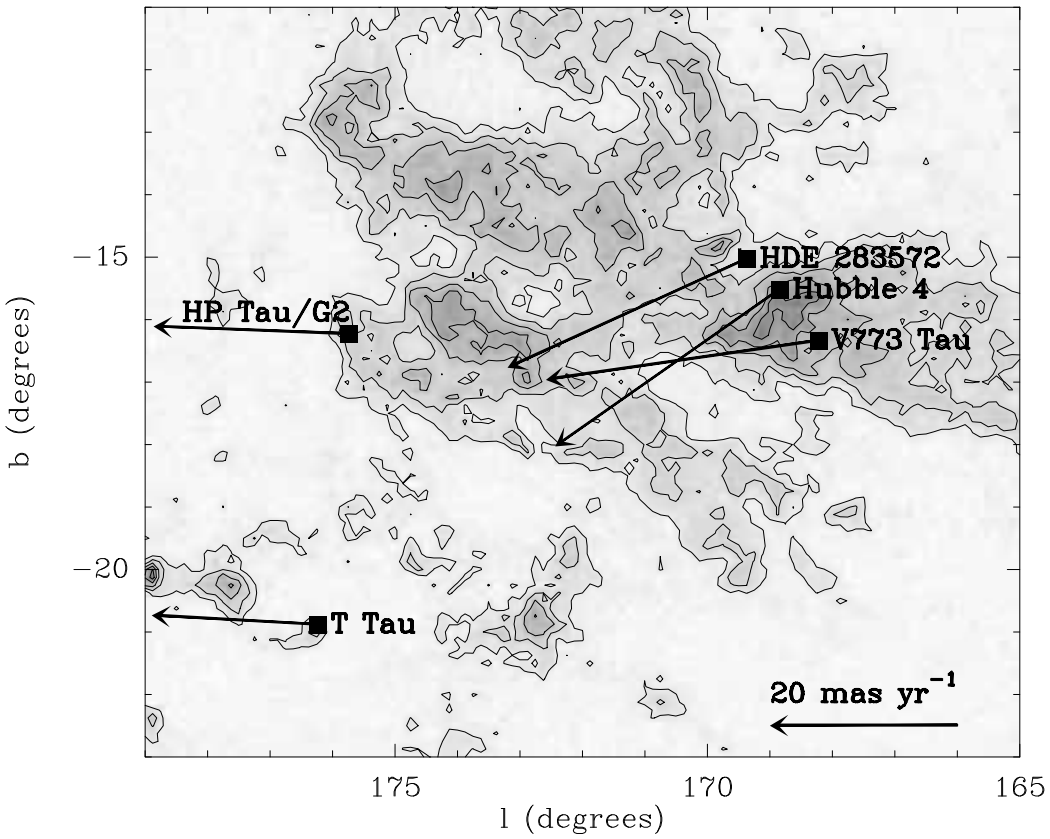

Figure 5.17 Positions and proper motions of T Tau, Hubble 4, HDE 283572, and HP Tau/G2 superposed on the CO(1-0) map of Taurus from Dame et al. (2001).

kinematics of Taurus.

Knowing the distance to the sources with high accuracy, it is possible to transform the observed proper motions into transverse velocities. Combining this information with radial (Heliocentric) velocities taken from the literature (second column of Tab. 5.4), it becomes possible to construct the three-dimensional velocity vectors. It is common to express these vectors on a rectangular (X, Y, Z) coordinate system centered in the Sun, with X pointing towards the Galactic center, Y in the direction of Galactic rotation, and Z towards the Galactic North Pole. In this system, the coordinates of the Heliocentric velocities will be written (U, V, W). As a final step, it is also possible to calculate the peculiar velocity of the stars. This involves two stages: first, the peculiar motion of the Sun must be removed to transform the

Heliocentric velocities into velocities relative to the LSR. Following Dehnen & Binney (1998), we will use $u_0 = +10.00$ km s^{-1}, $v_0 = +5.25$ km s^{-1}, and $w_0 = +7.17$ km s^{-1} for the peculiar velocity of the Sun expressed in the coordinate system defined above. The second stage consists in estimating the difference in circular velocity between Taurus and the Sun, so the peculiar velocities are expressed relative to the LSR appropriate for Taurus, rather than relative to the LSR of the Sun. This was done assuming the rotation curve of Brand & Blitz (1993), and represents a small correction of only about 0.3 km s^{-1}. We will write (u, v, w) the coordinates of the peculiar velocity of the sources. Both (U, V, W) and (u, v, w) are given in Tab. 5.4 for the four sources considered here. Their projections onto the (X, Y), (X, Z), and (Y, Z) planes are shown in Fig. 5.18.

The mean heliocentric velocity and the velocity dispersion of the four sources are:

$$U = -17.1 \pm 1.7 \text{ km s}^{-1}$$
$$V = -12.9 \pm 1.2 \text{ km s}^{-1}$$
$$W = -9.0 \pm 3.8 \text{ km s}^{-1}.$$

These values are similar to those reported by Bertout & Genova (2006) for a larger sample of young stars in Taurus with optically measured proper motions. Note that the velocity dispersion in the W direction is somewhat artificially high because Hubble 4 and HDE 283572 on the one hand, and T Tau and HP Tau/G2 on the other, clearly have different vertical velocities. They likely belong to two different kinematic sub-groups.

The mean peculiar velocity of the four sources considered here is:

$$u = -7.1 \pm 1.7 \text{ km s}^{-1}$$
$$v = -7.7 \pm 1.2 \text{ km s}^{-1}$$
$$w = -1.8 \pm 3.8 \text{ km s}^{-1}.$$

We argue that this is a good estimate of the mean peculiar velocity of the Taurus complex. This velocity is almost entirely in the (X, Y) plane. Thus, although Taurus is located significantly out of the mid-plane of the Galaxy (about 40 pc to its south), it appears to be moving very little in the vertical direction. The motion in the (X, Y) plane, on the other hand, is fairly large, leading to a total peculiar velocity $(u^2 + v^2 + w^2)^{0.5} = 10.6$ km s^{-1}.

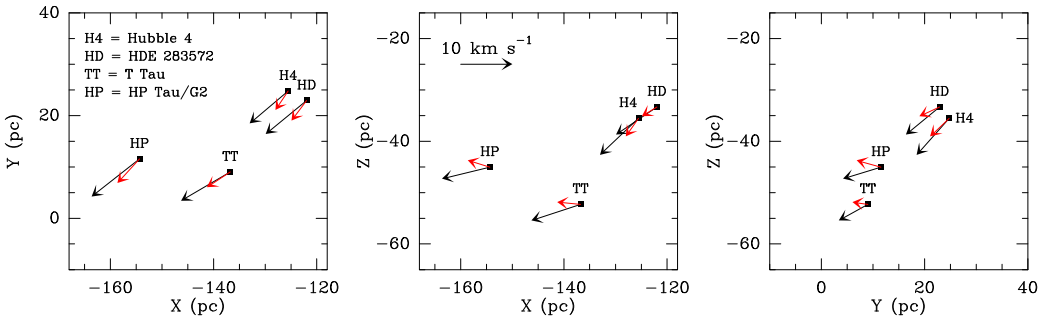

Figure 5.18 Heliocentric velocities (black arrows) and peculiar velocities (red arrows) for the four stars in Taurus with VLBA-based distance determinations.

According to Stark & Brand (1989), the one-dimensional velocity dispersion of giant molecular clouds within 3 kpc of the Sun is about 8 km s^{-1}. As a consequence, each component of the peculiar velocity of a given molecular cloud is expected to be of that order, and our determination of the mean peculiar velocity of Taurus is in reasonable agreement with that prediction. Another useful comparison is with the velocity dispersion of young main sequence stars. For the bluest stars in their sample (corresponding to early A stars), Dehnen & Binney (1998) found velocity dispersions of about 6 km s^{-1} in the vertical direction, and of 10-14 km s^{-1} in the X and Y directions. The young stars in Taurus are significantly younger than typical main sequence early A stars, so one would expect young stars in Taurus to have peculiar velocities somewhat smaller than 6 km s^{-1} in the vertical direction, and than 10–14 km s^{-1} in the X and Y directions. This is indeed what is observed. Note, however, that Taurus is not among the star-forming regions with the smallest peculiar velocities. In Orion, Gómez et al. (2005) found a difference between expected and observed proper motions smaller than 0.5 km s^{-1}.

5.1.3 Three-dimensional structure of Taurus

Two of the five objects observed in Taurus have measured Hipparcos parallaxes (Bertout et al. 1999): T Tau Sb with 5.66 ± 1.58 mas, and HDE 283572 with 7.81 ± 1.30 mas. Our results are consistent with these values, but one to two orders of magnitude more accurate. Also, the parallax of both Hubble 4 and HDE 283572 were estimated by Bertout & Genova (2006) using a modified convergent point method. Their results (8.12 ± 1.50 mas for Hubble 4 and 7.64 ± 1.05 mas for HDE 283572) are also consistent with our results,

but again more than one order of magnitude less accurate. The distance to V773 Tau A had been obtained using radio VLBI observations before ($d = 148.4 \pm 5.3$ pc; Lestrade et al. 1999). Our result is only marginally consistent with this earlier figure, and we argue that the discrepancy is due to the fact that Lestrade et al. (1999) did not model the binarity of the source in their analysis. We obtained a mostly independent estimate of the distance to V773 Tau A by modeling the physical orbit of the binary using a combination of optical radial velocity measurements, Keck Interferometer observations, and our own VLBA data (see Sect. 5.4). The distance obtained by this alternative method was found 134.5 ± 3.2 pc, in excellent agreement with the value obtained from our parallax measurement, but again only marginally consistent with the older VLBI value.

Taking the mean of the five VLBA-based parallax measurements available, we can estimate the mean parallax to the Taurus complex to be $\bar{\pi} = 7.18$ mas. This corresponds to a mean distance of $\bar{d} = 139$ pc, in good agreement with previous estimates (Kenyon et al. 1994). The angular size of Taurus is about 10°, corresponding to a physical size of roughly 25 pc. It would be natural to expect that the depth of Taurus might be similar, since HP Tau/G2 is about 30 pc farther than Hubble 4, HDE 283572 or V773 Tau A. This has a trivial but important consequence: even if the mean distance of the Taurus association were known to infinite accuracy, one would still make errors as large as 10–20% by using the mean distance indiscriminately for all sources in Taurus. To reduce this systematic source of error, one needs to establish the three-dimensional structure of the Taurus association, and observations similar to those presented here currently represent the most promising avenue toward that goal. Indeed, the observations of the five stars presented here already provide some hints of what the three-dimensional structure of Taurus might be. Hubble 4, HDE 283572, and V773 Tau A which were found to be at about 130 pc, are also located in the same portion of Taurus, near Lynds 1495. T Tau Sb is located in the southern part of Taurus near Lynds 1551, its tangential velocity is clearly different from that of Hubble 4, HDE 283572, and V773 Tau A, and it appears to be somewhat farther from us. Finally, HP Tau/G2 is located near the (Galactic) eastern edge of Taurus, and it is the farthest of the four sources considered here. Although additional observations are needed to draw definite conclusions, our data, therefore, suggest that the region around Lynds 1495 corresponds to the near side of the Taurus complex at about 130 pc, while the eastern side of Taurus corresponds to the far side

at 160 pc. The region around Lynds 1551 and T Tau Sb appears to be at an intermediate distance of about 147 pc.

Taurus has long been known to present a filamentary structure. The two main filaments are roughly parallel to one another, and have an axis ratio of about 7:1. Our observations suggest that these filaments are oriented nearly along the line of sight, i.e. roughly along the Galactic center–anticenter axis. This peculiar orientation might indeed explain the low star-forming efficiency of Taurus compared with other nearby star-forming regions (Ballesteros-Paredes et al., 2009).

5.1.4 Three-dimensional structure of Ophiuchus

Ophiuchus is composed of a compact core, only about 2 pc across, and filamentary structures (called "streamers") extending (in projection) to about 10 pc. The Ophiuchus core is sufficiently compact that we do not expect to resolve any structure along the line of sight. Thus, the weighted mean of the two parallaxes for S1 and DoAr 21 is 8.33 ± 0.30, corresponding to a distance of $120.0^{+4.5}_{-4.3}$ pc. Since both S1 and DoAr 21 are *bone fide* members of the Ophiuchus core, this figure must represent a good estimate of the distance to Ophiuchus. It is in good agreement with several recent determinations (e.g. de Geus et al. 1989, Knude & Hog 1998, Lombardi et al. ibid), but with a significantly improved relative error of 4%.

There could potentially be distance gradients of several parsecs across the streamers. We note, however, that Schaefer et al. (2008) determined the physical orbit of the binary system Haro 1-14C, and deduced a distance of 111 ± 19 pc, in good agreement with our determination. Haro 1-14C is located in the northern streamer associated with the darks clouds L1709/L1704 (see Fig. 5.19), so the result of Schaefer et al. (2008) suggests that that streamer is, if anything, somewhat closer that the core. This is, indeed, in agreement with recent results of Lombardi et al. (2008). On the other hand, Imai et al. (2007) used the Japanese VLBI system (VERA) to determine the parallax to the very young protostar IRAS 16293–2422 deeply embedded in the southern Ophiuchus streamer (in L1689N, see Fig. 5.19). They obtain a distance of 178^{+18}_{-37} pc, which would be more consistent with the older value of 165 pc. Even including the streamers, Ophiuchus is only 10 pc across in projection, so it is unlikely to be 60 pc deep. Thus, if the results of Imai et al. (2007) are confirmed, they would indicate the existence of several unrelated star-

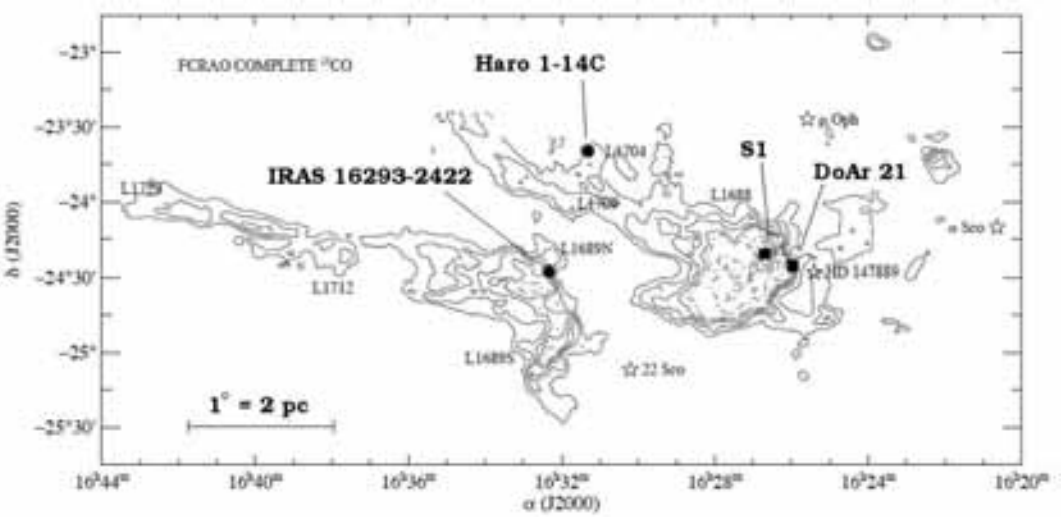

Figure 5.19 Positions of four stars superposed on the ^{13}CO map of Ophiuchus from Ridge et al. (2006). The two stars studied here (S1 and DoAr 21) are shown as a squares; Haro 1-14C and IRAS 16293–2422 are shown as a circles.

forming regions along the line of sight. More observations –some of which have already been collected and partially analyzed– will be necessary to settle this issue.

5.2 Variability

In 1953 Haro & Morgan discovered that flares are common in T Tauri stars and stellar associations, implying that the flare process is stronger in the younger stars. Since T Tauri stars present high levels of magnetic activity (Feigelson & Montmerle, 1999), and that radio emission generally depends on the characteristics of the magnetic field (see Chapter 2), the variability due to flares is expected for non-thermal sources.

In Fig. 5.20 we present the flux evolution for T Tau Sb, Hubble 4, HP Tau/G2, S1, and DoAr 21. A similar figure for V773 Tau A system is shown in Fig. 5.21. The dotted horizontal lines in each plot correspond to the mean flux density of all observations. All seven sources have variability on timescales from months to years. In some cases the sources underwent flaring events that move the average flux up. To give a classification scheme for the young stars in the thesis, we constructed Table 5.5 that contains the mean bright-

Table 5.5. Mean brightness temperature and mean fluxes for all sources in the thesis.

Source	$\bar{T_b}$	$\bar{f_\nu}$	rms	$f_\nu{}^{\max}$	$f_\nu{}^{\min}$	F_1 *	F_2 **	F_3 ***
	[10^7 K]	[mJy]				[%]		
T Tau Sb	17.68	1.68	0.59	2.30	0.92	82	37	45
Hubble 4	19.89	1.59	1.41	4.66	0.65	252	193	59
HDE 283572	29.78	2.50	2.43	7.13	0.51	265	185	80
HP Tau/G2	11.75	1.07	0.72	3.06	0.63	227	186	41
V773 Tau A	127.75	14.34	11.15	41.16	0.87	281	187	94
V773 Tau Aa.....	52.42	6.15	3.92	36.44	0.87	578	493	86
V773 Tau Ab.....	97.36	8.25	7.50	28.89	0.76	341	250	91
S1.....	46.73	4.81	1.15	7.03	3.29	72	46	32
DoAr 21	54.37	5.48	7.09	20.34	0.39	364	271	93

* $F_1 = \bar{f_\nu}^{-1}[f_\nu^{\max} - f_\nu^{\min}] \times 100$

** $F_2 = \bar{f_\nu}^{-1}[f_\nu^{\max} - \bar{f_\nu}] \times 100$

*** $F_3 = \bar{f_\nu}^{-1}[\bar{f_\nu} - f_\nu^{\min}] \times 100$

ness temperature and the mean flux density in Cols. [2] and [3]. Additional columns were added in order to understand the degree of variability for each source: maximum and minimum flux densities in Cols. [5] and [6]; the difference between maximum and minimum flux density in Col. [7]; the difference between maximum and mean flux density in Col. [8]; finally, the difference between minimum and mean flux density in Col. [9]. Note that the last three columns are weighted by the mean flux density. With these values in mind, we can give the next classification scheme in accordance with the flux evolution shown in light curves as well.

Small variability— The mean fluxes of T Tau Sb and S1 in our data are 1.68 and 4.81 mJy with a dispersion of 0.59 and 1.15 mJy, respectively. The values for $r.m.s.$, F_1, F_2 and F_3 in Tab. 5.5 are smaller for both T Tau Sb and S1 respect to the other sources, this shows that T Tau Sb and S1 are variable at low levels.

Single flares— HP Tau/G2, Hubble 4 and HDE 283572 have small $r.m.s.$ but high F_1, these values mean that the flux of the sources were fairly constant around a few mJy at all of our observations, except for one epoch (or two in the case of HDE 283572) where the sources underwent flaring events.

Multiple flares— V773 Tau A and DoAr 21 were detected with highly

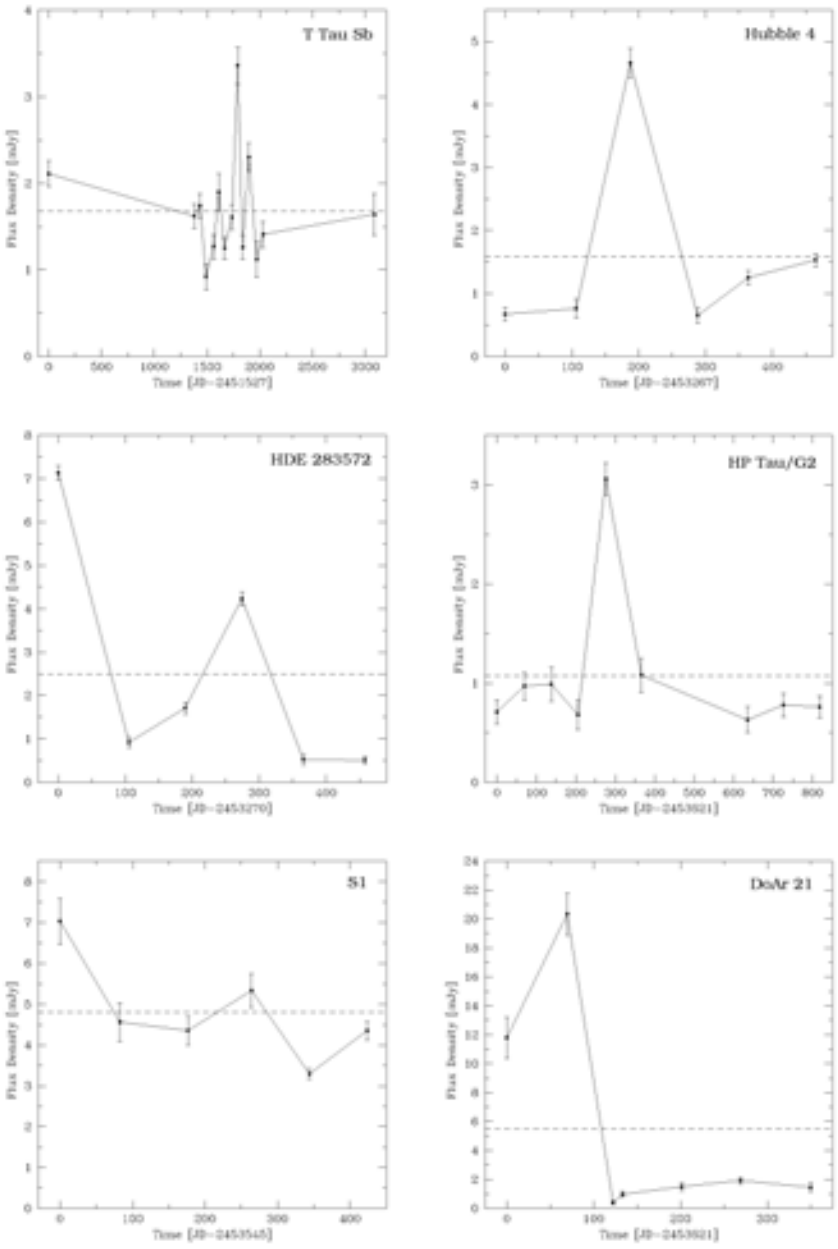

Figure 5.20 Flux evolution of T Tau Sb, Hubble 4, HDE 283572, HP Tau/G2, S1, and DoAr 21. The horizontal dotted lines in correspond to the mean flux density of the observations. Note that all six sources have variability on timescales from months to years.

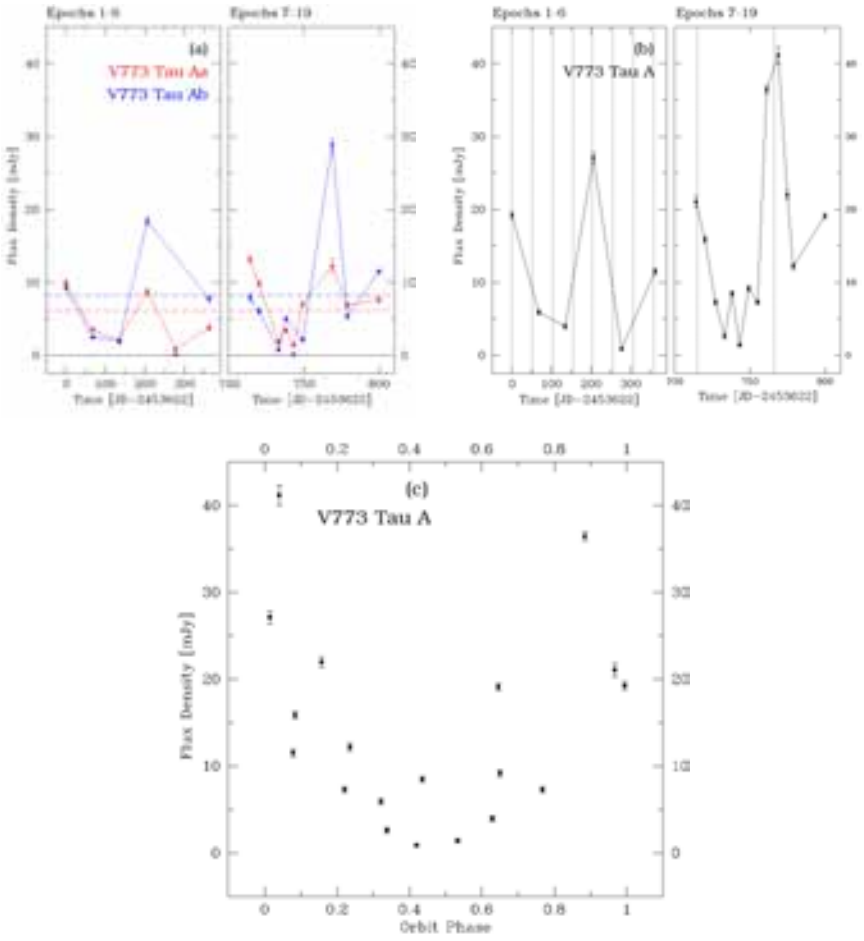

Figure 5.21 In left side of (a) and (b): the first 6 epochs of V773 Tau A that were obtained every 3 months. In the right side of (a) and (b): the last 13 epochs that were obtained over one orbital period of the system (observations every $\sim$ 4 days). (a) Flux evolution for each member of the system. It was not taken in to account the flux for the epochs where we did not resolve the sources (epochs 9, 14, 15, 17). For the primary (in *red*) we used the flux for the remaining 15 epochs, and for the secondary (in *blue*) we used the flux for the 13 epochs where we detected the source (see Sect. 5.1). The *horizontal dotted lines* correspond to the mean flux density of the observations. Note that the flux for the primary is lower than that for the secondary in almost all epochs. (b) Total flux evolution in the system at all 19 epochs. The periastron passages are shown in *vertical dotted lines*. Note that the total flux at periastron is highest than that at apoastron. (c) Total flux density of the system vs. orbit phase.

variable flux densities. The values for *r.m.s.*, F_1, F_2, and F_3 are high for both V773 Tau A and DoAr 21 sources. In the case of V773 Tau A the flux was found to be highest near periastron, and lowest around apoastron (see Fig. 5.21d), in agreement with the results by Massi et al. (2002, 2006), who showed that the variability had the same periodicity as the orbital motion, with the radio flux being highest at periastron. Interestingly, DoAr 21 was found to be double during our second observation. This suggests that the same mechanism that enhances the radio emission when the two binary components are nearest, might be at work in both objects. The separation between the two components of DoAr 21 in our second observation is about 5 mas. This value, of course, corresponds to the projected separation; the actual distance between them must be somewhat larger. Moreover, if the mechanisms at work in DoAr 21 and V773 Tau A are similar, then DoAr 21 must have been near periastron during our second epoch, and the orbit must be somewhat eccentric. As a consequence of these two effects, the semi-major axis of the orbit is likely to be a few times larger than the measured separation between the components at our second epoch, perhaps 10 to 15 mas. At the distance of DoAr 21, this corresponds to 1.2 to 1.8 AU. For a mass of 2.2 $M_\odot$, the corresponding orbital period is 0.4 to 1.3 yr, and one would expect the source to oscillate with this kind of periodicity.

Short timescale variability— As we mentioned before, the flux density for V773 Tau A system tends to increase when the sources are near periastron. This is clear in Fig. 5.21. In order to investigate how is the flux evolution at short timescales, we used epochs from 7 to 19 for imaging the system each hour. Unfortunately it was not possible for the first six observations because our observation time was only 2 hours (see Tab. 4.2). In Fig. 5.22 is shown the flux density (left side) and circular polarization (right side) of V773 Tau A system. Each plot have 13 panels, where each one corresponds to 1 epoch. Blue points shown the flux evolution in timescales of 5 hours. Red points corresponds to the average total flux (exactly the same flux showed in Fig. 5.21b). It is clear that more flux variations (stokes I, and stokes V) were detected when V773 Tau Aa and V773 Tau Ab are closer (epochs 7, 8, 15, 16, 17), suggesting a magnetospheric interaction between those stars.

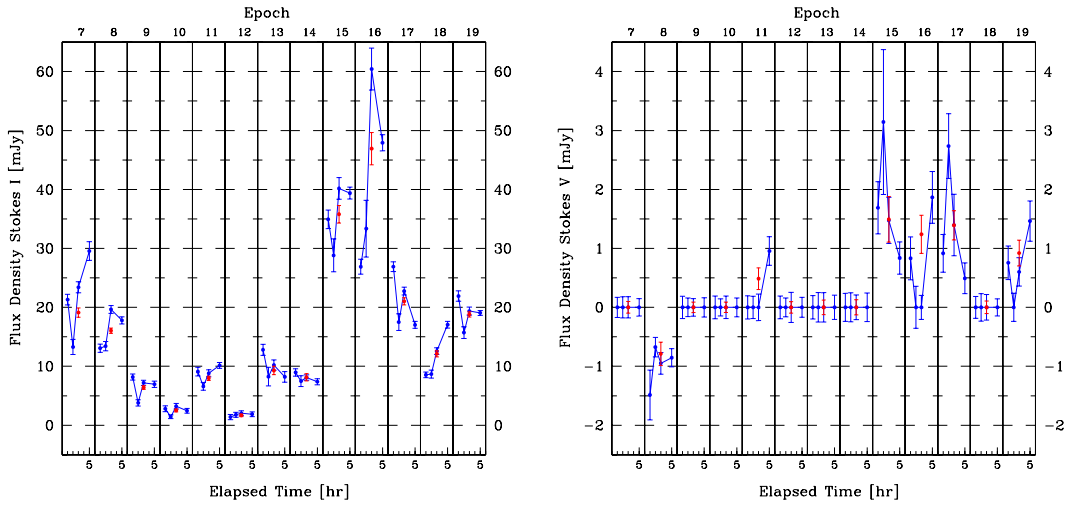

Figure 5.22 The last 13 epochs of V773 Tau A system were observed for 5 hours each one. Each panel in figures correspond to one epoch. *Blue points* show the flux evolution in timescales of 5 hours, while *red points* correspond to the average total flux for the whole epoch. Total flux density (stokes I) on left side, and circular polarization (stokes V) on right side.

5.3 Implications for the properties of the stars

5.3.1 T Tau system

Having obtained an improved distance estimate to the T Tauri system, we are now in a position to refine the determination of the intrinsic properties of each of the components of that system. Since the orbital motion between T Tau N and T Tau S is not yet known to very good precision, we will use synthetic spectra fitting to obtain the properties of T Tau N. For the very obscured T Tau S companion, on the other hand, we will refine the mass determinations based on the orbital fit obtained by Duchêne et al. (2006).

T Tau N— The stellar parameters ($T_{\rm eff}$ and $L_{\rm bol}$) of T Tau N were obtained by fitting synthetic spectra (Lejeune et al. 1997) to the optical part of the spectral energy distribution. In the absence of recently published optical spectra with absolute flux calibration, we decided to use narrow-band photometry taken at six different epochs from 1965 to 1970 (Kuhi 1974). In order to eliminate the contamination by the UV/blue (magnetospheric accretion) and red/IR (circumstellar disk) excesses, we restricted the fit to the range

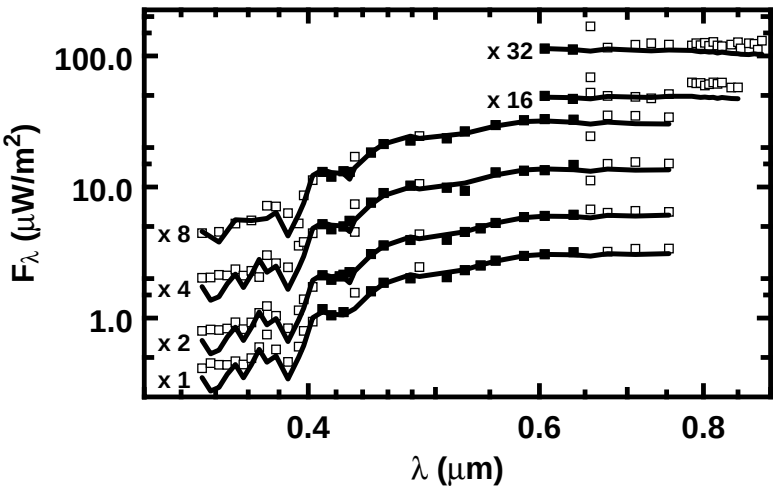

Figure 5.23 Fit to the photometry at six different epochs. Black squares are point that have been fitted; white squares represent other wavelengths excluded from the fit.

0.41–0.65 μm. Two points at 0.4340, 0.4861 μm display large variations between epochs, they were also discarded as they are likely to be contaminated by emission lines. As a consequence, 56 photometric measurements at 13 wavelengths and 6 epochs had to be fitted. (See Fig. 5.23). We assumed that the star kept constant intrinsic parameters over the 5 years of observation, but allowed the circumstellar extinction to vary. Such an hypothesis is supported by long-term photometric observations (1986-2003) that show color-magnitude diagrams of T Tau elongated along the extinction direction (Mel'Nikov & Grankin 2005); Kuhi (1974) also measured significant extinction variation in the period 1965-1970 using color excesses.

The non-linear fitting procedure used the Levenberg-Marquardt method and the determination of errors was done using a Monte Carlo simulation. The synthetic spectra were transformed into narrow-band photometry by integration over the bandwidth of the measurements (typically 0.05 μm). As the fitting procedure could not constrain the metallicity, we assumed a solar one. Several fits using randomly chosen initial guesses for $T_{\rm eff}$, $L_{\rm bol}$, and extinctions were performed in order to ensure that a global minimum χ^2 was indeed reached. The errors reported by Kuhi (1974; 1.2%) had to be renormalized to 5.9% in order to achieve a reduced χ^2 of 1. This could result from an underestimation by the author or from positive and negative contamination

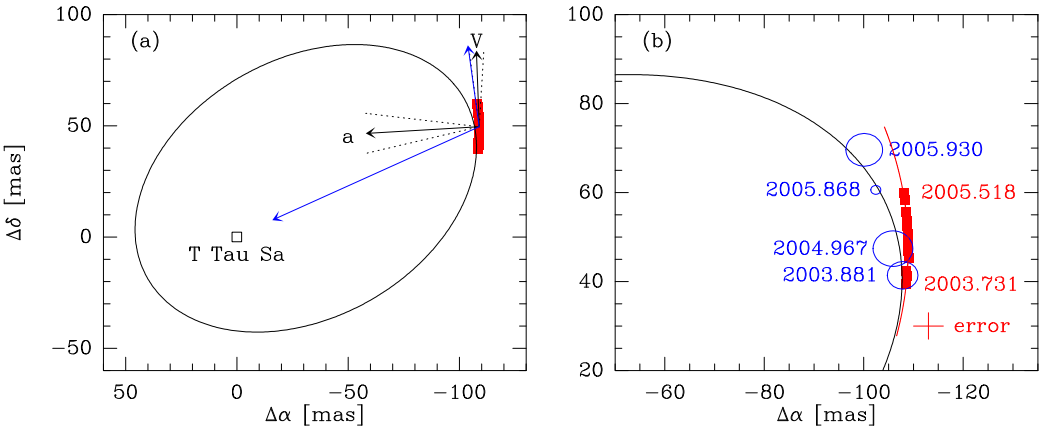

Figure 5.24 (a) VLBA positions (*red squares*) registered to T Tau Sa overimposed on the elliptical fit proposed by Duchêne et al. (2006). Also shown are the velocity and acceleration vectors for our mean epoch deduced from our observations, as well as their counterparts from the fit by Duchêne et al. (2006; *blue arrows*). The dotted black lines around the measured acceleration and velocity show the error cone on the direction of each of these vectors. (b) Zoom on the region corresponding to our observations. In addition to the orbit and the VLBA positions, we show (in *red curve*) our best parabolic fit to our first 12 positions, as well as several recent infrared positions (*blue ellipses*). The 2003.881 position is from Duchêne et al. (2005), the 2004.967 and 2005.868 positions are from Duchêne et al. (2006), and the 2005.930 position is from Schaefer et al. (2006).

by spectral lines –indeed, Gahm (1970) reports contamination as high as 20% for RW Aur. The best least-squares fit is represented in Fig. 5.24, and yields $T_{\rm eff} = 5112^{+99}_{-97}$ K and $L_{\rm bol} = 5.11^{+0.76}_{-0.66}\,L_{\odot}$. The extinction varies between 1.02 and 1.34, within 1-σ of the values determined by Kuhi (1974) from color excesses. The effective temperature is consistent with a K1 star as reported by Kuhi (1974).

In order to derive the age and mass of T Tau N, pre-main-sequence isochrones by D'Antona & Mazzitelli (1996) and Siess et al. (2000) were used. The fitting procedure was identical to the previous one: the age and mass were converted into effective temperature and luminosity, which in turn were converted into narrow-band photometry using the synthetic spectra. The derived parameters are shown in Tab. 5.6. The masses ($1.83^{+0.20}_{-0.16}$ and $2.14^{+0.11}_{-0.10}$ $M_{\odot}$) have overlapping error bars and are consistent with values found in the literature (e.g. Duchêne et al. 2006). The predicted ages, on the other hand, differ by a factor of 2. While the isochrones by D'Antona & Mazzitelli (1996) give an age in the commonly accepted range ($1.15^{+0.18}_{-0.16}$ Myr), a somewhat larger

Table 5.6. Parameters of T Tau N.

Parameter	Value
Age [Myr]	$2.39^{+0.31}_{-0.27}$ [a]
	$1.15^{+0.18}_{-0.16}$ [b]
Mass [$M_\odot$]	$2.14^{+0.11}_{-0.10}$ [a]
	$1.83^{+0.20}_{-0.16}$ [b]
$T_{\rm eff}$ [K]	5112^{+99}_{-97}
$L_{\rm bol}$ [$L_\odot$]	$5.11^{+0.76}_{-0.66}$
$R_\star$ [$R_\odot$]	$2.89^{+0.24}_{-0.21}$
$A_{V\,\rm MJD39095.2}$	1.34 ± 0.17
$A_{V\,\rm MJD39153.2}$	1.37 ± 0.17
$A_{V\,\rm MJD39476.3}$	1.20 ± 0.17
$A_{V\,\rm MJD40869.4}$	1.02 ± 0.17
$A_{V\,\rm MJD39485.1}$	1.36 ± 0.19
$A_{V\,\rm MJD39524.1}$	1.16 ± 0.19

[a]Siess et al. (2000)

[b]D'Antona & Mazzitelli (1997)

value ($2.39^{+0.31}_{-0.27}$) is derived from Siess et al. (2000). Note that the errors on the derived parameters are entirely dominated by the modeling errors; the uncertainty on the distance now represents a very small fraction of the error budget.

T Tau S— The two members of the T Tau S system have been studied in detail by Duchêne and coworkers in a series of recent articles (Duchêne et al. 2002, 2005, 2006). The most massive member of the system (T Tau Sa) belongs to the mysterious class of "infrared companions", and is presumably the precursor of an intermediate-mass star. T Tau Sb, on the other hand is a very obscured, but otherwise normal, pre-main sequence M1 star. The mass of both T Tau Sa and T Tau Sb were estimated by Duchêne et al. (2006) using a fit to their orbital paths. Those authors used the distance to T Tauri that we deduced without acceleration terms. Using the new distance determination obtained in Sect. 5.1, we can re-normalize those masses. We obtain $M_{\rm Sa} = 3.10 \pm 0.34$ M$_\odot$, and $M_{\rm Sb} = 0.69 \pm 0.18$ M$_\odot$. These values may need to be adjusted somewhat, however, as the fit to the orbital path of the T Tau Sa/Sb system is improved (see Sect. 5.4). Note finally, that the main sources of errors on the masses are related to the orbital motion modeling

rather than to the uncertainties of the distance.

5.3.2 HP Tau system and HDE 283572

As mentioned in Chapter 1, HP Tau/G2 is a member of a compact group of four young stars, comprising HP Tau itself, HP Tau/G1, G2, and G3. Given the small angular separations between them, the members of this group are very likely to be physically associated –indeed, HP Tau/G2 and G3 are thought to form a bound system. They are, therefore, very likely to be at the same distance from the Sun. Using our accurate estimate of the distance to HP Tau/G2, we are now in a position to refine the determination of the luminosities of all four stars. Little is known about HP Tau/G1, but the effective temperature and the bolometric luminosity (obtained assuming $d = 142$ pc) of the other three members are given in Briceño et al. (2002). Those values (corrected to the new distance) allow us to place the stars accurately on an HR diagram (Fig. 5.25).

From their position on the HR diagram, one can (at least in principle) derive the mass and age of the stars using theoretical pre-main sequence evolutionary codes. Several such models are available, and we will use four of them here: those of Siess et al. (2000), Demarque et al. (2004; known as the Yonsei-Yale Y^2 models), D'Antona & Mazzitelli (1997), and Palla & Stahler (1999; the models by Baraffe et al. (1998) will not be used because they do not cover the mass range of our stars). The isochrones for those four models at 1, 3, 5, 7, and 10 Myr are shown as solid black lines in Fig. 5.25. Also shown are the evolutionary tracks (from the same models) for stars of 1.0, 1.5, and 2.0 $M_\odot$. The three HP Tau members are shown as blue symbols, and HDE 283572 is shown as a red symbol.

A number of interesting points can be seen from Fig. 5.25. First, there is reasonable agreement (within 40%, see below) between the masses predicted by different models. The best case is that of HP Tau/G2, for which the different models predict masses consistent with each other at the 10% level (between 1.7 and 1.9 $M_\odot$). The situation for HP Tau is somewhat less favorable, since the models of Siess et al. (2000) or Palla & Stahler (1999) predict a mass of ~ 1.5 $M_\odot$, whereas those of D'Antona & Mazzitelli (1997) predicts a significantly smaller mass of ~ 1.0 $M_\odot$. Thus, there is a 35% spread in the values predicted by different models for the mass of that source. The least favorable situation is for HP Tau/G3. The mass of that source is about

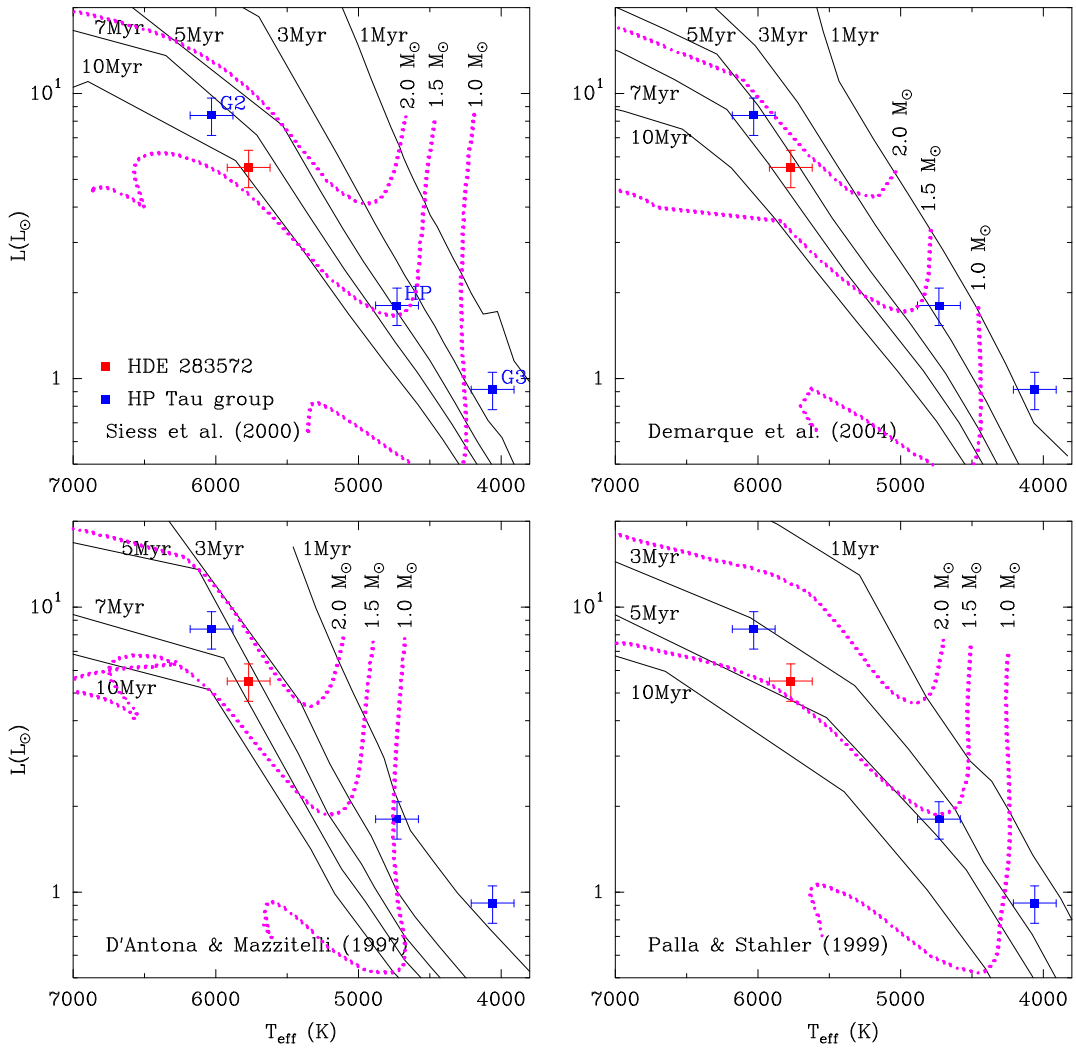

Figure 5.25 Positions of the three HP Tau members (*blue symbols*) and of HDE 283572 (*red symbol*) on an HR diagram. From the coolest to the warmest, the three stars in the HP Tau group are HP Tau/G3, HP Tau, and HP Tau/G2, as indicated in the first panel. Isochrones (*full back lines*) are shown at 1, 3, 5, 7, and 10 Myr for various models. For the same models, evolutionary tracks for stars of 1.0, 1.5, and 2.0 $M_\odot$ are also shown as *dotted magenta lines*.

0.8 $M_\odot$ according to the models of Siess et al. (2000), but slightly less than 0.5 $M_\odot$ according to those of D'Antona & Mazzitelli (1997). This is a 40% discrepancy. This tendency for pre-main sequence evolutionary models to

become more discrepant at lower masses had been noticed before, and is discussed at length in Hillenbrand et al. (2008). In the absence of dynamically measured masses, it is impossible to assess which of the models used here provides the "best" answer.

Another interesting issue is related to the age predictions of the different models. Since the different members of the HP Tau group are likely to be physically associated, they are expected to be nearly coeval. This is particularly true of HP Tau/G2 and HP Tau/G3 which are believed to form a loose binary system. Interestingly, most models predict significantly different ages for the three sources (see Fig. 5.25). The models by Siess et al. (2000) predict ages of about 8 Myr and 3 Myr for HP Tau/G2 and HP Tau/G3, respectively. A similar 5 Myr age difference is found for the models of Demarque et al. (2004) and D'Antona & Mazzitelli (1997): both predict ages slightly smaller than 1 Myr for HP Tau/G3, and somewhat larger than 5 Myr for HP Tau/G2. It is possible that those differences could be real, however, it should be noticed that the vast majority of low-mass stars in Taurus (with spectral types M and late K) have ages smaller than 3 Myr (Briceño et al. 2002). Moreover, mass-dependent systematic effects in the age predictions made by evolutionary tracks have been reported before. In particular, Hillenbrand et al. (2008) argued that existing models could significantly overpredict the age of relatively massive stars ($M \gtrsim 1.5\ M_{\odot}$). HP Tau/G2 is precisely such a fairly massive star. So is HDE 283572, another young star in Taurus with an accurate distance. The age estimate for that star based on the models by Siess et al. (2000), Demarque et al. (2004) and D'Antona & Mazzitelli (1997) is 6–10 Myr (Fig. 5.25), somewhat larger than would be expected for Taurus. The only of the four models considered here to predict similar ages for the three members of the HP Tau group is that of Palla & Stahler (1999). Within the errors, all three stars fall on the 3 Myr isochrone. Note that this value is also consistent with the ages of lower mass stars in Taurus (Briceño et al. 2002).

5.4 Relative astrometry

5.4.1 T Tau S orbit

The nature of the orbital motion between T Tau Sa and T Tau Sb has been somewhat disputed in recent years. Using 20 years of VLA observations, Loinard et al. (2003) concluded that the orbit between T Tau Sa and T Tau Sb had been dramatically altered after a recent periastron passage around 1996. Numerous near-infrared observations obtained mostly between 2002 and now have been used by several authors to constrain the orbital path. Perhaps the most complete study published so far is that of Duchêne et al. (2006) who proposed an orbit that could simultaneously reproduce the VLA observations used by Loinard et al. (2003) and the near-infrared observations. The orbital period proposed by these authors is 21 years, implying that the system has completed a full revolution since the first VLA observations published by Loinard et al. (2003). More recent near-infrared observations, however, appear to be incompatible with the orbit proposed by Duchêne et al. (2006). Instead, they suggest a significantly longer orbital period of about 90 years (Köhler et al. 2008). Such a longer orbital period, however, would be incompatible with the measured VLA positions 20–25 years ago, and would again require that something peculiar happened either to the radio source associated with T Tau Sb or to the orbit of the T Tau Sa/Sb system.

In order to understand the relative motion between the members of the T Tau S system, we need to express the motion of T Tau Sb relative to the other members (T Tau N and T Tau Sa). Since only T Tau Sb is detected in our VLBA observations, however, registering the positions reported here to the other members of the system involves a number of steps. The absolute position and proper motion of T Tau N has been measured to great precision using over 20 years of VLA observations (Loinard et al. 2003), so registering the position and motion of T Tau Sb relative to T Tau N is fairly straightforward. Combining the data used by Loinard et al. (2003) with several more recent VLA observations, we obtained the following absolute

position (at epoch J2000.0) and proper motion for T Tau N:

$$\begin{aligned}
\alpha_{J2000.0} &= 04^{\rm h}21^{\rm m}59\overset{s}{.}4321 \pm 0\overset{s}{.}0001 \\
\delta_{J2000.0} &= 19^\circ 32' 06\overset{''}{.}419 \pm 0\overset{''}{.}002 \\
\mu_\alpha \cos\delta &= 12.35 \pm 0.04 \text{ mas yr}^{-1} \\
\mu_\delta &= -12.80 \pm 0.06 \text{ mas yr}^{-1}.
\end{aligned}$$

Subtracting these values from the absolute positions and proper motion of T Tau Sb, we can obtain the positional offset between T Tau Sb and T Tau N, as well as their relative proper motion. For the median epoch of our observations, we obtain:

$$\begin{aligned}
\mu_\alpha \cos\delta(\text{Sb/N}) &= -8.33 \pm 0.07 \text{ mas yr}^{-1} \\
\mu_\delta(\text{Sb/N}) &= +11.62 \pm 0.11 \text{ mas yr}^{-1}.
\end{aligned}$$

The second step consists in registering the position and motion of T Tau Sb to the center of mass of T Tau S using the parabolic fits provided by Duchêne et al. (2006). Here, both the proper motion and the acceleration must be taken into account. For the mean epoch of our observations, we obtain:

$$\begin{aligned}
\mu_\alpha \cos\delta(\text{Sb/CM}) &= +0.3 \pm 0.9 \text{ mas yr}^{-1} \\
\mu_\delta(\text{Sb/CM}) &= +9.3 \pm 0.8 \text{ mas yr}^{-1} \\
a_\alpha \cos\delta(\text{Sb/CM}) &= +1.4 \pm 0.2 \text{ mas yr}^{-2} \\
a_\delta(\text{Sb/CM}) &= -0.1 \pm 0.3 \text{ mas yr}^{-2}.
\end{aligned}$$

The last correction to be made is the registration of the positions, proper motions, and accelerations to T Tau Sa rather than to the center of mass of T Tau S. This is obtained by simply multiplying the values above by the ratio of the total mass of T Tau S (i.e. $M_{\rm Sa} + M_{\rm Sb}$) to the mass of T Tau Sa. Using the masses given by Duchêne et al. (2006), we obtain:

$$\begin{aligned}
\mu_\alpha \cos\delta(\text{Sb/Sa}) &= +0.4 \pm 1.1 \text{ mas yr}^{-1} \\
\mu_\delta(\text{Sb/Sa}) &= +11.4 \pm 1.0 \text{ mas yr}^{-1} \\
a_\alpha \cos\delta(\text{Sb/Sa}) &= +1.7 \pm 0.2 \text{ mas yr}^{-2} \\
a_\delta(\text{Sb/Sa}) &= -0.1 \pm 0.3 \text{ mas yr}^{-2}.
\end{aligned}$$

These two vectors are shown in Fig. 5.24 together with the VLBA positions registered to T Tau Sa, several infrared observations and the elliptical fit obtained by Duchêne et al. (2006). The final error on the VLBA positions is the combination of the original uncertainty on their measured absolute position, and of the errors made at each of the steps described above. The final uncertainty is about 3 mas in both right ascension and declination, and is shown near the bottom right corner of Fig. 5.24b.

Given the uncertainties, the position of the VLBA source is generally in good agreement with the infrared source position measured at similar epochs. Indeed, the first 2 VLBA observations were obtained almost exactly at the

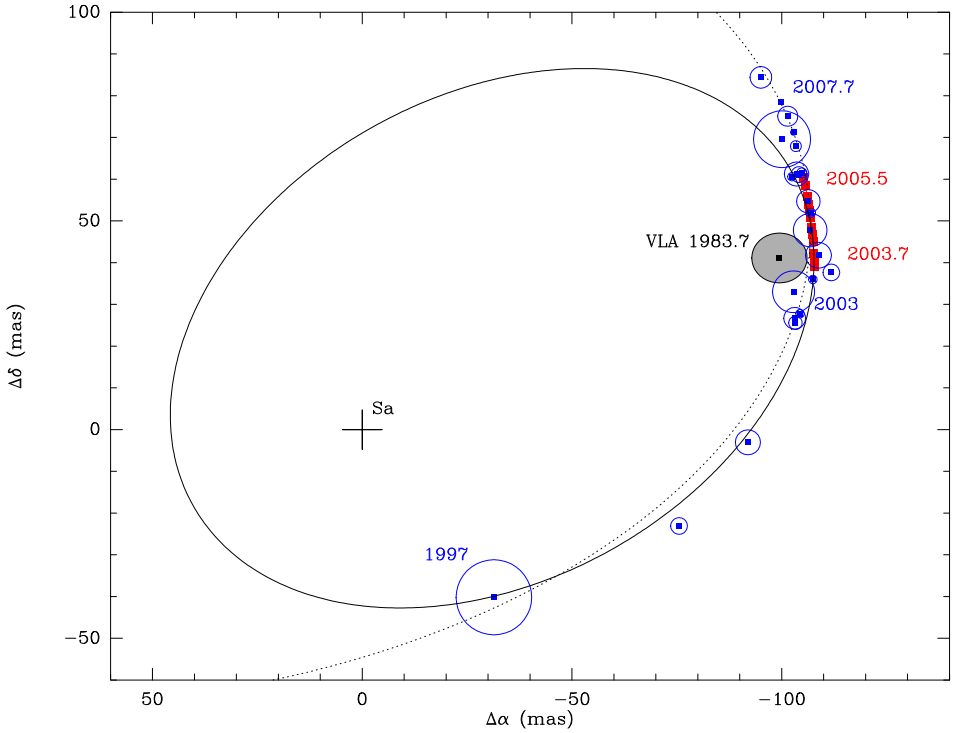

Figure 5.26 Relative position between T Tau Sb and T Tau Sa (located at the origin of the system at position (0,0)). The *blue symbols* correspond to all the infrared observations tabulated by Köhler et al. (2008) as well as Keck observations kindly provided by G. Schaefer. The *solid line* correspond to the fit published by Duchêne et al. (2006; with a period of about 21 yr) and the *dotted line* to the fit proposed by Köhler et al. (2008; with a period of about 90 yr). Our first 12 VLBA observations (*red squares*) were superimposed over the fits. The position of the VLA source in 1983.7 is shown as a *grey symbol*.

same time as the infrared image published by Duchêne et al. (2005), and the positions match exactly. The position of the VLBA source at the end of 2004 is also in agreement within 1σ with the position of the infrared source at the same epoch reported by Duchêne et al. (2006). The situation at the end of 2005, however, is somewhat less clear. Extrapolating from the last VLBA observation ($\sim$ 2005.5) to the end of 2005 gives a location that would be in reasonable agreement with the position given by Schaefer et al. (2006) but clearly not with the position obtained by Duchêne et al. (2006). Note, indeed, that the two infrared positions are only very marginally consistent with one another.

Our VLBA observations suggest that T Tau Sb passed at the westernmost point of its orbit around 2005.0, whereas according to the fit proposed by Duchêne et al. (2006), this westernmost position was reached slightly before 2004.0. As a consequence, the trajectory described by the VLBA source is on average almost exactly north-south, whereas according to the fit proposed by Duchêne et al. (2006), T Tau Sb is already moving back toward the east (Fig. 5.24). We note, however, that the fit proposed by Duchêne et al. (2006, which gives an orbital period of 21.7 ± 0.9 yr) is very strongly constrained by their 2005.9 observation. Shaefer et al. (2006), who measured a position at the end of 2005 somewhat more to the north (in better agreement with our VLBA positions), argue that they cannot discriminate between orbital periods of 20, 30 or 40 yr. Orbits with longer periods bend back toward the east somewhat later (see Fig. 10 in Schaefer et al. 2006), and would be in better agreement with our VLBA positions.

Another element that favors a somewhat longer orbital period is the acceleration measured here. According to the fit proposed by Duchêne et al. (2006), the expected transverse proper motion and acceleration are (G. Duchêne, private communication):

$$\begin{aligned}
\mu_\alpha \cos\delta(\mathrm{Sb/Sa}) &= +1.7 \pm 0.2 \text{ mas yr}^{-1} \\
\mu_\delta(\mathrm{Sb/Sa}) &= +12.1 \pm 1.2 \text{ mas yr}^{-1}. \\
a_\alpha \cos\delta(\mathrm{Sb/Sa}) &= +3.1 \pm 0.5 \text{ mas yr}^{-2} \\
a_\delta(\mathrm{Sb/Sa}) &= -1.4 \pm 0.2 \text{ mas yr}^{-2}.
\end{aligned}$$

Table 5.7. Separations between T Tau Sa and T Tau Sb from VLBA and near-infrared observations.

Mean Date [years]	$\Delta\alpha$ [mas]	$\sigma_{\Delta\alpha}$	$\Delta\delta$ [mas]	$\sigma_{\Delta\delta}$
1999.956224	-88.26	0.47	-10.60	0.75
2003.732340	-107.19	0.05	40.05	0.08
2003.882523	-107.20	0.05	41.89	0.08
2004.041542	-106.96	0.06	43.21	0.13
2004.238134	-107.11	0.05	46.13	0.09
2004.369194	-106.86	0.05	47.72	0.09
2004.522099	-106.68	0.05	49.38	0.09
2004.713224	-106.46	0.05	51.72	0.08
2004.860668	-106.16	0.05	53.53	0.08
2004.994459	-105.94	0.05	54.90	0.09
2005.150749	-105.52	0.05	56.79	0.08
2005.355532	-105.21	0.09	59.50	0.19
2005.519358	-104.71	0.05	61.36	0.09
2008.412872	-90.88	0.15	90.96	0.19
1997.780304	-31.40	7.89	-40.18	8.33
2000.139633	-75.55	2.08	-23.09	2.70
2000.887083	-91.95	2.99	-3.05	2.56
2002.829587	-103.12	2.60	26.66	2.60
2002.950055	-104.37	1.06	27.76	1.65
2002.955530	-103.28	1.56	25.55	0.81
2002.980172	-102.83	4.99	33.01	4.91
2003.881607	-108.76	3.12	41.74	3.23
2003.947317	-111.84	2.03	37.63	2.23
2003.947317	-107.45	1.07	35.95	1.53

Table 5.7 (cont'd)

Mean Date [years]	$\Delta\alpha$ [mas]	$\sigma_{\Delta\alpha}$	$\Delta\delta$ [mas]	$\sigma_{\Delta\delta}$
2004.941841	-106.96	1.13	51.93	1.21
2004.969220	-106.80	3.83	47.77	3.07
2004.982909	-106.37	2.83	54.66	2.89
2005.109516	-104.11	1.90	61.08	1.89
2005.186178	-103.55	2.91	61.24	2.92
2005.227246	-104.80	1.22	61.48	1.25
2005.802207	-103.39	1.30	67.91	1.29
2005.867917	-102.43	1.36	60.58	1.85
2005.930889	-100.10	6.80	69.57	6.80
2006.777566	-102.85	1.37	71.22	1.83
2006.963744	-101.45	2.33	75.07	2.27
2007.709118	-99.80	0.57	78.54	0.60
2008.046544	-95.05	2.63	84.38	2.63

Thus, while the expected and observed proper motions are in good agreement, the expected acceleration is significantly larger that the observed value (see also Fig. 5.24). A smaller value of the acceleration would be consistent with a somewhat longer orbital period.

In order to summarize the last paragraphs, Fig. 5.26 illustrates the problem: our VLBA positions (red squares) and the VLA position around 1984 (grey symbol) are superimposed on the fits proposed by Duchêne et al. (2006; solid line) and Köhler et al. (2008; dotted line). VLBA data appear to be in reasonable agreement with all the published infrared positions obtained over the last few years in the plot, except for the 2005.9 observation reported by Duchêne et al. (2006). Thus, our observations are in better agreement with the most recent infrared observations and with the fit proposed by Köhler et al. (2008). The difficulty with such a long orbital period is related to the older VLA position. Clearly, the observed VLA position would be consistent with the 20–22 yr orbital period proposed by Duchêne et al. (2006): between the old VLA observation and the IR or VLBA data corresponding to 2003–2005, T Tau Sb would have complete a full orbit. For a 90 yr orbital period, however, the position expected for 1984 is located at about $\Delta\alpha \sim +100$ mas; $\Delta\delta \sim -70$ mas. This is clearly inconsistent with the VLA position observed

at that epoch.

A new VLBA observation were obtained for T Tau Sb on May 2008 (epoch 13 in Tab. 5.1) to definitely allow us to discriminate between the two orbits shown in Fig. 5.26, or to provide crucial evidence for an orbit with an intermediate period. In addition, there exists a good quality observation of T Tau Sb in the VLBA archive from the end of 1999 (published by Smith et al. 2003; epoch 14 in Tab. 5.1). Our 14 VLBA positions (red squares)

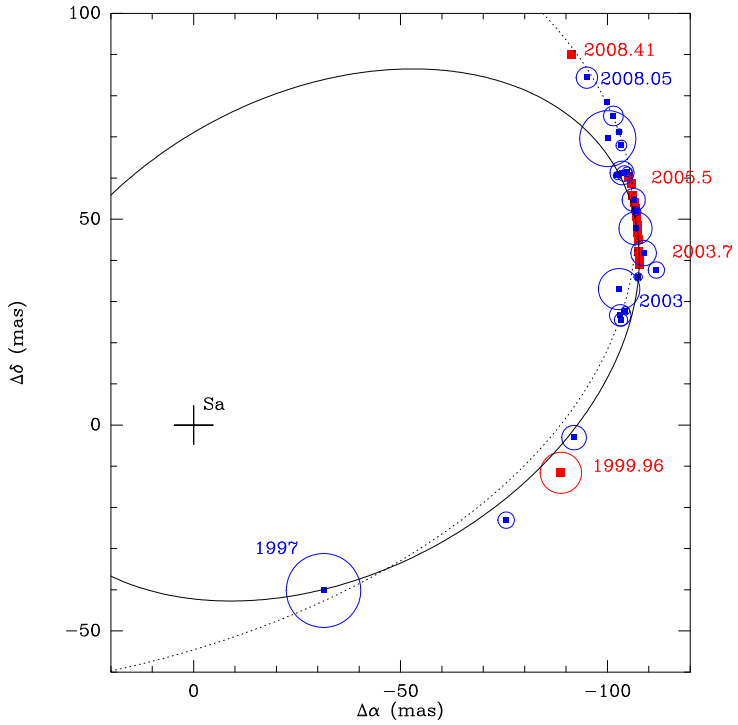

Figure 5.27 Relative position between T Tau Sb and T Tau Sa (located at the origin of the system at position (0,0)). The *blue symbols* correspond to all the infrared observations tabulated by Köhler et al. (2008) as well as Keck observations kindly provided by G. Schaefer. The *solid line* correspond to the fit published by Duchêne et al. (2006; with a period of about 21 yr) and the *dotted line* to the fit proposed by Köhler et al. (2008; with a period of about 90 yr). Our 14 VLBA observations (*red squares*) were superimposed over the fits. The series of VLBA observations between 2003 and 2005 (epochs 1 to 12 in Tab. 4.2) has been used to measure the parallax to T Tau Sb. The point at 1999.96 is from VLBA archive (observations by Smith et al. 2003; epoch 14 in Tab. 4.2). And the point at 2008.41 is the new VLBA observation (epoch 13 in Tab. 4.2). Note that the series of 14 VLBA observations agrees better with the latter fit.

were superimposed on the fits proposed by Duchêne et al. (2006; solid line) and Köhler et al. (2008; dotted line) in Fig. 5.27, and it is clear that VLBA points are in agreement with the fit proposed by Köhler et al. (2008).

However, to obtain an orbital fit of T Tau Sa/Sb system, we made use of our 14 VLBA observations, and of all infrared observations tabulated by Köhler et al. (2008) as well as Keck observations kindly provided by G. Schaefer. The angular separations ($\Delta\alpha$, $\Delta\delta$) between the primary (T Tau Sa) and the secondary (T Tau Sb) are given in Tab. 5.7 for both infrared and radio observations. The preliminary orbital parameters derived with those data are: period of 25.83 ± 8 yr, eccentricity of 0.78, inclination of 53.14°, and semi-major axis of 0.12 arcsec. Although the VLBA red points superimposed in Fig. 5.27 agrees better with the fit by Köhler et al. (2008), an entirely new fit with near-infrared and VLBA data, gives a period more like that from Duchêne et al. (2006). Our orbit model is shown in Fig. 5.28, but we should stress that the present fit must still be considered preliminary. In order to

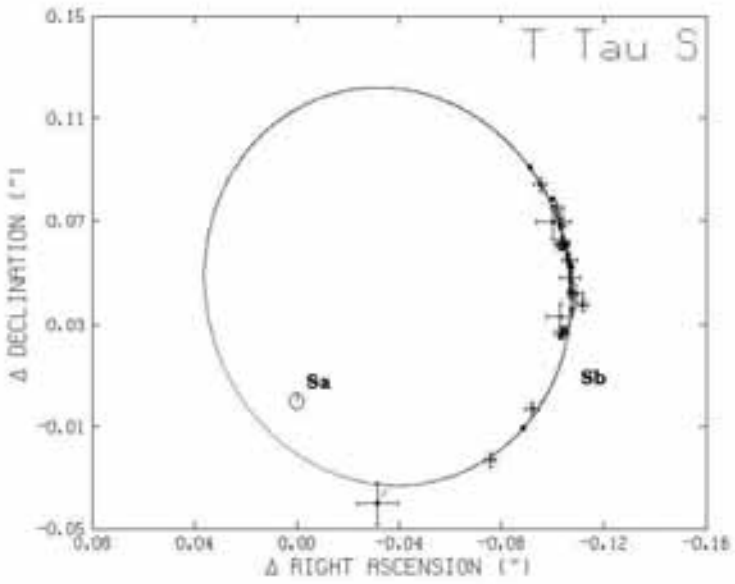

Figure 5.28 Relative position between T Tau Sb and T Tau Sa (located at the origin of the system at position (0,0)). The crosses are near-infrared (all the observations tabulated by Köhler et al. (2008) as well as Keck observations kindly provided by G. Schaefer) and VLBA observations. The solid line is our preliminary fit that corresponds to a period of about 24 yr.

give a definitive orbit, we are now in the process of analyzing the 20 years of VLA data and infrared observations from 1989 to 2009 in our data set.

5.4.2 V773 Tau A orbit

We will concentrate on the 13 epochs when the source was double (epochs 1, 2, 3, 4, 6, 7, 8, 10, 11, 13, 16, 18, 19), and analyze the relative position of the two sub-components. As established by Phillips et al. (1996) and Boden et al. (2007, hereafter B2007), these double source observations reflect the relative astrometry of the V773 Tau A components and as such can be used to assess and update the physical orbit obtained by B2007. There is, however, one difficulty. The mechanism producing the radio emission is not directly related to the mass of the star, so the primary is not necessarily the brightest radio source in the system (in the present case, it is the brightest in only about 60% of the cases). This introduces a degeneracy in the relative position angle between the stars, which we removed using the preliminary orbital fit of B2007. The corresponding angular separations ($\Delta\alpha$, $\Delta\delta$) between the primary and the secondary are given in Tab. 5.8 for the 13 epochs when the source is double. The uncertainties on ($\Delta\alpha$, $\Delta\delta$) quoted in Tab. 5.8 are based on the errors delivered by JMFIT, and are almost certainly underestimated.

Figure 5.29 shows all available relative astrometry data on V773 Tau A (from Phillips et al. 1993, B2007, and this work), along with several orbit models including that from B2007 (dashed line). Clearly there is general agreement between the old and new VLBA relative astrometry on V773 Tau A, and the B2007 orbit model. A close inspection of the VLBA separations and the B2007 orbit model in Fig. 5.29, however, shows an interesting trend in the VLBA astrometry. At most orbit phases the VLBA-derived separations and B2007 orbit model are in good agreement. But in most observations near periastron (secondary south-west of the primary) the VLBA separations appear systematically smaller (i.e. secondary nearer the primary) than predicted by the B2007 orbit. This suggests one of two possibilities: there is a possible bias in the B2007 orbit solution, or a possible bias in the VLBA-derived astrometry near periastron (where there is known enhancement in the radio flaring; Massi et al. 2002, 2006).

To investigate this issue we considered two different prescriptions for integrating the new VLBA data into the orbit modeling. In the first "VLBA + RV" model we considered the possibility that the KI visibilities were the

Table 5.8. Orbit phases and measured separations between two components of V773 Tau A system.

Epoch	Mean Date JD	$\Delta\alpha$ (mas)	$\sigma_{\Delta\alpha}$	$\Delta\delta$ (mas)	$\sigma_{\Delta\delta}$	ϕ
1	2453622.00	−1.43	0.01	−0.70	0.04	0.99
2	2453689.81	1.90	0.03	1.85	0.06	0.32
3	453756.63	2.79	0.04	0.78	0.12	0.63
4	2453827.44	−1.31	0.01	−0.71	0.03	0.01
5	2453899.24	.....	....	.....	....	0.42
6	2453984.01	−1.34	0.02	−0.35	0.05	0.08
7	2454336.05	−1.96	0.03	−1.34	0.06	0.97
8	2454342.03	−1.21	0.02	0.08	0.03	0.08
9	2454349.01	.....	....	.....	....	0.22
10	2454354.99	2.61	0.11	1.75	0.18	0.33
11	2454359.98	2.92	0.03	1.69	0.05	0.43
12	2454364.97	.....	....	.....	....	0.53
13	2454370.95	2.82	0.06	0.43	0.11	0.65
14	2454376.93	.....	....	.....	....	0.77
15	2454382.92	.....	....	.....	....	0.88
16	2454390.89	−1.40	0.02	−0.60	0.05	0.04
17	2454396.88	.....	....	.....	....	0.16
18	2454400.87	0.77	0.03	1.36	0.05	0.24
19	2454421.81	2.73	0.01	0.57	0.03	0.64

Table 5.9. Orbital parameters of V773 Tau.

Orbital Parameter	B2007	"Full Hybrid"
Period (days)	51.1039±0.0021	51.1028±0.0019
T_o (MJD)	53059.73±0.33	53059.68±0.30
e	0.2717±0.0085	0.2732±0.0070
K_A (km s^{-1})	35.90±0.53	35.94±0.53
K_B (km s^{-1})	41.5±1.4	41.5±1.4
γ (km s^{-1})	0.02±0.32	0.03±0.32
ω_A (deg)	4.6±2.4	5.0±2.3
Ω (deg)	63.5±1.7	62.7±1.1
i (deg)	66.0±2.4	67.8±1.6
a (mas)	2.811±0.047	2.810±0.034

source of a possible orbit bias in B2007, and used only the (old and new) VLBA-derived relative astrometry and double-lined RV from B2007 to derive an orbit model. In the second "Full Hybrid" model we used all available data (VLBA astrometry, KI visibilities, and RV), but assume that the VLBA separations near periastron were biased by the enhanced flaring activity (e.g. if the enhanced flares preferentially occur between the two stars), assigning these points lower weight (specifically a factor of 50% larger 1-sigma error

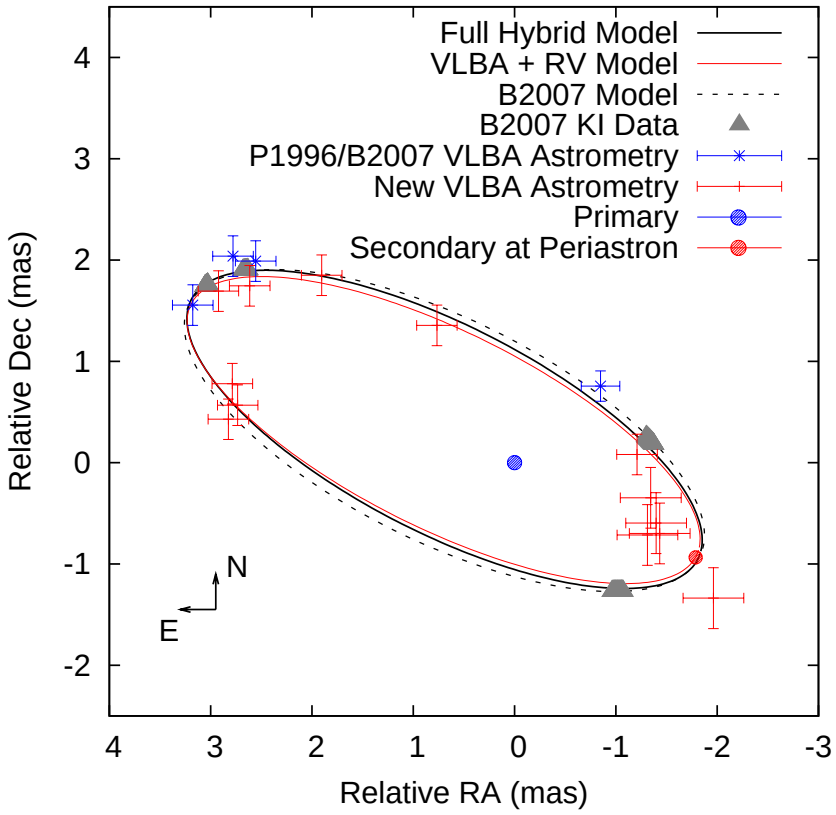

Figure 5.29 VLBA Relative astrometry and orbit models of V773 Tau A. Here VLBA relative astrometry from P1996, B2007 and this work is shown with orbit model renderings for the B2007 orbit and two models derived here (the "VLBA + RV" and "Full Hybrid" models described in the text). We render the primary (Aa) component at the origin and the secondary (Ab) at periastron. The apparent sizes of the V773 Tau A components are estimated by SED modeling (B2007) and rendered to scale.

per axis for orbit phases within 10% of periastron).[1] We find that both new orbit solutions are in excellent agreement with the original B2007 model, and renderings of both these orbit models are included in Fig. 5.29. It is clear that the KI visibility data is reliable at its stated uncertainties, and the most plausible hypothesis is that the VLBA relative astrometry near periastron contains biases associated with the enhanced flaring activity documented by Massi et al. (2002, 2006). This astrometric bias was discussed in section 5.2. Tab. 5.9 gives a direct comparison between the orbit models from B2007 and the "Full Hybrid" model derived here; in all cases the orbital parameters between the two models (which share a significant amount of underlying data) are in excellent statistical agreement. For all subsequent analysis we adopt this "Full Hybrid" model for the updated V773 Tau A orbit.

Given the agreement between the "Full Hybrid" model and the B2007 orbit model, the updated physical parameters are highly consistent with B2007 estimates. Component dynamical masses resulting from this orbit model 1.48 ± 0.12 $M_\odot$ and 1.28 ± 0.07 $M_\odot$, for the primary and the secondary respectively – consistent with the B2007 estimates to 4% and 0.5-sigma. Similarly, the system distance estimate derived from the updated orbit model is 134.5 ± 3.2 pc, again consistent with the value from B2007 to 1% and 0.4-sigma. As a final note, we should stress that the present fit must still be considered preliminary as astrometric and RV observations to assess the gravitational effect of the two other members of the system (V773 Tau B and C) are ongoing.

[1] Our methods for orbit modeling with heterogeneous RV and astrometric/visibility datasets are described in Boden et al. (2000) and are not repeated here. In all the orbit modeling we have weighted all VLBA astrometry consistently with the weighting derived in B2007, at 0.2 mas per axis 1-sigma, except as noted for points near periastron in the "Full Hybrid".

6
Conclusions

6.1 General conclusions

6.1.1 Taurus

Distances— For T Tau Sb, a resulting parallax of 6.82 ± 0.03 mas was obtained, corresponding to a distance of $d = 146.7 \pm 0.6$ pc. For Hubble 4 and HDE 283572, obtained the parallaxes of 7.53 ± 0.03 mas ($d = 132.8 \pm 0.5$ pc) and 7.78 ± 0.04 mas ($d = 128.5 \pm 0.6$ pc), respectively. HP Tau/G2 yielded a parallax of 6.20 ± 0.03 mas, corresponding to $d = 161.2 \pm 0.9$ pc. Finally, for V773 Tau A we obtained a parallax of 7.57 ± 0.20 mas, corresponding to $d = 132.0 \pm 3.5$ pc. This increase the precision of the distance to this star-forming region by 1-2 orders of magnitude.

Proper motions— The proper motion of HDE 283572 was found to be linear and uniform, but for Hubble 4 and HP Tau/G2 we find significant residuals in declination (but not in right ascension). It is unclear at the moment whether these residuals are the consequence of an unseen companion, of structure in the magnetospheres of the star, or of residual phase errors in our calibration. V773 Tau A was found to be a resolved double radio source. The physical orbit of the system was constrained by combining optical radial

velocity measurements, Keck Interferometer data, and our own VLBA data. This fit allowed us to refine the determination of the masses of the two stars in the system, and to deduce the position of the barycenter of the system at each epoch. A fit assuming a uniformly accelerated proper motion appeared to provide an adequate description of the trajectory of T Tau Sb. In this case, our observations are not sufficient to constrain the orbit of the system, but they provide information consistent with, and complementary, existing near infrared data.

Three-dimensional structure— The resulting mean distance to the Taurus complex is about 139 pc, in excellent agreement with previous determinations. The total spatial extent of Taurus on the sky is about 10°, corresponding to a physical size of about 25 pc. The observations of the five stars presented already provide some hints of what the three-dimensional structure of Taurus might be. Hubble 4, HDE 283572, and V773 Tau A which were found to be at about 130 pc, are located in the same portion of Taurus, near Lynds 1495. T Tau Sb is located in the southern part of Taurus near Lynds 1551, its tangential velocity is clearly different from that of Hubble 4, HDE 283572, and V773 Tau A, and it appears to be somewhat farther from us. Finally, HP Tau/G2 is located near the (Galactic) eastern edge of Taurus, and is the farthest of the four sources considered here. Although additional observations are needed to draw definite conclusions, our data, therefore, suggest that the region around Lynds 1495 corresponds to the near side of the Taurus complex at about 130 pc, while the eastern side of Taurus corresponds to the far side at 160 pc. The region around Lynds 1551 and T Tau Sb appears to be at an intermediate distance of about 147 pc. Taurus has long been known to present a filamentary structure. The two main filaments are roughly parallel to one another, and have an axis ratio of about 7:1. Our observations suggest that these filaments are oriented nearly along the line of sight, i.e. roughly along the Galactic center–anticenter axis. This peculiar orientation might indeed explain the low star-forming efficiency of Taurus compared with other nearby star-forming regions.

6.1.2 Ophiuchus

Distances— The resulting parallaxes of S1 and DoAr 21 are 8.55 ± 0.50 mas and 8.20 ± 0.37 mas, respectively. This corresponds to $d = 116.9^{+7.2}_{-6.4}$ pc for S1 and $d = 121.9^{+5.8}_{-5.3}$ pc for DoAr 21. The resulting mean distance to

the Ophiuchus complex is $120.0^{+4.5}_{-4.2}$ pc, in excellent agreement with several recent determination (e.g. Knude & Hog 1999; de Geus et al. 1989; Lombardi et al. 2008).

Proper motions— Assuming the proper motion of S1 to be uniform appears to provide an adequate fit, but with roughly periodic residuals (in both right ascension and declination) with a period of about 0.7 years. This is of the correct order of magnitude to be interpreted as the reflex motion of S1 due to its known companion. DoAr 21 was found to behave much like S1: a uniform proper motion provides a good fit but with roughly periodic residuals (with a period of about 1.2 years in this case), and the source was found to be double in at least one of our images. We conclude that DoAr 21 is likely to belong to a binary system.

Three-dimensional structure— Ophiuchus is composed of a compact core, only about 2 pc across, and filamentary structures (called "streamers") extending (in projection) to about 10 pc. The Ophiuchus core is sufficiently compact that we do not expect to resolve any structure along the line of sight, and our observations show that it is at a distance of 120 pc. There could potentially be distance gradients of several parsecs across the streamers. We note, however, that Schaefer et al. (2008) determined the physical orbit of the binary system Haro 1-14C, and deduced a distance of 111 ± 19 pc, in good agreement with our determination. Haro 1-14C is located in the northern streamer (associated with the darks clouds L1709/L1704), so the result of Schaefer et al. (2008) suggests that that streamer is, if anything, somewhat closer that the core. This is, indeed, in agreement with recent results of Lombardi et al. (2008). On the other hand, Imai et al. (2007) used the Japanese VLBI system (VERA) to determine the parallax to the very young protostar IRAS 16293–2422 deeply embedded in the southern Ophiuchus streamer (in L1689N). They obtain a distance of 178^{+18}_{-37} pc, which would be more consistent with the older value of 165 pc. Even including the streamers, Ophiuchus is only 10 pc across in projection, so it is unlikely to be 60 pc deep. Thus, if the results of Imai et al. (2007) are confirmed, they would indicate the existence of several unrelated star-forming regions along the line of sight.

6.1.3 Multiplicity and variability

At least 4 of the 7 sources in our sample (57%) turn out to be tight binary systems with separations between a few and a few tens of milli-arcseconds. This represents a binarity fraction much larger than that of main sequence stars for the same separation range. We argue that a strong selection effect is likely to be at work. The systems considered in this thesis were selected because they were known to be non-thermal emitters previously detected with VLBI techniques. The high binary rate may, therefore, indicate that tight binaries are more likely to emit non-thermal radio emission than looser binaries or single stars. This idea is reinforced by the observations of V773 Tau A where we confirm that the emitted flux depends strongly on the separation between the two stars (the flux is strongest near the periastron of the system, and weakest near apoastron). Non-thermal emission is believed to be created during reconnection events in the active magnetospheres of the stars. Reconnection events *between* the stars (in addition to those within the individual magnetospheres) in tight binary systems might naturally explain the higher radio flux of such systems.

6.2 Future prospects

The results presented in this thesis have allowed us to refine the determination of the distance to two important regions of nearby low-mass star-formation and to start examine the three-dimensional structure of Taurus and Ophiuchus complexes. They also raised a number of issues that could be tackled with new data and suggested several follow-up studies.

Interacting binary V773 Tau Aa/Ab— The radio flux of V773 Tau A depends on the orbit phase, being highest at periastron and weakest at apoastron. In most of our observations, it is resolved into two components associated with the two stars in the system. Our observations have shown, however, that near periastron, the position of the radio sources is significantly displaced from the position of the associated star. This is additional evidence that the non-thermal emission in such systems is affected by the presence of a close companion. In a recently accepted proposal, we requested time to observe V773 Tau A near periastron with the High Sensitivity Array (a composite VLBI array comprised of the Very Large Baseline Array, the Green Bank Telescope, and the Very Large Array plus the Arecibo dish in Puerto

Rico). These observations will allow us to examine the spatial evolution of this interacting binary when it is near periastron over a six hour period. This ought to shed light on the origin of the variability of the source.

Stellar structure and emission of pre-main sequence stars— We found interesting characteristics in the structure and emission of the sources in both Taurus and Ophiuchus complexes. **(1)** T Tau Sb was found to be somewhat extended toward the northeast direction, and with a low brightness extension probably associated with an accretion disk (Loinard et al. 2005). **(2)** Hubble 4 was found to have large declination residuals, that can be explained if Hubble 4 had a companion, and the residuals reflect the corresponding reflex motion (Torres et al. 2007), but the residuals are relatively poorly constrained with the existing data, and additional observations would help to confirm the periodicity in the residuals. **(3)** For one epoch we detect that HP Tau/G2 underwent a flaring event, reaching a flux 4 times higher than at other epochs. One year after the flare, we found that the source is extended with a deconvolved size in the north-south direction of about 2.5 mas. This increase in the source size might be due to variation in the structure of the active magnetosphere (Torres et al. 2009).

We are interested in studying with more detail, the structure and emission mechanism of these stellar systems. Since we found that V773 Tau A system experienced large changes in structure and flux in about one hour, we would like to observe some stars again and re-analyze the data that have already been collected.

Along the line of sight to Ophiuchus— To decide whether or not several unrelated star-forming regions exist along the line of sight to Ophiuchus, we need more observations of several new sources in the direction of the complex. VSSG 14 is a source in line of sight to Oph-B subregion, and we have been observed at 14 epochs from 2005 to 2007. Also, we have been obtained new observations of the source Rox 39 that belongs to the region between L1686 and L1689. We are in the process of reducing both VSSG 14 and Rox 39 data. Additionally we would like to obtain observations in the southern streamer of Ophiuchus, in particular of IRAS 16293–2422 to check whether or not it is at nearly 180 pc, as reported by Imai et al. (2007).

Serpens and Perseus star-forming regions— Several other nearby star-forming regions have been studied in detail at many wavelengths but have poorly determined distances. Non-thermal sources are known to exist in these

regions, so multi-epoch VLBA observations would allow significant improvements in the determination of their distances. New observations of Serpens are currently obtained to measure the parallax to sources in these regions. Perseus will be the subject of forthcoming proposals. These regions have been actively studied in recently years, and our observations will provide distances with a precision of about 3-5%.

A survey of radio emitting stars in Taurus and Ophiuchus— Our existing data already provide hints of the structure of both Taurus and Ophiuchus. In addition, we have made a limited survey (VLBA+VLA) of 17 sources in the Taurus star forming region recently, that allowed us to detect several new sources. A large systematic VLBA survey would almost certainly reveal many new non-thermal sources in Taurus and Ophiuchus, that could then be observed to get their parallax and proper motions. This, in turn, would allow us to construct a high quality three-dimensional map of these two interesting star-forming regions. We are planning to submit a large VLBA proposal to initiate a large search for non-thermal radio sources in Ophiuchus and Taurus. The sources that will be detected will be observed at multiple epochs.

A

Multiepoch VLBA Observations of T Tauri South

Laurent Loinard, Amy J. Mioduszewski, Luis F. Rodríguez, Rosa A. González-Lópezlira, Mónica Rodríguez & Rosa M. Torres
The Astrophysical Journal, 619, L179, 2005

Abstract. We present a series of seven observations of the compact, nonthermal radio source associated with T Tauri South made with the Very Long Baseline Array (VLBA) over the course of 1 year. The emission is found to be composed of a compact structure most certainly originating from the magnetosphere of an underlying pre-main sequence star and a low brightness extension that may result from reconnection flares at the star-disk interface. The accuracy of the absolute astrometry offered by the VLBA allows us to make very precise determinations of the trigonometric parallax and proper motion of T Tau South. The proper motion derived from our VLBA observations agrees with that measured with the Very Large Array over a similar period to better than 2 mas yr^{-1}, and it is fully consistent with the infrared proper motion of T Tau Sb, the pre-main-sequence M star with which the radio source has traditionally been associated. The parallax, $\pi = 7.07 \pm 0.14$ mas, corresponds to a distance of $141.5^{+2.8}_{-2.7}$ pc.

The Astrophysical Journal, 619:L179–L182, 2005 February 1

MULTIEPOCH VLBA OBSERVATIONS OF T TAURI SOUTH

Laurent Loinard,[1] Amy J. Mioduszewski,[2] Luis F. Rodríguez,[1] Rosa A. González,[1]
Mónica I. Rodríguez,[1] and Rosa M. Torres[1]

Received 2004 November 1; accepted 2004 December 20; published 2005 January 10

ABSTRACT

In this Letter, we present a series of seven observations of the compact, nonthermal radio source associated with T Tauri South made with the Very Long Baseline Array (VLBA) over the course of 1 year. The emission is found to be composed of a compact structure most certainly originating from the magnetosphere of an underlying pre–main-sequence star and a low brightness extension that may result from reconnection flares at the star-disk interface. The accuracy of the absolute astrometry offered by the VLBA allows us to make very precise determinations of the trigonometric parallax and proper motion of T Tau South. The proper motion derived from our VLBA observations agrees with that measured with the Very Large Array over a similar period to better than 2 mas yr^{-1}, and it is fully consistent with the infrared proper motion of T Tau Sb, the pre–main-sequence M star with which the radio source has traditionally been associated. The parallax, $\pi = 7.07 \pm 0.14$ mas, corresponds to a distance of $141.5^{+2.8}_{-2.7}$ pc.

Subject headings: astrometry — binaries: general — magnetic fields — radiation mechanisms: nonthermal — radio continuum: stars — stars: formation

1. INTRODUCTION

T Tauri was initially identified as a single optical star, with unusual variability and peculiar emission lines (Barnard 1895, Joy 1945, and references therein). Early infrared observations then revealed the existence of a heavily obscured companion (hereafter T Tau S) located about 0.″7 to the south of the visible star (Dyck et al. 1982) and most likely gravitationally bound to it (Ghez et al. 1991). Recently, this infrared companion was itself found to contain two sources (T Tau Sa and T Tau Sb; Koresko 2000 and Köhler et al. 2000) in rapid relative motion (Duchêne et al. 2002; Furlan et al. 2003). Thus, T Tau is now acknowledged to be at least a triple stellar system. At radio wavelengths, T Tau has long been known to be a double source (Schwartz et al. 1986). The northern radio component is associated with the optical star and mostly traces the base of its thermal jet (e.g., Johnston et al. 2003), whereas the southern radio source is related to the infrared companion and is thought to be the superposition of a compact component of magnetic origin and an extended halo, presumably related to stellar winds (Johnston et al. 2003; Loinard et al. 2003).

The relative motions between the various components of the T Tau system have recently been under enhanced scrutiny, following the suggestion, based on multiepoch Very Large Array (VLA) observations, that one of the components might have seen its path dramatically altered by a recent chaotic encounter (Loinard et al. 2003). This interpretation was disputed by Johnston et al. (2003, 2004a) and Tamazian (2004), who fitted the same VLA data with stable orbits. It is noteworthy, however, that the residuals between their best fits and the actual radio positions (0.″03–0.″04) are often significantly larger than the nominal observational errors ($\lesssim$0.″01), especially at recent epochs (see Table 6 in Johnston et al. 2004a). To resolve this discrepancy, Johnston et al. (2004a, 2004b) proposed that the structure of T Tau S at radio wavelengths was affected by erratic internal variations, which made the centroid of the VLA source dither around the position of the underlying pre–main-sequence (PMS) star. To reconcile the radio observations obtained in the last few years with the orbital fits, the VLA source centroid needs to have moved about 25 mas yr^{-1} faster than the associated PMS star. Clearly, this would render the existing 20 years of VLA observations useless as tracers of the stellar trajectories, in spite of the high-quality astrometry naturally provided by radio interferometry.

The nonthermal mechanisms at the origin of the compact radio emission in T Tau S require the presence of an underlying, magnetically active star (Skinner 1993). Specifically, the emission is expected to be either gyrosynchrotron radiation associated with reconnection flares in the stellar magnetosphere and at the star-disk interface or coherently amplified cyclotron emission from magnetized accretion funnels connecting the disk to the star (Dulk 1985; Feigelson & Montmerle 1999; Smith et al. 2003). In all cases, the emission is produced within less than about 10 stellar radii (roughly 30 $R_\odot$) of the star itself. Indeed, 3.6 cm VLBI observations recently revealed the existence, near the expected position of T Tau Sb, of a source with an angular size less than about 15 $R_\odot$ (Smith et al. 2003). Because it is so small, any structural changes in this compact radio component would occur on such small scales that the effects on the astrometry would be very limited. Thus, observations focusing on it should accurately trace the path of the underlying PMS star.

2. OBSERVATIONS

Here, we present the results of a series of seven continuum 3.6 cm (8.42 GHz) observations of T Tau S obtained every 2 months between 2003 September and 2004 September with the 10-element Very Long Baseline Array (VLBA) of the National Radio Astronomy Observatory (NRAO; Table 1). Since the VLBA is only sensitive to compact emission structures with high surface brightness, it will effectively filter out the extended radio halo of T Tau S and will provide images of the nonthermal source alone. Our phase center was at $\alpha_{J2000.0} = 04^h21^m59^s.4263$, $\delta_{J2000.0} = +19°32'05''.730$, the position of the compact source detected by Smith et al. (2003). Each observation consisted of a series of cycles

[1] Centro de Radiostronomía y Astrofísica, Universidad Nacional Autónoma de México, Apartado Postal 72-3 (Xangari), 58089 Morelia, Michoacán, Mexico; l.loinard@astrosmo.unam.mx.
[2] National Radio Astronomy Observatory, Array Operations Center, 1003 Lopezville Road, Socorro, NM 87801.

TABLE 1
OBSERVATIONAL PARAMETERS

UT Date	Epoch (yr)	Synthesized Beam $\Delta\theta_{max} \times \Delta\theta_{min}$; P.A. (mas × mas; deg)	rms (μJy beam^{-1})	Flux Density (mJy)	Peak Flux (mJy beam^{-1})
2003 Sep 24	2003.7300	1.88 × 0.78; −8.99	70.5	1.69	1.43
2003 Nov 18	2003.8804	1.87 × 0.79; −5.19	64.3	1.70	1.17
2004 Jan 15	2004.0387	2.17 × 1.00; +11.94	68.0	1.03	0.84
2004 Mar 26	2004.2349	1.90 × 0.80; −2.24	65.5	1.51	0.76
2004 May 13	2004.3657	1.92 × 0.76; −10.66	76.3	1.79	1.18
2004 Jul 8	2004.5183	1.90 × 0.78; −6.00	62.9	1.13	0.54
2004 Sep 16	2004.7090	2.06 × 0.80; −8.94	68.7	1.70	0.98

with 2 minutes spent on-source and 1 minute spent on the phase-referencing quasar J0428+1732 ($\alpha_{J2000.0} = 04^h28^m35^s.633679$, $\delta_{J2000.0} = +17°32'05''.58799$), located 2°.6 away. The secondary quasar J0431+1731 ($\alpha_{J2000.0} = 04^h31^m57^s.379244$, $\delta_{J2000.0} = +17°31'35''.77538$) was also observed periodically (about every 30 minutes); it was not used in the phase calibration process but served as a check on the final astrometry. Based on the dispersion on the measured position of that quasar, we estimate our astrometric uncertainties to be about 0.25 mas in both α and δ. Data editing, amplitude calibration, and fringe fitting (carried out only on the calibrators, since the target is much too weak) were made in a standard way using NRAO's AIPS software. Once calibrated, the visibilities were imaged with a pixel size of 0.25 mas after weights intermediate between natural and uniform were applied.

3. STRUCTURE OF THE EMISSION

The compact radio source associated with T Tau S was detected at all seven epochs with high signal-to-noise ratio (Table 1). Its flux density varies significantly, from a maximum of nearly 1.8 mJy down to a minimum of just over 1.0 mJy. Moreover, its peak brightness in units of millijanskys per beam is found to be always significantly smaller than its flux density in millijanskys (on average by 35%; Table 1). This suggests that the emission is somewhat extended since equal numerical values are expected for a point source. This possibility gains further credibility when one considers the restored images (Figs. 1*a*–1*c*), where the emission is consistently found to be composed of a compact source (most certainly associated with a stellar magnetosphere) and a low brightness "spur" extending eastward. Although this latter component was not reported by Smith et al. (2003), inspection of their published image (their Fig. 1) reveals a source structure quite similar to that found here, with a weak spur extending toward the northeast of a compact component. When our seven observations are combined, the low brightness spur becomes even more evident (Fig. 1*d*); its position angle (P.A.) is between +70° and +80°, and its deconvolved extent in that direction is about 1 mas. Since the measured parallactic and proper motions (§ 4) imply a maximum displacement of about 0.02 mas during any one of our 6 hr observing runs, the measured size is not affected by smearing effects. The observed spur is also very unlikely to be a consequence of random errors in the phase calibration, since its characteristics repeat themselves from one epoch to the next.

T Tau S contains two infrared sources, so one might be tempted to associate the eastern spur to this preferred direction of the system. However, extrapolating from the latest published infrared observations (Furlan et al. 2003; G. Duchêne et al. 2005, in preparation), we estimate that the position angle between T Tau Sb and T Tau Sa at the median epoch of our VLBA observations must have been about 110°, significantly larger than the position angle of the spur. Another unlikely possibility is that it would trace a weak secondary component. Given the short distance that would then separate the two VLBA sources, orbital motions should have been easily detected over the course of our observations. Interestingly, the spur is nearly exactly perpendicular to the jet acknowledged to be powered by T Tau S (Solf & Böhm 1999). This might suggest that the low brightness extension is associated with an accretion disk and that it results from reconnection flares at the star-disk interface. Indeed, Duchêne et al. (2002) reported the detection of a wavelength-dependent infrared excess around T Tau Sb, which strongly suggests the existence of an accretion disk there. Typically, the inner edge of that disk is expected to be at a radius of about $5R_*$, where R_* is the stellar radius (Ostriker & Shu 1995). A low-mass PMS star such as T Tau Sb is expected to have a radius of about 3 $R_\odot$ (Siess et al. 2000). Hence, the inner disk edge is expected to be at 15 $R_\odot$ (0.07 AU). At a distance of 141.5 pc (see § 4), this corresponds to an angular scale of about 0.5 mas. After convolution with our beam size in α (on average 0.82 mas), we obtain an ex-

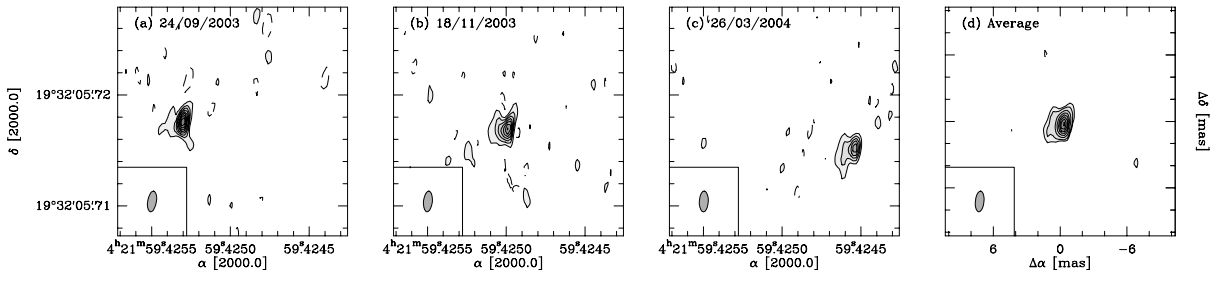

FIG. 1.—(*a*–*c*) 3.6 cm images of the T Tau system obtained at three different epochs. The first contour and the contour interval are at 0.165 mJy beam^{-1}. (*d*) Average of the 6 epochs. The first contour is at 0.08 mJy beam^{-1}, and the subsequent ones increase exponentially by a factor $\sqrt{2}$. The synthesized beam is indicated at the bottom left-hand corner of each panel.

FIG. 2.—Trajectory on the plane of the sky of the compact radio component in T Tau S. The crosses represent the measured positions of the source with their error bars, the dotted line shows the best fit to the data, and the filled squares display the positions of the source as predicted by the best fit for each observed epoch.

pected observed extent of 0.9 mas for the spur. This is in very good agreement with the measured extent. In this scheme, however, it is somewhat puzzling that we only see structure on one side of the star.

4. ASTROMETRY

As Figures 1*a*–1*c* readily show, the absolute position of the source changes significantly from one epoch to the next. These displacements most certainly result from parallactic and proper motions[3] and can be modeled in terms of the source position at epoch J2000.0 ($\alpha_{\rm J2000.0}$ and $\delta_{\rm J2000.0}$), its proper motion in right ascension and declination (μ_α and μ_δ), and its parallax π. These five astrometric elements were deduced from the measured positions of the source by minimizing the χ^2 associated with this description using an iterative scheme (Fig. 2). The results for the five astrometric parameters are as follows:

$$\alpha_{\rm J2000.0} = 04^{\rm h}21^{\rm m}59\overset{\rm s}{.}424015 \pm 0\overset{\rm s}{.}000009,$$

$$\delta_{\rm J2000.0} = 19°32'05\overset{''}{.}71957 \pm 0\overset{''}{.}00013,$$

$$\mu_\alpha \cos\delta = 3.29 \pm 0.30 \text{ mas yr}^{-1},$$

$$\mu_\delta = -0.75 \pm 0.31 \text{ mas yr}^{-1},$$

$$\pi = 7.07 \pm 0.14 \text{ mas}.$$

The postfit rms is found to be 0.25 mas in both α and δ, in agreement with our expected individual positional errors.

The parallax reported here for T Tau corresponds to a distance $d = 141.5^{+2.8}_{-2.7}$ pc, a value much more precise than, and barely within the 1 σ error bar of, that obtained by the *Hipparcos* satellite for T Tau N ($d = 177^{+70}_{-39}$ pc; Perryman et al. 1997). With this measurement, T Tau becomes the second PMS star in Taurus with a distance known to this level of precision. The first was V773 Tau, for which Lestrade et al. (1999) determined a parallax of 6.74 ± 0.25 mas ($d = 148.3^{+5.7}_{-5.3}$ pc) using multiepoch global VLBI observations. For V773 Tau, the VLBI distance was also significantly more precise than, and only marginally within the 1 σ error bar of, the *Hipparcos* value ($d = 101^{+40}_{-22}$ pc). As already discussed by Bertout et al. (1999), one must exercise caution when using *Hipparcos* parallaxes for faint individual PMS stars. In particular, while *Hipparcos* suggested that the southern part of the Taurus complex might be somewhat farther than its central regions (170 pc vs. 125 pc; Bertout et al. 1999), we find T Tau (which is part of Taurus South) and V773 Tau (which belongs to the central parts of Taurus) to be at very similar distance. Indeed, the two VLBI measurements are consistent with the entire Taurus complex lying at 145 ± 4 pc.

To decide if the magnetically active PMS star responsible for the compact radio source detected here can be identified with the infrared source T Tau Sb (as is usually believed) and if the VLA observations can be used to trace its motion, one would ideally like to compare the absolute positions of the infrared, VLA, and VLBA sources at a common time. The fit presented above can provide accurate estimates of the absolute position of the VLBA source at any time during or within a few years of our observing time span. Unfortunately, this cannot easily be compared with the infrared and VLA positions, because the infrared data lack accurate absolute astrometry information, while the VLA and VLBA reference frames may not match perfectly in spite of being both based on distant quasars. The latter effect is a consequence of the differing *u*-*v* plane coverages of the VLA and the VLBA, which will tend to make them sensitive to different components of even the same quasar. Consequently, it is preferable to compare the motions of the sources rather than their positions; if two sources share the same proper motion, it is very unlikely that they are different objects.

The proper motion of the VLA source was measured over a time span similar to that covered by our VLBA observations using the two most recent 2 cm images available to us: the 2001 January 19 observation reported in Loinard et al. (2003) and Johnston et al. (2003) and a more recent (still unpublished) image we obtained on 2003 August 19. The latter was processed following the exact same procedure as that used in Loinard et al. (2003). The phase-referencing quasar was 0403+260 ($\alpha_{\rm J2000.0} = 04^{\rm h}03^{\rm m}05\overset{\rm s}{.}5860$, $\delta_{\rm J2000.0} = +26°00'01\overset{''}{.}502$) for both observations. The calibrated visibilities were restored using pixels of 0.″02 and weights intermediate between uniform and natural. The VLA source positions (Table 2) were determined from two-dimensional Gaussian fits and were corrected for parallactic motions. They yield proper motions of

$$\mu_\alpha \cos\delta = 3.94 \pm 0.50 \text{ mas yr}^{-1},$$

$$\mu_\delta = 0.46 \pm 0.47 \text{ mas yr}^{-1},$$

very similar to those found for the VLBA source. The differences (<2 mas yr^{-1}) are at least an order of magnitude smaller

[3] At least one more year of observations will be needed before acceleration terms can be measured reliably.

TABLE 2
VLA SOURCE POSITIONS

Epoch	α_{2000} ($04^{\rm h}21^{\rm m}$)	δ_{2000} (19°32′)
2001.052	$59\overset{\rm s}{.}42502 \pm 0\overset{\rm s}{.}00007$	$05\overset{''}{.}7179 \pm 0\overset{''}{.}0009$
2003.636	$59\overset{\rm s}{.}42574 \pm 0\overset{\rm s}{.}00006$	$05\overset{''}{.}7191 \pm 0\overset{''}{.}0008$

than the values required to reconcile the VLA observations with the orbital fits proposed by Johnston et al. (2004a). Instead, it appears that the VLA and the VLBA observations trace the trajectory of the same magnetically active star.

Because of the lack of absolute astrometry information for the infrared observations, the proper motions required to compare the radio and infrared data must be measured relatively to a third source. Here, we shall register all motions on T Tau N, which is seen at both radio and infrared wavelengths and has a well-determined linear proper motion (e.g., Loinard et al. 2003). For the radio source, we obtain a relative motion between T Tau S and T Tau N of

$$\mu_\alpha \cos\delta = -8.3 \pm 0.8 \quad \text{or} \quad -8.9 \pm 0.7 \text{ mas yr}^{-1};$$
$$\mu_\delta = +13.2 \pm 0.8 \quad \text{or} \quad +12.0 \pm 0.7 \text{ mas yr}^{-1},$$

depending on whether the VLA or the VLBA data are used. Using the infrared data in G. Duchêne et al. (2005, in preparation), we can also estimate the relative motion between the infrared source T Tau Sb and T Tau N during a time span (2001 November–2003 December) similar to that covered by the radio observations. We obtain

$$\mu_\alpha \cos\delta = -10.4 \pm 3.5 \text{ mas yr}^{-1},$$
$$\mu_\delta = 12.4 \pm 3.5 \text{ mas yr}^{-1}.$$

The excellent agreement between the infrared and the radio proper motions confirms that the magnetically active PMS star generating the compact radio emission is T Tau Sb and that the radio data (from both VLA and VLBA) can be used to trace its trajectory.

5. CONCLUSIONS AND PERSPECTIVES

The VLBA data presented here have allowed us to make a detailed study of the structure and astrometry of the compact radio source associated with T Tau S. The emission is found to be composed of a compact core most certainly originating from a stellar magnetosphere and a low brightness extension that may result from reconnection flares at the star-disk interface. The accuracy of the absolute astrometry offered by the VLBA has made it possible for us to demonstrate that the infrared, the VLA, and the VLBA observations all trace the same underlying star (T Tau Sb). This implies, in particular, that any orbital fit to the T Tau system must be able to reproduce the positions measured by the VLA in the last 20 years. Finally, the VLBA data have allowed us to measure the distance to T Tau with unprecedented accuracy: $d = 141.5^{+2.8}_{-2.7}$ pc. This is in good agreement with the traditionally accepted value for Taurus ($d = 140 \pm 10$ pc; Kenyon et al. 1994) and seemingly rules out the possibility of large distance gradients across Taurus.

We are indebted to Walter Brisken for providing VLBA pulsar data so that we could check our astrometry results, and we are indebted to Gaspard Duchêne for sending us his infrared positions ahead of publication. L. L., L. F. R., and R. A. G. acknowledge the financial support of DGAPA, UNAM, and CONACyT, México; A. J. M. acknowledges support from the NRAO. The National Radio Astronomy Observatory is a facility of the National Science Foundation operated under cooperative agreement by Associated Universities, Inc.

REFERENCES

Barnard, E. E. 1895, MNRAS, 55, 442
Bertout, C., Robichon, N., & Arenou, F. 1999, A&A, 352, 574
Duchêne, G., Ghez, A. M., & McCabe, C. 2002, ApJ, 568, 771
Dulk, G. A. 1985, ARA&A, 23, 169
Dyck, H. M., Simon, T., & Zuckerman, B. 1982, ApJ, 255, L103
Feigelson, E. D., & Montmerle, T. 1999, ARA&A, 37, 363
Furlan, E., Forrest, W. J., Watson, D. M., Uchida, K. I., Brandl, B. R., Keller, L. D., & Herter, T. L. 2003, ApJ, 596, L87
Ghez, A. M., Neugebauer, G., Gorham, P. W., Haniff, C. A., Kulkarni, S. R., Matthews, K., Koresko, C., & Beckwith, S. 1991, AJ, 102, 2066
Johnston, K. J., Fey, A. L., Gaume, R. A., Claussen, M. J., & Hummel, C. A. 2004a, AJ, 128, 822
Johnston, K. J., Fey, A. L., Gaume, R. A., Hummel, C. A., Garrington, S., Muxlow, T., & Thomasson, P. 2004b, ApJ, 604, L65
Johnston, K. J., Gaume, R. A., Fey, A. L., de Vegt, C., & Claussen, M. J. 2003, AJ, 125, 858
Joy, A. H. 1945, ApJ, 102, 168
Kenyon, S. J., Dobrzycka, D., & Hartmann, L. 1994, AJ, 108, 1872
Köhler, R., Kasper, M., & Herbst, T. M. 2000, in Birth and Evolution of Binary Stars, ed. B. Reipurth & H. Zinnecker (Potsdam: Astrophys. Inst.), 63
Koresko, C. D. 2000, ApJ, 531, L147
Lestrade, J.-F., Preston, R. A., Jones, D. L., Phillips, R. B., Rogers, A. E. E., Titus, M. A., Rioja, M. J., & Gabuzda, D. C. 1999, A&A, 344, 1014
Loinard, L., Rodríguez, L. F., & Rodríguez, M. I. 2003, ApJ, 587, L47
Ostriker, E. C., & Shu, F. H. 1995, ApJ, 447, 813
Perryman, M. A. C., et al. 1997, A&A, 323, L49
Siess, L., Dufour, E., & Forestini, M. 2000, A&A, 358, 593
Skinner, S. L. 1993, ApJ, 408, 660
Smith, K., Pestalozzi, M., Güdel, M., Conway, J., & Benz, A. O. 2003, A&A, 406, 957
Solf, J., & Böhm, K.-H. 1999, ApJ, 523, 709
Schwartz, P. R., Simon, T., & Campbell, R. 1986, ApJ, 303, 233
Tamazian, V. S. 2004, AJ, 127, 2378

B

VLBA Distance to Nearby Star-Forming Regions I. The Distance to T Tauri with 0.4 % Accuracy

Laurent Loinard, Rosa M. Torres, Amy J. Mioduszewski, Luis F. Rodríguez, Rosa A. Gónzalez-López lira, Régis Lachaume, Virgilio Vázquez & Erandy González
The Astrophysical Journal, 671, 546, 2007

Abstract. We present the results of a series of 12 3.6 cm radio continuum observations of T Tau Sb, one of the companions of the famous young stellar object T Tauri. The data were collected roughly every 2 months between 2003 September and 2005 July with the Very Long Baseline Array (VLBA). Thanks to the remarkably accurate astrometry delivered by the VLBA, the absolute position of T Tau Sb could be measured with a precision typically better than about 100 μas at each of the 12 observed epochs. The trajectory of T Tau Sb on the plane of the sky could therefore be traced very precisely and was modeled as the superposition of the trigonometric parallax of the source and an accelerated proper motion. The best fit yields a distance to T Tau Sb of 147.6 ± 0.6 pc. The observed positions of T Tau Sb are in good agreement with recent infrared measurements, but they seem to favor a somewhat longer orbital period than that recently reported by Duchêne and coworkers for the T Tau Sa/T Tau Sb system.

The Astrophysical Journal, 671:546–554, 2007 December 10

VLBA DETERMINATION OF THE DISTANCE TO NEARBY STAR-FORMING REGIONS. I. THE DISTANCE TO T TAURI WITH 0.4% ACCURACY

Laurent Loinard and Rosa M. Torres
Centro de Radiostronomía y Astrofísica, Universidad Nacional Autónoma de México, Apartado Postal 72-3 (Xangari), 58089 Morelia, Michoacán, Mexico; l.loinard@astrosmo.unam.mx

Amy J. Mioduszewski
National Radio Astronomy Observatory, Array Operations Center, 1003 Lopezville Road, Socorro, NM 87801

Luis F. Rodríguez, Rosa A. González-López lira, and Régis Lachaume
Centro de Radiostronomía y Astrofísica, Universidad Nacional Autónoma de México, Apartado Postal 72-3 (Xangari), 58089 Morelia, Michoacán, Mexico

and

Virgilio Vázquez and Erandy González
Universidad Tecnológica de la Mixteca, Carretera Huajuapan-Acatlima, 69000 Huajuapan de León, Oaxaca, Mexico
Received 2007 June 25; accepted 2007 August 7

ABSTRACT

In this article, we present the results of a series of 12 3.6 cm radio continuum observations of T Tau Sb, one of the companions of the famous young stellar object T Tauri. The data were collected roughly every 2 months between 2003 September and 2005 July with the Very Long Baseline Array (VLBA). Thanks to the remarkably accurate astrometry delivered by the VLBA, the absolute position of T Tau Sb could be measured with a precision typically better than about 100 μas at each of the 12 observed epochs. The trajectory of T Tau Sb on the plane of the sky could therefore be traced very precisely and was modeled as the superposition of the trigonometric parallax of the source and an accelerated proper motion. The best fit yields a distance to T Tau Sb of 147.6 ± 0.6 pc. The observed positions of T Tau Sb are in good agreement with recent infrared measurements, but they seem to favor a somewhat longer orbital period than that recently reported by Duchêne and coworkers for the T Tau Sa/T Tau Sb system.

Subject headings: astrometry — binaries: general — magnetic fields — radiation mechanisms: nonthermal — radio continuum: stars — stars: formation

1. INTRODUCTION

To provide accurate observational constraints for pre–main-sequence evolutionary models and thereby improve our understanding of star formation, it is crucial to measure the properties (age, mass, luminosity, etc.) of individual young stars as accurately as possible. The determination of most of these parameters, however, depends critically on the often poorly known distance to the object under consideration. While the average distance to nearby low-mass star-forming regions (e.g., Taurus or Ophiuchus) has been estimated to about 20% precision using indirect methods (Elias 1978a, 1978b; Kenyon et al. 1994; Knude & Høg 1998), the line-of-sight depth of these regions is largely unknown, and accurate distances to individual objects are still missing. Even the highly successful *Hipparcos* mission (Perryman et al. 1997) did little to improve the situation (Bertout et al. 1999), because young stars are still heavily embedded in their parental clouds and are therefore faint in the optical bands observed by *Hipparcos*. Future space missions such as *Gaia* will undoubtedly have the capacity to accurately measure the trigonometric parallax of optically fainter stars, but these missions will still be unable to access very deeply embedded sources, and they will only start to provide results in about a decade. In the meantime, extremely high quality infrared and X-ray surveys of many star-forming regions are being obtained (e.g., Evans et al. 2003; Güdel et al. 2007), and their potential cannot be fully exploited because of the unavailability of good distance estimates.

Low-mass young stars often generate nonthermal continuum emission produced by the interaction of free electrons with the intense magnetic fields that tend to exist near their surfaces (e.g., Feigelson & Montmerle 1999). Since the magnetic field strength decreases quickly with the distance to the stellar surface (as r^{-3} in the magnetic dipole approximation), the emission is strongly concentrated to the inner few stellar radii. If the magnetic field intensity and the electron energy are sufficient, the resulting compact radio emission can be detected with very long baseline interferometry (VLBI; e.g., André et al. 1992). The relatively recent possibility of accurately calibrating the phase of VLBI observations of faint, compact radio sources using nearby quasars makes it possible to measure the absolute position of these objects (or, more precisely, the angular offset between them and the calibrating quasar) to better than a tenth of a milliarcsecond (Loinard et al. 2005; see also below). This level of precision is sufficient to constrain the trigonometric parallax of sources within a few hundred parsecs of the Sun (in particular, of nearby young stars) with a precision of better than a few percent using multiepoch VLBI observations.

Taking advantage of this situation, we have recently initiated a large project aimed at accurately measuring the trigonometric parallax of a significant sample of magnetically active young stars in nearby star-forming regions (Taurus, Ophiuchus, Perseus, Serpens, and Cepheus) using the 10 element Very Long Baseline Array (VLBA) of the National Radio Astronomy Observatory (NRAO). In the present article, we concentrate on T Tau Sb, one of the members of the famous young stellar system T Tauri (see, e.g., Duchêne et al. [2006] for a recent summary of the properties of that system). T Tau Sb has long been known to be associated with a compact nonthermal radio source (Skinner & Brown

TABLE 1
SOURCE POSITION AND FLUX

Mean UT Date (yyyy.mm.dd hh:mm) (1)	α (J2000.0) (2)	σ_α (s) (3)	δ (J2000.0) (4)	σ_δ (arcsec) (5)	F_ν (mJy) (6)	σ (μJy) (7)
2003.09.24 11:33	04 21 59.4252942	0.0000013	19 32 05.717618	0.000043	1.62	74
2003.11.18 08:02	04 21 59.4249805	0.0000015	19 32 05.716554	0.000043	1.74	66
2004.01.15 04:09	04 21 59.4245823	0.0000036	19 32 05.715322	0.000108	0.92	72
2004.03.26 23:26	04 21 59.4245420	0.0000017	19 32 05.715333	0.000050	1.27	70
2004.05.13 20:17	04 21 59.4248818	0.0000016	19 32 05.716034	0.000055	1.90	111
2004.07.08 16:37	04 21 59.4253464	0.0000020	19 32 05.716652	0.000058	1.25	64
2004.09.16 11:59	04 21 59.4255476	0.0000015	19 32 05.716602	0.000042	1.61	70
2004.11.09 08:27	04 21 59.4252999	0.0000015	19 32 05.715631	0.000039	3.36	104
2004.12.28 05:14	04 21 59.4249488	0.0000015	19 32 05.714344	0.000050	1.26	70
2005.02.24 01:26	04 21 59.4247667	0.0000016	19 32 05.713826	0.000042	2.30	80
2005.05.09 20:32	04 21 59.4251475	0.0000060	19 32 05.714852	0.000182	1.12	106
2005.07.08 16:36	04 21 59.4256679	0.0000019	19 32 05.715598	0.000060	1.41	75

NOTE.—Units of right ascension are hours, minutes, and seconds, and units of declination are degrees, arcminutes, and arcseconds.

1994; Phillips et al. 1993; Johnston et al. 2003) characterized by strong variability and significant circular polarization. An extended thermal radio halo studied in detail by Loinard et al. (2007) and probably related to stellar winds also exists around T Tau Sb. While this extended structure contributes to the total radio flux as measured, for instance, with the VLA, it is effectively filtered out in VLBI experiments. Indeed, in the intercontinental VLBI observations published by Smith et al. (2003), only about 40% of the simultaneously measured VLA flux density is retrieved. The radio source detected by Smith et al. (2003) is very compact ($R < 15\ R_\odot$), and its flux was about 3 mJy at the time of their observations. Its trajectory over the plane of the sky was studied by Loinard et al. (2005) using a series of seven VLBA observations. Unfortunately, these data were recently found to have been affected by a bug that caused the VLBA correlator to use the predicted rather than measured Earth Orientation Parameters (EOPs).[1] This problem corrupted the visibility phases and strongly affected the quality of the astrometry of the data published in Loinard et al. (2005). The postfit rms for the Loinard et al. (2005) data was about 250 mas, compared with 60–90 mas for the present data (see below). Here we reanalyze these VLBA data and combine them with five newer observations to measure the trigonometric parallax and study the proper motion of T Tau Sb.

2. OBSERVATIONS AND DATA CALIBRATION

In this paper, we make use of a series of 12 continuum 3.6 cm (8.42 GHz) observations of T Tau Sb obtained every 2 months between 2003 September and 2005 July with the VLBA (Table 1). Our phase center was at $\alpha_{J2000.0} = 04^h21^m59.4263^s$, $\delta_{J2000.0} = +19^\circ32'05.730''$, which is the position of the compact source detected by Smith et al. (2003). Each observation consisted of a series of cycles with 2 minutes spent on-source and 1 minute spent on the main phase-referencing quasar J0428+1732, located 2.6° away. J0428+1732 is a very compact extragalactic source whose absolute position ($\alpha_{J2000.0} = 04^h28^m35.633679^s$, $\delta_{J2000.0} = 17^\circ32'23.58799''$) is known to better than 1 mas ($\sigma_\alpha = 0.59$ mas, $\sigma_\delta = 0.89$ mas; Beasley et al. 2002). During the first six observations, the secondary quasar J0431+1731 was also observed periodically, about every 30 minutes, both to check the astrometric quality of the data and to enable us to compare our results with those of Smith et al. (2003), who used J0431+1731 as their phase calibrator. A detailed comparison with the results of Smith et al. (2003) and with the numerous VLA observations available from the literature, however, will be postponed to a forthcoming article.

The data were edited and calibrated using the Astronomical Image Processing System (AIPS; Greisen 2003). The basic data reduction followed the standard VLBA procedures for phase-referenced observations. First, the most accurate measured EOPs obtained from the US Naval Observatory database were applied to the data in order to correct the erroneous values initially used by the VLBA correlator. Second, we accounted for dispersive delays caused by free electrons in the Earth's atmosphere, using an estimate of the electron content of the ionosphere derived from Global Positioning System (GPS) measurements. An a priori amplitude calibration based on the measured system temperatures and standard gain curves was then applied. The fourth step was to correct the phases for antenna parallactic angle effects, and the fifth was to remove residual instrumental delays caused by the VLBA electronics. This was done by measuring the delays and phase residuals for each antenna and IF, using the fringes obtained on a strong calibrator. The final step of this initial calibration was to remove global frequency- and time-dependent phase errors by using a global fringe-fitting procedure on the main phase calibrator (J0428+1732), which was assumed at this stage to be a point source.

In this initial calibration, the solutions from the global fringe fit were only applied to the main phase calibrator itself. The corresponding calibrated visibilities were then imaged, and several passes of self-calibration were performed to improve the overall amplitude and phase calibration. In the image obtained after the self-calibration iterations, the main phase calibrator was found to be slightly extended. To take this into account, the final global fringe-fitting part of the reduction was repeated, this time using the image of the main phase calibrator as a model instead of assuming it to be a point source. Note that a different phase calibrator model was produced for each epoch in order to account for possible small changes in the main calibrator structure from epoch to epoch. The solutions obtained after repeating this final step were edited for bad points and applied to the target source. Using an image model for the calibrator rather than assuming a point source improved the position accuracy by a few tens of microseconds.

Because of the significant overheads that were necessary to properly calibrate the data, only about 3 of the 6 hr of telescope time allocated to each of our observations were actually spent on-source. Once calibrated, the visibilities were imaged with a

[1] See http://www.vlba.nrao.edu/astro/messages/eop/.

TABLE 2
Julian Dates and Earth Coordinates

Mean UT Date (yyyy.mm.dd hh.mm)	Julian Date	Earth Barycentric Coordinates (AU)		
		X	*Y*	*Z*
2003.09.24 11:33	2,452,906.981522	+1.006064570	+0.012414145	+0.005329883
2003.11.18 08:02	2,452,961.834705	+0.563031813	+0.744728145	+0.322808936
2004.01.15 04:09	2,453,019.672980	−0.401044530	+0.820090543	+0.355473794
2004.03.26 23:26	2,453,091.476395	−0.987542097	−0.107099184	−0.046513144
2004.05.13 20:17	2,453,139.345324	−0.599629779	−0.745571223	−0.323319720
2004.07.08 16:37	2,453,195.192419	+0.297481514	−0.894474582	−0.387883413
2004.09.16 11:59	2,453,264.999583	+1.003677539	−0.099008512	−0.043027999
2004.11.09 08:27	2,453,318.852141	+0.676914299	+0.666368259	+0.288787192
2004.12.28 05:14	2,453,367.718351	−0.111308860	+0.895710071	+0.388210192
2005.02.24 01:26	2,453,425.559664	−0.896015668	+0.377089952	+0.163364585
2005.05.09 20:32	2,453,500.355214	−0.655044089	−0.701050689	−0.304055855
2005.07.08 16:36	2,453,560.191348	+0.293538593	−0.893249243	−0.387385193

pixel size of 50 μas after weights intermediate between natural and uniform (ROBUST = 0 in AIPS) were applied. This resulted in a typical rms noise level of 70 μJy for most observations, although for a few epochs with less favorable weather conditions, the noise level exceeded 100 μJy (Table 1). T Tau Sb was detected with a signal-to-noise ratio of better than 10 at each epoch (Table 1), and its absolute position (listed in cols. [2] and [4] of Table 1) was determined using a two-dimensional Gaussian fitting procedure (task JMFIT in AIPS). This task provides an estimate of the position error (cols. [3] and [5] of Table 1) based on the expected theoretical astrometric precision of an interferometer (Condon 1997). Systematic errors, however, usually limit the actual precision of VLBI astrometry to several times this theoretical value (e.g., Fomalont 1999; Pradel et al. 2006). At the frequency of the present observations, the main sources of systematic errors are inaccuracies in the troposphere model used, as well as clock, antenna, and a priori source position errors. These effects combine to produce a systematic phase difference between the calibrator and the target that limits the precision with which the target position can be determined. We did not attempt to correct for these systematic effects here and will therefore assume that the true error on each measurement is the quadratic sum of the random error listed in Table 1 and a systematic contribution. The latter is difficult to estimate a priori and will be deduced from the fits to the data.

3. ASTROMETRY FITS

The displacement of T Tau Sb on the celestial sphere is the combination of its trigonometric parallax (π) and its proper motion. For isolated sources, it is common to consider linear and uniform proper motions, so the right ascension (α) and the declination (δ) vary as a function of time t as

$$\alpha(t) = \alpha_0 + (\mu_\alpha \cos\delta)t + \pi f_\alpha(t), \quad (1)$$

$$\delta(t) = \delta_0 + \mu_\delta t + \pi f_\delta(t), \quad (2)$$

where α_0 and δ_0 are the coordinates of the source at a given reference epoch, μ_α and μ_δ are the components of the proper motion, and f_α and f_δ are the projections over α and δ, respectively, of the parallactic ellipse. The latter functions are given by (e.g., Seidelman & Fukushima 1992)

$$f_\alpha(t) = (X \sin\alpha_1 - Y \cos\alpha_1)/15 \cos\delta_1, \quad (3)$$

$$f_\delta(t) = X \cos\alpha_1 \sin\delta_1 + Y \sin\alpha_1 \sin\delta_1 - Z \cos\delta_1, \quad (4)$$

where (X, Y, Z) are the barycentric coordinates of the Earth in units of AU, and where $\alpha_1 = \alpha - \pi f_\alpha(t)$ and $\delta_1 = \delta - \pi f_\delta(t)$ are the coordinates of the barycentric place of the source at each epoch. Note that f_α and f_δ depend implicitly on time (through X, Y, and Z) and explicitly on the coordinates of the source. The latter dependence on α_1 and δ_1 (which are only known if the trigonometric parallax is known) implies that the fitting procedure must be iterative. The barycentric coordinates of the Earth (as well as the Julian date of each observation) were calculated using the Multiyear Interactive Computer Almanac (MICA), which was distributed as a CD-ROM by the US Naval Observatory. They are given explicitly in Table 2 for all epochs.

As mentioned earlier, T Tau Sb is a member of a multiple system (e.g., Loinard et al. 2003; Duchêne et al. 2006 and references therein), so its proper motion is likely to be affected by the gravitational influence of the other members of the system. As a consequence, the motion is likely to be curved and accelerated rather than linear and uniform. To take this into account, we have also made fits to the data that include acceleration terms. This leads to functions of the form

$$\alpha(t) = \alpha_0 + (\mu_{\alpha 0} \cos\delta)t + \frac{1}{2}(a_\alpha \cos\delta)t^2 + \pi f_\alpha(t), \quad (5)$$

$$\delta(t) = \delta_0 + \mu_{\delta 0} t + \frac{1}{2} a_\delta t^2 + \pi f_\delta(t), \quad (6)$$

where $\mu_{\alpha 0}$ and $\mu_{\delta 0}$ are the proper motions at a reference epoch and a_α and a_δ are the projections of the uniform acceleration. Note that the acceleration undergone by a body in Keplerian orbit is usually not uniform. Assuming a uniform acceleration is acceptable here, however, because our data cover only a small portion ($\sim$2 yr) of the orbital period (a few decades; Duchêne et al. 2006) of T Tau Sb. If VLBA data are obtained regularly in the next few decades, a full orbital fit will become possible, and indeed necessary.

The astrometric parameters were determined by least-squares–fitting the data points with either equations (1) and (2) or equations (5) and (6), using a singular value decomposition (SVD) scheme (see the Appendix for details). To check our results, we also performed two other fits to the data: a linear one based on the associated normal equations, and a nonlinear one based on the Levenberg-Marquardt algorithm. They gave results identical to those

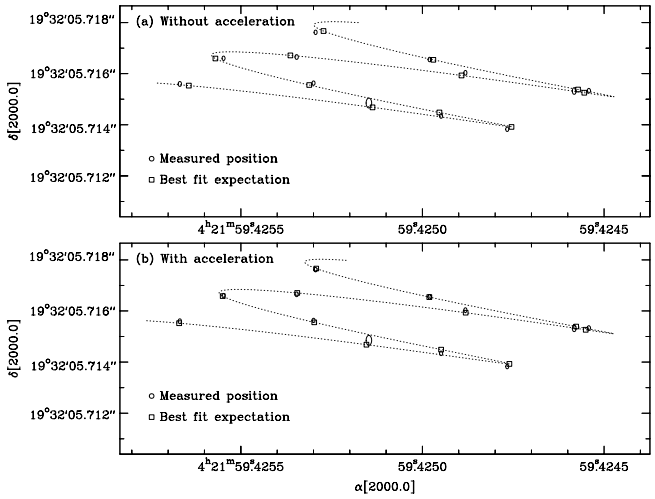

FIG. 1.—Measured positions of T Tau Sb and best fits, both (*a*) without and (*b*) with acceleration terms. The observed positions are shown as ellipses, the size of which represents the magnitude of the errors. Note the very significant improvement when acceleration terms are included.

obtained using the SVD method. The reference epoch was taken at the mean of our observations (JD 2453233.586 ≡ J2004.627).

4. RESULTS

The fit to the data points by equations (1) and (2) (Fig. 1*a*) yields the following astrometric parameters:

$$\alpha_{\mathrm{J2004.627}} = 04^{\mathrm{h}}21^{\mathrm{m}}59.425081^{\mathrm{s}} \pm 0.000005^{\mathrm{s}},$$
$$\delta_{\mathrm{J2004.627}} = 19^{\circ}32'05.71566'' \pm 0.00003'',$$
$$\mu_{\alpha} \cos\delta = 4.00 \pm 0.12 \text{ mas yr}^{-1},$$
$$\mu_{\delta} = -1.18 \pm 0.05 \text{ mas yr}^{-1},$$
$$\pi = 6.90 \pm 0.09 \text{ mas}.$$

This corresponds to a distance of 145 ± 2 pc. The postfit rms, however, is not very good (particularly in right ascension: ~0.2 mas), as the fit does not pass through many of the observed positions (Fig. 1*a*). As a matter of fact, 75 μas and, most notably, 16.5 μs of time had to be added quadratically to the formal errors listed in Table 1 to obtain a reduced χ^2 of 1 in both right ascension and declination; the errors on the fitted parameters quoted above include this systematic contribution. These large systematic errors most certainly reflect the fact mentioned earlier that the proper motion of T Tau Sb is not uniform because it belongs to a multiple system. Indeed, the fit in which acceleration terms are included is significantly better (Fig. 1*b*), with a postfit rms of 60 μas in right ascension and 90 μas in declination. It yields the following parameters:

$$\alpha_{\mathrm{J2004.627}} = 04^{\mathrm{h}}21^{\mathrm{m}}59.425065^{\mathrm{s}} \pm 0.000002^{\mathrm{s}},$$
$$\delta_{\mathrm{J2004.627}} = 19^{\circ}32'05.71566'' \pm 0.0004'',$$
$$\mu_{\alpha,\,\mathrm{J2004.627}} \cos\delta = 4.02 \pm 0.03 \text{ mas yr}^{-1},$$
$$\mu_{\delta,\,\mathrm{J2004.627}} = -1.18 \pm 0.05 \text{ mas yr}^{-1},$$
$$a_{\alpha} \cos\delta = 1.53 \pm 0.13 \text{ mas yr}^{-2},$$
$$a_{\delta} = 0.00 \pm 0.19 \text{ mas yr}^{-2},$$
$$\pi = 6.82 \pm 0.03 \text{ mas}.$$

To obtain a reduced χ^2 of 1 in both right ascension and declination, one must add quadratically 3.8 μs of time and 75 μas to the statistical errors listed in Table 1. The uncertainties reported above and in the rest of this article include this systematic contribution. Note also that the reduced χ^2 for the fit without acceleration terms is almost 8 if the latter systematic errors (rather than those mentioned earlier) are used.

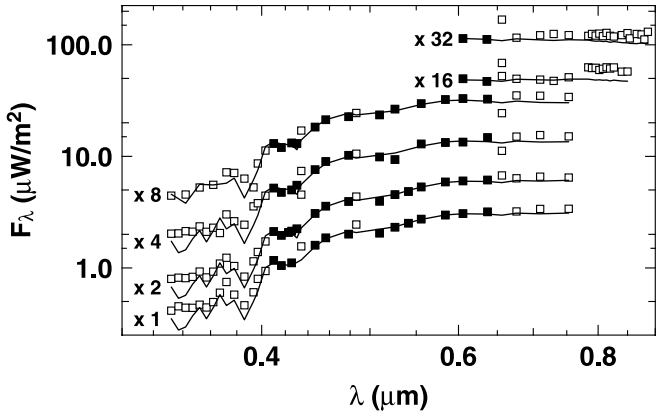

FIG. 2.—Fit to the photometry at six different epochs. Filled squares indicate points that have been fitted; open squares represent other wavelengths that were excluded from the fit.

The trigonometric parallax obtained when acceleration terms are included corresponds to a distance of 146.7 ± 0.6 pc, which is somewhat larger than, but consistent within 1.5 σ of, the value reported by Loinard et al. (2005). Recall, however, that this 2005 result was based on data that had been corrupted by a problem in the VLBA correlator; we consider the present value to be significantly more reliable. The present distance determination is somewhat smaller than, but within 1 σ of, the distance obtained by *Hipparcos* ($d = 177^{+68}_{-39}$ pc). Note that the relative error of our distance is about 0.4%, against nearly 30% for the *Hipparcos* result, a gain of almost 2 orders of magnitude.

5. IMPLICATIONS FOR THE PROPERTIES OF THE STARS

Having obtained an improved distance estimate to the T Tauri system, we are now in a position to refine the determination of the intrinsic properties of each of the components of that system. Since the orbital motion between T Tau N and T Tau S is not yet known to very good precision, we will use synthetic spectra fitting to obtain the properties of T Tau N. For the very obscured T Tau S companion, on the other hand, we will refine the mass determinations on the basis of the orbital fit obtained by Duchêne et al. (2006).

5.1. *T Tau N*

The stellar parameters (T_{eff} and L_{bol}) of T Tau N were obtained by fitting synthetic spectra (Lejeune et al. 1997) to the optical part of the spectral energy distribution. In the absence of recently published optical spectra with absolute flux calibration, we decided to use narrowband photometry taken at six different epochs from 1965 to 1970 (Kuhi 1974). In order to eliminate the contamination by the UV/blue (magnetospheric accretion) and red/IR (circumstellar disk) excesses, we restricted the fit to the range 0.41–0.65 μm. Two points at 0.4340 and 0.4861 μm display large variations between epochs, and these were also discarded, as they are likely to be contaminated by emission lines. As a consequence, 56 photometric measurements at 13 wavelengths and six epochs had to be fitted (see Fig. 2). We assumed that the star had constant intrinsic parameters over the 5 yr of observation, but we allowed the circumstellar extinction to vary.

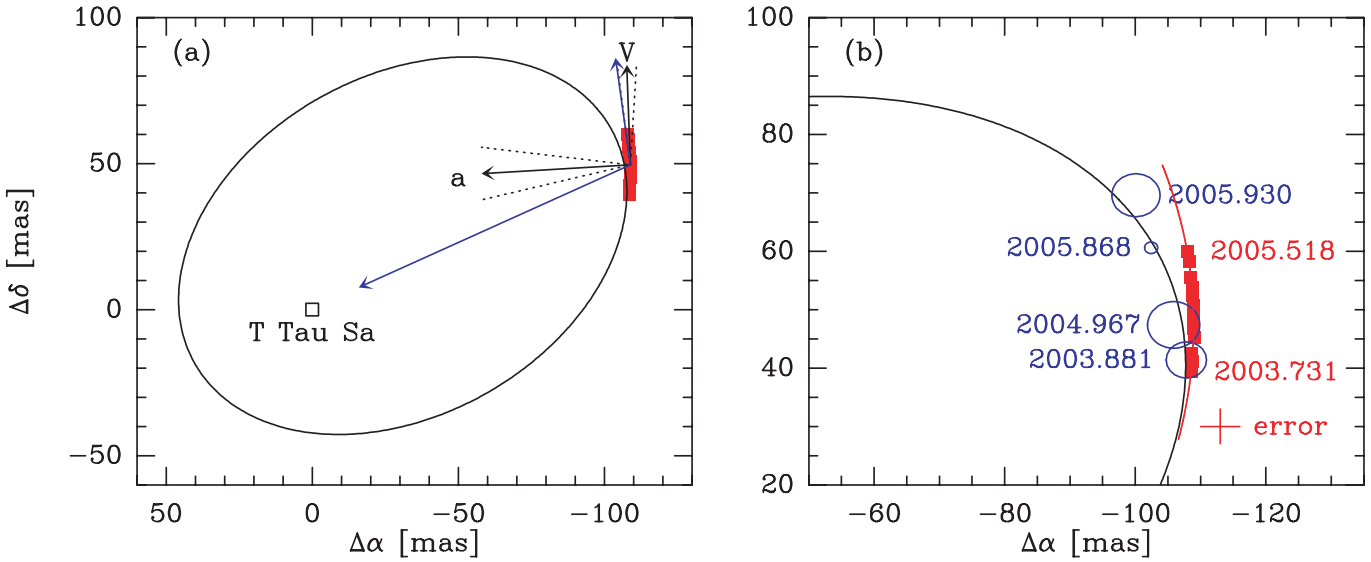

FIG. 3.—(*a*) VLBA positions (*red squares*) registered to T Tau Sa, superimposed on the elliptical fit proposed by Duchêne et al. (2006). Also shown are the velocity and acceleration vectors for our mean epoch that we deduced from our observations, as well as their counterparts from the fit by Duchêne et al. (2006; *blue arrows*). The dotted black lines around the measured acceleration and velocity show the error cones on the direction of each of these vectors. (*b*) Zoom on the region corresponding to our observations. In addition to the orbit and the VLBA positions, we show our best parabolic fit to our positions (*red curve*), as well as several recent infrared positions (*blue ellipses*). The 2003.881 position is from Duchêne et al. (2005), the 2004.967 and 2005.868 positions are from Duchêne et al. (2006), and the 2005.930 position is from Schaefer et al. (2006).

Such an hypothesis is supported by long-term photometric observations (1986–2003) that show color-magnitude diagrams of T Tau elongated along the extinction direction (Mel'nikov & Grankin 2005); Kuhi (1974) also measured significant extinction variation in the period 1965–1970, using color excesses.

The nonlinear fitting procedure used the Levenberg-Marquardt method, and the determination of errors was done using a Monte Carlo simulation. The synthetic spectra were transformed into narrowband photometry by integration over the bandwidth of the measurements (typically 0.05 μm). As the fitting procedure could not constrain the metallicity, we assumed a solar one. Several fits using randomly chosen initial guesses for $T_{\rm eff}$, $L_{\rm bol}$, and extinctions were performed in order to ensure that a global minimum χ^2 was indeed reached. The errors reported by Kuhi (1974; 1.2%) had to be renormalized to 5.9% in order to achieve a reduced χ^2 of 1. This could result from an underestimation by the author or from positive and negative contamination by spectral lines; indeed, Gahm (1970) reports contamination as high as 20% for RW Aur. The best least-squares fit is represented in Figure 3, and it yields $T_{\rm eff} = 5112^{+99}_{-97}$ K and $L_{\rm bol} = 5.11^{+0.76}_{-0.66}\ L_{\odot}$. The extinction varies between 1.02 and 1.34, within 1 σ of the values determined by Kuhi (1974) from color excesses. The effective temperature is consistent with a K1 star, as reported by Kuhi (1974).

In order to derive the age and mass of T Tau N, pre–main-sequence isochrones by D'Antona & Mazzitelli (1996) and Siess et al. (2000) were used. The fitting procedure was identical to the previous one: the age and mass were converted into effective temperature and luminosity, which in turn were converted into narrowband photometry using the synthetic spectra. The derived parameters are shown in Table 3. The masses ($1.83^{+0.20}_{-0.16}$ and $2.14^{+0.11}_{-0.10}\ M_{\odot}$) have overlapping error bars and are consistent with values found in the literature (e.g., Duchêne et al. 2006). The predicted ages, on the other hand, differ by a factor of 2. While the isochrones by D'Antona & Mazzitelli (1996) give an age in the commonly accepted range ($1.15^{+0.18}_{-0.16}$ Myr), a somewhat larger value ($2.39^{+0.31}_{-0.27}$) is derived from those of Siess et al. (2000). Note that the errors on the derived parameters are entirely dominated by the modeling errors; the uncertainty on the distance now represents a very small fraction of the error budget.

5.2. *T Tau S*

The two members of the T Tau S system have been studied in detail by Duchêne and coworkers in a series of recent articles (Duchêne et al. 2002, 2005, 2006). The most massive member of the system (T Tau Sa) belongs to the mysterious class of "infrared companions" and is presumably the precursor of an intermediate-mass star. T Tau Sb, on the other hand, is a very obscured but otherwise normal pre–main-sequence M1 star. The masses of both T Tau Sa and T Tau Sb were estimated by Duchêne et al. (2006), using a fit to their orbital paths. Those authors used the distance to T Tauri that was deduced by Loinard et al. (2005). Using the new distance determination obtained here, we can renormalize those masses. We obtain $M_{\rm Sa} = 3.10 \pm 0.34\ M_{\odot}$ and $M_{\rm Sb} = 0.69 \pm 0.18\ M_{\odot}$. These values may need to

TABLE 3
PARAMETERS OF T TAURI N

Parameter	Value
Age (Myr)	$2.39^{+0.31}_{-0.27}$ (Siess et al. 2000)
	$1.15^{+0.18}_{-0.16}$ (D'Antona & Mazzitelli 1996)
Mass ($M_{\odot}$)	$2.14^{+0.11}_{-0.10}$ (Siess et al. 2000)
	$1.83^{+0.20}_{-0.16}$ (D'Antona & Mazzitelli 1996)
$T_{\rm eff}$ (K)	5112^{+99}_{-97}
$L_{\rm bol}$ ($L_{\odot}$)	$5.11^{+0.76}_{-0.66}$
$R_{\star}$ ($R_{\odot}$)	$2.89^{+0.24}_{-0.21}$
A_V, MJD 39095.2	1.34 ± 0.17
A_V, MJD 39153.2	1.37 ± 0.17
A_V, MJD 39476.3	1.20 ± 0.17
A_V, MJD 40869.4	1.02 ± 0.17
A_V, MJD 39485.1	1.36 ± 0.19
A_V, MJD 39524.1	1.16 ± 0.19

be adjusted somewhat, however, as the fit to the orbital path of the T Tau Sa/T Tau Sb system is improved (see below). Note, finally, that the main sources of errors on the masses are related to the orbital motion modeling rather than to the uncertainties of the distance.

6. IMPLICATIONS FOR THE ORBITAL MOTIONS

T Tau Sb is a member of a multiple system, so it would be desirable to give its position and express its motion relative to the other members of the system: T Tau N and, particularly, T Tau Sa. Since only T Tau Sb is detected in our VLBA observations, however, registering the positions reported here to the other members of the system involves a number of steps. The absolute position and proper motion of T Tau N has been measured to great precision using over 20 years of VLA observations (Loinard et al. 2003), so registering the position and motion of T Tau Sb relative to T Tau N is fairly straightforward. Combining the data used by Loinard et al. (2003) with several more recent VLA observations, we obtained the following absolute position (at epoch J2000.0) and proper motion for T Tau N:

$$\alpha_{\rm J2000.0} = 04^{\rm h}21^{\rm m}59.4321^{\rm s} \pm 0.0001^{\rm s},$$
$$\delta_{\rm J2000.0} = 19^{\circ}32'06.419'' \pm 0.002'',$$
$$\mu_\alpha \cos\delta = 12.35 \pm 0.04 \text{ mas yr}^{-1},$$
$$\mu_\delta = -12.80 \pm 0.06 \text{ mas yr}^{-1}.$$

Subtracting these values from the absolute positions and proper motion of T Tau Sb, we can obtain the positional offset between T Tau Sb and T Tau N, as well as their relative proper motion. For the median epoch of our observations, we obtain

$$(\mu_\alpha \cos\delta)({\rm Sb/N}) = -8.33 \pm 0.07 \text{ mas yr}^{-1},$$
$$\mu_\delta({\rm Sb/N}) = +11.62 \pm 0.11 \text{ mas yr}^{-1}.$$

The second step consists of registering the position and motion of T Tau Sb to the center of mass of T Tau S, using the parabolic fits provided by Duchêne et al. (2006). Here both the proper motion and the acceleration must be taken into account. For the mean epoch of our observations, we obtain

$$(\mu_\alpha \cos\delta)({\rm Sb/CM}) = +0.3 \pm 0.9 \text{ mas yr}^{-1},$$
$$\mu_\delta({\rm Sb/CM}) = +9.3 \pm 0.8 \text{ mas yr}^{-1},$$
$$(a_\alpha \cos\delta)({\rm Sb/CM}) = +1.4 \pm 0.2 \text{ mas yr}^{-2},$$
$$a_\delta({\rm Sb/CM}) = -0.1 \pm 0.3 \text{ mas yr}^{-2}.$$

The last correction to be made is the registration of the positions, proper motions, and accelerations to T Tau Sa, rather than to the center of mass of T Tau S. This is obtained by simply multiplying the values above by the ratio of the total mass of T Tau S (i.e., $M_{\rm Sa} + M_{\rm Sb}$) to the mass of T Tau Sa. Using the masses given by Duchêne et al. 2006), we obtain

$$(\mu_\alpha \cos\delta)({\rm Sb/Sa}) = +0.4 \pm 1.1 \text{ mas yr}^{-1},$$
$$\mu_\delta({\rm Sb/Sa}) = +11.4 \pm 1.0 \text{ mas yr}^{-1},$$
$$(a_\alpha \cos\delta)({\rm Sb/Sa}) = +1.7 \pm 0.2 \text{ mas yr}^{-2},$$
$$a_\delta({\rm Sb/Sa}) = -0.1 \pm 0.3 \text{ mas yr}^{-2}.$$

These two vectors are shown in Figure 3, together with the VLBA positions registered to T Tau Sa, several recent infrared observations, and the elliptical fit obtained by Duchêne et al. (2006). The final error on the VLBA positions is the combination of the original uncertainty on their measured absolute position and of the errors made at each of the steps described above. The final uncertainty is about 3 mas in both right ascension and declination and is shown near the bottom right corner of Figure 3*b*.

Given the uncertainties, the position of the VLBA source is generally in good agreement with the infrared source position measured at similar epochs. Indeed, the first two VLBA observations were obtained at almost exactly the same time as the infrared image published by Duchêne et al. (2005), and these positions match exactly. The position of the VLBA source at the end of 2004 is also in agreement within 1 σ with the position of the infrared source at the same epoch reported by Duchêne et al. (2006). The situation at the end of 2005, however, is somewhat less clear. Extrapolating from the last VLBA observation ($\sim$2005.5) to the end of 2005 gives a location that would be in reasonable agreement with the position given by Schaefer et al. (2006), but clearly not in agreement with the position obtained by Duchêne et al. (2006). Note, indeed, that the two infrared positions are only very marginally consistent with one another.

Our VLBA observations suggest that T Tau Sb passed the westernmost point of its orbit at around 2005.0, whereas according to the fit proposed by Duchêne et al. (2006), this westernmost position was reached slightly before 2004.0. As a consequence, the trajectory described by the VLBA source is on average almost exactly north-south, whereas according to the fit proposed by Duchêne et al. (2006), T Tau Sb is already moving back toward the east (Fig. 3). We note, however, that the fit proposed by Duchêne et al. (2006; which gives an orbital period of 21.7$\pm$ 0.9 yr) is very strongly constrained by their 2005.9 observation. Schaefer et al. (2006), who measured a position at the end of 2005 that was somewhat further to the north (in better agreement with our VLBA positions), argue that they cannot discriminate between orbital periods of 20, 30, or 40 yr. Orbits with longer periods bend back toward the east somewhat later (see Fig. 10 in Schaefer et al. 2006) and would be in better agreement with our VLBA positions.

Another element that favors a somewhat longer orbital period is the acceleration measured here. According to the fit proposed by Duchêne et al. (2006), the expected transverse proper motion and acceleration are (G. Duchêne 2007, private communication)

$$(\mu_\alpha \cos\delta)({\rm Sb/Sa}) = +1.7 \pm 0.2 \text{ mas yr}^{-1},$$
$$\mu_\delta({\rm Sb/Sa}) = +12.1 \pm 1.2 \text{ mas yr}^{-1},$$
$$(a_\alpha \cos\delta)({\rm Sb/Sa}) = +3.1 \pm 0.5 \text{ mas yr}^{-2},$$
$$a_\delta({\rm Sb/Sa}) = -1.4 \pm 0.2 \text{ mas yr}^{-2}.$$

Thus, while the expected and observed proper motions are in good agreement, the expected acceleration is significantly larger than the observed value (see also Fig. 3). A smaller value of the acceleration would be consistent with a somewhat longer orbital period.

In summary, our observations appear to be in reasonable agreement with all the published infrared positions obtained over the last few years, except for the 2005.9 observation reported by Duchêne et al. (2006). As a consequence, our data favor an orbital period somewhat longer than that obtained by Duchêne et al. (2006). Exactly how much longer is difficult to assess for the following reason. The orbit proposed by Duchêne et al. (2006) was obtained by fitting the observed positions *simultaneously* with a superposition of an elliptical path (of T Tau Sb around

T Tau Sa) and a parabolic trajectory (of T Tau Sa around T Tau N). As a consequence, a modification of the T Tau Sa/T Tau Sb elliptical orbit (as may be required by our data) will result in a change in the parameters of the parabolic fit. But we use the latter to register our VLBA positions, proper motions, and accelerations against T Tau Sa. Thus, an entirely new fit will be needed in order to take into account the present VLBA observations. Such a fit will be presented in a forthcoming paper, in which the numerous VLA observations available from the literature, as well as the VLBI observation from Smith et al. (2003), will also be taken into account.

7. CONCLUSIONS AND PERSPECTIVES

Using a series of 12 radio-continuum VLBA observations of T Tau Sb that were obtained roughly every 2 months between 2003 September and 2005 July, we have measured the trigonometric parallax and characterized the proper motion of this member of the T Tauri multiple system with unprecedented accuracy. The distance to T Tau Sb was found to be 146.7 ± 0.6 pc, which is somewhat larger than the canonical value of 140 pc that has been traditionally used. Using this precise estimate, we have recalculated the basic parameters of all three members of the system. The VLBA positions are in good agreement with recent infrared positions, but our data seem to favor a somewhat longer orbital period than that recently reported by Duchêne et al. (2006) for the T Tau Sa/T Tau Sb system. Finally, it should be pointed out that if observations similar to those presented here were obtained regularly in the coming 5–10 years, they would greatly help to constrain the orbital path (and, therefore, the mass) of the T Tau Sa/T Tau Sb system.

L. L., R. M. T., L. F. R., and R. A. G. acknowledge the financial support of DGAPA, UNAM, and CONACyT, México. The NRAO is a facility of the National Science Foundation operated under cooperative agreement by Associated Universities, Inc. We are indebted to Gaspard Duchêne for calculating the expected velocity and acceleration from his fit, and for his comments on the manuscript. We also thank the anonymous referee for his/her constructive comments on this paper.

APPENDIX

FITTING PROCEDURES

The parameters determined in this article (position at a reference epoch, trigonometric parallax, proper motions, and accelerations) were obtained by minimizing the sum ($\chi^2_\alpha + \chi^2_\delta$) of the residuals in right ascension and declination. The corresponding general mathematical problem is that when two functions x and y depend linearly on N independent parameters (a_i and b_i for x and y, respectively) and M common parameters c_i,

$$x(t) = \sum_{i=1}^{N} a_i u_i(t) + \sum_{j=1}^{M} c_j w_j^x(t),$$
$$y(t) = \sum_{i=1}^{N} b_i v_i(t) + \sum_{j=1}^{M} c_j w_j^y(t).$$

The values x_k and y_k of the functions x and y have been measured at P epochs, t_k, with errors σ_k^x and σ_k^y, respectively, and the total χ^2 can be written as

$$\chi^2 = \chi_x^2 + \chi_y^2 = \sum_{k=1}^{P} \left(\left\{ \frac{x_k - \left[\sum_{i=1}^{N} a_i u_i(t_k) + \sum_{j=1}^{M} c_j w_j^x(t_k) \right]}{\sigma_k^x} \right\}^2 + \left\{ \frac{y_k - \left[\sum_{i=1}^{N} b_i v_i(t_k) + \sum_{j=1}^{M} c_j w_j^y(t_k) \right]}{\sigma_k^y} \right\}^2 \right). \quad \text{(A1)}$$

Defining the following matrix elements,

$$\alpha_{ki} = \frac{u_i(t_k)}{\sigma_k^x}, \qquad \beta_{ki} = \frac{v_i(t_k)}{\sigma_k^y},$$
$$\gamma_{kj} = \frac{w_j^x(t_k)}{\sigma_k^x}, \qquad \delta_{kj} = \frac{w_j^y(t_k)}{\sigma_k^y},$$
$$\theta_k = \frac{x_k}{\sigma_k^x}, \qquad \psi_k = \frac{y_k}{\sigma_k^y},$$

we can rewrite the total χ^2 given by equation (A1) as

$$\chi^2 = \sum_{k=1}^{P} \left[\left(\theta_k - \sum_{i=1}^{N} \alpha_{ki} a_i - \sum_{j=1}^{M} \gamma_{kj} c_j \right)^2 + \left(\psi_k - \sum_{i=1}^{N} \beta_{ki} b_i - \sum_{j=1}^{M} \delta_{kj} c_j \right)^2 \right].$$

This sum of quadratic terms can clearly be seen as the squared norm of the vector

$$\begin{pmatrix} \theta_1 - \sum_{i=1}^{N} \alpha_{1i} a_i - \sum_{j=1}^{M} \gamma_{1j} c_j \\ \theta_2 - \sum_{i=1}^{N} \alpha_{2i} a_i - \sum_{j=1}^{M} \gamma_{2j} c_j \\ \cdots \\ \theta_P - \sum_{i=1}^{N} \alpha_{Pi} a_i - \sum_{j=1}^{M} \gamma_{Pj} c_j \\ \psi_1 - \sum_{i=1}^{N} \beta_{1i} b_i - \sum_{j=1}^{M} \delta_{1j} c_j \\ \psi_2 - \sum_{i=1}^{N} \beta_{2i} b_i - \sum_{j=1}^{M} \delta_{2j} c_j \\ \cdots \\ \psi_P - \sum_{i=1}^{N} \beta_{Pi} b_i - \sum_{j=1}^{M} \delta_{Pj} c_j \end{pmatrix}.$$

Rearranging the terms in this expression, we can rewrite the total χ^2 as

$$\chi^2 = \left\| \begin{pmatrix} \alpha & 0 & \gamma \\ 0 & \beta & \delta \end{pmatrix} \begin{pmatrix} a \\ b \\ c \end{pmatrix} - \begin{pmatrix} \theta \\ \psi \end{pmatrix} \right\|^2. \tag{A2}$$

The procedure then consists of finding the vector $\boldsymbol{X}$ that minimizes an expression of the form

$$||\mathbf{A}\boldsymbol{X} - \mathbf{B}||^2.$$

An efficient algorithm with which to perform this operation is known as singular value decomposition (SVD; see Press et al. 1992). This method is based on the linear algebra theorem that states that any $I \times J$ rectangular matrix $\mathbf{M}$ whose number of rows I is greater than or equal to its number of columns J can written as the product of an $I \times J$ column-orthogonal matrix $\mathbf{U}$, a $J \times J$ diagonal matrix $\mathbf{W}$ with nonnegative (positive or zero) elements, and the transpose of a $J \times J$ orthogonal matrix $\mathbf{V}$:

$$\mathbf{M} = \mathbf{U}\mathbf{W}\mathbf{V}^T. \tag{A3}$$

The rectangular matrix in equation (A2) has $2P$ rows (24 in our case) and $2N + M$ columns (either 5 or 7 for uniform or accelerated proper motions, respectively) and can clearly be decomposed in that fashion. Since both $\mathbf{U}$ and $\mathbf{V}$ in the previous expression are orthogonal, their inverses are just their transposes. Also, if none of its diagonal elements are zero (which will be the case in all situations considered here), the inverse of $\mathbf{W}$ is a diagonal matrix whose elements are just the inverses of those of $\mathbf{W}$. Thus, the inverse of matrix $\mathbf{M}$ can be written as

$$\mathbf{M}^{-1} = \mathbf{V}\mathbf{W}^{-1}\mathbf{U}^T.$$

It can be shown (see Press et al. 1992) that if the matrix $\mathbf{M}$ can be decomposed as above, then the vector $\boldsymbol{X}$ that minimizes the expression $||\mathbf{A}\boldsymbol{X} - \mathbf{B}||^2$ is simply

$$\boldsymbol{X} = \mathbf{V}\mathbf{W}^{-1}\mathbf{U}^T\mathbf{B}. \tag{A4}$$

An efficient way of solving our least-squares fitting problem is, therefore, to form the rectangular matrix that appears in equation (A2), decompose it as in equation (A3), and calculate the values of the a_i, b_i, and c_i using equation (A4). This method was implemented in FORTRAN following Press et al. (1992).

REFERENCES

André, P., Deeney, B. D., Phillips, R. B., & Lestrade, J.-F. 1992, ApJ, 401, 667
Beasley, A. J., Gordon, D., Peck, A. B., Petrov, L., MacMillan, D. S., Fomalont, E. B., & Ma, C. 2002, ApJS, 141, 13
Bertout, C., Robichon, N., & Arenou, F. 1999, A&A, 352, 574
Condon, J. J. 1997, PASP, 109, 166
D'Antona, F., & Mazzitelli, I. 1996, ApJ, 456, 329
Duchêne, G., Beust, H., Adjali, F., Konopacky, Q. M., & Ghez, A. M. 2006, A&A, 457, L9
Duchêne, G., Ghez, A. M., & McCabe, C. 2002, ApJ, 568, 771
Duchêne, G., Ghez, A. M., McCabe, C., & Ceccarelli, C. 2005, ApJ, 628, 832
Elias, J. H. 1978a, ApJ, 224, 453
———. 1978b, ApJ, 224, 857
Evans, N. J., II, et al. 2003, PASP, 115, 965
Feigelson, E. D., & Montmerle, T. 1999, ARA&A, 37, 363
Fomalont, E. B. 1999, in ASP Conf. Ser. 180, Synthesis Imaging in Radio Astronomy II, ed. G. B. Taylor, C. L. Carilli, & R. A. Perley (San Francisco: ASP), 463
Gahm, G. F. 1970, ApJ, 160, 1117
Greisen, E. W. 2003, in Information Handling in Astronomy, ed. A. Heck (Dordrecht: Kluwer), 109
Güdel, M., et al. 2007, A&A, 468, 353
Johnston, K. J., Gaume, R. A., Fey, A. L., de Vegt, C., & Claussen, M. J. 2003, AJ, 125, 858
Kenyon, S. J., Dobrzycka, D., & Hartmann, L. 1994, AJ, 108, 1872

Knude, J., & Høg, E. 1998, A&A, 338, 897
Kuhi, L. V. 1974, A&AS, 15, 47
Lejeune, T., Cuisinier, F., & Buser, R. 1997, A&AS, 125, 229
Loinard, L., Mioduszewski, A. J., Rodríguez, L. F., González, R. A., Rodríguez, M. I., & Torres, R. M. 2005, ApJ, 619, L179
Loinard, L., Rodríguez, L. F., D'Alessio, P., Rodríguez, M. I., & González, R. F. 2007, ApJ, 657, 916
Loinard, L., Rodríguez, L. F., & Rodríguez, M. I. 2003, ApJ, 587, L47
Mel'nikov, S. Y., & Grankin, K. N. 2005, Astron. Lett., 31, 427
Perryman, M. A. C., et al. 1997, A&A, 323, L49
Phillips, R. B., Lonsdale, C. J., & Feigelson, E. D. 1993, ApJ, 403, L43
Pradel, N., Charlot, P., & Lestrade, J.-F. 2006, A&A, 452, 1099
Press, W. H., Teukolsky, S. A., Vetterling, W. T., & Flannery, B. P. 1992, Numerical Recipes (2nd ed.; Cambridge: Cambridge Univ. Press)
Schaefer, G. H., Simon, M., Beck, T. L., Nelan, E., & Prato, L. 2006, AJ, 132, 2618
Seidelmann, P. K. 1992, Explanatory Supplement to the Astronomical Almanac (Mill Valley: University Science Books)
Siess, L., Dufour, E., & Forestini, M. 2000, A&A, 358, 593
Skinner, S. L., & Brown, A. 1994, AJ, 107, 1461
Smith, K., Pestalozzi, M., Güdel, M., Conway, J., & Benz, A. O. 2003, A&A, 406, 957

C

VLBA Distance to Nearby Star-Forming Regions II. Hubble 4 and HDE 283572 in Taurus

Rosa M. Torres, Laurent Loinard, Amy J. Mioduszewski & Luis F. Rodríguez
The Astrophysical Journal, 671, 1813, 2007

Abstract.The nonthermal 3.6 cm radio continuum emission from the naked T Tauri stars Hubble 4 and HDE 283572 in Taurus has been observed with the Very Long Baseline Array (VLBA) at six epochs between 2004 September and 2005 December with a typical separation between successive observations of 3 months. Thanks to the remarkably accurate astrometry delivered by the VLBA, the trajectory described by both stars on the plane of the sky could be traced very precisely and modeled as the superposition of their trigonometric parallax and uniform proper motion. The best fits yield distances to Hubble 4 and HDE 283572 of 132.8 ± 0.5 and 128.5 ± 0.6 pc, respectively. Combining these results with the other two existing VLBI distance determinations in Taurus, we estimate the mean distance to the Taurus association to be 137 pc with a dispersion (most probably reflecting the depth of the complex) of about 20 pc.

The Astrophysical Journal, 671:1813–1819, 2007 December 20

VLBA DETERMINATION OF THE DISTANCE TO NEARBY STAR-FORMING REGIONS. II. HUBBLE 4 AND HDE 283572 IN TAURUS

Rosa M. Torres and Laurent Loinard
Centro de Radiostronomía y Astrofísica, Universidad Nacional Autónoma de México, Apartado Postal 72–3 (Xangari), 58089 Morelia, Michoacán, Mexico; r.torres@astrosmo.unam.mx

Amy J. Mioduszewski
National Radio Astronomy Observatory, Array Operations Center, 1003 Lopezville Road, Socorro, NM 87801

and

Luis F. Rodríguez
Centro de Radiostronomía y Astrofísica, Universidad Nacional Autónoma de México, Apartado Postal 72–3 (Xangari), 58089 Morelia, Michoacán, Mexico
Received 2007 July 13; accepted 2007 August 30

ABSTRACT

The nonthermal 3.6 cm radio continuum emission from the naked T Tauri stars Hubble 4 and HDE 283572 in Taurus has been observed with the Very Long Baseline Array (VLBA) at six epochs between 2004 September and 2005 December with a typical separation between successive observations of 3 months. Thanks to the remarkably accurate astrometry delivered by the VLBA, the trajectory described by both stars on the plane of the sky could be traced very precisely and modeled as the superposition of their trigonometric parallax and uniform proper motion. The best fits yield distances to Hubble 4 and HDE 283572 of 132.8 ± 0.5 and 128.5 ± 0.6 pc, respectively. Combining these results with the other two existing VLBI distance determinations in Taurus, we estimate the mean distance to the Taurus association to be 137 pc with a dispersion (most probably reflecting the depth of the complex) of about 20 pc.

Subject headings: astrometry — magnetic fields — radiation mechanisms: nonthermal — radio continuum: stars — stars: formation

1. INTRODUCTION

While our understanding of the main-sequence evolution of solar-type stars is now very solid, our comprehension of their youth is significantly less advanced. Increasingly detailed pre-main-sequence theoretical models, as well as improved observational constraints are clearly needed and are actively sought (see Klein et al. 2007; White et al. 2007; Güdel et al. 2007 for recent reviews). On the observational front, significant progress is currently being made thanks to large on-going X-ray and infrared surveys of nearby star-forming regions carried out with space observatories (e.g., Evans et al. 2003; Güdel et al. 2007). It should be noticed, however, that some of the stellar parameters (luminosity, mass, etc.) most relevant to constrain theoretical models depend critically both on the quality of the data used to estimate them *and* on the distance to the object under consideration. Unfortunately, the distance to even the nearest star-forming complexes (e.g., Taurus or Ophiuchus) are not known to better than 20% (Elias 1978a, 1978b; Kenyon et al. 1994; Knude & Hog 1998; Bertout & Genova 2006). This is, in part, a consequence of the fact that the otherwise highly successful *Hipparcos* mission (Perryman et al. 1997) performed comparatively poorly in star-forming regions (Bertout et al. 1999) because young stars—being still heavily embedded in their parental clouds—are faint in the optical bands observed by *Hipparcos*.

Future space missions such as *Gaia* will certainly be able to detect stars much fainter than those accessible to *Hipparcos*, but these missions will still be unable to access the most deeply embedded populations and are still at least a decade away. Radio observations with Very Long Baseline Interferometers (VLBIs) provide an interesting alternative avenue, because they can deliver extremely accurate absolute astrometry (better than 0.1 mas) if proper calibration is applied. In the last few years, such observations have proven capable of measuring the trigonometric parallax of sources within a few kiloparsecs of the Sun with a precision of a few percent (Brisken et al. 2000, 2002; Loinard et al. 2005, 2007; Xu et al. 2006; Hachisuka et al. 2006; Hirota et al. 2007; Sandstrom et al. 2007). Because the sensitivity of VLBI experiments is limited, only compact nonthermal emitters can usually be detected. In star-forming regions, two kinds of such nonthermal sources exist: masers and magnetically active young stars. Masers are ubiquitous in regions where massive stars are formed, but they are absent or unpredictably variable in low- and intermediate-mass star-forming sites. Low-mass young stars, on the other hand, tend to have active magnetospheres that can generate detectable nonthermal continuum emission (e.g., André et al. 1992; Feigelson & Montmerle 1999; Dulk 1985). Thus, the distance to nearby star-forming regions can be measured very accurately if adequate nonthermal sources are identified in them, and multiepoch observations are obtained over the course of a few years. This method has been successfully applied to water and methanol masers in nearby massive star-forming regions (Xu et al. 2006; Hachisuka et al. 2006; Hirota et al. 2007) and to the nonthermal continuum emission associated with low-mass T Tauri stars (Loinard et al. 2005, 2007; Sandstrom et al. 2007). In all these cases, a precision typically an order of magnitude better than previous estimates was achieved. Since adequate nonthermal sources are available in essentially all the nearby sites of star formation, multiepoch VLBI observations have the potential of improving significantly our knowledge

TABLE 1
Measured Source Positions and Fluxes

Mean UT Date (1)	α (J2000.0) (2)	σ_α (s) (3)	δ (J2000.0) (4)	σ_δ (arcsec) (5)	F_ν (mJy) (6)	σ (μJy) (7)
			Hubble 4			
2004.09.19 11:47	04 18 47.0327419	0.0000020	28 20 07.398977	0.000050	0.67	54
2005.01.04 04:46	04 18 47.0319609	0.0000022	28 20 07.389009	0.000071	0.76	73
2005.03.25 23:44	04 18 47.0318775	0.0000009	28 20 07.381391	0.000021	4.66	114
2005.07.04 16:51	04 18 47.0328115	0.0000022	28 20 07.375000	0.000053	0.65	58
2005.09.18 11:52	04 18 47.0330740	0.0000019	28 20 07.370321	0.000040	1.25	53
2005.12.28 05:15	04 18 47.0323418	0.0000012	28 20 07.360573	0.000025	1.53	51
			HDE 283572			
2004.09.22 11:35	04 21 58.8521561	0.0000004	28 18 06.389421	0.000010	7.13	81
2005.01.06 04:39	04 21 58.8514573	0.0000048	28 18 06.380015	0.000091	0.92	58
2005.03.30 23:34	04 21 58.8514676	0.0000022	28 18 06.372534	0.000038	1.71	65
2005.06.23 17:34	04 21 58.8523648	0.0000007	28 18 06.367852	0.000014	4.23	80
2005.09.23 11:32	04 21 58.8528216	0.0000070	28 18 06.363175	0.000140	0.52	62
2005.12.24 05:31	04 21 58.8522172	0.0000028	28 18 06.354808	0.000070	0.51	47

Note.—Units of right ascension are hours, minutes, and seconds, and units of declination are degrees, arcminutes, and arcseconds. Dates are yyyy.mm.dd hh:mm.

of the space distribution of star-forming regions around the Sun. With this goal in mind, we have initiated a large project aimed at accurately measuring the trigonometric parallax of a sample of magnetically active young stars in the most prominent and often-studied northern star-forming regions within 1 kpc of the Sun (Taurus, Ophiuchus, Perseus, Serpens, and Cepheus; the distance to Orion has already been measured using VLBI techniques; Hirota et al. 2007; Sandstrom et al. 2007) using the 10-element Very Long Baseline Array (VLBA) of the National Radio Astronomy Observatory (NRAO). In the present article, we concentrate on HDE 283572 and Hubble 4, two young stars in Taurus. This allows us to examine in more detail the distribution and kinematics of young stars in this important star-forming region.

Hubble 4 is a K7 naked T Tauri star with an effective temperature of 4060 K (Briceño et al. 2002). It has long been known to have a particularly active magnetosphere that produces nonthermal radio emission characterized by significant variability, large circular polarization, and a nearly flat spectral index (Skinner 1993). It was detected in VLBI experiments, with a flux of a few millijanskys by Phillips et al. (1991), and is also an X-ray source (Güdel et al. 2007). The superficial magnetic field of Hubble 4 has been estimated to be about 2.5 kG using Zeeman-sensitive Ti I lines (Johns-Krull et al. 2004). HDE 283572, on the other hand, is a somewhat hotter ($T_{\rm eff} = 5770$ K; Kenyon & Hartmann 1995) G5 naked T Tauri star. Early observations with the *Einstein* satellite showed that it has a fairly bright X-ray counterpart (Walter et al. 1987). It was initially detected as a radio source by O'Neal et al. (1990) and in VLBI observations by Phillips et al. (1991) with a flux of about 1 mJy.

2. OBSERVATIONS AND DATA CALIBRATION

In this paper, we will make use of a series of six continuum 3.6 cm (8.42 GHz) observations of Hubble 4 and HDE 283572 obtained roughly every three months between 2004 September and 2005 December with the VLBA (Table 1). Our pointing directions were at $\alpha_{\rm J2000.0} = 04^{\rm h}18^{\rm m}47.033^{\rm s}$, $\delta_{\rm J2000.0} = +28^\circ20'07.398''$ and $\alpha_{\rm J2000.0} = 04^{\rm h}21^{\rm m}58.847^{\rm s}$, $\delta_{\rm J2000.0} = +28^\circ18'06.502''$ for Hubble 4 and HDE 283572, respectively. Each observation consisted of series of cycles with 2 minutes on source and 1 minute on the main phase-referencing quasar J0429+2724 (the same for both targets). Each 24 minutes, we also observed three secondary calibrators (J0433+2905, J0408+3032, and J0403+2600) forming a triangle around the astronomical source (Fig. 1). All four calibrators are very compact extragalactic sources whose absolute positions are known to better than 1 mas (Beasley et al. 2002).

The data were edited and calibrated using the Astronomical Image Processing System (AIPS; Greisen 2003). The basic data reduction followed the standard VLBA procedures for phase-referenced observations. First, the most accurate measured Earth Orientation Parameters obtained from the US Naval Observatory database were applied to the data to improve the values initially used by the VLBA correlator. Second, dispersive delays caused by free electrons in the Earth's atmosphere were accounted for using estimates of the electron content of the ionosphere derived from Global Positioning System (GPS) measurements. A priori amplitude calibration based on the measured system temperatures and standard gain curves was then applied. The fourth step was to correct the phases for antenna parallactic angle effects,

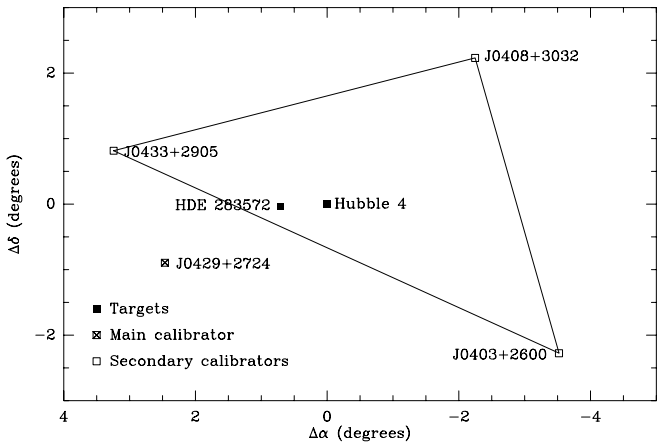

Fig. 1.—Relative position of the astronomical targets (Hubble 4 and HDE 283572), the main calibrator (J0429+2724), and the secondary calibrators (J0433+2905, J0408+3032, and J0403+2600).

and the fifth was to remove residual instrumental delays caused by the VLBA electronics. This was done by measuring the delays and phase residuals for each antenna and IF using the fringes obtained on a strong calibrator. The final step of this initial calibration was to remove global frequency- and time-dependent phase errors using a global fringe-fitting procedure on the main phase calibrator (J0429+2724), which was assumed at this stage to be a point source.

In this initial calibration, the solutions from the global fringe fit were only applied to the main phase calibrator itself. The corresponding calibrated visibilities were then imaged, and several passes of self- calibration were performed to improve the overall amplitude and phase calibration. In the image obtained after the self-calibration iterations, the main phase calibrator is found to be slightly extended. To take this into account, the final global fringe-fitting part of the reduction was repeated using the image of the main phase calibrator as a model instead of assuming it to be a point source. Note that a different phase calibrator model was produced for each epoch to account for possible small changes in the main calibrator structure from epoch to epoch. The solutions obtained after repeating this final step were edited for bad points and applied to the astronomical targets and to the main and secondary calibrators.

The astrometry precision of VLBI observations such as those presented here depends critically on the quality of the phase calibration. Systematic errors, unremoved by the standard calibration procedures described above, usually dominate the phase calibration error budget and limit the astrometric precision achieved to several times the value expected theoretically (e.g., Fomalont 1999; Pradel et al. 2006). At the frequency of the present observations, the main sources of systematic errors are inaccuracies in the troposphere model used, as well as clock, antenna, and a priori source position errors. These effects combine to produce a systematic phase difference between the calibrator and the target, causing position shifts. One effective strategy to measure and correct these systematic errors consists of including observations of more than one phase calibrator chosen to surround the target (Fomalont & Kogan 2005). This allows phase gradients around the source, due to errors in the troposphere model or related to uncertainties in the cataloged position of the calibrators, to be measured and corrected. This strategy was applied to our observations using the three secondary calibrators mentioned earlier (Fig. 1) and resulted in significant improvements in the final phase calibration and image quality.

Because of the time spent on the calibrators, only about 5 of the 9 hr of telescope time allocated to each of our observations were actually spent on source. Once calibrated, the visibilities were imaged with a pixel size of 50 μas after weights intermediate between natural and uniform (ROBUST = 0 in AIPS) were applied. This resulted in typical rms noise levels of 50–80 μJy beam^{-1} (Table 1). Both sources were detected with a signal-to-noise ratio better than 10 at each epoch (Table 1). The source absolute positions at each epoch (also listed in Table 1) were determined using a two-dimensional Gaussian fitting procedure (task `jmfit` in AIPS). This task provides an estimate of the position error (cols. [3] and [5] of Table 1) based on the expected theoretical astrometric precision of an interferometer:

$$\sigma = \frac{\lambda}{2\pi B}\frac{1}{\mathrm{SNR}}, \quad (1)$$

where λ is the wavelength, B the baseline, and SNR the image signal-to-noise ratio (Thompson et al. 1986). In spite of the extra calibration steps taken to improve the phase calibration, uncorrected systematic errors still exist and must be added quadratically to the values deduced from equation (1). These remaining systematic errors are difficult to estimate a priori and may depend on the structure of the source under consideration. Here we will estimate these systematic effects from the fits to the data (see below).

3. RESULTS

The displacement of the sources on the celestial sphere is the combination of their trigonometric parallax (π) and proper motions (μ). The reference epoch was taken at the mean epoch of each series of observations: JD 2,453,500 (≡2005.355) for both sources. Since the sources considered here appear to be isolated, we considered linear and uniform proper motions. The astrometric parameters were calculated using the singular value decomposition (SVD) decomposition fitting scheme described by Loinard et al. (2007). The necessary barycentric coordinates of the Earth, as well as the Julian date of each observation, were calculated using the Multiyear Interactive Computer Almanac (MICA) distributed as a CD-ROM by the US Naval Observatory. They are given explicitly in Table 2 for all epochs and sources. The best fits (Fig. 2) give the following parameters:

$$\begin{aligned}
\alpha_{\mathrm{J2005.355}} &= 04^{\mathrm{h}}18^{\mathrm{m}}47.032414^{\mathrm{s}} \pm 0.000001^{\mathrm{s}},\\
\delta_{\mathrm{J2005.355}} &= 28^{\circ}20'07.3792 \pm 0.0002'',\\
\mu_{\alpha} &= 4.30 \pm 0.05 \text{ mas yr}^{-1},\\
\mu_{\delta} &= -28.9 \pm 0.3 \text{ mas yr}^{-1},\\
\pi &= 7.53 \pm 0.03 \text{ mas}
\end{aligned}$$

and

$$\begin{aligned}
\alpha_{\mathrm{J2005.355}} &= 04^{\mathrm{h}}21^{\mathrm{m}}58.852030^{\mathrm{s}} \pm 0.00002^{\mathrm{s}},\\
\delta_{\mathrm{J2005.355}} &= 28^{\circ}18'06.37128'' \pm 0.00005'',\\
\mu_{\alpha} &= 8.88 \pm 0.06 \text{ mas yr}^{-1},\\
\mu_{\delta} &= -26.6 \pm 0.1 \text{ mas yr}^{-1},\\
\pi &= 7.78 \pm 0.04 \text{ mas}
\end{aligned}$$

for Hubble 4 and HDE 283572, respectively. The measured parallaxes correspond to distances of 132.8 ± 0.5 pc for Hubble 4 and 128.5 ± 0.6 pc for HDE 283572. The postfit rms (dominated by the remaining systematic errors mentioned at the end of § 2) is quite good for HDE 283572: 60 and 90 μas in right ascension and declination, respectively. For Hubble 4, on the other hand, the residual is good in right ascension (40 μas) but large in declination (240 μas). To obtain a reduced χ^2 of one both in right ascension and declination, one must add quadratically 3.1 μs of time and 340 μas to the formal errors delivered by `jmfit` for Hubble 4, and 4.3 μs of time and 115 μas for HDE 283572. All the errors quoted in the paper include these systematic contributions.

The origin of the large declination residual for Hubble 4 (which does not affect strongly the parallax determination, because the latter is dominated by the right ascension measurements) is not entirely clear. The fact that the residual is only (or, at least, mostly) detected in declination (Fig. 3) would suggest a calibration issue. Indeed, astrometric fitting of phase-referenced VLBI observations is usually worse in declination than in right ascension (e.g., Fig. 1 in Chatterjee et al. 2004) as a result of residual zenith phase delay errors (Reid et al. 1999). We consider this possibility fairly unlikely here, however, because such

TABLE 2

JULIAN DATES AND EARTH COORDINATES FOR HUBBLE 4 AND HDE 283572

Mean UT Date[a]	JD	Earth Barycentric Coordinates (AU)		
Hubble 4				
2004.09.19 11:47	2,453,267.99	+1.006998486	−0.052084106	−0.022682627
2005.01.04 04:46	2,453,374.70	−0.231331103	+0.875675935	+0.379526720
2005.03.25 23:44	2,453,454.48	−0.990029933	−0.069134209	−0.030092055
2005.07.04 16:51	2,453,556.20	+0.228244142	−0.908947748	−0.394190784
2005.09.18 11:52	2,453,631.99	+1.005815421	−0.069425778	−0.030225422
2005.12.28 05:15	2,453,732.72	−0.107253794	+0.898552365	+0.389430205
HDE 283572				
2004.09.22 11:35	2,453,270.98	+1.007690418	−0.005037832	−0.002285078
2005.01.06 04:39	2,453,376.69	−0.265058725	+0.867496343	+0.375981760
2005.03.30 23:34	2,453,460.46	−0.978622564	−0.163101149	−0.070826870
2005.06.23 17:34	2,453,545.23	+0.044465499	−0.930888246	−0.403696737
2005.09.23 11:32	2,453,636.98	+1.007380117	+0.008930420	+0.003741574
2005.12.24 05:31	2,453,728.73	−0.037702136	+0.903636825	+0.391632177

[a] Dates are yyyy.mm.dd hh:mm.

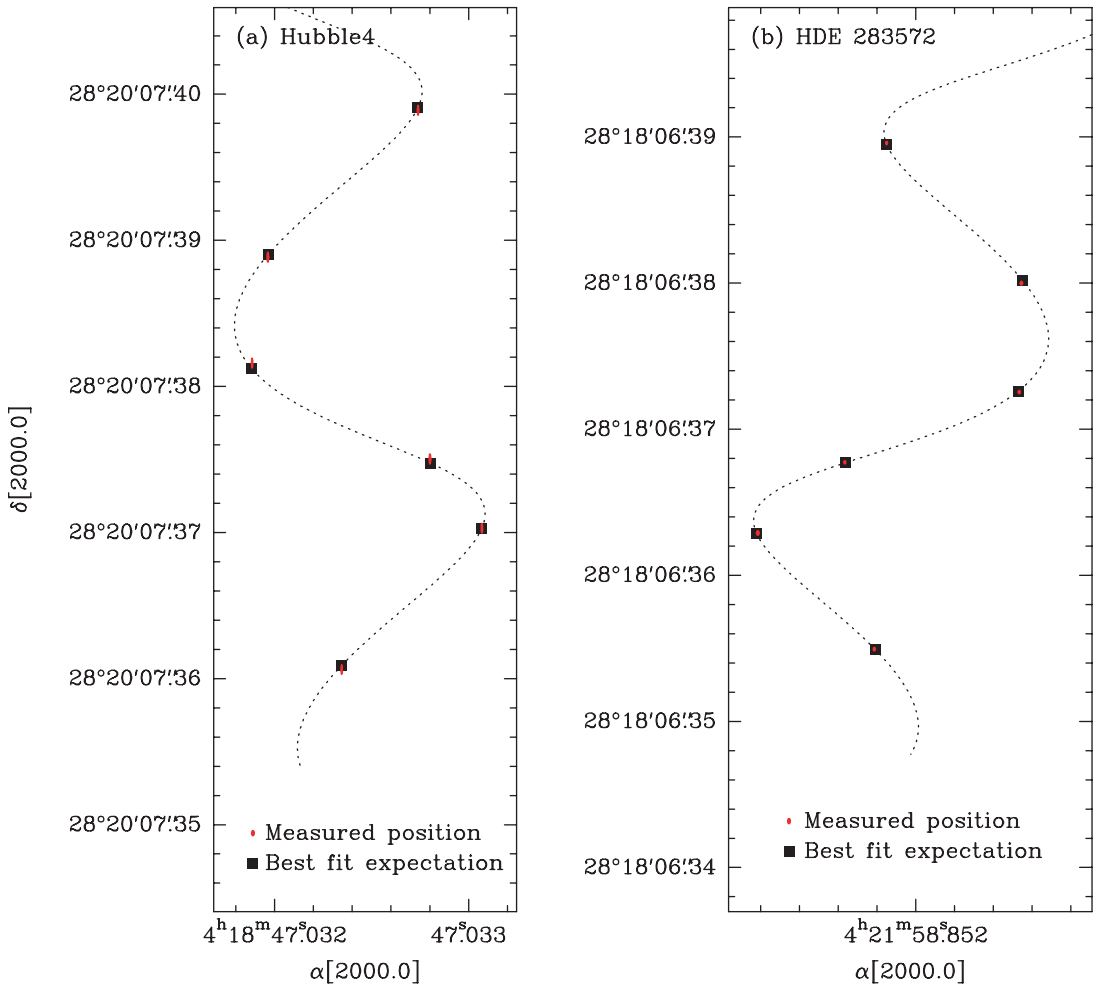

FIG. 2.—Measured positions and best fit for (*a*) Hubble 4 and (*b*) HDE 283572. The observed positions are shown as ellipses, the size of which represents the error bars.

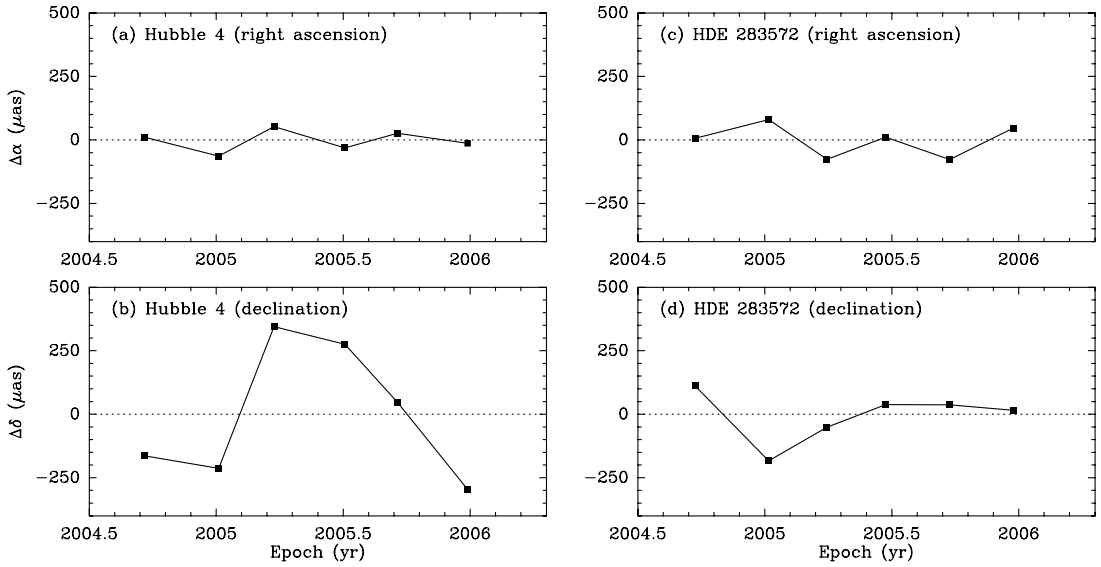

FIG. 3.—Postfit residuals for Hubble 4 (*left*) and HDE 283572 (*right*) in right ascension (*top*) and declination (*bottom*).

a problem would have been detected during the multisource calibration, and because the observations and reduction of Hubble 4 and HDE 283572 (which does not appear to be affected by any calibration issue) were performed following identical protocols and over the same period of time. Another element that argues against a calibration problem is that the large residual is not the result of one particularly discrepant observation: in addition to the fit mentioned above, in which all six observations of Hubble 4 are taken into account, we made five fits where we sequentially discarded one of the epochs. All five fits gave similar astrometric parameters and a similarly large declination residual. Thus, we argue that this large residual might be real, rather than related to a calibration problem. At the distance of Hubble 4, 240 μas correspond to 0.032 AU, or about 7 $R_\odot$. Hubble 4 is estimated to have a radius of about 3.4 $R_\odot$ (Johns-Krull et al. 2004), so the amplitude of the residual is just about 2 R_*. Baring this figure in mind, at least two mechanisms could potentially explain the large declination residual: (1) the magnetosphere of Hubble 4 could be somewhat more extended than its photosphere, and the residuals could reflect variations in the structure of the magnetosphere; (2) Hubble 4 could have a companion, and the residuals could reflect the corresponding reflex motion. Let us examine the pros and cons of these two possibilities.

If the residuals were related to a variable extended magnetosphere, one would expect the emission to be occasionally somewhat extended. Interestingly, Phillips et al. (1991) reported that Hubble 4 was slightly resolved in their VLBI data, and we find it to be resolved in at least two of our own observations as well. On the other hand, if the emission were related to variations in the magnetosphere, one would expect to see variations with the periodicity of the rotational period of the star (about 12/sin i days; Johns-Krull et al. 2004). Given that the separation between our successive observations is typically 3 months, we would expect the residuals to be essentially random. Instead, those residuals seem to show a periodicity of about 1.2 yr (Fig. 3*b*). This would be more consistent with our alternative proposal that the residuals are related to the reflex motion of Hubble 4 due to the presence of an unseen companion. The semimajor axis corresponding to a period of 1.2 yr and a mass of 0.7 $M_\odot$ (see below) is just about 1 AU. Since the ratio between the amplitude of the reflex motion and that of the orbital path is the inverse of the ratio between the mass of the primary and that of the companion, the mass of the companion would have to be $0.7(0.032/1) = 0.02\ M_\odot$. The companion would then have to be a very low mass star or a brown dwarf. Note, however, that the residuals are relatively poorly constrained with the existing data and that additional observations aimed—in particular—at confirming the periodicity in the residuals will be needed to resolve this issue.

4. DISCUSSION

4.1. *Distance to the Taurus Association*

HDE 283572 was one of the few Taurus members with a parallax estimate from *Hipparcos* ($\pi = 7.81 \pm 1.30$ mas, $d = 128^{+26}_{-18}$ pc; Bertout et al. 1999). The present determination is well within 1 σ of the *Hipparcos* value, but more that 1 order of magnitude more precise. Bertout & Genova (2006) estimated the distance to both Hubble 4 ($\pi = 8.12 \pm 1.5$ mas, $d = 123^{+28}_{-29}$ pc) and HDE 283572 ($\pi = 7.64 \pm 1.05$ mas, $d = 131^{+21}_{-26}$ pc) using a modified convergent point method. Again, our values are within 1 σ of these determinations, but more than 1 order of magnitude more precise. Only two other Taurus members have VLBI-based distance determinations: T Tau ($\pi = 6.82 \pm 0.03$ mas, $d = 146.7 \pm 0.6$ pc; Loinard et al. 2007) and V773 Tau ($\pi = 6.74 \pm 0.25$ mas, $148.4^{+5.7}_{-5.3}$ pc; Lestrade et al. 1999). The weighted mean of these four values is $\bar{\pi} = 7.30$ mas ($\bar{d} = 137.0$ pc) and the rms dispersion about that mean 0.45 mas ($\equiv 9$ pc). Although the number of sources with VLBI distances remains small, we argue that the mean value represents a good estimate of the mean distance to the Taurus association and that the dispersion provides a good guess of its depth. Note, however, that the latter value was calculated as a dispersion; the corresponding FWHM (which may represent a better estimate of the full depth of the complex) is 21 pc. In comparison, the angular size of Taurus projected on the plane of the sky is about 10°, corresponding to about 23 pc at that distance. The significant depth of the complex implies, in particular, that however well measured the mean distance to Taurus may be, using it indiscriminately for all Taurus members will result in systematic errors that may be as large as 15%. For higher precision, accurate individual distances to a larger sample of Taurus members will be needed. VLBI measurements such as those presented here

TABLE 3
SPACE VELOCITY FOR THE FOUR TAURUS SOURCES WITH VLBI-BASED DISTANCE DETERMINATIONS

	V_r (km s^{-1})		V_α (km s^{-1})		V_δ (km s^{-1})		V_ℓ (km s^{-1})		V_b (km s^{-1})		
SOURCE	Observed	Expected	Observed	Expected	Observed	Expected	Observed	Expected	Observed	Expected	REFERENCES
Hubble 4	15.0 ± 1.7	9.82	2.71 ± 0.03	1.28	−18.2 ± 0.2	−8.21	15.1 ± 0.1	6.84	−10.5 ± 0.1	−4.71	1, 2
HDE 283572.....	15.0 ± 1.5	9.88	5.41 ± 0.04	1.12	−16.2 ± 0.1	−8.21	15.55 ± 0.08	6.78	−7.07 ± 0.05	−4.77	1, 3
T Tau[a].....	19.1 ± 1.2	11.35	8.59 ± 0.04	1.22	−8.90 ± 0.06	−6.53	12.35 ± 0.05	5.74	+0.69 ± 0.03	−3.34	2, 4
V773 Tau[b].....	13.8 ± 0.9	9.71	0.3 ± 0.2	1.48	−16.4 ± 0.7	−8.16	12.0 ± 0.5	6.89	−11.2 ± 0.5	−4.62	5, 6

[a] The radial velocity and proper motions used here are those of T Tau N. The radial velocities for T Tau Sa and T Tau Sb are available in Duchêne et al. (2002) and are very similar.
[b] The radial velocity used here is that of the center of mass of the spectroscopic binary V773 Tau A+B.
REFERENCES.—(1) This work; (2) Hartmann et al. 1986; (3) Walter et al. 1988; (4) Loinard et al. 2007; (5) Welty 1995; (6) Lestrade et al. 1999.

most probably represent the best hope of obtaining such a large sample in the near future.

4.2. *Kinematics*

The tangential velocity of the four sources mentioned in the previous section (Hubble 4, HDE 283572, T Tau, and V773 Tau) can be deduced from their measured distances and proper motions. Also, for these four sources, radial velocities are available from the literature, so their complete velocity vectors can be reconstructed (Table 3, Fig. 4). Hubble 4 and HDE 283572, which are very close on the plane of the sky and are at very similar distances, also have very similar space velocities. This strongly suggests that they belong to the same subgroup (but see below). V773 Tau, which in projection also appears near Hubble 4 and HDE 283572 but is at a significantly different distance, has a somewhat different space velocity. Not surprisingly, T Tau, at the south of the Taurus complex, has a significantly different velocity.

The measured radial and tangential velocities can be compared to the values expected from the differential rotation of the Galaxy. The proper motions determined with the VLBA are measured with respect to the Sun. To obtain the corresponding values expected theoretically, we adopt a model for the local rotation of the Galaxy where the Oort constants are $A = 14.4$ and $B = -12.0$ km s^{-1} kpc^{-1} (Allen 2000) and where the distance from the Sun to the Galactic center is $R_\odot = 8.5$ kpc. For the peculiar motion of the Sun (required to transform values relative to the local standard of rest (LSR) to the barycentric coordinates provided by the VLBA), we use $U_\odot = +9.0$, $V_\odot = +12.0$, and $W_\odot = +7.0$ km s^{-1} (Allen 2000). Here we follow the traditional convention according to which U runs from the Sun to the Galactic center, V is in the Galactic plane, perpendicular to U and positive in the direction of Galactic rotation, and W is perpendicular to the Galactic plane, positive toward the Galactic north pole. It is noteworthy from the comparison between the observed and expected velocities that the Taurus members considered here have very significant peculiar motions (of amplitude $\sim$10 km s^{-1}). Since our measured values are very similar to the mean radial velocities and proper motions in catalogs of optically selected Taurus members (e.g., Ducourant et al. 2005; Bertout & Genova 2006), this large peculiar velocity appears to be characteristic of the entire Taurus complex. This is a notable contrast with the stars in the Orion cluster where the expected and measured mean proper motions agree to better than 0.5 km s^{-1} (Gómez et al. 2005).

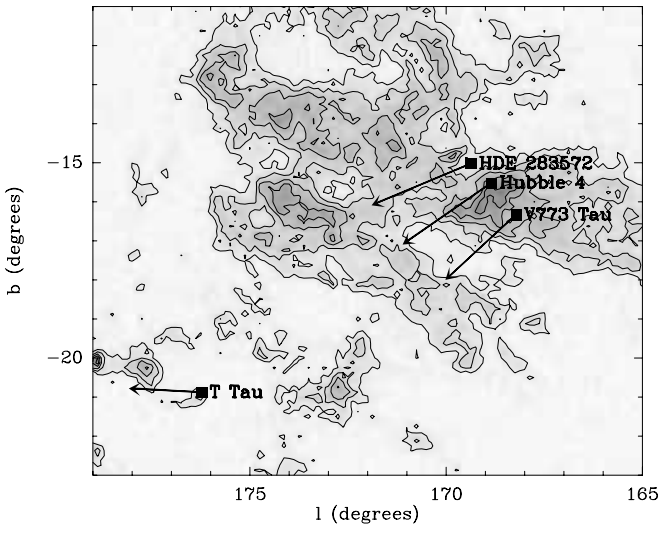

FIG. 4.—Positions and proper motions of the four sources in Taurus with VLBI distance measurements superposed on the CO integrated intensity map of Dame et al. (2001).

Section 4.1 and the present kinematics analysis show that if a sufficiently large sample of Taurus members had VLBI-based distance determinations, it would become possible to accurately map the three-dimensional distribution of stars in the complex, as well as their detailed kinematics. Using a dynamical analysis, it would then become possible to estimate the total mass of the complex in a way totally independent of the traditionally used molecular observations. Also, coupled with pre-main-sequence evolutionary models (see below), it would become possible to study the space distribution of stars as a function of their age, and thereby reconstruct the history of star formation in Taurus.

4.3. *Physical Parameters of the Stars*

Having measured the distance to two stars in Taurus, we are now in a position to recalculate their luminosities and place them better on an isochrone. We will use here the pre-main-sequence evolutionary models of Siess et al. (2000) available on the World Wide Web. The effective temperature of Hubble 4 is 4060 K (Briceño et al. 2002), and its bolometric luminosity scaled with the present distance determination is $2.7(132.8/142)^2 = 2.4\,L_\odot$ (Briceño et al. 2002). For HDE 283572, the effective temperature is 5770 K (Güdel et al. 2007) and the scaled bolometric luminosity $6.5(128.5/140)^2 = 5.5\,L_\odot$. Using these values as inputs for the evolutionary models, we obtain $M = 0.7\,M_\odot$, $R = 2.9\,R_\odot$ and $M = 1.6\,M_\odot$, $R = 2.2\,R_\odot$, for Hubble 4 and HDE 283572, respectively. The corresponding ages are 0.74 and 9.0 Myr, respectively. This last result is quite surprising because—as mentioned earlier—Hubble 4 and HDE 283572

are very near each other and share the same kinematics. In these conditions, one would expect them to be coeval. Surprisingly, however, their ages appear to differ by 1 order of magnitude.

5. CONCLUSIONS AND PERSPECTIVES

In this article, we have reported multiepoch VLBA observations of two naked T Tauri stars in the Taurus complex and used these data to measure their trigonometric parallax and proper motions. Both stars appear to be located at about 130 pc, somewhat nearer than the other two Taurus stars (T Tauri and V773 Tau) with VLBI distance estimates (both of which are at $\sim$147 pc). The declination of Hubble 4 shows small but systematic postfit residuals that may be the result of an extended, time-variable magnetosphere or of the presence of a companion, low-mass star or brown dwarf.

Hubble 4 and HDE 283572 appear to share the same kinematics and most probably belong to the same Taurus subgroup. Surprisingly, however, pre-main-sequence evolutionary models suggest that their ages differ by an order of magnitude. The mean distance to Taurus obtained by averaging all four existing VLBI-based distance estimates is 137 pc, and the depth of the complex appears to be about 20 pc, very similar to the size of the complex projected on the plane of the sky.

It is noteworthy that if observations similar to those presented here were obtained for a significantly larger sample of Taurus members, it would be possible to map the three-dimensional distribution and kinematics of the complex, and establish the history of star formation in this important nearby star-forming site.

R. M. T., L. L., and L. F. R. acknowledge the financial support of DGAPA, UNAM, and CONACyT, México. We are grateful to Tom Dame for sending us a digital version of the integrated CO(1–0) map of Taurus. The National Radio Astronomy Observatory is a facility of the National Science Foundation operated under cooperative agreement by Associated Universities, Inc.

REFERENCES

Allen, C. W. 2000, Allen's Astrophysical Quantities, ed. A. N. Cox (4th ed.; New York: AIP)
André, P., Deeney, B. D., Phillips, R. B., & Lestrade, J.-F. 1992, ApJ, 401, 667
Beasley, A. J., Gordon, D., Peck, A. B., Petrov, L., MacMillan, D. S., Fomalont, E. B., & Ma, C. 2002, ApJS, 141, 13
Bertout, C., & Genova, F. 2006, A&A, 460, 499
Bertout, C., Robichon, N., & Arenou, F. 1999, A&A, 352, 574
Briceño, C., et al. 2002, ApJ, 580, 317
Brisken, W. F., Benson, J. M., Beasley, A. J., Fomalont, E. B., Goss, W. M., & Thorsett, S. E. 2000, ApJ, 541, 959
Brisken, W. F., Benson, J. M., Goss, W. M., & Thorsett, S. E. 2002, ApJ, 571, 906
Chatterjee, S., Cordes, J. M., Vlemmings, W. H. T., Arzoumanian, Z., Goss, W. M., & Lazio, T. J. W. 2004, ApJ, 604, 339
Dame, T. M., Hartmann, D., & Thaddeus, P. 2001, ApJ, 547, 792
Duchêne, G., Ghez, A. M., & McCabe, C. 2002, ApJ, 568, 771
Ducourant, C., Teixeira, R., Périé, J. P., Lecampion, J. F., Guibert, J., & Sartori, M. J. 2005, A&A, 438, 769
Dulk, G. A. 1985, ARA&A, 23, 169
Elias, J. H. 1978a, ApJ, 224, 857
———. 1978b, ApJ, 224, 453
Evans, N. J., II, et al. 2003, PASP, 115, 965
Feigelson, E. D., & Montmerle, T. 1999, ARA&A, 37, 363
Fomalont, E. B. 1999, in ASP Conf. Ser. 180, Synthesis Imaging in Radio Astronomy II, ed. G. B. Taylor, C. L. Carilli, & R. A. Perley (San Francisco: ASP), 463
Fomalont, E. B., & Kogan, L. 2005, ATMCA: Phase Referencing Using More Than One Calibrator (AIPS Memo 111; Charlottesville: NRAO)
Gómez, L., Rodríguez, L. F., Loinard, L., Lizano, S., Poveda, A., & Allen, C. 2005, ApJ, 635, 1166
Greisen, E. W. 2003, in Information Handling in Astronomy: Historical Vistas, ed. A. Heck (Dordrecht: Kluwer), 109
Güdel, M., et al. 2007, A&A, 468, 353
Hachisuka, K., et al. 2006, ApJ, 645, 337
Hartmann, L., Hewett, R., Stahler, S., & Mathieu, R. D. 1986, ApJ, 309, 275
Hirota, T., et al. 2007, PASJ, in press (arXiv:0705.3792v1)
Johns-Krull, C. M., Valenti, J. A., & Saar, S. H. 2004, ApJ, 617, 1204
Kenyon, S. J., Dobrzycka, D., & Hartmann, L. 1994, AJ, 108, 1872
Kenyon, S. J., & Hartmann, L. 1995, ApJS, 101, 117
Klein, R. I., Inutsuka, S.-I., Padoan, P., & Tomisaka, K. 2007, Protostars and Planets V, ed. V. Mannings, A. P. Boss, & S. S. Russell (Tucson: Univ. Arizona Press), 99
Knude, J., & Hog, E. 1998, A&A, 338, 897
Lestrade, J.-F., et al. 1999, A&A, 344, 1014
Loinard, L., Mioduszewski, A. J., Rodríguez, L. F., González, R. A., Rodríguez, M. I., & Torres, R. M. 2005, ApJ, 619, L179
Loinard, L., Torres, R. M., Mioduszewski, A. J., Rodríguez, L. F., González, R. A., Lachaume, R., Vázquez, V., & González, E. 2007, ApJ, 671, 546 (Paper I)
O'Neal, D., Feigelson, E. D., Mathieu, R. D., & Myers, P. C. 1990, AJ, 100, 1610
Perryman, M. A. C., et al. 1997, A&A, 323, L49
Phillips, R. B., Lonsdale, C. J., & Feigelson, E. D. 1991, ApJ, 382, 261
Pradel, N., Charlot, P., & Lestrade, J.-F. 2006, A&A, 452, 1099
Reid, M. J., Readhead, A. C. S., Vermeulen, R. C., & Treuhaft, R. N. 1999, ApJ, 524, 816
Sandstrom, K. M., et al. 2007, ApJ, 667, 1161
Siess, L., Dufour, E., & Forestini, M. 2000, A&A, 358, 593
Skinner, L. L. 1993, ApJ, 408, 660
Thompson, A. R., Moran, J. M., & Swenson, G. W. 1986, Interferometry and Synthesis in Radio Astronomy (New York: Wiley)
Walter, F. M., Brown, A., Mathieu, R. D., Myers, P. C., & Vrba, F. J. 1988, AJ, 96, 297
Walter, F. M., et al. 1987, ApJ, 314, 297
Welty, A. D. 1995, AJ, 110, 776
White, R. J., Greene, T. P., Doppmann, G. W., Covey, K. R., & Hillenbrand, L. A. 2007, Protostars and Planets V, ed. V. Mannings, A. P. Boss, & S. S. Russell (Tucson: Univ. Arizona Press), 117
Xu, Y., Reid, M. J., Zheng, X. W., & Menten, K. M. 2006, Science, 311, 54

D

A Preliminary Distance to the Core of Ophiuchus, with an Accuracy of 4 %

Laurent Loinard, Rosa M. Torres, Amy J. Mioduszewski & Luis F. Rodríguez
The Astrophysical Journal, 675, L29, 2008

Abstract. The nonthermal 3.6 cm radio continuum emission from the young stars S1 and DoAr 21 in the core of Ophiuchus has been observed with the VLBA at 6 and 7 epochs, respectively, between June 2005 and August 2006. The typical separation between successive observations was 2-3 months. Thanks to the remarkably accurate astrometry delivered by the Very Long Baseline Array (VLBA), the trajectory described by both stars on the plane of the sky could be traced very precisely, and modeled as the superposition of their trigonometric parallax and a uniform proper motion. The best fits yield distances to S1 and DoAr 21 of $116.9^{+7.2}_{-6.4}$ and $121.9^{+5.8}_{-5.3}$ pc, respectively. Combining these results, we estimate the mean distance to the Ophiuchus core to be $120.0^{+4.5}_{-4.2}$ pc, a value consistent with several recent indirect determinations, but with a significantly improved accuracy of 4%. Both S1 and DoAr 21 happen to be members of tight binary systems, but our observations are not frequent enough to properly derive the corresponding orbital parameters. This could be done with additional data, however, and would result in a significantly

improved accuracy on the distance determination.

The Astrophysical Journal, 675:L29–L32, 2008 March 1

A PRELIMINARY VLBA DISTANCE TO THE CORE OF OPHIUCHUS, WITH AN ACCURACY OF 4%

Laurent Loinard,[1] Rosa M. Torres,[1] Amy J. Mioduszewski,[2] and Luis F. Rodríguez[1]

Received 2008 January 3; accepted 2008 January 16; published 2008 February 11

ABSTRACT

The nonthermal 3.6 cm radio continuum emission from the young stars S1 and DoAr 21 in the core of Ophiuchus has been observed with the Very Long Baseline Array (VLBA) at 6 and 7 epochs, respectively, between June 2005 and August 2006. The typical separation between successive observations was 2–3 months. Thanks to the remarkably accurate astrometry delivered by the VLBA, the trajectory described by both stars on the plane of the sky could be traced very precisely, and modeled as the superposition of their trigonometric parallax and a uniform proper motion. The best fits yield distances to S1 and DoAr 21 of $116.9^{+7.2}_{-6.4}$ and $121.9^{+5.8}_{-5.3}$ pc, respectively. Combining these results, we estimate the mean distance to the Ophiuchus core to be $120.0^{+4.5}_{-4.2}$ pc, a value consistent with several recent indirect determinations, but with a significantly improved accuracy of 4%. Both S1 and DoAr 21 happen to be members of tight binary systems, but our observations are not frequent enough to properly derive the corresponding orbital parameters. This could be done with additional data, however, and would result in a significantly improved accuracy on the distance determination.

Subject headings: astrometry — binaries: general — magnetic fields — radiation mechanisms: nonthermal — stars: formation — stars: individual (Dolidze-Arakelyan 21, S1)

1. INTRODUCTION

Ophiuchus is one of the most active regions of star formation within a few hundred parsecs of the Sun (e.g., Lada & Lada 2003). It has played an important role in the development of our understanding of star formation and remains an important benchmark for this field of research. Indeed, it has been one of the key targets of the *Spitzer* c2d Legacy program (Padgett et al. 2008) and has been observed in detail at numerous other wavelengths, including X-rays (Ozawa et al. 2005; Gagné et al. 2004), near-infrared (e.g., Haisch et al. 2002; Duchêne et al. 2004; and references therein), submillimeter (Motte et al. 1998; Johnstone et al. 2004), and radio (e.g., André et al. 1987; Leous et al. 1991).

The detailed analysis of this wealth of observational data has been somewhat hampered by the relatively large uncertainty concerning the distance to the Ophiuchus complex. Traditionally assumed to be at 165 pc (Chini 1981), it has recently been suggested to be somewhat closer. For example, de Geus et al. (1989) found a mean photometric distance of 125 ± 25 pc. Knude & Hog (1998), who examined the reddening of stars in the direction of Ophiuchus as a function of their *Hipparcos* distances, also found a clear extinction jump at 120 pc. Using a similar method, Lombardi et al. (2008) also find a distance of about 120 pc for the Ophiuchus core. Finally, Mamajek (2007) identified reflection nebulae within 5° of the center of Ophiuchus and obtained the trigonometric parallax of the illuminating stars from the *Hipparcos* catalog. From the average of these *Hipparcos* parallaxes, he obtains a mean distance to Ophiuchus of 135 ± 8 pc.

This latter result is based on parallax measurements but also takes in a fairly large area around Ophiuchus. It could, therefore, include objects unrelated to Ophiuchus itself. The former results are restricted to regions more concentrated in Ophiuchus, but they are based on indirect distance determinations. Here, we will present measurements of the trigonometric parallax of two young stars (S1 and DoAr 21) directly associated with the Ophiuchus core. This will allow us to estimate directly the distance to this important region of star formation.

2. OBSERVED SOURCES

The star S1 (of spectral type B4; $M \sim 6\ M_\odot$) is among the brightest red and near-infrared objects in Ophiuchus (Grasdalen et al. 1973). It is also the brightest far-infrared member of the cluster (Fazio et al. 1976), a very bright X-ray source (ROXs 14; Montmerle et al. 1983), and the brightest steady radio stellar object in Ophiuchus[3] (Leous et al. 1991). S1 is fairly heavily obscured ($A_V \sim 10$), and there is clear evidence for an interaction between S1 and the dense gas associated with Oph A and traced by DCO^+ emission (Loren et al. 1990). Moreover, the age of the H II region excited by S1 is estimated to be about 5000 yr (André et al. 1988). All this demonstrates that S1 can safely be assumed to be a member of the Ophiuchus core.

DoAr 21 (Dolidze-Arakelyan 21) is a somewhat less massive star (~2.2 $M_\odot$) of spectral type K1 (E. Jensen et al., in preparation). Like S1, it is fairly obscured ($A_V \sim 6$–7) and probably younger than 10^6 yr. It is associated with a bright X-ray source (ROXs 8; Montmerle et al. 1983) and with a strongly variable radio source (Feigelson & Montmerle 1985). Although it has long been classified as a naked T Tauri star (e.g., André et al. 1990), it was recently found to show a substantial infrared excess at 25 μm (E. Jensen et al., in preparation) suggestive of a circumstellar disk. Given its youth and its location in the Ophiuchus core, DoAr 21 is almost certainly also a bona fide member of the Ophiuchus complex.

As mentioned above, both S1 and DoAr 21 are fairly strong radio sources. Indeed, both have been detected at 6 cm in previous very long baseline interferometry (VLBI) experiments: S1 with a flux density of 6–9 mJy (André et al. 1991) and DoAr 21 with a flux density of nearly 10 mJy (Phillips et al. 1991).

[1] Centro de Radiostronomía y Astrofísica, Universidad Nacional Autónoma de México, Apartado Postal 72-3 (Xangari), 58089 Morelia, Michoacán, México; l.loinard@astrosmo.unam.mx.

[2] National Radio Astronomy Observatory, Array Operations Center, 1003 Lopezville Road, Socorro, NM 87801.

[3] As shown by Feigelson & Montmerle (1985), and as we shall confirm in §§ § 4.1 and § 4.2, DoAr 21 can occasionally become brighter than S1.

TABLE 1
OBSERVATION RESULTS

Date	JD	α (J2000.0) 16^h26^m	δ (J2000.0) $-24°23'$	Flux (mJy)	Noise (mJy beam^{-1})
S1:					
2005 Jun 24	2,453,545.73	34.s1739533 ± 0.s0000015	28.″426953 ± 0.″000056	7.03 ± 0.56	0.28
2005 Sep 15	2,453,628.50	34.s1736922 ± 0.s0000020	28.″432094 ± 0.″000062	4.56 ± 0.47	0.23
2005 Dec 17	2,453,722.25	34.s1743677 ± 0.s0000012	28.″441493 ± 0.″000044	4.35 ± 0.35	0.19
2006 Mar 15	2,453,810.01	34.s1746578 ± 0.s0000019	28.″451273 ± 0.″000048	5.33 ± 0.41	0.17
2006 Jun 03	2,453,889.79	34.s1740172 ± 0.s0000006	28.″455940 ± 0.″000023	3.29 ± 0.13	0.07
2006 Aug 22	2,453,969.54	34.s1732962 ± 0.s0000012	28.″462601 ± 0.″000050	4.35 ± 0.22	0.09
DoAr 21:					
2005 Sep 08	2,453,621.52	03.s0189304 ± 0.s0000065	36.″343394 ± 0.″00013	11.78 ± 1.41	0.35
2005 Nov 16	2,453,691.33	03.s0191097 ± 0.s0000023	36.″344504 ± 0.″00005	20.34 ± 1.42	0.55
2006 Jan 08	2,453,744.19	03.s0191069 ± 0.s0000059	36.″355803 ± 0.″00023	0.39 ± 0.12	0.05
2006 Jan 19	2,453,755.16	03.s0191795 ± 0.s0000028	36.″355677 ± 0.″00013	0.97 ± 0.19	0.11
2006 Mar 28	2,453,822.97	03.s0189625 ± 0.s0000070	36.″361924 ± 0.″00020	1.49 ± 0.28	0.13
2006 Jun 04	2,453,890.78	03.s0182041 ± 0.s0000019	36.″363763 ± 0.″00010	1.92 ± 0.23	0.11
2006 Aug 24	2,453,971.53	03.s0169857 ± 0.s0000037	36.″369957 ± 0.″00016	1.45 ± 0.32	0.16

3. OBSERVATIONS

In this Letter, we will make use of two series of continuum 3.6 cm (8.42 GHz) observations obtained with the VLBA. Six observations of S1 were collected between June 2005 and August 2006, and seven observations of DoAr 21 were obtained between September 2005 and August 2006 (see Table 1 for details). Each observation consisted of a series of cycles, with 2 minutes spent on-source and 1 minute spent on the phase-referencing quasar J1625−2527, located 1° south of both targets. J1625−2527 is a very compact extragalactic source whose absolute position ($\alpha_{J2000.0} = 16^h25^m46.^s8916$, $\delta_{J2000.0} = -25°27'38.''327$) is known to better than 0.5 mas (Beasley et al. 2002). The data were edited and calibrated using the Astronomical Image Processing System (AIPS; Greisen 2003). The basic data reduction followed the standard VLBA procedures for phase-referenced observations and was described in detail in Loinard et al. (2007). Since the density of compact quasars known around Ophiuchus at the time of our observations was insufficient, we could not apply the multisource calibration described in Torres et al. (2007).

Because of the significant overheads that were necessary to properly calibrate the data, only about 2 of the 4 hr of telescope time allocated to each of our observations were actually spent on-source. Once calibrated, the visibilities were imaged with a pixel size of 50 μas after weights intermediate between natural and uniform (ROBUST = 0 in AIPS) were applied. This resulted in typical rms noise levels of 0.1–0.3 mJy, depending on the weather conditions and source strength (Table 1). Both S1 and DoAr 21 were detected with a signal-to-noise ratio of better than 7 at each epoch (Table 1).

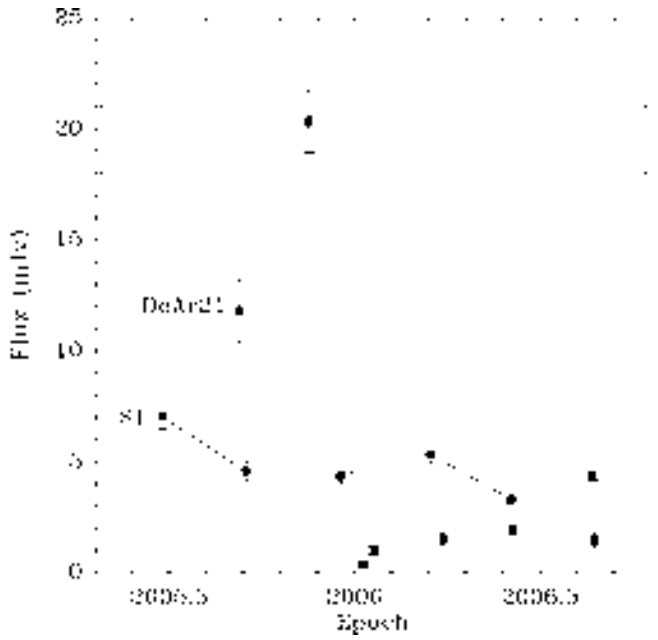

FIG. 1.—Radio flux of S1 (*solid line*) and DoAr 21 (*dotted line*) as a function of time.

4. RESULTS, DISCUSSIONS, AND CONCLUSIONS

4.1. *Properties of S1*

The mean 3.6 cm flux of S1 in our data is 4.8 mJy, and the dispersion about that mean is 1.2 mJy (see Fig. 1). This shows that S1 is variable at the level of about 25% on timescales of months to years. This modest level of variability is certainly not unexpected for a nonthermal source associated with an active stellar magnetosphere (Feigelson & Montmerle 1999). As mentioned earlier, André et al. (1991) reported a VLBI detection of S1 at 6 cm. They found that, among many other things, the source was somewhat resolved in their observations, with an FWHM extension of about 1.7 mas. The radio emission associated with S1 is also found to be resolved in *all* six of our observations, with a deconvolved mean FWHM of about 0.95 mas. This is somewhat smaller than the figure reported by André et al. (1991), but we note (1) that our observations and those of André et al. (1991) were obtained at different wavelengths and (2) that, at some of our epochs, the size of the emission reached 1.5 mas, whereas, at other epochs, it was smaller than 0.5 mas. At the distance of S1 (see below), 0.95 mas corresponds to about 24 $R_\odot$. The diameter of S1 is expected to be about 8.5 $R_\odot$ (André et al. 1991), so its magnetosphere appears to be, on average, 3 times more extended than its photosphere.

The fact that S1 is resolved and that its size varies from epoch to epoch likely produces small random shifts in the photocenter of the radio emission, with an amplitude of a fraction of the size of the emitting region. Therefore, the true uncertainties on the position of S1 are likely to be somewhat larger than the figures quoted in Table 1. Another factor that must be taken into account is that S1 is known to be a member of a binary system with a separation of about 20 mas (Richichi et al. 1994). The companion is inferred to be about 4 times dimmer than the primary at the K band, so it is likely to be significantly less massive (Richichi et al. 1994). If we assume

S1 to be a 6 $M_\odot$ star (as suggested by its B4 spectral type), we expect the orbital period to be about 0.7 yr and the reflex motion of S1 to be about 1–2 mas, if the companion is 10–20 times less massive than S1. Thus, the amplitude of the reflex motion is expected to be larger than the formal errors on the positions of S1 listed in Table 1.

4.2. *Properties of DoAr 21*

The total radio flux of DoAr 21 has long been known to be highly variable (Feigelson & Montmerle 1985). Our observations certainly confirm this strong variability, since the ratio between the highest and the lowest measured flux exceeds 50 (Fig. 1). In particular, the flux during our first two observations (10–20 mJy) is systematically about an order of magnitude higher than that (0.4–2 mJy) at any of the following five observations. Unfortunately, our time coverage is too coarse to decide whether these first two epochs correspond to two different flares or to a single long-duration one.

The extreme variability of DoAr 21, while at odds with the situation in S1, is reminiscent of the case of the spectroscopic binary V773 Tau (e.g., Massi et al. 2002). In the latter source, Massi et al. (2002) showed that the variability had the same periodicity as the orbital motion, with the radio flux being highest at periastron. Interestingly, DoAr 21 was found to be double during our second observation.[4] This suggests that the same mechanism that enhances the radio emission when the two binary components are nearest might be at work in both objects. The separation between the two components of DoAr 21 in our second observation is about 5 mas. This value, of course, corresponds to the projected separation; the actual distance between them must be somewhat larger. Moreover, if the mechanisms at work in DoAr 21 and V773 Tau are similar, then DoAr 21 must have been near periastron during our second epoch, and the orbit must be somewhat eccentric. As a consequence of these two effects, the semimajor axis of the orbit is likely to be a few times larger than the measured separation between the components at our second epoch, perhaps 10–15 mas. At the distance of DoAr 21, this corresponds to 1.2–1.8 AU. For a mass of 2.2 $M_\odot$ (see § 1), the corresponding orbital period is 0.4–1.3 yr, and one would expect the source to oscillate with this kind of periodicity.

4.3. *Astrometry*

The absolute positions of S1 and DoAr 21 (listed in the third and fourth columns of Table 1) were determined using a two-dimensional Gaussian-fitting procedure (task JMFIT in AIPS). This task provides an estimate of the position errors (also given in the third and fourth columns of Table 1) based on the expected theoretical astrometric precision of an interferometer (Condon 1997). Systematic errors, however, usually limit the actual precision of VLBI astrometry to several times this theoretical value (e.g., Pradel et al. 2006; Loinard et al. 2007). Moreover, we have just seen that the extended magnetosphere of S1 and the reflex motions of both S1 and DoAr 21 are likely to produce significant shifts in the positions of the source photocenters. While the effect of an extended magnetosphere might be to produce a random jitter, the reflex orbital motions ought to generate oscillations with a periodicity equal to that of the orbital motions. Our observations, however, are currently insufficient to properly fit full Keplerian orbits. Instead, in the present Letter, we represent the possible systematic calibration errors, as well as the jitter due to extended magnetospheres and the oscillations due to reflex motions, by a constant error term (the value of which will be determined below) that we add quadratically to the errors given in Table 1. The displacements of both S1 and DoAr 21 on the celestial sphere are then modeled as a combination of their trigonometric parallaxes (π) and their proper motions (μ_α and μ_δ), assumed to be uniform and linear. The astrometric parameters were determined using a least-square fit based on a singular value decomposition scheme (see Loinard et al. 2007 for details). The reference epoch was taken at the mean of each set of observations (JD 2,453,757.63 $\equiv$ J2006.061 for S1 and JD 2,453,796.52 $\equiv$ J2006.167 for DoAr 21). The best fit for S1 (Fig. 2*a*) yields the following astrometric parameters:

$$\alpha_{\rm J2006.061} = 16^{\rm h}26^{\rm m}34\overset{\rm s}{.}174127 \pm 0\overset{\rm s}{.}000026,$$
$$\delta_{\rm J2006.061} = -24^\circ 23' 28\overset{''}{.}44498 \pm 0\overset{''}{.}00028,$$
$$\mu_\alpha \cos\delta = -3.88 \pm 0.87 \text{ mas yr}^{-1},$$
$$\mu_\delta = -31.55 \pm 0.69 \text{ mas yr}^{-1},$$
$$\pi = 8.55 \pm 0.50 \text{ mas}.$$

For DoAr 21, on the other and, we get (Fig. 2*b*) the following astrometric parameters:

$$\alpha_{\rm J2006.167} = 16^{\rm h}26^{\rm m}03\overset{\rm s}{.}018535 \pm 0\overset{\rm s}{.}000020,$$
$$\delta_{\rm J2006.167} = -24^\circ 23' 36\overset{''}{.}35830 \pm 0\overset{''}{.}00022,$$
$$\mu_\alpha \cos\delta = -26.47 \pm 0.92 \text{ mas yr}^{-1},$$
$$\mu_\delta = -28.23 \pm 0.73 \text{ mas yr}^{-1},$$
$$\pi = 8.20 \pm 0.37 \text{ mas}.$$

To obtain a reduced χ^2 of 1 in both right ascension and declination, one must add quadratically 0.062 ms of time, and 0.67 mas to the statistical errors of S1 listed in Table 1, and 0.053 ms of time, and 0.57 mas to the statistical errors of DoAr 21. These figures include all the unmodeled sources of positional shifts mentioned earlier. Interestingly, the residuals of the fit to the S1 data (inset in Fig. 2*a*) are not random but seem to show an ~0.7 yr periodicity, as expected from the reflex motions (§ 4.1). Similarly, the residuals from the fit to DoAr 21 seem to show a periodicity of ~1.2 yr (Fig. 2*b*, *inset*), within the range of expected orbital periods of that system (§ 4.2). This suggests that the errors are largely dominated by the unmodeled binarity of both sources and that additional observations designed to provide a better characterization of the orbits ought to improve significantly the precision on the trigonometric parallax determinations.

The distance to S1 deduced from the parallax calculated above is $116.9^{+7.2}_{-6.4}$ pc, whereas the distance deduced for DoAr 21 is $121.9^{+5.8}_{-5.3}$ pc. The weighted mean of these two parallaxes is 8.33 ± 0.30, corresponding to a distance of $120.0^{+4.5}_{-4.2}$ pc. Since both S1 and DoAr 21 are bona fide members of the Ophiuchus core, this figure must represent a good estimate of the distance to this important region of star formation. Note that it is in good agreement with several recent determinations (e.g., de Geus et al. 1989; Knude & Hog 1998; Lombardi et al. 2008), but with a significantly improved relative error of 4%. This level of accuracy is likely to be further improved

[4] The position given in Table 1 is that of the brightest of the two components. The second component is offset by more than 5 mas from the position of the steady component expected from the astrometry fits presented in § 4.3.

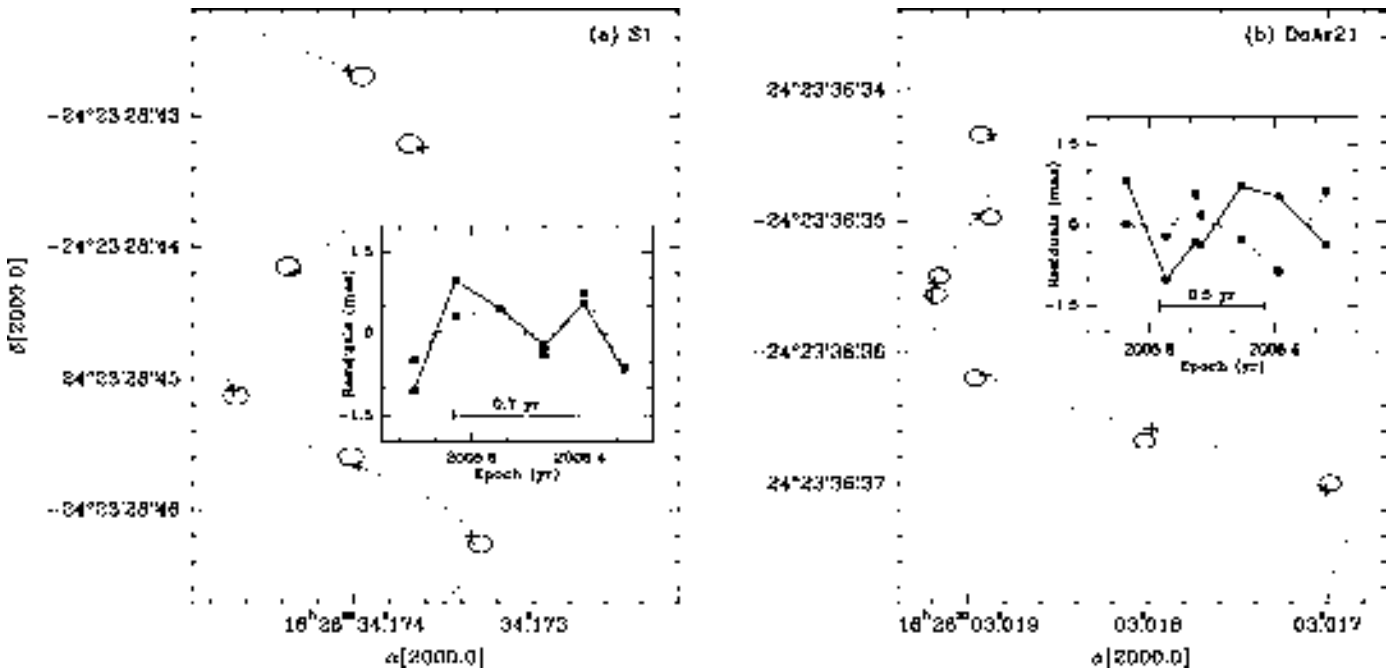

FIG. 2.—Measured positions and best fits for S1 (*a*) and DoAr 21 (*b*). The observed positions are shown as ellipses, the sizes of which represent the magnitudes of the errors. The positions at each epoch expected from the best fits are shown as plus signs. The insets show the residuals (fit observation) in right ascension (*solid line*) and declination (*dotted line*).

once additional observations of S1 and DoAr 21, designed to characterize their orbital motions, are available. Such observations are currently being collected at the VLBA. A significant improvement in the distance estimate will also be obtained once the parallax to other sources (also currently observed at the VLBA) are measured.

L. L., R. M. T, and L. F. R. acknowledge the financial support of DGAPA, UNAM, and CONACyT, México. NRAO is a facility of the National Science Foundation operated under cooperative agreement by Associated Universities, Inc.

REFERENCES

André, P., Montmerle, T., & Feigelson, E. D. 1987, AJ, 93, 1182
André, P., Montmerle, T., Feigelson, E. D., & Steppe, H. 1990, A&A, 240, 321
André, P., Montmerle, T., Feigelson, E. D., Stine, P. C., & Klein, K.-L. 1988, ApJ, 335, 940
André, P., Phillips, R. B., Lestrade, J.-F., & Klein, K.-L. 1991, ApJ, 376, 630
Beasley, A. J., Gordon, D., Peck, A. B., Petrov, L., MacMillan, D. S., Fomalont, E. B., & Ma, C. 2002, ApJS, 141, 13
Chini, R. 1981, A&A, 99, 346
Condon, J. J. 1997, PASP, 109, 166
de Geus, E. J., de Zeeuw, P. T., & Lub, J. 1989, A&A, 216, 44
Duchêne, G., Bouvier, J., Bontemps, S., André, P., & Motte, F. 2004, A&A, 427, 651
Fazio, G. G., Low, F. J., Wright, E. L., & Zeilik, M., II 1976, ApJ, 206, L165
Feigelson, E. D., & Montmerle, T. 1985, ApJ, 289, L19
Feigelson, E. D., & Montmerle, T., 1999, ARA&A, 37, 363
Gagné, M., Skinner, S. L., & Daniel, K. J. 2004, ApJ, 613, 393
Grasdalen, G. L., Strom, K. M., & Strom, S. E. 1973, ApJ, 184, L53
Greisen, E.W. 2003, in Information Handling in Astronomy—Historical Vistas, ed. A. Heck (Dordrecht: Kluwer), 109
Haisch, K. E., Jr., Barsony, M., Greene, T. P., & Ressler, M. E. 2002, AJ, 124, 2841
Johnstone, D., Di Francesco, J., & Kirk, H. 2004, ApJ, 611, L45
Knude, J., & Hog, E. 1998, A&A, 338, 897
Lada, C. J., & Lada, E. A. 2003, ARA&A, 41, 57
Leous, J. A., Feigelson, E. D., Andre, P., & Montmerle, T. 1991, ApJ, 379, 683
Loinard, L., Torres, R. M., Mioduszewski, A. J., Rodríguez, L. F., González-Lópezlira, R. A., Lachaume, R., Vázquez, V., & González, E. 2007, ApJ, 671, 546
Lombardi, M., Lada, C. J., & Alves, J. 2008, A&A, in press
Loren, R. B., Wootten, A., & Wilking, B. A. 1990, ApJ, 365, 269
Mamajek, E. E. 2007, preprint (astro-ph/0709.0505)
Massi, M., Menten, K., & Neidhöfer, J. 2002, A&A, 382, 152
Montmerle, T., Koch-Miramond, L., Falgarone, E., & Grindlay, J. E. 1983, ApJ, 269, 182
Motte, F., Andre, P., & Neri, R. 1998, A&A, 336, 150
Ozawa, H., Grosso, N., & Montmerle, T. 2005, A&A, 438, 661
Padgett, D. L., et al. 2008, ApJ, 672, 1013
Phillips, R. B., Lonsdale, C. J., & Feigelson, E. D. 1991, ApJ, 382, 261
Pradel, N., Charlot, P., & Lestrade, J.-F. 2006, A&A, 452, 1099
Richichi, A., Leinert, C., Jameson, R., & Zinnecker, H. 1994, A&A, 287, 145
Torres, R. M., Loinard, L., Mioduszewski, A. J., & Rodríguez, L. F. 2007, ApJ, 671, 1813

E

Tidal Forces as a Regulator of Star Formation in Taurus

Javier Ballesteros-Paredes, Gilberto Gómez, Laurent Loinard, Rosa M. Torres & Bárbara Pichardo

Monthly Notices of the Royal Astronomical Society: Letters, 395, L81, 2009

Abstract. Only a few molecular clouds in the solar neighbourhood exhibit the formation of only low-mass stars. Traditionally, these clouds have been assumed to be supported against more vigorous collapse by magnetic fields. The existence of strong magnetic fields in molecular clouds, however, poses serious problems for the formation of stars and of the clouds themselves. In this Letter, we review the three-dimensional structure and kinematics of Taurus –the archetype of a region forming only low-mass stars– as well as its orientation within the Milky Way. We conclude that the particularly low star formation efficiency in Taurus may naturally be explained by tidal forces from the Galaxy, with no need for magnetic regulation or stellar feedback.

Mon. Not. R. Astron. Soc. **395,** L81–L84 (2009) doi:10.1111/j.1745-3933.2009.00647.x

Tidal forces as a regulator of star formation in Taurus

Javier Ballesteros-Paredes,[1⋆] Gilberto C. Gómez,[1⋆] Laurent Loinard,[1⋆] Rosa M. Torres[1⋆] and Bárbara Pichardo[2⋆]

[1]*Centro de Radioastronomía y Astrofísica, Universidad Nacional Autónoma de México, Apdo. Postal 72-3 (Xangari), Morelia, Michocán 58089, México*
[2]*Instituto de Astronomía, Universidad Nacional Autónoma de México, Apdo. Postal 70-264, 04510, México, D.F., México*

Accepted 2009 February 26. Received 2009 February 21; in original form 2009 January 16

ABSTRACT

Only a few molecular clouds in the solar neighbourhood exhibit the formation of only low-mass stars. Traditionally, these clouds have been assumed to be supported against more vigorous collapse by magnetic fields. The existence of strong magnetic fields in molecular clouds, however, poses serious problems for the formation of stars and of the clouds themselves. In this Letter, we review the three-dimensional structure and kinematics of Taurus – the archetype of a region forming only low-mass stars – as well as its orientation within the Milky Way. We conclude that the particularly low star formation efficiency in Taurus may naturally be explained by tidal forces from the Galaxy, with no need for magnetic regulation or stellar feedback.

Key words: stars: formation – ISM: clouds – ISM: kinematics and dynamics – galaxies: kinematics and dynamics.

1 INTRODUCTION

Few nearby molecular clouds (e.g. Taurus, Chamaeleon I and II) are observed to form only low-mass stars. Assuming a universal initial mass function, the lack of high-mass young stars in these regions indicates a low overall star-forming rate compared with clouds-like Orion where both low- and high-mass stars are actively being formed. Traditionally, the clouds forming only low-mass stars have been assumed to be supported against more vigorous collapse by magnetic fields. In such a scheme, stars can form only after substantial magnetic flux has been removed locally via ambipolar diffusion (e.g. Shu, Adams & Lizano 1987). The Taurus Molecular Cloud (TMC) is often cited as the archetype for this picture of isolated, low-mass star formation.

There are, however, some difficulties with this scenario. On one hand, strong magnetic fields ought to prevent the formation of molecular clouds by large-scale compressions in the first place (Hartmann, Ballesteros-Paredes & Bergin 2001). In addition, there is a problem with the synchronization of star formation along large distances. While molecular clouds have dynamical time-scales of the order of 10–20 Myr, most active star-forming regions (i.e. those still containing molecular gas) have populations with ages $\leq$3 Myr (Hartmann et al. 2001). The lack of old stars associated with molecular clouds (the so-called post-T Tauri problem, see Herbig 1978; Herbig, Vrba & Rydgren 1986) has been explained in terms of rapid assembling of molecular clouds by large-scale flows, which may be able to trigger star formation over large regions almost simultaneously. Such a rapid assembling of molecular clouds and synchronized events of star formation over large distances require magnetic fields to *not* be dominant (Hartmann et al. 2001).

Moreover, the ambipolar diffusion time-scale is not unique. It depends, among other parameters, on the ionization fraction, which in turn depends on the precise local shielding conditions. Differences in the degree of ionization and magnetic field intensities should introduce an unobserved spread of at least several Myr in the onset of star formation. This brings us back to the post-T Tauri problem (Ballesteros-Paredes & Hartmann 2007).

Different numerical work has examined the picture of rapid molecular cloud assembling from different points of view and found it to be a viable mechanism (see Ballesteros-Paredes et al. 2007, and references therein). An important difficulty, however, is the low star formation efficiency observed in actual molecular clouds, compared with those reported in simulations. As discussed by Heitsch & Hartmann (2008), most simulations are performed in closed boxes, with no stellar energy feedback. In such a situation, the amount of mass in collapsed objects after one crossing time is usually large, with values between 10 and 30 per cent, depending on the mass and the level of turbulence of the model (Klessen, Heitsch & Mac Low 2000; Vázquez-Semadeni et al. 2003; Vázquez-Semadeni, Kim & Ballesteros-Paredes 2005). In comparison, typical values of the star formation efficiency observed in molecular clouds are only a few per cent (Myers et al. 1986). When feedback from massive stars is included in the simulations, the measured efficiencies are significantly smaller (Passot, Vázquez-Semadeni & Pouquet 1995), suggesting that massive stars are a key ingredient in regulating the

⋆E-mail: j.ballesteros@crya.unam.mx (JB-P); g.gomez@crya.unam.mx (GCG); l.loinard@crya.unam.mx (LL); r.torres@crya.unam.mx (RMT); barbara@astroscu.unam.mx (BP)

efficiency of star formation (see also Ballesteros-Paredes 2004, and references therein).

In regions where no massive stars are formed, however, a different mechanism is clearly required. And since magnetic regulation brings a number of additional problems, it is worth looking for alternative possibilities.

Recently, Ballesteros-Paredes et al. (2009, hereafter Paper I) have analysed the complete gravitational content of molecular clouds within a given spiral galaxy. They write the total gravitational energy of a molecular cloud, W, as follows

$$W = -\frac{1}{2}\int_V \rho\Phi_{\rm cl}{\rm d}V - \int_V x_i\rho\frac{\partial\Phi_{\rm ext}}{\partial x_i}{\rm d}V, \quad (1)$$

where ρ is the density, $\Phi_{\rm cl}$ is the gravitational potential due to the mass of the cloud, i.e. the mass inside its volume V, $\Phi_{\rm ext}$ is the gravitational potential due to the mass outside the cloud, and x_i is the ith component of the position vector. The first term on the right-hand side is the gravitational energy $E_{\rm grav}$, while the second term is the energy due to the mass outside of the cloud, which we call the tidal energy. This second term may cause a compression or a disruption of molecular clouds, depending on their size, position and orientation within the host galaxy. Thus, tidal interactions may play a significant role in the overall stability of molecular clouds, and, therefore, on the efficiency of star formation within them.

In this Letter, we investigate the role that tidal interactions might play in the regulation of star formation in the TMC. In Section 2, we examine the three-dimensional structure and the orientation of Taurus within the Milky Way using recent data. We then calculate the relative contribution of self-gravity and tidal interactions for such a configuration (Section 3) and discuss our results in Section 4. The conclusions are given in Section 5.

2 THREE-DIMENSIONAL STRUCTURE OF TAURUS

In CO maps, the TMC extends for about 10° on the sky, with filaments that have aspect ratios between 5:1 and 10:1 (e.g. Goldsmith et al. 2008). It has a total molecular mass between 10^4 and $\sim 2.4 \times 10^4\,{\rm M}_\odot$ (Goldsmith et al. 2008), and is located roughly towards the Galactic anticentre (at $l \sim 170°$–$176°$) but at a Galactic latitude of $-15°$ to $-16°$. Recent multi-epoch VLBA observations have provided distances to several young stars located across the TMC complex with accuracies better than 1 per cent (corresponding to absolute errors of ∼0.5–1 pc) (Loinard et al. 2005, 2007; Torres et al. 2007, 2009). The obtained distances range from about 160 pc for HP Tau, near the eastern edge of the complex at $(l, b) \sim (175°, -16°)$ (Torres et al. 2009), down to about 130 pc for the closest stars, Hubble 4 and HDE 283572, in the western part of the TMC at $(l, b) \sim (170°, -15°)$ (Torres et al. 2007). This situation is quite unlike that in the core of Ophiuchus (Loinard et al. 2008a) or the Orion nebula (Menten et al. 2007) where different stars are found at very similar distances.

The properties mentioned above indicate that it is appropriate to model the TMC as a $10^4\,{\rm M}_\odot$ elongated filament (a prolate spheroid) centred at a distance of 145 pc from the Sun in the direction $(l, b) = (172.5, -15°)$ (see Fig. 1 for a schematic view). This places the TMC about 37.5 pc below the Galactic plane. The long axis of the spheroid was taken to be of 32.37 pc long and, assuming an angular width for the cloud of about 5°, the short axes are 5 pc in length. The density of the spheroid was taken to be constant; for our choice of parameters, its value is $n = 405\,{\rm cm}^{-3}$.

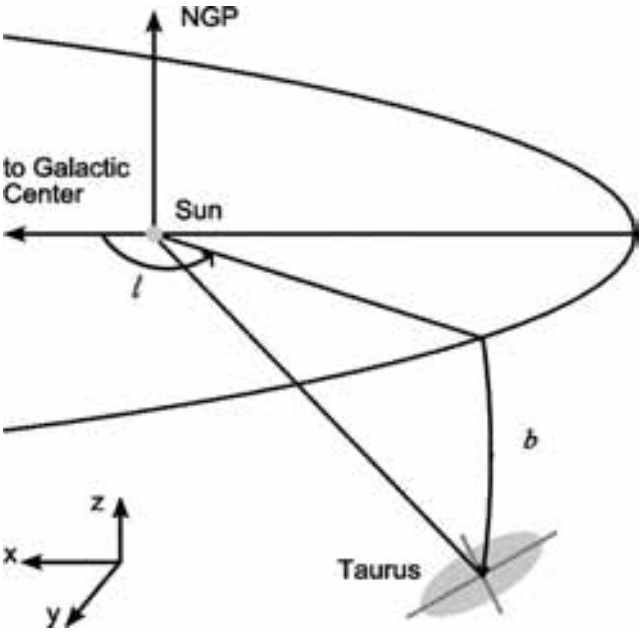

Figure 1. Schematic view of the TMC, according to the distances and positions reported by Loinard et al. (2005, 2007), Torres et al. (2007) and Torres et al. (2009).

We performed an energetics analysis similar to that presented in Paper I, but with one important difference. In our previous work, every parcel of the test cloud had a velocity given by the circular velocity. As most nearby star-forming cloud, however, the TMC has a substantial peculiar velocity (Torres et al. 2009). Therefore, although the calculation of the tidal energy $W_{\rm ext}$ is performed in the standard of rest of the centre of the spheroid, the effective potential must involve the peculiar velocities of the filament. In order to account for those velocities, we calculated the components of the peculiar velocities (u, v, w) using radial velocities from the CO observations (Ungerechts & Thaddeus 1987, see also figs 2 and 3 in Ballesteros-Paredes et al. 1999), and the proper motions of the stars reported by Torres et al. (2007, 2009). We note that the proper motions have been determined with a very good accuracy (± 0.15 mas yr^{-1} in the worst case). However, since the line profile of the gas has some spread around the maximum intensity, we have used radial velocities (express relative to the local standard of rest) ranging from 5 to 5.5 km s^{-1} near the eastern edge of the cloud, and from 5.5 to 6 km s^{-1} for the western part.

3 RESULTS

As in Paper I, the gravitational potential used to calculate the tidal energy $W_{\rm ext}$ includes a Galactic axisymmetric background potential that represents a bulge, a flattened disc and a massive halo, and a bisymmetric potential describing a logarithmic spiral pattern. Our choice of parameters describing this potential reproduces, in particular, the Oort constants, the rotation curve and the local escape velocity (see Pichardo et al. 2003, and references therein). The exact position of the TMC with respect to the Galactic stellar spiral arms is not well known. Thus, we have calculated the ratio between the tidal and the gravitational energy, $W_{\rm ext}/E_{\rm grav}$, as a function of galactocentric angle, θ (Fig. 2). The different curves are the results of our calculations assuming a slightly different radial velocities, in order to account for the scatter in the CO emission (see Section 2).

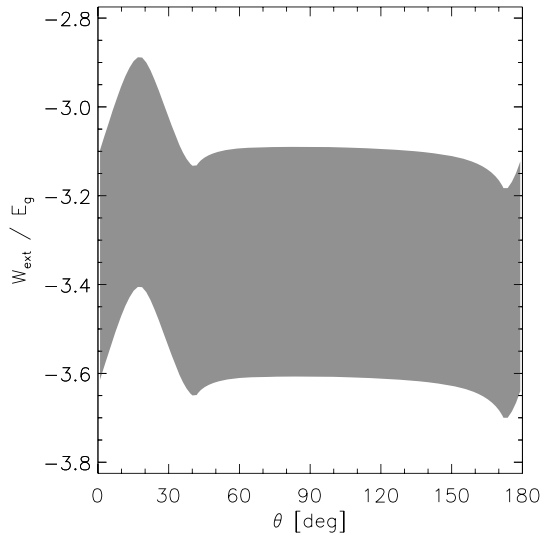

Figure 2. $W_{\rm ext}/E_{\rm grav}$ ratio for an elongated spheroid at the position and orientation, and with the kinematical properties of the TMC as a function of galactocentric angle θ. The shadded area covers the range of radial velocities at the extrema of the spheroid (see Section 2).Since the potential is bisymmetric, we plot the results only for the range $\theta \in [0^\circ, 180^\circ]$.

Since the ratio $W_{\rm ext}/E_{\rm grav}$ scales with density as $1/\rho$ (see Paper I for details), it is straightforward to scale it to a different total mass.

Fig. 2 shows some important points. First of all, the ratio $W_{\rm ext}/E_{\rm grav}$ is always negative, with values between -3 and -3.6 (shaded region), depending on the detailed velocity field assumed for the cloud. This indicates that the tidal energy $W_{\rm ext}$ acts against the gravitational energy, i.e. by trying to disrupt the cloud. Secondly, for this configuration, the tidal energy is larger than the gravitational energy for any azimuthal angle. Thirdly, even close to the spiral arms ($\theta \sim 15^\circ$ in our figure), an elongated cloud highly aligned with the galactocentric radius will also be disrupted.

We have performed the same calculations for smaller clumps at the same position, but with different aspect ratios, densities and sizes. Our results indicate that for smaller and denser regions, the situation is reversed and the gravitational energy exceeds the tidal energy by factors of 10 to 10^5, depending on the properties of the clumps/cores. The situation considered in these calculations corresponds to individual clumps within the TMC, such as Heiles Cloud 2, or Lynds 1495 (see Goldsmith et al. 2008, for details) or to individual dense cores like TMC-1C or Lynds 1517.

This means that if the volume filling factor of the gas is smaller than unity, the small, compact, dense fragments will collapse, but the cloud as a whole will not. By disrupting the cloud, tidal forces prevent global collapse.

4 DISCUSSION

As mentioned in Section 1, magnetic fields and massive stars have been the usual mechanisms invoked to explain the low efficiency of star formation observed in star-forming regions. In the case of Taurus, feedback by massive stars clearly cannot be invoked since there are no such stars. Large magnetic fields, on the other hand, are difficult to reconcile with the synchronized star formation observed in molecular clouds in the solar neighbourhood.

About 10 yr ago, it was proposed that molecular clouds, in general, and Taurus, in particular, could be produced by converging large-scale flows (Ballesteros-Paredes, Hartmann & Vázquez-Semadeni 1999), explaining how star formation can occur simultaneously in dynamically disconnected regions. Hartmann et al. (2001) pointed out that the interstellar gas in the solar neighbourhood becomes gravitationally unstable at the same time that it becomes molecular, and typical magnetic fields are not strong enough to inhibit rapid molecular cloud and star formation. More recently, different authors have reported that turbulent motions may have a gravitational origin (Burkert & Hartmann 2004; Ballesteros-Paredes 2006; Hartmann & Burkert 2007; Vázquez-Semadeni et al. 2007; Field, Blackman & Keto 2008; Heitsch & Hartmann 2008). This revived the idea originally proposed by Goldreich & Kwan (1974) that the supersonic linewidths have a gravitational origin. In particular, Vázquez-Semadeni et al. (2007) showed that collapsing clouds develop a 'virial' type relationship,[1] in which kinetic and gravitational energies are within a factor of 2 of each other. Moreover, Heitsch & Hartmann (2008) have found that, although molecular clouds and their substructures are formed by colliding turbulent flows, some degree of gravitational contraction must occur along the direction perpendicular to the collision of the streams to allow molecular cloud and star formation.

All the work mentioned above suggest that molecular clouds must be, to some degree, in a state of global collapse that typical magnetic fields cannot detain. In this situation, magnetic support cannot be invoked to regulate star formation, and massive stars are seemingly the only agents able to keep the star formation efficiency at a reasonably low value. But what regulates star formation in clouds, like Taurus, which do not harbour massive stars?

The results of the previous section allow us to propose a solution. Like every known large molecular cloud, the TMC has a mass much larger than its Jeans mass, so it could be collapsing vigorously. Because of it position and orientation within the Milky Way, however, it appears to suffer significant large-scale tidal disruptions. This ought to prevent global collapse and limit the efficiency of star formation. Note, however, that tidal disruption is irrelevant at small scales (see Section 3), so lateral collapse (Heitsch & Hartmann 2008) and star formation can proceed in dense cores (as is indeed observed).

According to our results, what defines whether a given molecular cloud develops a large or a small star formation rate is its particular position and orientation in the Galaxy. It would be interesting to test this proposal with other regions of star formation. According to Hartmann & Burkert (2007), Orion has a large degree of global collapse. Our results would then suggest that this complex should not be very elongated along the galactocentric radius. Existing observations in the region of the Orion Nebula (Menten et al. 2007) are consistent with this idea, but the distance to young stars spread over a more extended area will have to be measured to test our prediction. Another region where this proposal could be tested is Ophiuchus, where low- and intermediate-mass stars are present. Although precise distances have been measured for this region (Loinard et al. 2008a), the three-dimensional structure is still not well constrained because of possible confusion with background stars (Loinard et al. 2008b). Perseus would also be an interesting region to study because, like Taurus, it appears to have a filamentary structure. Again, however, an accurate distance is only known for one part of the complex (NGC 1333; Hirota et al. 2008).

[1] It has been proposed to call it 'energy equipartition' relationship, rather than virial relationship, since observations do not allow us to distinguish between energy equipartition and true virial balance (Ballesteros-Paredes 2006).

5 CONCLUSIONS

Our analysis of the full gravitational content of the TMC, i.e. considering not only the gravitational energy, but also the tidal contribution from the Galaxy, indicates that TMC must be suffering significant tidal disruption. This suggests that, unlike other clouds (e.g. Orion see Hartmann & Burkert 2007), TMC is not found in a state of global collapse, explaining thus why it only forms low-mass stars. Small-scale collapse within the complex, on the other hand, is permitted. Such local collapse enhances the formation of molecular gas from H I, and accounts for the rapid formation of stars (Heitsch & Hartmann 2008).

Our result could be tested further if multi-epoch observations similar to those obtained in Taurus by Loinard et al. (2007) and Torres et al. (2007, 2009) are performed for different star-forming regions exhibiting different efficiencies. Such observations are currently underway.

ACKNOWLEDGMENTS

We thank Paola D'Alessio and Lee Hartmann for a careful reading and useful comments on this manuscript. This work was supported by UNAM-PAPIIT grant numbers 110606, IN111007 and IN119708 to JBP, LL and BP, respectively, and CONACYT grant numbers J50402-F, 47860, 50720 and 60581 to GCG, LL, BP and BP, respectively. We have made extensive use of the NASA-ADS data base. The calculations were performed on both the cluster at CRyA-UNAM acquired with grant 36571-E and the cluster Platform 4000 (KanBalam) at DGSCA, UNAM.

REFERENCES

Ballesteros-Paredes J., 2004, Ap&SS, 289, 243
Ballesteros-Paredes J., 2006, MNRAS, 372, 443
Ballesteros-Paredes J., Hartmann L., 2007, Rev. Mex. Astron. Astrofis., 43, 123
Ballesteros-Paredes J., Hartmann L., Vázquez-Semadeni E., 1999, ApJ, 527, 285
Ballesteros-Paredes J., Klessen R. S., Mac Low M., Vázquez-Semadeni E., 2007, in Reipurth B., Jewitt D., Keil K., eds, Protostars and Planets V. Univ. Arizona Press, Tucscon, p. 63
Ballesteros-Paredes J., Gómez G. C., Pichardo B., Vázquez-Semadeni E., 2009, MNRAS, 393, 1563 (Paper I)
Burkert A., Hartmann L., 2004, ApJ, 616, 288
Field G. B., Blackman E. G., Keto E. R., 2008, MNRAS, 385, 181
Goldreich P., Kwan J., 1974, ApJ, 189, 441
Goldsmith P. F., Heyer M., Narayanan G., Snell R., Li D., Brunt C., 2008, ApJ, 680, 428
Hartmann L., Burkert A., 2007, ApJ, 654, 988
Hartmann L., Ballesteros-Paredes J., Bergin E. A., 2001, ApJ, 562, 852
Heitsch F., Hartmann L., 2008, ApJ, 689, 290
Herbig G. H., 1978, in Mirzoyan V., ed., Problems of Physics and Evolution of the Universe. Acad. Sci. Armenian SSR, Yerevan, p. 171
Herbig G. H., Vrba F. J., Rydgren A. E., 1986, AJ, 91, 575
Hirota T. et al., 2008, PASJ, 60, 37
Klessen R. S., Heitsch F., Mac Low M.-M., 2000, ApJ, 535, 887
Loinard L., Miodusewski A. J., Rodriguez L. F., Gonzalez R. A., Rodriguez M. I., Torres R. M., 2005, ApJ, 619, L179
Loinard L., Torres R. M., Mioduszewski A. J., Rodriguez L. F., González-Lópezlira R. A., Lachaume R., Vàzquez V., Gonzáléz E., 2007, ApJ, 671, 546
Loinard L., Torres R. M., Mioduszewski A. J., Rodríguez, L. F., 2008a, ApJ, 675, L29
Loinard L., Torres R. M., Mioduszewski A. J., Rodríguez L. F., 2008b, in Jin W.-J., Platais I., Perryman M. A. C., eds, Proc. IAU Symp. Vol. 248, A Giant Step: From Milli- to Micro-Arcsecond Astrometry. Cambridge Univ. Press, Cambridge, p. 186
Menten K. M., Reid M. J., Forbrich J., Brunthaler A., 2007, A&A, 474, 515
Myers P. C., Dame T. M., Thaddeus P., Cohen R. S., Silverberg R. F., Dwek E., Hauser M. G., 1986, ApJ, 301, 398
Passot T., Vázquez-Semadeni E., Pouquet A., 1995, ApJ, 455, 536
Pichardo B., Martos M., Moreno E., Espresate J., 2003, ApJ, 582, 230
Shu F. H., Adams F. C., Lizano S., 1987, ARA&A, 25, 23
Torres R. M., Loinard L., Mioduszewski A. J., Rodríguez L. F., 2007, ApJ, 671, 1813
Torres R. M., Loinard L., Mioduszewski A. J., Rodríguez L. F. 2009, ApJ, submitted
Ungerechts H., Thaddeus P., 1987, ApJS, 63, 645
Vázquez-Semadeni E., Ballesteros-Paredes J., Klessen R. S., 2003, ApJ, 585, L131
Vázquez-Semadeni E., Kim J., Ballesteros-Paredes J., 2005, ApJ, 630, L49
Vázquez-Semadeni E., Gómez G. C., Jappsen A. K., Ballesteros-Paredes J., González R. F., Klessen R. S., 2007, ApJ, 657, 870

This paper has been typeset from a TEX/LATEX file prepared by the author.

F

VLBA Distance to Nearby Star-Forming Regions III. HP Tau/G2 and the 3D Structure of Taurus Cloud

Rosa M. Torres, Laurent Loinard, Amy J. Mioduszewski & Luis F. Rodríguez
The Astrophysical Journal, 698, 242, 2009

Abstract. Using multiepoch Very Long Baseline Array (VLBA) observations, we have measured the trigonometric parallax of the weak-line T Tauri star HP Tau/G2 in Taurus. The best fit yields a distance of 161.2 ± 0.9 pc, suggesting that the eastern portion of Taurus (where HP Tau/G2 is located) corresponds to the far side of the complex. Previous VLBA observations have shown that T Tau, to the south of the complex, is at an intermediate distance of about 147 pc, whereas the region around L1495 corresponds to the near side at roughly 130 pc. Our observations of only four sources are still too coarse to enable a reliable determination of the three-dimensional structure of the entire Taurus star-forming complex. They do demonstrate, however, that VLBA observations of multiple sources in a given star-forming region have the potential not only to provide a very accurate estimate of its mean distance, but also to reveal its internal structure. The proper motion measurements obtained simultaneously with the parallax allowed us to study the kinematics of the young stars in Taurus. Combining the four observations available so far, we estimate the pe-

culiar velocity of Taurus to be about 10.6 km s^{-1} almost completely in a direction parallel to the Galactic plane. Using our improved distance measurement, we have refined the determination of the position on the H-R diagram of HP Tau/G2, and of two other members of the HP Tau group (HP Tau itself and HP Tau/G3). Most pre-main sequence evolutionary models predict significantly discrepant ages (by 5 Myr) for those three stars –expected to be coeval. Only in the models of Palla & Stahler do they fall on a single isochrone (at 3 Myr).

The Astrophysical Journal, 698:242–249, 2009 June 10 doi:10.1088/0004-637X/698/1/242

VLBA DETERMINATION OF THE DISTANCE TO NEARBY STAR-FORMING REGIONS. III. HP TAU/G2 AND THE THREE-DIMENSIONAL STRUCTURE OF TAURUS

Rosa M. Torres[1], Laurent Loinard[1], Amy J. Mioduszewski[2], and Luis F. Rodríguez[1]
[1] Centro de Radiostronomía y Astrofísica, Universidad Nacional Autónoma de México, Apartado Postal 72–3 (Xangari), 58089 Morelia, Michoacán, Mexico; r.torres@astrosmo.unam.mx
[2] National Radio Astronomy Observatory, Array Operations Center, 1003 Lopezville Road, Socorro, NM 87801, USA
Received 2008 December 16; accepted 2009 March 31; published 2009 May 19

ABSTRACT

Using multiepoch Very Long Baseline Array (VLBA) observations, we have measured the trigonometric parallax of the weak-line T Tauri star HP Tau/G2 in Taurus. The best fit yields a distance of 161.2 ± 0.9 pc, suggesting that the eastern portion of Taurus (where HP Tau/G2 is located) corresponds to the far side of the complex. Previous VLBA observations have shown that T Tau, to the south of the complex, is at an intermediate distance of about 147 pc, whereas the region around L1495 corresponds to the near side at roughly 130 pc. Our observations of only four sources are still too coarse to enable a reliable determination of the three-dimensional structure of the entire Taurus star-forming complex. They do demonstrate, however, that VLBA observations of multiple sources in a given star-forming region have the potential not only to provide a very accurate estimate of its mean distance, but also to reveal its internal structure. The proper motion measurements obtained simultaneously with the parallax allowed us to study the kinematics of the young stars in Taurus. Combining the four observations available so far, we estimate the peculiar velocity of Taurus to be about 10.6 km s^{-1} almost completely in a direction parallel to the Galactic plane. Using our improved distance measurement, we have refined the determination of the position on the H–R diagram of HP Tau/G2, and of two other members of the HP Tau group (HP Tau itself and HP Tau/G3). Most pre-main-sequence evolutionary models predict significantly discrepant ages (by 5 Myr) for those three stars—expected to be coeval. Only in the models of Palla & Stahler do they fall on a single isochrone (at 3 Myr).

Key words: astrometry – magnetic fields – radiation mechanisms: non-thermal – radio continuum: stars – stars: formation – stars: individual (HP Tau/G2)

1. INTRODUCTION

Several recent observations (e.g., Loinard et al. 2005, 2007, 2008; Torres et al. 2007; Menten et al. 2007; Xu et al. 2006) have demonstrated that multiepoch VLBI observations can be used to measure the trigonometric parallax of nearby young stars to better than a few percent. Since the indirect methods traditionally used to estimate the distance to nearby star-forming regions (e.g., Elias 1978a, 1978b; Kenyon et al. 1994; Knude & Hog 1998) typically have uncertainties of 20%, VLBI observations have the potential of dramatically improving our knowledge of the space distribution of star-formation around the Sun. With this goal in mind, we have initiated a large project aimed at accurately measuring the trigonometric parallax of a sample of nearby magnetically active young stars using the 10 element Very Long Baseline Array (VLBA) of the National Radio Astronomy Observatory (NRAO). In the previous papers of this series, we have reported the distance and proper motions of three young stars in Taurus (T Tauri—Loinard et al. 2007; Hubble 4 and HDE 283572—Torres et al. 2007). In the present article, we will concentrate on HP Tau/G2, a young star located near the eastern edge of the Taurus complex.

The well-known variable star HP Tau was discovered by Cohen & Kuhi (1979) to be surrounded by a small group of young stars (called HP Tau/G1, HP Tau/G2, and HP Tau/G3). HP Tau/G1 is located about 20″ north of HP Tau, whereas HP Tau/G2 and HP Tau/G3 are about 15″ to its southeast (see the finding charts in Figure 22 of Cohen & Kuhi 1979). HP Tau/G2 and HP Tau/G3 are believed to form a gravitationally bound system with a separation of about 10″. Recently, HP Tau/G3 was itself found to be a tight binary (Richichi et al. 1994), so the HP Tau/G2–HP Tau/G3 system appears to be a hierarchical triple system. HP Tau/G2 is a weak-line T Tauri star of spectral type G0, with an effective temperature of 6030 K (Briceño et al. 2002). It is somewhat obscured ($A_V \sim$ 2.1 mag) and has a bolometric luminosity of 6.5 $L_\odot$ (Briceño et al. 2002; Kenyon & Hartmann 1995). This corresponds to an age of about 10.5 Myr and a mass of 1.58 $M_\odot$ (Briceño et al. 2002). The first radio detection of HP Tau/G2 was reported by Bieging et al. (1984) who found a 5 GHz flux of 5–7 mJy. A few years later, however, the flux had fallen to only about 0.3 mJy (Cohen & Bieging 1986). Such strong variability is suggestive of nonthermal processes (e.g., Feigelson & Montmerle 1999). The successful detection of HP Tau/G2 in VLBI experiments (at levels of 1–3 mJy) by Phillips et al. (1991) confirmed the nonthermal origin of the radio emission.

2. OBSERVATIONS AND DATA CALIBRATION

In this paper, we will make use of a series of nine continuum 3.6 cm (8.42 GHz) observations of HP Tau/G2 obtained between 2005 September and 2007 December with the VLBA (Table 1). Our phase center was at $\alpha_{J2000.0} = 04^h35^m54^s.161$, $\delta_{J2000.0} = +22^\circ54'13''.492$. Each observation consisted of series of cycles with 2 minutes spent on source, and 1 minute spent on the main phase-referencing quasar J0426+2327, located 2°.14 away. J0426+2327 is a compact ICRF source (Fey et al. 2004) whose absolute position is known to better than 0.7 mas. Every 24 minutes, we also observed two secondary calibrators (J0435+2532 and J0449+1754) which, together with the primary calibrator, form a triangle around the astronomical target (Figure 1).

The data were edited and calibrated using the Astronomical Image Processing System (AIPS; Greisen 2003). The basic data

Table 1
Measured Source Positions and Flux Densities

Mean UT date (yyyy.mm.dd hh:mm)	Julian Day	α (J2000.0) 04^h35^m	σ_α	δ (J2000.0) $22^\circ54'$	σ_δ	f_ν (mJy)	σ (mJy beam^{-1})
2005.09.07 12:36	2453621.02	$54^s.1613574$	$0^s.0000034$	13″.41131	0″.00009	0.71	0.06
2005.11.16 08:01	2453690.83	$54^s.1612212$	$0^s.0000019$	13″.40798	0″.00007	0.97	0.07
2006.01.23 03:33	2453758.65	$54^s.1609360$	$0^s.0000042$	13″.40439	0″.00010	0.99	0.07
2006.03.31 23:06	2453826.46	$54^s.1610940$	$0^s.0000032$	13″.40161	0″.00010	0.68	0.07
2006.06.10 18:27	2453897.27	$54^s.1617432$	$0^s.0000008$	13″.39959	0″.00002	3.06	0.08
2006.09.08 12:33	2453987.02	$54^s.1623557$	$0^s.0000024$	13″.39681	0″.00007	1.08	0.06
2007.06.04 18:56	2454256.29	$54^s.1627018$	$0^s.0000038$	13″.38267	0″.00013	0.63	0.07
2007.09.03 12:53	2454347.04	$54^s.1633509$	$0^s.0000025$	13″.38127	0″.00008	0.78	0.06
2007.12.04 06:51	2454438.79	$54^s.1631378$	$0^s.0000037$	13″.37605	0″.00009	0.76	0.05

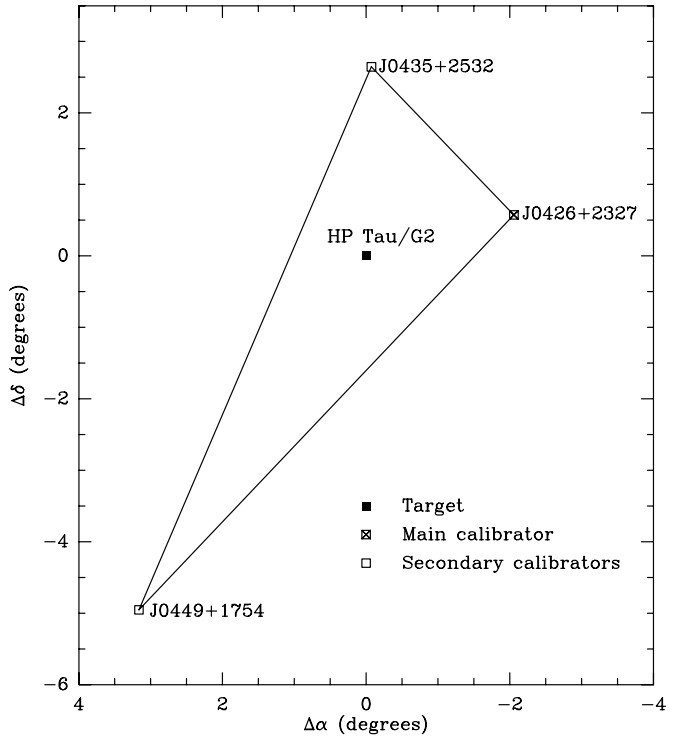

Figure 1. Relative position of the astronomical target, the main calibrator (J0426+2327), and the secondary calibrators (J0435+2532, and J0449+1754).

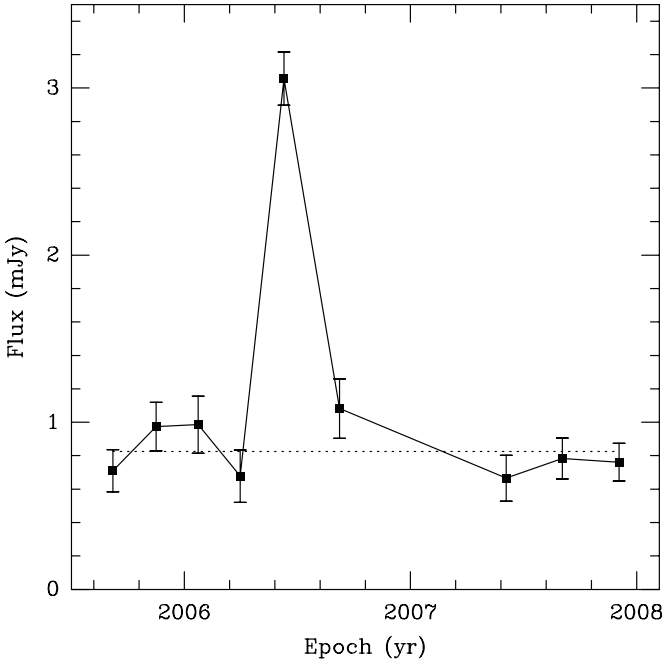

Figure 2. Time evolution of the 3.6 cm flux of HP Tau/G2. Note the flare during the fifth observation.

reduction followed the standard VLBA procedure for phase-referenced observations, and was described in detail in Loinard et al. (2007). Using the secondary calibrators, we applied the multisource calibration strategy described in Torres et al. (2007) to correct for systematic errors due to inaccuracies in the troposphere model used, and to clock, antenna, and source position errors. This resulted in significant improvements in the final phase calibration and image quality.

Six hours of telescope time were allocated to each of the first six observations, whereas 9 hr were allocated for each of the last three. Because of the time spent on the calibrators, however, only about 3 and 5 hr were actually spent on source during the first six and the following three observations, respectively. Once calibrated, the visibilities were imaged with a pixel size of 50 μas after weights intermediate between natural and uniform (ROBUST = 0 in AIPS) were applied. This resulted in typical rms noise levels of 0.06–0.08 and 0.05–0.07 mJy beam^{-1} during the first six and the last three observations, respectively (Table 1). The source was detected with a signal-to-noise ratio of 10 or better at each epoch (Table 1). The source position (also listed in Table 1) was determined using a two-dimensional Gaussian fitting procedure (task JMFIT in AIPS). This task provides an estimate of the position error (Columns 4 and 6 of Table 1) based on the expected theoretical astrometric precision of an interferometer (Condon 1997). However, in spite of the extra calibration steps taken to improve the phase calibration, uncorrected systematic errors still exist, and must be added quadratically to the values listed in Table 1. These remaining systematic errors are difficult to estimate a priori, and may depend on the structure of the source under consideration. Here, we will estimate them from the fits to the data (see below).

3. RESULTS

3.1. Variability and Morphological Changes

The flux of HP Tau/G2 was fairly constant around 0.8 mJy at eight of our nine observations. During the fifth observation (2006 June), however, HP Tau/G2 clearly underwent a flaring event, reaching a flux 3–4 times higher than that at the other epochs (Figure 2). This type of variability is not unexpected for nonthermal sources such as HP Tau/G2 (e.g., Feigelson & Montmerle 1999; Loinard et al. 2008), and is consistent with previous radio measurements (Bieging et al. 1984; Cohen &

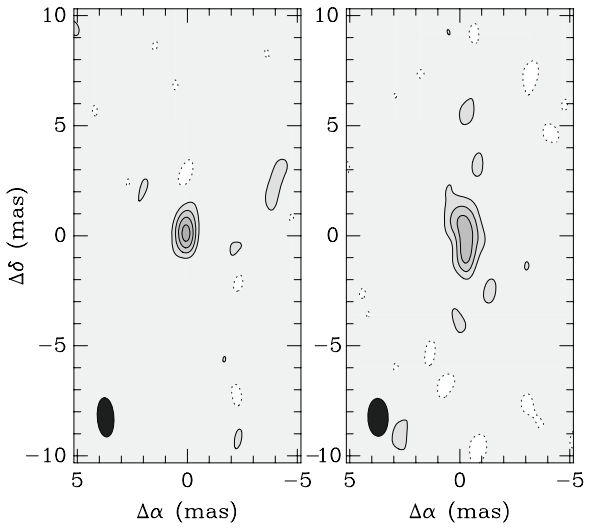

Figure 3. Images of HP Tau/G2 at the sixth (left) and seventh (right) epochs. The first contour and the contour spacing in both images is 0.12 mJy beam^{-1}, and the synthesized beams are shown at the bottom left of each panel. Note how the source is elongated in the north–south direction during the seventh epoch, whereas it is unresolved during the sixth observation.

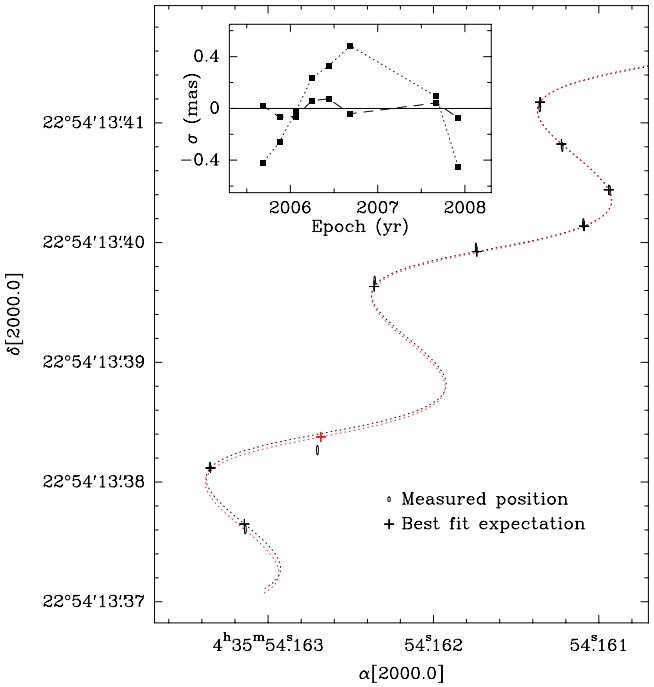

Figure 4. Measured positions and best fits for HP Tau/G2. The observed positions are shown as ellipses, the size of which represents the error bars. Two fits are shown: the dotted black line corresponds to the fit where the seventh epoch is ignored, whereas the dotted red line is the fit where it is included. Note that the seventh observation falls significantly to the south of either fit. The inset shows the fit residuals (of the fit without the seventh epoch) in right ascension (dashed line) and declination (dotted line). Note the large residuals in declination.

Bieging 1986; Phillips et al. 1991; see Section 1). The radio source was found to be unresolved at all epochs except the seventh (obtained in 2007 June) when it was clearly extended in the north–south direction, with a deconvolved size in that direction of about 2.5 mas (Figure 3). This increase in the source size might be due to changes in the structure of the active magnetosphere of HP Tau/G2. Interestingly, however, this observation does not correspond to an epoch when the source was particularly bright, nor particularly dim. In any event, the determination of the source position for that epoch is adversely affected by the fact that the source is extended (see below).

3.2. Astrometry

The displacement of HP Tau/G2 on the celestial sphere is the combination of its trigonometric parallax (π) and proper motion (μ). Since HP Tau/G2 is a member of a triple system (see Section 1), we should in principle describe its proper motion as the combination of the uniform motion of the center of mass and a Keplerian orbit. This is not necessary, however, because the orbital period of the system must be very much longer than the time span covered by our observations. If we assume that the total mass of the HP Tau/G2–HP Tau/G3 system is 2–3 $M_{\odot}$ and that the current observed separation is a good estimate of the system's semimajor axis, then the orbital period is expected to be 35,000–45,000 yr. This is indeed very much longer that the 2 yr covered by our observations, and the acceleration terms can be safely ignored. The astrometric parameters were calculated using the SVD-decomposition fitting scheme described by Loinard et al. (2007). The necessary barycentric coordinates of the Earth, as well as the Julian date of each observation, were calculated using the Multi-year Interactive Computer Almanac (MICA) distributed as a CDROM by the US Naval Observatory. The reference epoch was taken at the mean of our observations: JD 2454029.90 ≡ J2006.81.

Since the source was elongated in the north–south direction during the seventh observation, two different fits were made: one where the seventh epoch was included, and one where it was ignored. When the seventh epoch is included, we obtain the following astrometric parameters:

$$\begin{aligned}
\alpha_{J2006.81} &= 04^{\rm h}35^{\rm m}54\overset{\rm s}{.}162033 \pm 0\overset{\rm s}{.}000003\\
\delta_{J2006.81} &= 22^{\circ}54'13\overset{''}{.}49345 \pm 0\overset{''}{.}000020\\
\mu_{\alpha}\cos\delta &= 13.90 \pm 0.06 \text{ mas yr}^{-1}\\
\mu_{\delta} &= -15.6 \pm 0.3 \text{ mas yr}^{-1}\\
\pi &= 6.19 \pm 0.07 \text{ mas.}
\end{aligned}$$

This corresponds to a distance of 161.6 ± 1.7 pc. The post-fit rms in this case is 0.12 mas in right ascension and 0.51 mas in declination.[3] To obtain a reduced χ^2 of one in both right ascension and declination, one must add quadratically 8.8 μs and 0.59 mas in right ascension and declination, respectively, to the errors listed in Table 1. The uncertainties on the parameters quoted above include these systematic contributions. Note that the seventh epoch contributes significantly to the total post-fit rms since the position corresponding to that observation is farther from the fit (both in right ascension and declination) than that at any other epoch (Figure 4). If the seventh observation is ignored, the best fit yields the following parameters:

$$\begin{aligned}
\alpha_{J2006.81} &= 04^{\rm h}35^{\rm m}54\overset{\rm s}{.}162030 \pm 0\overset{\rm s}{.}000002\\
\delta_{J2006.81} &= 22^{\circ}54'13\overset{''}{.}49362 \pm 0\overset{''}{.}000014\\
\mu_{\alpha}\cos\delta &= 13.85 \pm 0.03 \text{ mas yr}^{-1}\\
\mu_{\delta} &= -15.4 \pm 0.2 \text{ mas yr}^{-1}\\
\pi &= 6.20 \pm 0.03 \text{ mas.}
\end{aligned}$$

All these parameters are consistent within 1σ with those obtained when the seventh observation is included. The

[3] The residual is much larger in declination than in right ascension. We will come back to this point in Section 3.3.

corresponding distance in this case is 161.2 ± 0.9 pc, and the post-fit rms is 0.058 mas in right ascension and 0.33 mas in declination, significantly better than in the previous fit. Indeed, to obtain a reduced χ^2 of one in both right ascension and declination, one must only add quadratically 3.65 μs and 0.38 mas to the formal errors delivered by JMFIT. Again, the uncertainties on the parameters quoted above include these systematic contributions.

As mentioned earlier, the source during the seventh epoch was extended, and the astrometry consequently less reliable. Since the fit when it is ignored is clearly much better than that when it is included, we consider the second fit above our best result.

3.3. Error Analysis

It is noteworthy that, whether or not the seventh epoch is included, the post-fit rms and the systematic error contribution that must be added to the uncertainties quoted in Table 1 are much larger in declination than in right ascension. Fortunately, this large declination contribution does not strongly affect the distance determination, because the strongest constraints on the parallax come from the right ascension measurements. Interestingly, this is, with Hubble 4 (Torres et al. 2007), the second source for which we find large systematic declination residuals. Astrometric fitting of phase-referenced VLBI observations is usually worse in declination than in right ascension (e.g., Figure 1 in Chatterjee et al. 2004) as a result of residual zenith phase delay errors (Reid et al. 1999). In the case of Hubble 4, however, we argued that the large post-fit declination rms might trace the reflex motion caused by an unseen companion, because a periodicity of about 1.2 yr could be discerned in the residuals. In the present source, the case for a periodicity is less clear (Figure 4, inset), but the residuals are clearly not random. Interestingly, the large residuals are in the same north–south direction as the extension of the source seen during our seventh observation. This orientation might, therefore, correspond to a preferred direction of the system along which it tends to vary more strongly. Additional observations will clearly be necessary to settle this issue.

4. DISCUSSION

4.1. Kinematics of the Sources in Taurus

For Galactic sources, it is interesting to express the proper motions in Galactic coordinates rather than in the equatorial system naturally delivered by the VLBA. The results for HP Tau, and the three sources previously observed with the VLBA are given in Columns 3 and 4 of Table 2. Interestingly, the proper motion of HP Tau/G2 is very similar to that of T Tau, but significantly different from those of Hubble 4 and HDE 283572 (which are themselves very similar to each other). HP Tau/G2 and T Tau also happen to both be located on the eastern side of the Taurus complex, whereas Hubble 4 and HDE 283572 are both around Lynds 1495 near the center of the complex (Figure 5).

There is a fifth star in Taurus (V773 Tau) with VLBI-based proper motion and trigonometric parallax measurements (Lestrade et al. 1999). V773 Tau is located about a degree southwest of Hubble 4, and the proper motions reported by Lestrade et al. (1999) are similar to those of Hubble 4 and HDE 283572 (see Figure 4 in Torres et al. 2007). It is now known that V773 Tau is a quadruple system composed of a tight spectroscopic binary orbited by two companions. The radio source observed by Lestrade et al. (1999) is associated

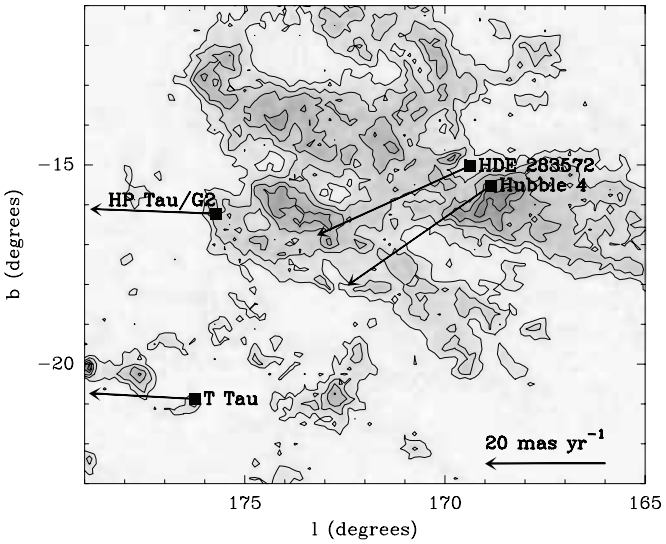

Figure 5. Positions and proper motions of Hubble 4, HDE 283572, T Tau, and HP Tau/G2 superposed on the CO(1–0) map of Taurus from Dame et al. (2001).

with the spectroscopic binary (the other two stars do not appear to be detectable radio emitters). In several VLBI observations (e.g., Phillips et al. 1991; Boden et al. 2007; Torres et al. 2008), the radio source has been reported to be double, with each component tracing one of the stars in the spectroscopic binary. This binarity was not taken into account by Lestrade et al. (1999), and may have affected their parallax measurement. Indeed, Boden et al. (2007) recently modeled the orbit of V773 Tau combining spectroscopic observations, Keck Interferometer data and VLBA imaging. The distance to V773 Tau that they obtain (136.2 ± 3.7 pc) is somewhat smaller than the value $\left(148.4^{+5.7}_{-5.3}\ \mathrm{pc}\right)$ reported by Lestrade et al. (1999). Because of this slight discrepancy, we will not include V773 Tau in the present analysis. It should be mentioned that we are currently analyzing new multiepoch VLBA observations of V773 Tau designed to constrain both its distance and orbital motions. These data will be published in a forthcoming paper.

Knowing the distance to the sources with high accuracy, it is possible to transform the observed proper motions into transverse velocities. Combining this information with radial (Heliocentric) velocities taken from the literature (the second column of Table 2), it becomes possible to construct the three-dimensional velocity vectors. It is common to express these vectors on a rectangular (X, Y, Z) coordinate system centered in the Sun, with X pointing toward the Galactic center, Y in the direction of Galactic rotation, and Z toward the Galactic North Pole. In this system, the coordinates of the Heliocentric velocities will be written (U, V, W). As a final step, it is also possible to calculate the peculiar velocity of the stars. This involves two stages: first, the peculiar motion of the Sun must be removed to transform the Heliocentric velocities into velocities relative to the LSR. Following Dehnen & Binney (1998), we will use $u_0 = +10.00$ km s^{-1}, $v_0 = +5.25$ km s^{-1}, and $w_0 = +7.17$ km s^{-1} for the peculiar velocity of the Sun expressed in the coordinate system defined above. The second stage consists in estimating the difference in circular velocity between Taurus and the Sun, so the peculiar velocities are expressed relative to the LSR appropriate for Taurus, rather than relative to the LSR of the Sun. This was done assuming the rotation curve of Brand & Blitz (1993), and represents a small correction of only about 0.3 km s^{-1}. We will write (u, v, w) the coordinates of the peculiar velocity of the sources. Both (U, V, W) and (u, v, w)

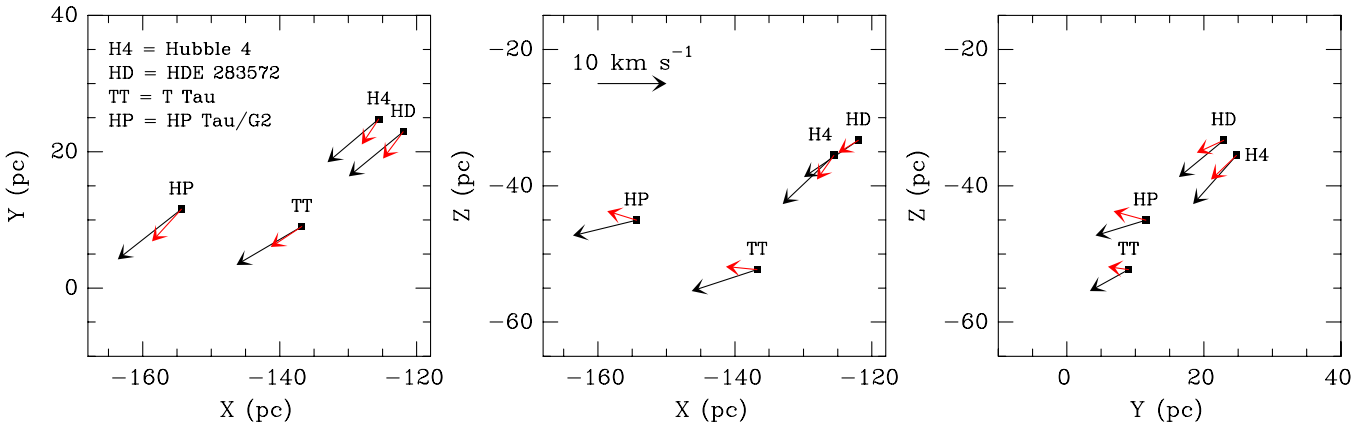

Figure 6. Heliocentric velocities (black arrows) and peculiar velocities (red arrows) for the four stars in Taurus with VLBA-based distance determinations.

Table 2
Radial Velocities, Proper Motions, Heliocentric, and Peculiar Velocities in Galactic Coordinates for the Four Sources Observed with the VLBA so Far

Source	V_r (km s^{-1})	$\mu_\ell \cos(b)$ (mas yr^{-1})	μ_b	U	V (km s^{-1})	W	u	v (km s^{-1})	w	References[a]
HP Tau/G2	17.7 ± 1.8	$+20.90 \pm 0.07$	$+0.82 \pm 0.10$	-18.59	-14.65	-4.50	-8.59	-9.40	$+2.67$	1,2
Hubble 4	15.0 ± 1.7	$+23.94 \pm 0.12$	-16.74 ± 0.15	-14.96	-12.66	-14.30	-4.96	-7.41	-7.13	3,4
HDE 283572	15.0 ± 1.5	$+25.53 \pm 0.05$	-11.61 ± 0.06	-15.89	-13.07	-10.84	-5.89	-7.82	-3.67	3,2
T Tau[b]	19.1 ± 1.2	$+17.76 \pm 0.03$	$+0.99 \pm 0.04$	-19.09	-11.27	-6.30	-9.09	-6.02	$+0.87$	4,5

Notes.
[a] 1=This work; 2=Walter et al. (1988); 3=Torres et al. (2007); 4=Hartmann et al. (1986); 5=Loinard et al. (2007).
[b] The radial velocity and proper motions used here are those of T Tau N. The radial velocities for T Tau Sa and T Tau Sb are available in Duchêne et al. (2002) and are very similar.

are given in Table 2 for the four sources considered here. Their projections onto the (X, Y), (X, Z), and (Y, Z) planes are shown in Figure 6.

The mean heliocentric velocity and the velocity dispersion of the four sources are

$$U = -17.1 \pm 1.7 \text{ km s}^{-1} \quad (1)$$
$$V = -12.9 \pm 1.2 \text{ km s}^{-1} \quad (2)$$
$$W = -9.0 \pm 3.8 \text{ km s}^{-1}. \quad (3)$$

These values are similar to those reported by Bertout & Genova (2006) for a larger sample of young stars in Taurus with optically measured proper motions. Note that the velocity dispersion in the W direction is somewhat artificially high because (as noted earlier) Hubble 4 and HDE 283572 on the one hand, and T Tau and HP Tau/G2 on the other, clearly have different vertical velocities. They likely belong to two different kinematic subgroups.

The mean peculiar velocity of the four sources considered here is

$$u = -7.1 \pm 1.7 \text{ km s}^{-1} \quad (4)$$
$$v = -7.7 \pm 1.2 \text{ km s}^{-1} \quad (5)$$
$$w = -1.8 \pm 3.8 \text{ km s}^{-1}. \quad (6)$$

We argue that this is a good estimate of the mean peculiar velocity of the Taurus complex. This velocity is almost entirely in the (X, Y) plane. Thus, although Taurus is located significantly out of the midplane of the Galaxy (about 40 pc to its south), it appears to be moving very little in the vertical direction. The motion in the (X, Y) plane, on the other hand, is fairly large, leading to a total peculiar velocity $(u^2+v^2+w^2)^{0.5} = 10.6 \text{ km s}^{-1}$. According to Stark & Brand (1989), the one-dimensional velocity dispersion of giant molecular clouds within 3 kpc of the Sun is about 8 km s^{-1}. As a consequence, each component of the peculiar velocity of a given molecular cloud is expected to be of that order, and our determination of the mean peculiar velocity of Taurus is in reasonable agreement with that prediction. Another useful comparison is with the velocity dispersion of young main-sequence stars. For the bluest stars in their sample (corresponding to early A stars), Dehnen & Binney (1998) found velocity dispersions of about 6 km s^{-1} in the vertical direction, and of 10–14 km s^{-1} in the X and Y directions. The young stars in Taurus are significantly younger than typical main-sequence early A stars, so one would expect young stars in Taurus to have peculiar velocities somewhat smaller than 6 km s^{-1} in the vertical direction, and than 10–14 km s^{-1} in the X and Y directions. This is indeed what is observed. Note, however, that Taurus is not among the star-forming regions with the smallest peculiar velocities. In Orion, Gómez et al. (2005) found a difference between expected and observed proper motions smaller than 0.5 km s^{-1}.

One last comment should be made here. The data presented here and in the other papers of this series yield proper motions and trigonometric parallaxes that, together, enable the measurement of transverse velocities with an accuracy of about 1%. For sources in Taurus, this corresponds to an absolute error better than 0.1 km s^{-1}. In comparison, the radial velocity measurements available in the literature have typical uncertainties of 1–2 km s^{-1}. To take full advantage of the VLBA data, it will become important to measure radial velocities with a significantly improved accuracy.

4.2. Distance and Structure of the Taurus Association

Taking the mean of the four VLBA-based parallax measurements available (HP Tau/G2, T Tau, Hubble 4, and HDE

283572), we can estimate the mean parallax to the Taurus complex to be $\bar{\pi} = 7.08$ mas. This corresponds to a mean distance $\bar{d}$ of 141.2 pc, in good agreement with previous estimates (Kenyon et al. 1994).

The angular size of Taurus is about 10°, corresponding to a physical size of roughly 25 pc. It would be natural to expect that the depth of Taurus might be similar, and that different sources may be found at significantly different distances from us. The observations presented here and in the previous papers of this series are, however, the first ones with enough accuracy to directly probe the depth of the Taurus complex. They reveal that HP Tau is about 30 pc farther than Hubble 4 and HDE 283572, and that Taurus is at least as deep as it is wide. A trivial but important consequence is that using the mean distance indiscriminately for all the stars in the complex will result in systematic errors at the levels of about 10%. To reach higher accuracy, one will have to reconstruct the complete three-dimensional structure of Taurus. The number of sources considered so far is obviously too limited to obtain such a complete view. It is interesting to note, however, that Hubble 4 and HDE 283572, which are very near one another in projection and share the same kinematics (See Section 4.2), are also found to be at similar distances from us (∼130 pc). This suggests that there exist in that region (corresponding to the surroundings of the dark cloud Lynds 1495) a coherent spatio-kinematical structure at about 130 pc. Observations with an astrometric precision similar to that of the data presented here for several dozen young stars would allow the identification of several such coherent groups across the complex. This, in turn, would allow a fairly accurate reconstruction of a three-dimensional structure of Taurus. Currently, very long baseline interferometry is the only technique with sufficient accuracy to carry out the necessary observations.

4.3. Comparison with Theoretical Evolutionary Tracks

As mentioned in Section 1, HP Tau/G2 is a member of a compact group of four young stars, comprising HP Tau itself, HP Tau/G1, G2, and G3. Given the small angular separations between them, the members of this group are very likely to be physically associated—-indeed, HP Tau/G2 and G3 are thought to form a bound system. They are, therefore, very likely to be at the same distance from the Sun. Using our accurate estimate of the distance to HP Tau/G2, we are now in a position to refine the determination of the luminosities of all four stars. Little is known about HP Tau/G1, but the effective temperature and the bolometric luminosity (obtained assuming $d = 142$ pc) of the other three members are given in Briceño et al. (2002). Those values (corrected to the new distance) allow us to place the stars accurately on an H–R diagram (Figure 7).

From their position on the H–R diagram, one can (at least in principle) derive the mass and age of the stars using theoretical pre-main-sequence evolutionary codes. Several such models are available, and we will use four of them here[4]: those of Siess et al. (2000); Demarque et al. (2004; known as the Yonsei-Yale Y^2 models); D'Antona & Mazzitelli (1997); and Palla & Stahler (1999). The isochrones for those four models at 1, 3, 5, 7, and 10 Myr are shown as solid black lines in Figure 7. Also shown are the evolutionary tracks (from the same models) for stars of 1.0, 1.5, and 2.0 $M_\odot$. The three HP Tau members are shown as blue symbols, and HDE 283572 (from Torres et al. 2007) is shown as a red symbol (we will discuss momentarily the reason for incorporating that source in the present analysis).

A number of interesting points can be seen from Figure 7. First, there is reasonable agreement (within 40%, see below) between the masses predicted by different models. The best case is that of HP Tau/G2, for which the different models predict masses consistent with each other at the 10% level (between 1.7 and 1.9 $M_\odot$). The situation for HP Tau is somewhat less favorable, since the models of Siess et al. (2000) or Palla & Stahler (1999) predict a mass of ∼1.5 $M_\odot$, whereas those of D'Antona & Mazzitelli (1997) predicts a significantly smaller mass of ∼1.0 $M_\odot$. Thus, there is a 35% spread in the values predicted by different models for the mass of that source. The least favorable situation is for HP Tau/G3. The mass of that source is about 0.8 $M_\odot$ according to the models of Siess et al. (2000), but slightly less than 0.5 $M_\odot$ according to those D'Antona & Mazzitelli (1997). This is a 40% discrepancy. This tendency for pre-main-sequence evolutionary models to become more discrepant at lower mass had been noticed before, and is discussed at length in Hillenbrand et al. (2008). In the absence of dynamically measured masses, it is impossible to assess which of the models used here provides the "best" answer.

Another interesting issue is related to the age predictions of the different models. Since the different members of the HP Tau group are likely to be physically associated, they are expected to be nearly coeval. This is particularly true of HP Tau/G2 and HP Tau/G3 which are believed to form a loose binary system. Interestingly, most models predict significantly different ages for the three sources (see Figure 7). The models by Siess et al. (2000) predict ages of about 8 Myr and 3 Myr for HP Tau/G2 and HP Tau/G3, respectively. A similar 5 Myr age difference is found for the models of Demarque et al. (2004) and D'Antona & Mazzitelli (1997): both predict ages slightly smaller than 1 Myr for HP Tau/G3, and somewhat larger than 5 Myr for HP Tau/G2. In principle, those differences could be real. In should be noticed, however, that the vast majority of low-mass stars in Taurus (with spectral types M and late K) have ages smaller than 3 Myr (Briceño et al. 2002). Moreover, mass-dependent systematic effects in the age predictions made by evolutionary tracks have been reported before. In particular, Hillenbrand et al. (2008) argued that existing models could significantly over-predict the age of relatively massive stars ($M \gtrsim 1.5\ M_\odot$). HP Tau/G2 is precisely such a fairly massive star. So is HDE 283572, another young star in Taurus with a recently measured accurate distance (Torres et al. 2007). The age estimate for that star based on the models by Siess et al. (2000), Demarque et al. (2004), and D'Antona & Mazzitelli (1997) is 6–10 Myr (Figure 7), somewhat larger than would be expected for Taurus. The only of the four models considered here to predict similar ages for the three members of the HP Tau group is that of Palla & Stahler (1999). Within the errors, all three stars fall on the 3 Myr isochrone. Note that this value is also consistent with the ages of lower mass stars in Taurus (Briceño et al. 2002; see above).

5. CONCLUSIONS AND PERSPECTIVES

In this article, we have reported multiepoch phase-referenced VLBA observations of the weak-line T Tauri star HP Tau/G2 located near the eastern edge of the Taurus star-forming complex. These observations allowed us to measure the trigonometric parallax of the target with an accuracy better than 1%, and to refine the determination of the intrinsic parameters of the source. Combined with previous similar results on other young stars

[4] The models by Baraffe et al. (1998) will not be used because they do not cover the mass range of our stars.

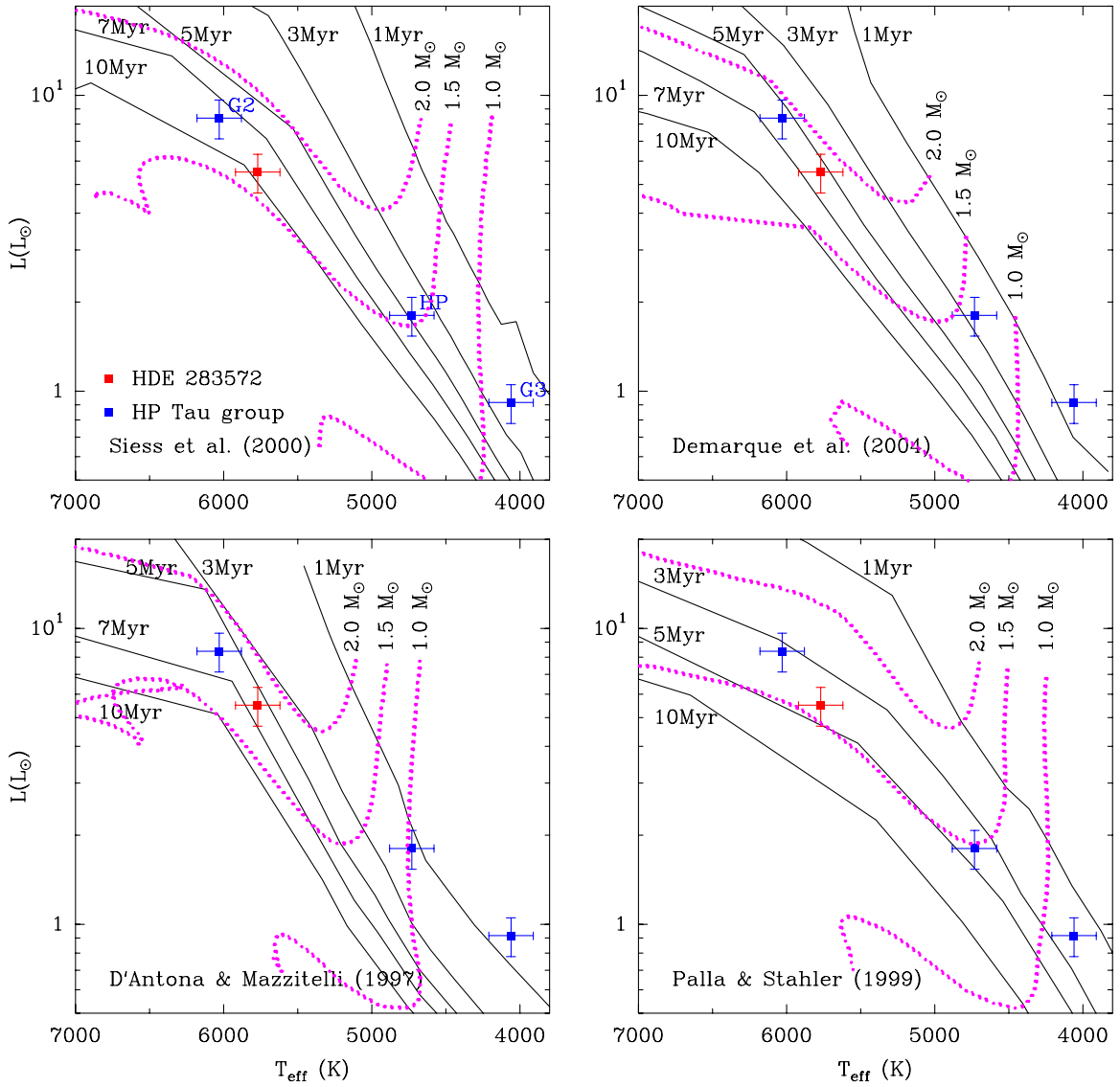

Figure 7. Positions of the three HP Tau members (blue symbols) and of HDE 283572 (red symbol) on an H–R diagram (from the coolest to the warmest, the three stars in the HP Tau group are HP Tau/G3, HP Tau, and HP Tau/G2, as indicated in the first panel). Isochrones (full back lines) are shown at 1, 3, 5, 7, and 10 Myr for various models. For the same models, evolutionary tracks for stars of 1.0, 1.5, and 2.0 $M_{\odot}$ are also shown as dotted magenta lines.

of Taurus, these data also enabled us to probe directly for the first time the depth of this important region of star-formation. We found that HP Tau/G2 is about 30 pc farther than two stars (Hubble 4 and HDE 283572) located close to the dark cloud Lynds 1495, near the central portion of Taurus. This implies that the Taurus complex is at least as deep as it is wide on the plane of the sky. The famous young star T Tauri, located to the south of the complex happens to be at an intermediate distance.

Our observations also allow us to determine the full velocity vector of our sources with excellent accuracy. Combining the results from the four stars considered so far, we estimate the mean peculiar velocity of Taurus to be about 10.6 km s^{-1}, oriented almost entirely along the direction of the Galactic plane. The lack of a significant vertical component may appear somewhat surprising given the location of Taurus about 40 pc below the Galactic midplane. This might suggest that Taurus has reached its farthest distance from the midplane and is about to fall back toward it. Overall, the peculiar velocity of Taurus appears to be in reasonable agreement with measurements of the velocity dispersion of giant molecular clouds and young main-sequence stars in the Solar neighborhood.

Using our improved distances, we have refined the determination of the location of the stars in the HP Tau group on an H–R diagram, and compared those positions with theoretical models available in the literature. There is reasonable agreement (within 40%) between the different models on the mass of the stars. It is noteworthy, however, that this agreement becomes progressively poorer as one considers less massive stars. Although the different members of the HP Tau group might be expected to be coeval, three of the theoretical models considered here predict significantly different ages for the various members. Moreover, those models predict ages for the most massive member of the group (HP Tau/G2) somewhat larger than would expected for Taurus. The only model for which all three stars in the HP Tau group fall on a single isochrone (3 Myr) is that of Palla & Stahler (1999). Similar studies of multiple young stellar systems would clearly help test and improve pre-main-sequence evolutionary models.

R.M.T., L.L., and L.F.R. acknowledge the financial support of DGAPA, UNAM, and CONACyT, Mexico. We are indebted to Tom Dame for sending us a digital version of the integrated CO(1–0) map of Taurus, to Andy Boden for his help with the PMS models, and to Cesar Briceño for his detailed comments of the errors affecting the determination of the luminosity and effective temperature of the young stars in the HP Tau group. We are also grateful to the anonymous referee, in particular for his/her comments which prompted us to expand significantly our discussion of the comparison with PMS models. The National Radio Astronomy Observatory is a facility of the National Science Foundation operated under cooperative agreement by Associated Universities, Inc.

REFERENCES

Baraffe, I., Chabrier, G., Allard, F., & Hauschildt, P. H. 1998, A&A, 337, 403
Bertout, C., & Genova, F. 2006, A&A, 460, 499
Bieging, J. H., Cohen, M., & Schwartz, P. R. 1984, ApJ, 282, 699
Boden, A. F., et al. 2007, ApJ, 670, 1214
Brand, J., & Blitz, L. 1993, A&A, 275, 67
Briceño, C., Luhman, K. L., Hartmann, L., Stauffer, J. R., & Kirkpatrick, J. D. 2002, ApJ, 580, 317
Chatterjee, S., Cordes, J. M., Vlemmings, W. H. T., Arzoumanian, Z., Goss, W. M., & Lazio, T. J. W. 2004, ApJ, 604, 339
Cohen, M., & Bieging, J. H. 1986, AJ, 92, 1396
Cohen, M., & Kuhi, L. V. 1979, ApJS, 41, 743
Condon, J. J. 1997, PASP, 109, 166
Dame, T. M., Hartmann, D., & Thaddeus, P. 2001, ApJ, 547, 792
D'Antona, F., & Mazzitelli, I. 1997, Mem. Soc. Astron. Ital., 68, 807
Demarque, P., Woo, J.-H., Kim, Y.-C., & Yi, S. K. 2004, ApJS, 155, 667
Dehnen, W., & Binney, J. J. 1998, MNRAS, 298, 387
Duchêne, G., Ghez, A. M., & McCabe, C. 2002, ApJ, 568, 771
Elias, J. H. 1978a, ApJ, 224, 857
Elias, J. H. 1978b, ApJ, 224, 453
Feigelson, E. D., & Montmerle, T. 1999, ARA&A, 37, 363
Fey, A. L., et al. 2004, AJ, 127, 3587
Gómez, L., Rodríguez, L. F., Loinard, L., Lizano, S., Poveda, A., & Allen, C. 2005, ApJ, 635, 1166
Greisen, E. W. 2003, in Information Handling in Astronomy—Historical Vistas, ed. A. Heck (Dordrecht: Kluwer) 109
Hartmann, L., Hewett, R., Stahler, S., & Mathieu, R. D. 1986, ApJ, 309, 275
Hillenbrand, L. A., Bauermeister, A., & White, R. J. 2008, in ASP Conf. Ser. 384, 14th Cambridge Workshop on Cool Stars, Stellar Systems, and the Sun, ed. G. Van Belle (San Francisco, CA: ASP) 200
Kenyon, S. J., Dobrzycka, D., & Hartmann, L. 1994, AJ, 108, 1872
Kenyon, S. J., & Hartmann, L. 1995, ApJS, 101, 117
Knude, J., & Hog, E. 1998, A&A, 338, 897
Lestrade, J.-F., Preston, R. A., Jones, D. L., Phillips, R. B., Rogers, A. E. E., Titus, M. A., Rioja, M. J., & Gabuzda, D. C. 1999, A&A, 344, 1014
Loinard, L., Mioduszewski, A. J., Rodríguez, L. F., González, R. A., Rodríguez, M. I., & Torres, R. M. 2005, ApJ, 619, L179
Loinard, L., Torres, R. M., Mioduszewski, A. J., & Rodríguez, L. F. 2008, ApJ, 675, L29
Loinard, L., Torres, R. M., Mioduszewski, A. J., Rodríguez, L. F., González, R. A., Lachaume, R., Vázquez, V., & González, E. 2007, ApJ, 671, 546
Menten, K. M., Reid, M. J., Forbrich, J., & Brunthaler, A. 2007, A&A, 474, 515
Palla, F., & Stahler, S. W. 1999, ApJ, 525, 772
Phillips, R. B., Lonsdale, C. J., & Feigelson, E. D. 1991, ApJ, 382, 261
Reid, M. J., Readhead, A. C. S., Vermeulen, R. C., & Treuhaft, R. N. 1999, ApJ, 524, 816
Richichi, A., Leinert, C., Jameson, R., & Zinnecker, H. 1994, A&A, 287, 145
Siess, L., Dufour, E., & Forestini, M. 2000, A&A, 358, 593
Stark, A. A., & Brand, J. 1989, ApJ, 339, 763
Torres, R. M., Loinard, L., Mioduszewski, A. J., & Rodríguez, L. F. 2007, ApJ, 671, 1813
Torres, R. M., Loinard, L., Mioduszewki, A. J., & Rodríguez, L. F. 2008, RevMexAA Conf. Ser., 34, 98
Walter, F. M., Brown, A., Mathieu, R. D., Myers, P. C., & Vrba, F. J. 1988, AJ, 96, 297
Xu, Y., Reid, M. J., Zheng, X. W., & Menten, K. M. 2006, Science, 311, 54

G

VLBA Distance to Nearby Star-Forming Regions IV. Distance and Dynamical Masses for V773 Tau A

Rosa M. Torres, Laurent Loinard, Andrew F. Boden, Amy J. Mioduszewski & Luis F. Rodríguez

In preparation for The Astrophysical Journal

Abstract. We present multi-epoch Very Long Baseline Array (VLBA) observations of the 51-day binary component in the quadruple young stellar system V773 Tau. Combined with previous interferometric and radial velocity measurements, these new data enable us to improve the characterization of the physical orbit of the system. In particular, we infer dynamical masses for the primary and the secondary of 1.48 ± 0.12 $M_\odot$, and 1.28 ± 0.07 $M_\odot$, respectively, and a distance to the system of 134.5 ± 3.2 pc. Using the improved orbit, we can calculate the absolute coordinates of the barycenter of the system from the VLBA observations, and fit for its trigonometric parallax and proper motion. The best fit yields a parallax of 7.7 ± 0.2 mas, corresponding to a distance of $130.2^{+3.5}_{-3.3}$ pc, in good agreement with the estimate based on the orbital fit. In projection, V773 Tau and two other young stars (Hubble 4 and HDE 283572) recently observed with the VLBA are located near the dark cloud Lynds 1495, in the central region of Taurus. These three stars appear to have similar proper motions and

trigonometric parallaxes, so we argue that the weighted mean of their parallaxes provides a good estimate of the distance to Lynds 1495. This weighted mean (7.62 ± 0.10 mas) corresponds to $d = 131.2\ ^{+1.8}_{-1.7}$ pc.

DRAFT VERSION OCTOBER 20, 2009
Preprint typeset using LaTeX style emulateapj v. 12/14/05

VLBA DETERMINATION OF THE DISTANCE TO NEARBY STAR-FORMING REGIONS IV. DISTANCE AND DYNAMICAL MASSES OF V773 TAU A

ROSA M. TORRES, LAURENT LOINARD
Centro de Radiostronomía y Astrofísica, Universidad Nacional Autónoma de México,
Apartado Postal 72–3 (Xangari), 58089 Morelia, Michoacán, México;
r.torres@crya.unam.mx

ANDREW F. BODEN
Division of Physics, Math, and Astronomy, California Institute of Technology,
1200 E California Blvd., Pasadena CA 91125

AMY J. MIODUSZEWSKI
National Radio Astronomy Observatory, Array Operations Center,
1003 Lopezville Road, Socorro, NM 87801

AND

LUIS F. RODRÍGUEZ
Centro de Radiostronomía y Astrofísica, Universidad Nacional Autónoma de México,
Apartado Postal 72–3 (Xangari), 58089 Morelia, Michoacán, México
Draft version October 20, 2009

ABSTRACT

We present multi-epoch Very Long Baseline Array (VLBA) observations of V773 Tau A, the 51-day binary subsystem in the quadruple young stellar system V773 Tau. Combined with previous interferometric and radial velocity measurements, these new data enable us to improve the characterization of the physical orbit of the subsystem. In particular, we infer updated dynamical masses for the primary and the secondary components of 1.48 ± 0.12 $M_\odot$, and 1.28 ± 0.07 $M_\odot$, respectively, and an updated distance to the system of 134.5 ± 3.2 pc, all consistent with previous estimates. Using the improved orbit, we can calculate the absolute coordinates of the barycenter of V773 Tau A from the VLBA observations, and fit for its trigonometric parallax and proper motion. The best fits without and with acceleration terms yield distances of $132.0^{+3.5}_{-3.4}$ and $130.9^{+2.2}_{-2.1}$ pc, respectively. These figures are in good agreement with the estimate based on the orbital fit, showing that the quoted errors provide a trustworthy measure of the accuracy of the results. The acceleration vector of the barycenter of V773 Tau A deduced from our best fit points (as expected) towards the position at the median epoch of our observations of V773 Tau B, the nearest other member in the system. In projection, V773 Tau and two other young stars (Hubble 4 and HDE 283572) recently observed with the VLBA are located near the dark cloud Lynds 1495, in the central region of Taurus. These three stars appear to have similar proper motions and trigonometric parallaxes, so we argue that the weighted mean of their parallaxes provides a good estimate of the distance to Lynds 1495 and its associated stellar population. This weighted mean (7.63 ± 0.11 mas) corresponds to $d = 131.1 \pm 1.9$ pc.

Subject headings: binaries: spectroscopic — astrometry — stars: individual (V773 Tau) — radio continuum: stars — stars: formation — stars: pre-main sequence

1. INTRODUCTION

In spite of significant progress in recent years, the formation and early evolution of stars are still not fully understood (e.g. Hillenbrand & White 2004, Mathieu et al. 2007). One way to foster progress is to measure as accurately as possible the intrinsic characteristics of individual young stars (luminosity, effective temperature, mass, disk properties, etc.), and compare them with the predictions of detailed theoretical models. A major obstacle, however, has been the fairly large uncertainties (typically 20 to 50%) affecting the distance to even the nearest star-forming regions. Significant progress has been possible in recent years thanks to direct trigonometric parallax measurements obtained using Very Long Baseline Interferometry (VLBI) multi-epoch observations (e.g. Loinard et al. 2005, 2007, 2008; Torres et al. 2007, 2009; Menten et al. 2007). Such observations deliver uncertainties of a few percent or better, that typically surpass the accuracy of previous determination by one to two orders of magnitude. Unfortunately, trigonometric parallax measurements based on VLBI observations are available for only a handful of young stars so far.

Young binary systems are particularly interesting for constraining theoretical pre-main sequence evolutionary models, because tracking their orbital motions provides a direct means to estimate their dynamical mass. In particular, if astrometric and spectroscopic data are combined, the physical orbit and the individual masses of the system members can be determined. The distance to the system can also be estimated with such data, providing a good alternative to a direct parallax measurement –or a complementary and independent determination if a parallax measurement exists.

In this paper, we will present new VLBI observations of V773 Tau, a young stellar system located in the surroundings of the dark cloud Lynds 1495 in Taurus. These data will be used both to help update the physical (three-dimensional) or-

bit of the system, and to measure its trigonometric parallax.

V773 Tau (HD 283447, HBC 367) has been known as a multiple system since it was found to be a double-line spectroscopic binary with an orbital period of about 51 days (Welty 1995), and to have a companion at about 150 mas (Ghez et al. 1993, Leinert et al. 1993). More recently, Duchêne et al. (2003) identified a fourth component in the system, showing that V773 Tau is (at least) a quadruple system. This fourth component belongs to the still poorly understood class of "infrared companions" (young stellar sources, fairly bright in the infrared but invisible at optical wavelengths, which have been discovered around a small number of T Tauri stars). It is interesting to point out that the four (almost certainly coeval) stars in V773 Tau have distinct spectral energy distributions: both members of the spectroscopic binary are weak line T Tauri stars (WTTS), the optical companion is a classical T Tauri (CTTS), and the fourth member is (as mentioned above) an infrared companion. Such a variety of apparently distinct evolutionary stages in a single system likely reflects the effect of multiplicity on the evolution of young stars and their circumstellar material.

To prevent confusion, it should be noted that several nomenclatures have been used to describe the different sources in V773 Tau. Duchêne et al. (2003) call the spectroscopic binary V773 Tau A/B, and the optical and infrared companions V773 Tau C and V773 Tau D, respectively. On the other hand, Boden et al. (2007, hereafter B2007; expanding upon Woitas 2003) refer to the spectroscopic binary as V773 Tau Aa/Ab, and to the two companions as V773 Tau B and V773 Tau C, respectively.[1] We will follow the latter nomenclature in this paper.

The relative orbital motion between the spectroscopic binary and the two companions has been monitored by Duchêne et al. (2003), and the orbit between the two members of the spectroscopic binary has recently been investigated in detail by B2007 who combined (optical) Radial Velocity (RV) measurements, Keck Interferometer (KI) visibility data, and radio VLBI images. Using these data, B2007 constructed a preliminary physical orbit for the system, yielding dynamical mass estimates of 1.54 and 1.33 $M_\odot$ for the primary and the secondary components, respectively. The distance to the system obtained from these data and modeling is 136.2 ± 3.7 pc. There is also a direct trigonometric parallax measurement based on multi-epoch VLBI observations for this source (Lestrade et al. 1999). This VLBI-based distance measurement ($d = 148.4^{+5.7}_{-5.3}$ pc) is roughly consistent (at the 2–3 σ level) with the value obtained from the orbit modeling.

V773 Tau A has long been known to be a strong radio source (Kutner et al. 1986).[2] Indeed, it was the strongest source in the 5 GHz VLA survey of WTTS in the Taurus-Auriga molecular cloud complex by O'Neal et al. (1990). From detailed multi-frequency observations, Feigelson et al. (1994) concluded that the radiation was most likely of non-thermal origin. This was confirmed by Phillips et al. (1991) who obtained VLBI observations, and resolved the radio emission into a clear double source, most likely corresponding to the two components of the spectroscopic binary. More recently, Massi et al. (2002, 2006) showed that the radio emission exhibits periodic variations with a period corresponding to the 51 day orbital period of the spectroscopic binary. This variability is due to an increase in the flaring activity near periastron and likely reflect interactions between the magnetospheres of the two stars when they get close to one another. Finally, B2007 and Massi et al. (2008) also resolved the radio emission from V773 Tau A into two components, which they associate with the two stars in the spectroscopic binary.

[1] Yet another nomenclature is used in the Double Star Catalog of Mason et al. (2001).

[2] The two companions V773 Tau B and C, on the other hand, are not detected at radio wavelengths at the level of sensitivity currently reachable.

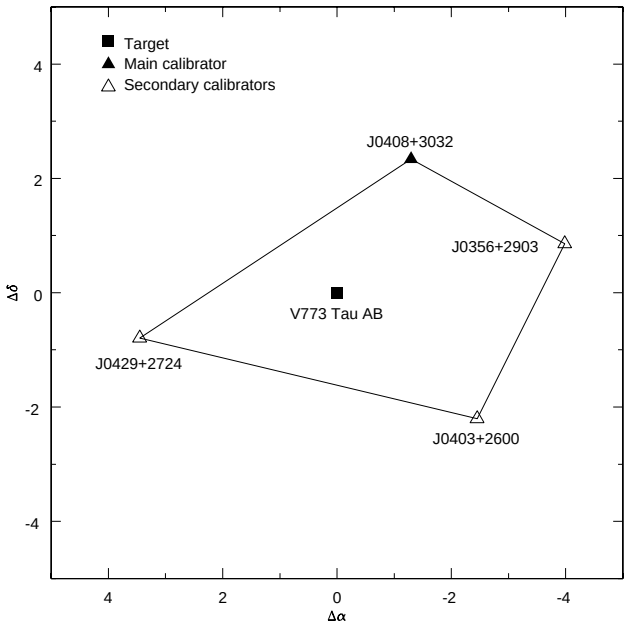

FIG. 1.— Relative position of the astronomical target, the main calibrator (J0408+3032), and the secondary calibrators (J0403+2600, J0429+2724, and J0356+2903).

2. OBSERVATIONS AND DATA CALIBRATION

In this article, we make use of two series of 3.6 cm (8.42 GHz) continuum observations of V773 Tau A obtained with the VLBA (see Tab. 1 for details). The first series (project code BL124 A) consists of 6 observations obtained every two to three months between September 2005 and September 2006, and was designed to follow the parallactic path of the source. The second series (project code BL146) corresponds to 13 observations obtained roughly every 7 days between August 29 and November 17, 2007. These observations span a total of 82 days (about 1.6 orbital periods of the system), and were designed to follow the orbital motion over a complete revolution. For all observations, our phase center was at $\alpha_{J2000.0} = 04^{\rm h}14^{\rm m}12\overset{\rm s}{.}922$, $\delta_{J2000.0} = +28^\circ12'12\overset{''}{.}180$. Each observation consisted of series of cycles with two minutes spent on source, and one minute spent on the main phase-referencing quasar J0408+3032, located $2\overset{\circ}{.}67$ away. Every 24 minutes, we also observed three secondary calibrators (J0403+2600, J0429+2724, and J0356+2903) which, together with J0408+3032 form a lozenge around the astronomical source (Fig. 1). All four calibrators are very compact extragalactic sources whose absolute positions are know to better than 2.0, 0.4, 0.3, and 1.64 mas, respectively (Fey et al. 2004, Ma et al. 1998, Beasley et al. 2002).

The data were edited and calibrated using the Astronomical Image Processing System (AIPS –Greisen 2003). The

TABLE 1
OBSERVING CODES AND DATES, MEASURED SOURCE POSITIONS AND SEPARATIONS, AND ORBIT PHASES.

Code	Mean UT date (yyyy.mm.dd hh:mm)	Julian Day	α (J2000.0) 04^h14^m	σ_α	δ (J2000.0) $28^\circ12'$	σ_δ	$\Delta\alpha$ (mas)	$\sigma_{\Delta\alpha}$	$\Delta\delta$ (mas)	$\sigma_{\Delta\delta}$	ϕ
BL124 AA	2005.09.08 12:01	2453622.00	$12^s.9215438$	$0^s.0000006$	$12''.20222$	$0''.00002$	-1.43	0.01	-0.70	0.04	0.99
			$12^s.9214354$	$0^s.0000009$	$12''.20152$	$0''.00003$					
BL124 AB	2005.11.15 07:31	2453689.81	$12^s.9211625$	$0^s.0000011$	$12''.19608$	$0''.00004$	1.90	0.03	1.85	0.06	0.32
			$12^s.9213067$	$0^s.0000019$	$12''.19793$	$0''.00005$					
BL124 AC	2006.01.21 03:11	2453756.63	$12^s.9207455$	$0^s.0000017$	$12''.19102$	$0''.00006$	2.79	0.04	0.78	0.12	0.63
			$12^s.9209564$	$0^s.0000027$	$12''.19180$	$0''.00010$					
BL124 AD	2006.04.01 22:31	2453827.44	$12^s.9211553$	$0^s.0000007$	$12''.18646$	$0''.00002$	-1.31	0.01	-0.71	0.03	0.01
			$12^s.9210561$	$0^s.0000007$	$12''.18575$	$0''.00003$					
BL124 AE	2006.06.12 17:48	2453899.24	$12^s.9218088$	$0^s.0000029$	$12''.18114$	$0''.00010$	.....	....	.....	....	0.42
BL124 AF	2006.09.05 12:14	2453984.01	$12^s.9226916$	$0^s.0000016$	$12''.17899$	$0''.00005$	-1.34	0.02	-0.35	0.05	0.08
			$12^s.9225899$	$0^s.0000006$	$12''.17865$	$0''.00003$					
BL146 B	2007.08.23 13:06	2454336.05	$12^s.9240420$	$0^s.0000009$	$12''.15627$	$0''.00002$	-1.96	0.03	-1.34	0.06	0.97
			$12^s.9238934$	$0^s.0000021$	$12''.15493$	$0''.00006$					
BL146 C	2007.08.29 12:42	2454342.03	$12^s.9240252$	$0^s.0000005$	$12''.15525$	$0''.00001$	-1.21	0.02	0.08	0.03	0.08
			$12^s.9239338$	$0^s.0000012$	$12''.15533$	$0''.00003$					
BL146 D	2007.09.05 12:15	2454349.01	$12^s.9240072$	$0^s.0000016$	$12''.15456$	$0''.00003$	.....	....	.....	....	0.22
BL146 E	2007.09.11 11:51	2454354.99	$12^s.9239067$	$0^s.0000036$	$12''.15360$	$0''.00011$	2.61	0.11	1.75	0.18	0.33
			$12^s.9241045$	$0^s.0000071$	$12''.15535$	$0''.00015$					
BL146 F	2007.09.16 11:32	2454359.98	$12^s.9238938$	$0^s.0000016$	$12''.15346$	$0''.00004$	2.92	0.03	1.69	0.05	0.43
			$12^s.9241150$	$0^s.0000012$	$12''.15516$	$0''.00003$					
BL146 G	2007.09.21 11:12	2454364.97	$12^s.9238903$	$0^s.0000031$	$12''.15329$	$0''.00009$	.....	....	.....	....	0.53
BL146 H	2007.09.27 10:48	2454370.95	$12^s.9239105$	$0^s.0000011$	$12''.15281$	$0''.00003$	2.82	0.06	0.43	0.11	0.65
			$12^s.9241242$	$0^s.0000045$	$12''.15324$	$0''.00010$					
BL146 I	2007.10.03 10:25	2454376.93	$12^s.9239656$	$0^s.0000011$	$12''.15305$	$0''.00003$	.....	....	.....	....	0.77
BL146 J	2007.10.09 10:01	2454382.92	$12^s.9240014$	$0^s.0000004$	$12''.15297$	$0''.00001$	.....	....	.....	....	0.88
BL146 K	2007.10.17 09:30	2454390.89	$12^s.9240531$	$0^s.0000015$	$12''.15221$	$0''.00005$	-1.40	0.02	-0.60	0.05	0.04
			$12^s.9239474$	$0^s.0000008$	$12''.15161$	$0''.00002$					
BL146 L	2007.10.23 09:06	2454396.88	$12^s.9239765$	$0^s.0000007$	$12''.15119$	$0''.00002$	.....	....	.....	....	0.16
BL146 M	2007.10.27 08:50	2454400.87	$12^s.9239199$	$0^s.0000014$	$12''.15043$	$0''.00004$	0.77	0.03	1.36	0.05	0.24
			$12^s.9239780$	$0^s.0000014$	$12''.15179$	$0''.00004$					
BL146 N	2007.11.17 07:28	2454421.81	$12^s.9237229$	$0^s.0000008$	$12''.14946$	$0''.00003$	2.73	0.01	0.57	0.03	0.64
			$12^s.9239298$	$0^s.0000005$	$12''.15003$	$0''.00002$					

basic data reduction followed the standard VLBA procedure for phase-referenced observations (including the multi-source calibration strategy) and was described in detail in Loinard et al. (2007) and Torres et al. (2007). Two hours of telescope time were allocated to each of the first six observations, whereas 4 hours were allocated for each of the following 13. Because of the time spent on the calibrators, however, only about 1 and 2 hours were actually spent on source during the first six and the following 13 observations, respectively. Once calibrated, the visibilities were imaged with a pixel size of 50 μas after weights intermediate between natural and uniform (ROBUST = 0 in AIPS) were applied. Four representative examples of the resulting images are shown in Fig. 2.

3. RESULTS

The source was detected at all 19 epochs, but with highly variable flux densities (from less than 1 mJy to over 40 mJy). The flux was found to be highest near periastron, and lowest around apoastron, in agreement with the results by Massi et al. (2002, 2006). Short timescale variability (< 1 hour) is clearly present and the level of that variability also happens to depend on the orbital phase. Finally, significant levels of circular polarization were found at several epochs, but no linear polarization was ever detected. All these elements clearly indicate that the emission is primarily of gyrosynchrotron origin.

The source was found to be double at 13 epochs, and single for the remaining 6. The source positions (listed in Tab. 1) were determined using a two-dimensional Gaussian fitting procedure (task JMFIT in AIPS); when the source was double, both components were fitted simultaneously. JMFIT provides an estimate of the errors on the source position based on the expectation for ideal interferometer data (those estimates are also given in Tab. 1). However, in typical VLBA observations where the main calibrator is located a few degrees from the astronomical target (such as those considered here), remaining systematic phase calibration errors normally dominate the error budget, so the errors provided by JMFIT underestimate the true uncertainties. As we shall see below, the actual errors were estimated *a posteriori* from the fits to the data.

3.1. *Relative Astrometry & Orbit Modeling*

In this section, we will concentrate on the 13 epochs when the source was double, and analyze the relative position of the two sub-components. As established by Phillips et al. (1996) and B2007, these double source observations reflect the relative astrometry of the V773 Tau A components,[3] and as such can be used to assess and update the physical orbit obtained by B2007. There is, however, one difficulty. The mechanism

[3] As will become apparent momentarily, the emission is indeed associated with the two stars, but in some cases, it is not exactly *coincident* with them.

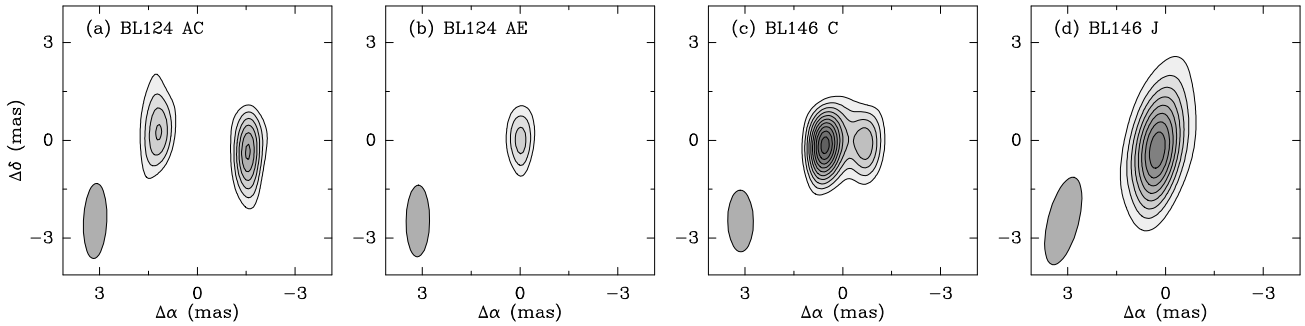

FIG. 2.— Sample VLBA images of V773 Tau A, exemplifying the variety of situations encountered. The synthesized beam is shown at the bottom-left of each panel. (a) Near apoastron (ϕ = 0.63), when the source is double. (b) Near apoastron (ϕ = 0.42) when the source is single (the detected source is always the primary in such situations), (c) Near periastron (ϕ = 0.08) when the sources are located in an east-west configuration, and resolved by our observations. (d) Just before or just after periastron (ϕ = 0.88 in the present case) when the sources are located in a north-south configuration, and cannot be resolved by our observations. Note that the source is clearly extended (i.e. significantly larger than the synthesized beam) in this last case. In the other three situations (panels a–c), the sources were either completely unresolved or very marginally resolved (the image source size was essentially equal to the synthesized beam size).

producing the radio emission is not directly related to the mass of the star, so the primary is not necessarily the brightest radio source in the system (in the present case, it is the brightest in only about 60% of the cases). This introduces a degeneracy in the relative position angle between the stars, which we removed using the preliminary orbital fit of B2007. The corresponding angular separations ($\Delta\alpha$, $\Delta\delta$) between the primary and the secondary are given in Tab. 1 for the 13 epochs when the source is double. The uncertainties on ($\Delta\alpha$, $\Delta\delta$) quoted in Tab. 1 are based on the errors delivered by JMFIT, and are almost certainly underestimated (see above).

Figure 3 shows all available relative astrometry data on V773 Tau A (from Phillips et al. 1993, B2007, and this work), along with several orbit models including that from B2007 (dashed line). Clearly there is general agreement between the old and new VLBA relative astrometry on V773 Tau A, and the B2007 orbit model. A close inspection of the VLBA separations and the B2007 orbit model in Fig. 3, however, shows an interesting trend in the VLBA astrometry. At most orbit phases the VLBA-derived separations and B2007 orbit model are in good agreement. But in most observations near periastron (secondary south-west of the primary) the VLBA separations appear systematically smaller (i.e. secondary nearer the primary) than predicted by the B2007 orbit. This suggests one of two possibilities: there is a possible bias in the B2007 orbit solution, or a possible bias in the VLBA-derived astrometry near periastron (where there is known enhancement in the radio flaring; Massi et al. 2002, 2006).

To investigate this issue we considered two different prescriptions for integrating the new VLBA data into the orbit modeling. In the first "VLBA + RV" model we considered the possibility that the KI visibilities were the source of a possible orbit bias in B2007, and used only the (old and new) VLBA-derived relative astrometry and double-lined RV from B2007 to derive an orbit model. In the second "Full Hybrid" model we used all available data (VLBA astrometry, KI visibilities, and RV), but assume that the VLBA separations near periastron were biased by the enhanced flaring activity (e.g. if the enhanced flares preferentially occur between the two stars), assigning these points lower weight (specifically a factor of 50% larger 1-sigma error per axis for orbit phases within 10% of periastron).[4] We find that both new orbit solutions are in excellent agreement with the original B2007 model, and renderings of both these orbit models are included in Fig. 3. It is clear that the KI visibility data is reliable at its stated uncertainties, and the most plausible hypothesis is that the VLBA relative astrometry near periastron contains biases associated with the enhanced flaring activity documented by Massi et al. (2002, 2006). This astrometric bias may be naturally explained in the helmet streamer scheme recently proposed by Massi et al. (2008). However, a more detailed analysis, which we defer to a forthcoming paper, will be necessary to understand better the origin of the apparent offset between the radio sources and the underlying stars. Table 2 gives a direct comparison between the orbit models from B2007 and the "Full Hybrid" model derived here; in all cases the orbital parameters between the two models (which share a significant amount of underlying data) are in excellent statistical agreement. For all subsequent analysis we adopt this "Full Hybrid" model for the updated V773 Tau A orbit.

TABLE 2
V773 TAU A ORBITAL PARAMETERS

Orbital Parameter	B2007	"Full Hybrid"
Period (days) ...	51.1039±0.0021	51.1028±0.0019
T_o (MJD)	53059.73±0.33	53059.68±0.30
e	0.2717±0.0085	0.2732±0.0070
K_A (km s^{-1})	35.90±0.53	35.94±0.53
K_B (km s^{-1})	41.5±1.4	41.5±1.4
γ (km s^{-1})	0.02±0.32	0.03±0.32
ω_A (deg)	4.6±2.4	5.0±2.3
Ω (deg)	63.5±1.7	62.7±1.1
i (deg)	66.0±2.4	67.8±1.6
a (mas)	2.811±0.047	2.810±0.034

Given the agreement between the "Full Hybrid" model and the B2007 orbit model, the updated physical parameters are highly consistent with B2007 estimates. Component dynamical masses resulting from this orbit model 1.48 ± 0.12 $M_\odot$ and 1.28 ± 0.07 $M_\odot$, for the primary and the secondary respectively – consistent with the B2007 estimates to 4% and 0.5-sigma. Similarly, the system distance estimate derived from the updated orbit model is 134.5 ± 3.2 pc, again consistent with the value from B2007 to 1% and 0.4-sigma. As a final note, we should stress that the present fit must still be considered preliminary as astrometric and RV observations to assess the gravitational effect of the two other members of the system (V773 Tau B and C) are ongoing.

[4] Our methods for orbit modeling with heterogenous RV and astrometric/visibility datasets are described in Boden et al. (2000) and are not repeated here. In all the orbit modeling we have weighted all VLBA astrometry consistently with the weighting derived in B2007, at 0.2 mas per axis 1-sigma, except as noted for points near periastron in the "Full Hybrid".

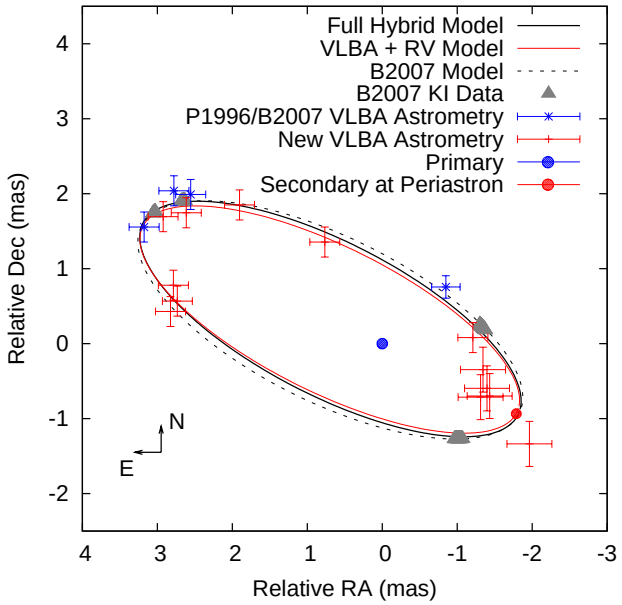

FIG. 3.— VLBA Relative Astrometry and Orbit Models of V773 Tau A. Here VLBA relative astrometry from P1996, B2007 and this work is shown with orbit model renderings for the B2007 orbit and two models derived here (the "VLBA + RV" and "Full Hybrid" models described in the text). We render the primary (Aa) component at the origin and the secondary (Ab) at periastron. The apparent sizes of the V773 Tau A components are estimated by SED modeling (B2007) and rendered to scale.

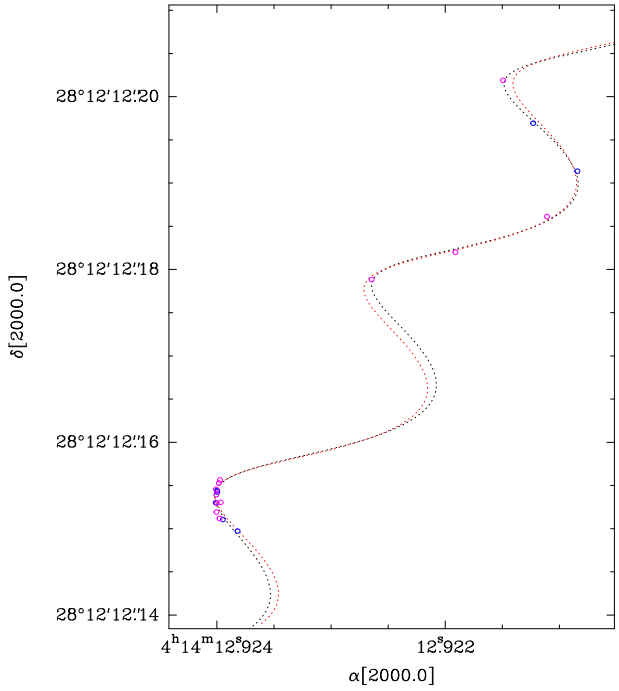

FIG. 4.— Measured barycenter positions and best astrometric fits for V773 Tau A. The observed positions are shown as ellipses, whose sizes are the error bars. Blue symbols represent the "best seven" observations, whereas magenta ones indicate the other 12 observations. Two fits are shown: the dotted red line corresponds to the best fit to all 19 observations without acceleration (at the scale shown here, this fit is undistinguishable from that to the "best seven" epochs discussed in Sect. 3.2.1). The black dotted line, on the other hand, indicates the best fit to the same data with acceleration.

3.2. *Absolute Astrometry & Parallax determination*

3.2.1. *First astrometric fit*

In addition to their separation, the VLBA provides the absolute position of each of the radio sources[5] (see Tab. 1). Once the orbital motion of the system has been determined, it can be subtracted from the positions listed in Tab. 1 to obtain the coordinates of the barycenter of the system. Of course, the only observations for which this can unambiguously be done are those when the source was double. For the corresponding 13 observations, the preferred strategy would be to combine the measured separation between the primary and the secondary (let us call it $\mathbf{r}$), and the masses deduced from the orbital fit. The separation $\mathbf{r}_1$ between the primary to the barycenter is then given by

$$\mathbf{r}_1 = \frac{m_s}{m_s + m_p}\mathbf{r}. \qquad (1)$$

Here, m_p and m_s are the masses of the primary and secondary, respectively. This strategy works well as long as the separation between the radio sources properly traces the separation between the stars. As we have seen earlier, this is a valid assumption except near periastron. As a consequence, we initially considered only the seven observations when the source was double and not near periastron. These observations are sufficiently well spread in time to provide a reasonable characterization of the trigonometric parallax and proper motion of the barycenter of V773 Tau A (see Fig. 4). The procedure used to perform the astrometric fit is described in detail in Loinard et al. (2007); the reference epoch was taken at the median of the observations (JD 2454056 ≡ 2006.88). The best fit to these "best seven observations" yields the parameters shown in the first line of Tab. 3. The post-fit rms is 0.26 mas and 0.24 mas in right ascension and declination, respectively. This is in good agreement with our assumed errors on the separation between the sources (Sect. 3.1). The parallax estimated above corresponds to a distance $d = 133.1^{+5.1}_{-4.7}$, in excellent agreement with the figure obtained from the orbital fitting.

[5] Strictly, the VLBA provides the angular offset between the source and the main calibrator. However, that calibrator is a distant quasar which can be assumed to be fixed, and whose coordinates are measured relative to the ICRF. Thus, the positions delivered by the VLBA are very nearly absolute.

3.2.2. *Second astrometry fit*

The astrometric fit obtained above only includes about a third of the VLBA observations available. Although the position of the barycenter of the system is deduced in a somewhat less direct fashion for the other two thirds of the data, it would still be desirable to incorporate them in a global astrometric fit. Moreover, the astrometric behavior of the source is important to help constrain the origin of the radio emission, particularly near periastron, as will be discussed below.

Resolved double near periastron — The six observations where the source was found to be double, and which were not included in the fit of Sect. 3.2.1, were taken when the system was near periastron. We saw in Sect. 3.1 that in such cases, the separation between the radio sources tended to be systematically smaller than the separation between the stars. This likely occurs because of enhanced flaring activity on either of the two stars, or on both of them. If both stars experience this enhanced activity, then the radio sources associated with them are likely to be similarly displaced from their respective star. The best strategy to obtain the position of the barycenter would still be to use Eq. (1) using the *measured* separation between the stars for the separation $\mathbf{r}$, because both $\mathbf{r}$ and $\mathbf{r}_1$

TABLE 3
ASTROMETRY FIT RESULTS

Fit	$\alpha_{J2006.78}$ 04^h14^m	$\delta_{J2006.78}$ $28^\circ12'$	μ_α (mas yr^{-1})	μ_δ (mas yr^{-1})	a_α (mas yr^{-2})	a_δ (mas yr^{-2})	π (mas)
w/o acceleration; seven best ..	$12^s.922271\pm0^s.000011$	$12''.17442\pm0''.00012$	17.29±0.20	–23.74±0.13	—	—	7.51±0.28
w/o acceleration; all	$12^s.922269\pm0^s.000009$	$12''.17454\pm0''.00008$	17.27±0.14	–23.79±0.09	—	—	7.57±0.20
w/ acceleration; all	$12^s.922193\pm0^s.000012$	$12''.17494\pm0''.00016$	16.95±0.09	–23.71±0.09	2.82 ± 0.40	–1.07 ± 0.42	7.64±0.12

are expected to be shrunk by a similar factor. If the enhanced activity only occurs on one of the stars, however, then only for that object will the radio source be offset from the star. A better strategy to derive the position of the barycenter of the system in this case would be to identify the star not affected by enhanced activity, and calculate the separation between that star and the barycenter using the *prediction* of the orbit model presented above (which provides the true separation between the stars) rather than the measured separation between the radio sources.

To test for these different possibilities, we ran three tests (all of which include the seven observations of fit A, in addition to the six resolved observations near periastron). In the first one, we assumed that both stars experienced enhanced activity and that the position of the barycenter should be obtained using the *measured* separation between the radio sources. In the second, we assumed that only the secondary suffered from enhanced activity, and used the measured position of the primary and the separation between the primary and the barycenter predicted by the orbit model to estimate the position of the barycenter. Finally, in the third test, we assumed that only the primary was affected by enhanced activity, and used the position of the secondary and a predicted secondary-barycenter separation. The astrometric parameters obtained from these three tests are very similar to one another, and well within one sigma of the results of the fit presented in Sect. 3.2.1. In terms of post-fit r.m.s., the best result is obtained when the position of the barycenter is deduced from the *measured* separation between the sources. This indicates that both stars experience enhanced activity near periastron, a result that was to be expected since *both* components of the system become brighter near periastron.

Single sources — When the radio source associated with V773 Tau A is single, one must again distinguish between two different situations. For two of these observations, the source is weak ($\sim$ 1 mJy), and the system was near apoastron (ϕ = 0.42 and 0.53; Tab. 1). Both sources are known to become dimer near apoastron, and one of them has clearly faded bellow our detection limit in these two cases. It is *a priori* unclear whether the detected source corresponds to the primary or the secondary. To find out, we estimated the position of the barycenter of the system using our orbit model (Sect. 3.1) assuming first that the detected source was the primary and then that it was the secondary. The positions derived assuming that the detected source is the primary fall almost exactly on the astrometry fits, whereas the positions deduced assuming that the detected source is the secondary fall several mas away from the fit. We conclude that in these two cases, the detected source is the primary.

For the remaining 4 observations, the source is single, but bright (at least several mJy). All four of these observations were obtained at an orbit phase of about 0.2 before or after periastron (see Tab. 1). In this situation, the two stars are located in projection almost exactly north-south of each other, with a projected separation of about 1 mas (see Fig. 3). Since our resolution in the north-south direction is about 2 mas, we do not expect to resolve the two stars in this situation, but instead to detect a single source slightly elongated in the north-south direction. This is in fact what happens (see Fig. 2, particularly panel d). Indeed, the mean deconvolved FWHM size of the emission for these four epochs is 1.33 mas, 50% larger than the corresponding figure (0.89 mas) when the source is double or single but near apoastron. In this situation, the measured position of the source is likely to provide a good approximation (to within a few tenths of a mas) of the position of the barycenter of the system.

To refine the determination of the parallax and proper motion of V773 A, we performed a second astrometric fit which includes

- The seven observations used to obtain the fit in Sect. 3.2.1.
- The six observations corresponding to double sources near periastron. The position of the barycenter in this case was calculated using Eq. (1) and the true separation for **r**.
- The two observations where the source was single and near apoastron. In this case, the detected source was the primary, and we obtained the position of the barycenter using a separation between the primary and the barycenter deduced from our orbit model.
- The four epochs at $\Delta\phi \sim 0.2$, for which the position of the barycenter was assumed to be that of the (single) source itself.

The results of this fit are shown on Fig. 4 and in the second line of Tab. 3, and are very similar to those of our initial fit. All the parameters are well within one sigma of one another. The distance corresponding to this global fit is $132.0^{+3.5}_{-3.4}$, in excellent agreement with both the fit to the best seven VLBA observations, and the figure obtained from the orbit model. The post-fit r.m.s. is 0.28 mas in declination (similar to that of our first fit), but somewhat poorer (0.49 mas) in right ascension.

3.2.3. *Third astrometric fit: including acceleration*

As mentioned earlier, V773 Tau A is part of a quadruple system. Because of the gravitational pull of the other two members, the proper motion of the barycenter of V773 Tau is not expected to be linear and uniform, but must contain acceleration terms. Since the orbital period of the system (nearly 50 years; Duchêne et al. 2003) is significantly longer than the time span of our observations (about 2 years), the acceleration over the course of our observations can be assumed to be constant (a situation similar to that of T Tau Sb as discussed by Loinard et al. 2007). Thus, we performed a third fit (to

TABLE 4
ABSOLUTE PROPER MOTION COMPARISONS.

	μ_α (mas yr^{-1})	μ_δ (mas yr^{-1})
Present work, w/o acceleration	17.27±0.14	–23.79±0.09
Present work w/ acceleration	16.95±0.09	–23.71±0.09
Lestrade et al.	0.42±0.29	–23.25±0.25
Hipparcos	0.65±2.61	–24.89±1.81

the 19 epochs considered in the second fit above; a fit with acceleration to only seven epochs would be very poorly constrained) but including a uniform acceleration term. This last fit is shown in Fig. 4 to be somewhat better than that without acceleration. In particular, the first two epochs are well reproduced when acceleration terms are included, whereas they were somewhat offset from the best fit without acceleration.[6] Quantitatively, the improvement is seen in the post-fit r.m.s. which is now 0.26 mas in right ascension, and 0.23 mas in declination. Since the acceleration appears to be mostly in right ascension (Tab. 3), the post-fit r.m.s. improvement is most noticeable along that direction. The parameter most affected by the inclusion of acceleration is the proper motion in right ascension; the other astrometric parameters are all highly consistent with the results of the fits without acceleration. In particular, the distance deduced from our third fit is 130.9 ± 2.1 pc. Since the corresponding fit yields the lowest post-fit r.m.s., we consider this last value is our preferred result.

The excellent agreement (better than 3%, or about 1σ) between the distance obtained from orbit model and the direct parallax measurement validates both methods, and demonstrates that the errors quoted represent the true accuracy (and not just the precision) of the results. We note, finally, that the distance obtained here is only marginally consistent with the the result obtained by Lestrade et al. (1999; d = 148.4 ± 5.3 pc). We attribute the discrepancy to the fact that Lestrade did not take into account the binarity of the source in their astrometric fits.

4. DISCUSSION

4.1. *Masses and comparison with PMS models*

Thanks to the improved characterization of the physical orbit of the V773 Tau A system presented here, we obtained updated masses for the two members of the system. Since these improved value are only very marginally different from those reported by B2007, we will not repeat the extensive pre-main sequence evolutionary model comparisons given in B2007. We merely show on Fig. 5 a comparison between the location on the HR diagram of the two members of V773 Tau A and the Yonsei-Yale Y^2 tracks and isochrones (Demarque et al. 2004). In particular, the tracks appropriate for the new mass determinations, as well as those for the values given by B2007 are shown. Note the good agreement between the models and the data, and the fact that the age of both stars appears to be consistent with about 3 Myr.

4.2. *Absolute proper motion and acceleration*

It is interesting to compare the value of the absolute proper motion of the barycenter of V773 Tau A obtained here

[6] There is an observation bias here: since most of our observations are clustered between JD 2454336 and JD 2454422 (Tab. 1), all fits are constrained to reproduce these positions, and the comparatively under-weighted first epochs are those most strongly affected when no acceleration is included.

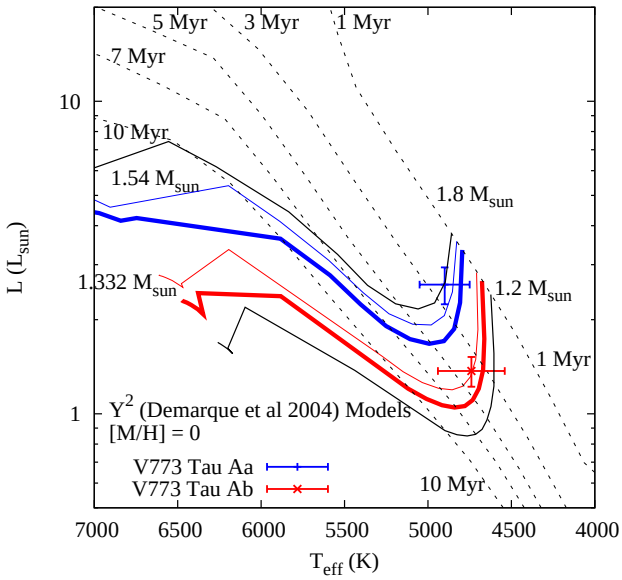

FIG. 5.— Comparison between the location on the HR diagram of the two members of V773 Tau A and the Yonsei-Yale Y^2 tracks and isochrones. The thick blue and red lines show the tracks for V773 Tau Aa and Ab, respectively, for the updated masses. The corresponding thin lines are the tracks for the slightly higher masses reported by B2007.

with previous determinations, particularly those reported by Lestrade et al. (1999) and in the Hipparcos catalog (Perryman et al. 1997). While the declination components agree fairly well (see Tab. 4), there is a large difference in right ascension between our determination on the one hand, and those of Lestrade et al. (1999) and the Hipparcos satellite, on the other. The difference is $\Delta(\mu_\alpha \cos\delta)$ = +16.6 ± 0.6 mas yr^{-1}, corresponding to Δv_α = +10.3 ± 0.4 km s^{-1}.

The mean epoch of the observations reported by Lestrade et al. (1999) and of the Hipparcos satellite are very similar (1993.88, and 1991.25, respectively). Our observations, however, have a significantly more recent mean epoch (2006.88). The difference between our results and those earlier ones, therefore, likely indicates that the vector velocity of the barycenter of V 773 Tau A has changed in the last decade. This is not particularly surprising since V773 Tau is a quadruple system: the gravitational pull of the other members of the system will induce a reflex motion for the barycenter of the primary.

According to the V773 Tau A/B orbit published by Duchêne et al. (2003; see their Fig. 4, reproduced as Fig. 6 here), in the early 1990s, the B component was located to the north-west of the A component and moving almost exactly due east. In 2006, however, the component would be expected to be to the south-east of A, and moving roughly due west (this is indeed confirmed by recent and still unpublished Adaptive Optics Keck observations). Thus, if one subtracts the velocity of the B component in the early 1990s from its velocity in 2006, one will obtain a vector pointing due west. The corresponding reflex motion of the barycenter of the A component would be expected to point due east (i.e. towards positive right ascension), as is indeed observed. Thus, the change of proper motion motion in right ascension in the last decade does agree qualitatively with what would be expected from the relative orbit between the A and B components.

Let us now examine the issue quantitatively. According to the observations published by Duchêne et al. (2003), the typ-

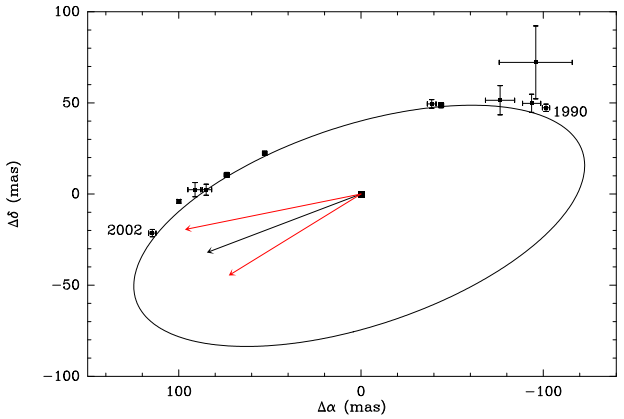

FIG. 6.— Observed separations between V773 Tau A and V773 Tau B between 1990 and 2002 and orbit model taken from Duchêne et al. (2003). The acceleration vector of V773 Tau A is shown as a black arrow, with its error cone indicated by the red arrows. Note that the acceleration vector points (as expected) towards the position where V773 Tau B is expected to have been located in 2006, at the median epoch of our observations.

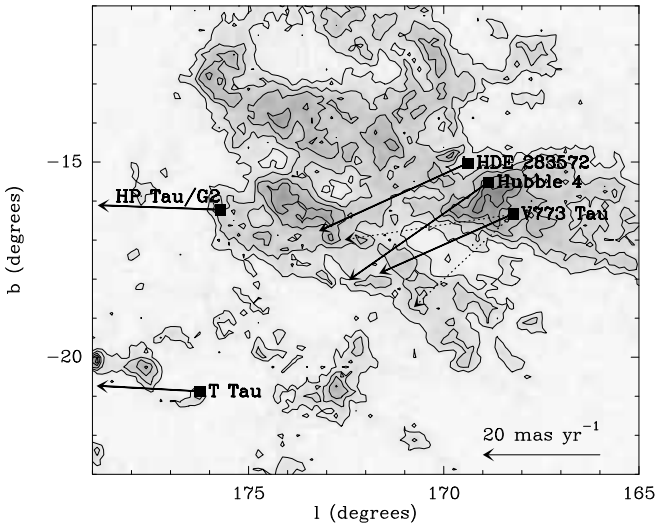

FIG. 7.— Positions and proper motions of Hubble 4, HDE 283572, T Tau, HP Tau/G2, and V773 Tau overimposed on the CO(1-0) map of Taurus from Dame et al. (2001). In each case, the arrows indicate the direction and amplitude of the proper motion. For V773 Tau, the two dotted arrows correspond our measurement and that of Lestrade et al. (2009). The full line is the mean of these two values.

ical proper motion of component B relative to component A is about 18 mas yr^{-1}. Thus, the difference in right ascension proper motion between the early 1990s and 2006 is expected to be about 36 mas yr^{-1} (recall that the motion changed from due east to due west, so the total change is twice the value at each epoch). This is slightly more than twice the observed change of proper motion of the barycenter of component A. Since the size of the orbit of each component is commensurate with the inverse of its mass, this result would indicate that the mass of component B is slightly less half of the total mass of component A, or about 1.3 $M_\odot$. This is somewhat larger than appears to be indicated by the spectral type of V773 Tau B (M $\sim$ 0.65 – 0.8 $M_\odot$ –Duchêne et al. 2003). However, our present discussion does not include a complete description of the V773 A/B orbit, nor of the gravitational influence of the C component. As a consequence, we consider that the change of proper motion observed in right ascension is quantitatively in reasonable agreement with the expectation based on the orbital motion of the system. A more detailed analysis combining the present observations and new high-resolution infrared observations will be presented in a forthcoming paper.

A further indication that the reflex motion of V773 tau A must be taken into account when studying the absolute motion of its barycenter is provided by the detection of its acceleration (Sect. 3.2.3). In Fig. 6, we compare the direction of the acceleration vector with measured relative positions of the V773 Tau A and B components, and with the orbital fit proposed by Duchêne et al. (2003). The acceleration vector appears to point towards the position where V773 Tau B is expected to have been at the mean epoch of our VLBA observations.

4.3. *Origin of the emission*

As mentioned earlier, the radio emission detected here is most likely of gyrosynchrotron origin. In young stars, this kind of emission is usually thought to be produced during flares associated with reconnections between magnetic loops. The fact that the emission is at most marginally resolved in our observations implies that the diameter of the radio emitting region is $\sim$ 1 mas (recall from Sect. 3.2.2 that the mean deconvolved size of the emission is about 0.9 mas). Both members of the V773 Tau A binary have radii of about 2 $R_\odot$ (B2007), so the magnetic loops appear to be mostly confined to a region (conventionally considered to be the magnetosphere) of radius $\sim 6\,R_*$.

Near periastron, the separation between the radio sources is typically 0.3 to 0.4 mas shorter than the separation between the stars (Fig. 3; Sect. 3.1). From the analysis of the absolute proper motions (Sect. 3.2), we concluded that in that configuration, both radio sources are roughly symmetrically displaced from their associated star, so each radio source is offset from its star by about 0.15–0.20 mas, or 2 to 3 R_*. Thus, the displacement between the star and the radio source near periastron is a fraction of the magnetosphere radius.

Interestingly, the radio flux appears to be strongly correlated to the separation between the stars (Sect. 3; Massi et al. 2002, 2006). At periastron, that separation is still about 2 mas, or 30 R_*. Thus, even at periastron, the magnetospheres of the two stars as defined above do not appear to overlap. How can the radio emission (which is clearly of magnetic origin) be affected by the separation between the stars, if the radius of the magnetospheres is several times smaller than the shortest separation between the stars?

A possible solution to this conundrum has recently been proposed by Massi et al. (2008) who suggested the existence of two kinds of magnetic structures around the stars in V773 Tau A. The first kind corresponds to compact, closed magnetic loops extending to only a few stellar radii. The second category are semi-open structures similar to the so-called helmet streamers observed around the Sun (e.g. Vourlidas 2006). Those streamers are anchored on the upper edge of a compact closed loop at a few stellar radii above the stellar surface, but they extend to about 30 stellar radii. Thus, reconnections between these extended loops could occur when the stars of V773 Tau A are near periastron, and naturally explain the associated radio flux increase. We note, however, that in all six observations that we obtained near periastron, the radio emission was still clearly resolved into two compact structures each at most few stellar radii across, but separated by more than 20 R_* (see Fig. 2, panel c). We find no evidence for strong radio emission midway between the stars. Thus, if the increased flux near periastron is indeed due to reconnections between helmet streamers, then the bulk of the associated ra-

dio emission must be generated near the anchor point of the streamers rather than along them. It is indeed noteworthy that the displacement of the radio sources near periastron (2–3 R_*) is so similar to the height above the stellar surface at which helmet streamers are expected to be anchored. The mechanism by which reconnection could occur anywhere along a streamer, but only produce radio emission at the anchor point remains unclear, and additional observations, particularly at higher angular resolution, will be necessary to understand this point.

4.4. *The distance to the L1495 region of Taurus*

In projection, V773 Tau is located near the dark cloud Lynds 1495 in the central region of Taurus. Two other young stars with recent VLBA-based parallax measurements (Hubble 4 and HDE 283572; Torres et al. 2007) are located in the same portion of Taurus. Interestingly, they appear to be at very similar distances (132.8 $\pm$ 0.5 pc for Hubble 4 and 128.5 $\pm$ 0.6 pc for HDE 283572, against 130.9 $\pm$ 2.1 pc for V773 Tau). Given the multiplicity of the source, the proper motion of V773 Tau in right ascension varies significantly with time (Sect. 4.2). In Fig. 6, we show our own measurement, that of Lestrade et al. (1999) and their mean value. The latter is probably the best estimate of true proper motion of V773 Tau, and appears to be very similar to the proper motions of Hubble 4 and HDE 283572. Thus, Hubble 4, HDE 283572, and V773 Tau not only are located in the same portion of Taurus, they also appear to share the same kinematics (Fig. 7). Therefore, they most likely belong to a common spatio-kinematical sub-group within the Taurus complex.[7] Thus, we argue that the weighted mean of our three parallax measurements provides a good estimate of the mean distance to Lynds 1495, and that the difference in distance between the nearest and farthest of those three stars reflects the total depth of the associated sub-group. We find a mean distance of 131.2 $\pm$ 0.4 pc, and a total depth of 4.3 pc. The projected separation between V773 Tau and HDE 283572 on the plane of the sky is about 1.8 degrees, or 4.1 pc (Fig. 7). Thus, the spatio-kinematical structure associated with Lynds 1495 appears to be about as deep as it is wide.

5. CONCLUSIONS

In this paper, we have described and analyzed new multi-epoch VLBA observations of the young stellar system V773 Tau. The data have been used both to improve the determination of the physical orbit of the compact binary at the center of the system, and to measure its trigonometric parallax. We show that the distance to the system obtained from the orbit model is fully consistent with the direct parallax measurement. The proper motion of the barycenter of V773 Tau A appears to be accelerated, and the acceleration vector points (as expected) towards the expected position at the median epoch of our observations of V773 Tau B, the nearest member of the system. Also as a consequence of the multiplicity of the system, the proper motion in right ascension has changed significantly in the past 15 years. A detailed discussion of the relative motion between V773 Tau A and its two companions V773 Tau B and V773 Tau B will be the subject of a forthcoming paper where new high-resolution infrared images will also be presented.

In about two thirds of our VLBA observations, the radio emission from V773 Tau A is resolved into a double source. Far from the periastron of the system, the two radio sources are coincident (to the accuracy of our observations) with the stars themselves. Near periastron, however, the separation between the radio sources is systematically somewhat smaller than the separation between the stars. This effect might be related to reconnection events between large magnetic structures associated with the two stars in V773 Tau A. However, the exact physical processes occurring during these reconnections remain unclear. Higher frequency and/or sensitivity VLBA observations obtained near periastron would clearly help elucidate this issue. Some such data are currently being gathered, and will be the subject of a forthcoming paper.

R.M.T., L.L. and L.F.R. acknowledge the financial support of DGAPA, UNAM and CONACyT, México. We are grateful to Tom Dame for sending us a digital version of the integrated CO(1-0) map of Taurus, and to Maria Massi for stimulating comments on a draft version of this paper. The National Radio Astronomy Observatory is a facility of the National Science Foundation operated under cooperative agreement by Associated Universities, Inc.

[7] We note that in a previous paper of this series (Torres et al. 2007), we reached an opposite conclusion because we used the distance to V773 Tau given by Lestrade et al. (1999). The present work shows that the latter distance was likely overestimated by about 15 pc.

REFERENCES

[1]Beasley, A. J., Gordon, D., Peck, A. B., Petrov, L., MacMillan, D. S., Fomalont, E. B., & Ma, C., 2002, ApJS, 141, 13
[2]Boden, A. F., Torres, G., Sargent, A. I., Akeson, R. L., Carpenter, J. M., Boboltz, D. A., Massi, M., Ghez, A. M., Latham, D. W., Johnston, K. J., Menten, K. M., Ros, E., 2007, ApJ, 670, 1214
[3]Demarque, P., Woo, J.-H., Kim, Y.-C., & Yi, S. K., 2004, ApJS, 155, 667
[4]DuchŘne, G., Ghez, A. M., McCabe, C., Weinberger, A. J., 2003, ApJ, 592, 288
[5]Feigelson, E. D., Welty, A. D., Imhoff, C., Hall, J. C., Etzel, P. B., Phillips, R. B., & Lonsdale, C. J., 1994, ApJ, 432, 373
[6]Fey, A. L., Ma, C., Arias, E. F., Charlot, P., Feissel-Vernier, M., Gontier, A.-M., Jacobs, C. S., Li, J., & MacMillan, D. S., 2004, AJ, 127, 3587
[7]Ghez, A. M., Neugebauer, G., & Matthews, K., 1993, AJ, 106, 2005
[8]Hillenbrand, L. A., White, R. J., 2004, ApJ, 604, 741
[9]Kutner, M. L., Rydgren, A. E., & Vrba, F. J., 1986, AJ, 92, 895
[10]Leinert, Ch., Zinnecker, H., Weitzel, N., Christou, J., Ridgway, S. T., Jameson, R., Haas, M., & Lenzen, R., 1993, A&A, 278, 129
[11]Lestrade, J.-F., Preston, R. A., Jones, D. L., Phillips, R. B., Rogers, A. E. E., Titus, M. A., Rioja, M. J., & Gabuzda, D. C., 1999, A&A, 344, 1014
[12]Loinard, L., Mioduszewski, A. J., RodrŠguez, L. F., GonzĞlez, R. A., RodrŠguez, M. I., & Torres, R. M., 2005, ApJ, 619, L179
[13]Loinard, L., Torres, R. M., Mioduszewski, A. J., RodrŠguez, L. F., GonzĞlez-LŮpezlira, R. A., Lachaume, R., VĞzquez, V., & GonzĞlez, E., 2007, ApJ, 671, 546
[14]Loinard, L., Torres, R. M., Mioduszewski, A. J., & RodrŠguez, L. F. 2008, ApJ, 675, L29
[15]Ma, C., Arias, E. F., Eubanks, T. M., Fey, A. L., Gontier, A.-M., Jacobs, C. S., Sovers, O. J., Archinal, B. A., & Charlot, P., 1998, AJ, 116, 516
[16]Massi, M., Menten, K., & NeidhŽfer, J., 2002, A&A, 382, 152
[17]Massi, M., Forbrich, J., Menten, K. M., Torricelli-Ciamponi, G., NeidhŽfer, J., Leurini, S., & Bertoldi, F., 2006, A&A, 453, 959
[18]Massi, M., Ros, E., Menten, K. M., Kaufman BernadŮ, M., Torricelli-Ciamponi, G., NeidhŽfer, J., Boden, A., Boboltz, D., Sargent, A., & Torres, G., 2008, A&A, 480, 489

[19]Mathieu, R. D., Baraffe, I., Simon, M., Stassun, K. G., & White, R., 2007, PRPL, 411
[20]Menten, K. M., Reid, M. J., Forbrich, J., & Brunthaler, A., 2007, A&A, 474, 515
[21]O'Neal, D., Feigelson, E. D., Mathieu, R. D., & Myers, P. C., 1990, AJ, 100, 1610
[22]Perryman, M. A. C., Lindegren, L., Kovalevsky, J., Hoeg, E., Bastian, U., Bernacca, P. L., CrŐzŐ, M., Donati, F., Grenon, M., van Leeuwen, F., van der Marel, H., Mignard, F., Murray, C. A., Le Poole, R. S., Schrijver, H., Turon, C., Arenou, F., FroeschlŐ, M., & Petersen, C. S., 1997, A&A, 323, L49
[23]Phillips, R. B., Lonsdale, C. J., & Feigelson, E. D., 1993, ApJ, 403L, 43
[24]Phillips, R. B., Lonsdale, C. J., Feigelson, E. D., & Deeney, B. D., 1996, AJ, 111, 918
[25]Torres, R. M., Loinard, L., Mioduszewski, A. J., & Rodriguez, L. F., 2007, ApJ, 671, 1813
[26]Torres, R. M., Loinard, L., Mioduszewski, A. J., & Rodriguez, L. F., 2009, ApJ, 698, 242
[27]Vourlidas, A. 2006, Solar Activity and its Magnetic Origin, ed. V. Bothmer, & A. Hady (Cambridge University Press), 197
[28]Welty, A. D., 1995, AJ, 110, 776
[29]Woitas, J., 2003, A&A, 406, 685

H

The Very Long Baseline Array

The Very Long Baseline Array (VLBA) is a system of ten radio telescopes controlled remotely from the Domenici Science Operations Center (DSOC) in Socorro, New Mexico (USA) by the National Radio Astronomy Observatory (NRAO). The array works together as the world largest dedicated, full-time astronomical instrument using the technique of VLBI. From Mauna Kea on the Big Island of Hawaii to St. Croix in the U.S. Virgin Islands, the VLBA spans more than 5,000 miles. This Appendix attempts to summarize the instrument information for astronomers who does not used the VLBA before. All the information here has been adapted from the VLBA observational status summary available through the VLBA astronomer page at http://www.vlba.nrao.edu/astro/. It is included here for completeness.

H.1 Antenna sites

Tab. H.1 gives the surveyed geographic locations of the 10 antennas comprising the VLBA. All locations are based on the WGS84 ellipsoid used

Table H.1. Locations of VLBA and HSA telescopes.

Location	Latitud	Longitud	Elevation
Saint Croix, Vinginia (SC)	17°45′23″.68	64°35′01″.07	16
Hancock, New Hampshire (HN)	42°56′00″.99	71°59′11″.69	296
North Liberty, Iowa (NL)	41°46′17″.13	91°34′26″.88	222
Fort Davis, Texas (FD)	30°38′06″.11	103°56′41″.34	1606
Los Alamos, New Mexico (LA)	35°46′30″.45	106°14′44″.15	1962
Pie Town, New Mexico (PT)	34°18′03″.61	108°07′09″.06	2365
Kitt Peak, Arizona (KP)	31°57′22″.70	111°36′44″.72	1902
Owens Valley, California (OV)	37°13′53″.95	118°16′37″.37	1196
Brewster, Washington (BR)	48°07′52″.42	119°40′59″.80	250
Mauna Kea, Hawaii (MK)	19°48′04″.97	155°27′19″.81	3763
Arecibo, Puerto Rico (AR)	18°20′36″.60	66°45′11″.10	497
Green Bank, West Virginia (GB)	38°25′59″.24	79°50′23″.41	807
VLA, New Mexico (Y27)	34°04′43″.75	107°37′05″.91	2115
Effelsberg, Germany (EB)	50°31′30″.00	-6°53′00″.30	319

by the GPS system, with Earth radius $a = 6378.137$ km and flattening $1/f = 298.257223563$ (Napier 1995).

Several other radio telescopes often participate in VLBI observing in conjunction with the VLBA. These include the Very Large Array (VLA), either with up to 27 antennas added in phase (Y27) or with a single antenna (Y1); the Green Bank Telescope (GBT); Arecibo (AR); Effelsberg (Eb); the European VLBI Network (EVN); plus (occasionally) various geodetic antennas or the NASA Deep Space Network.

A total of up to 100 hours per four-month trimester has been reserved for a High Sensitivity Array (HSA) composed of the VLBA, VLA, GBT, AR, and Eb. The VLA and GBT are NRAO facilities, while Arecibo is operated by the National Astronomy and Ionosphere Center (NAIC), and Effelsberg is operated by Max Planck Institut für Radioastronomie (MPIfR). Tab. H.1 also lists the locations of the HSA telescopes.

H.2 Antennas

The main reflector of each VLBA antenna is a 25 m diameter dish which is a shaped figure of revolution with a focal-length-to-diameter ratio of 0.354.

A 3.5 m diameter Cassegrain subreflector with a shaped asymmetric figure is used at all frequencies above 1 GHz, while the prime focus is used at lower frequencies. The antenna features a wheel-and-track mount, with an advanced-design reflector support structure. Elevation motion occurs at a rate of 30° per minute between a hardware limit of 2° and a software limit of 90°. Azimuth motion has a rate of 90° per minute between limits of −90° and 450°. Antennas are stowed to avoid operation in high winds, or in case of substantial snow or ice accumulation.

H.3 Performance parameters

Tab. H.2 gives the nominal frequency ranges for the receiver/feed combinations available on all or most VLBA antennas (Thompson 1995). Passband-limiting filters are described by Thompson (1995). Measured frequency ranges are broader than nominal. Measured frequency ranges may be especially important for avoiding radio frequency interference (RFI), and for programs involving extragalactic lines, rotation measures (Cotton 1995; Kemball 1999), and multi-frequency synthesis (Conway & Sault 1995; Sault & Conway 1999).

Also appearing in Tab. H.2 are parameters characterizing the performance of a typical VLBA antenna for the various receiver/feed combinations. Columns [3] and [5] give typical VLBA system equivalent flux densities ($SEFD$s) at zenith and opacity-corrected gains at zenith, respectively. These were obtained from averages of right circularly polarized (RCP) and left circularly polarized (LCP) values from 10 antennas, measured at the frequencies in column [4] by VLBA operations personnel during regular pointing observations. In 2007, Germany's Max Planck Insitut für Radioastronomie funded a program to enhance the 1 cm sensitivity of the VLBA by installing modern low noise amplifiers to replace the original VLBA hardware. This program, implemented by NRAO, was completed in early 2008 and achieved its goal of reducing the zenith $SEFD$s by more than 30%.

The typical zenith $SEFD$s can be used to estimate rms noise levels on a baseline between 2 VLBA antennas (ΔS for a single polarization) and in a VLBA image ($\Delta I_{\rm m}$ for a single polarization). Characteristic values for $\Delta S^{256,2{\rm m}}$ assuming a fringe-fit interval of $\tau_{\rm ff} = 2$ minutes and for $\Delta I_{\rm m}^{256,8{\rm h}}$ assuming a total integration time on source of $t_{\rm int} = 8$ hours also appear in

Table H.2. Frequency ranges and typical performance parameters.

Receivers and Feeds	Nominal Frequency Range [GHz]	Typical Zenith SEFD [Jy]	Center Frequency for SEFD [GHz]	Typical Zenith Gain [K Jy^{-1}]	Baseline Sensitivity $\Delta S^{256.2m}$ [mJy]	Image Sensitivity $\Delta I_m^{256.8m}$ [μJy $beam^{-1}$]
90 cm	0.312 - 0.342	2227	0.326	0.097	51.1[a]	350
50 cm	0.596 - 0.626	2216	0.611	0.088	101.1[b]	700[b]
21 cm[c]	1.35 - 1.75	296	1.438	0.096	3.3	32
18 cm[c]	1.35 - 1.75	303	1.658	0.100	3.7	36
13 cm[d]	2.15 - 2.35	322	2.275	0.093	3.6	35
13 cm[d]	2.15 - 2.35	337	2.275	0.090	3.8	37
6 cm	4.6 - 5.1	312	4.999	0.130	3.5	34
4 cm	8.0 - 8.8	307	8.425	0.113	3.6	35
4 cm[e]	8.0 - 8.8	407	8.425	0.106	4.7	46
2 cm	12.0 - 15.4	550	15.369	0.104	6.2	60
1 cm[f]	21.7 - 24.1	502	22.236	0.107	5.9	57
1 cm[f]	21.7 - 24.1	441	23.799	0.107	5.1	50
7 mm	41.0 - 45.0	1436	43.174	0.078	22.2[g]	151
3 mm[h]	80.0 - 90.0	4000	86.2	0.025	57[i]	850[j]

[a] Assumes a fringe-fit interval of 1 minute.

[b] Assumes a fringe-fit interval of 1 minute and a data rate of 32 Mbps.

[c] Different settings of the same 20 cm receiver.

[d] Filters at NL, LA, and OV restrict frequencies to 2200-2400 MHz.

[e] With 13/4 cm dichroic.

[f] Different settings of the same 1 cm receiver. Continuum performance is better at 23.8 GHz, away from the water line.

[g] Performance may be worse on some baselines due to poor subreflector orprimary reflector shapes or poor atmospheric conditions (almost universal at SC).

[h] "Average" 3 mm antennas are assumed.

[i] Assumes a fringe-fit interval of 30 seconds and a recording rate of 512 Mbps.

[j] Assumes 4 hours of integration with 7 antennas recording at a rate of 512 Mbps.

Tab. H.2. The tabulated baseline sensitivities for 90 cm, 50 cm, and 7 mm assume a fringe-fit interval of 1 minute, since 2 minutes is unrealistically long. All the baseline and image sensitivities in the table, except for 50 cm and 3 mm, assume an aggregate recording bit rate equal to the typical value of 256 Mbps. This rate is commonly achieved by recording a total bandwidth $\Delta\nu$ of 64 MHz (usually 32 MHz per polarization) with 2-bit (4-level) sampling.

Opacity-corrected zenith gains are needed for current techniques for amplitude calibration. These zenith gains vary from antenna to antenna, and are monitored by VLBA operations and communicated to users. The typical values appearing in Tab. H.2 are meant to be illustrative only.

H.4 VLBA signal path

This section describes the devices in the signal path at a VLBA antenna site. Devices from 1 to 6 and 8 to 11 are located at the antenna; all others are in the site control building (Napier 1995; Thompson 1995; Rogers 1995). In collaboration with the South African KAT group, MIT Haystack Observatory, and the CASPER group at UC Berkeley, NRAO currently is developing a digital back end that will enable data to be delivered to recording systems at a rate of 4 Gbps. The new back end systems will be implemented in 2010.

(1) *Antenna and subreflector*— These concentrate the radio frequency (RF) radiation. Antenna pointing and subreflector position are controlled by commands from the site computer based on the current observing schedule and/or provided by the array operators or by the site technicians.

(2) *Feed*— The feed collects the RF radiation. All feeds and receivers are available at any time, and are selected by subreflector motion controlled by the computer. The shaped subreflector illuminates all feeds above 1 GHz; these feeds are located on a ring at the Cassegrain focus, and changes from one feed to another (hence changes in observing band) take only a few seconds. In addition, a permanently installed dichroic enables simultaneous 2.3/8.4 GHz observations. The 330 and 610 MHz feeds are crossed dipoles mounted on the subreflector near prime focus. Therefore, it is possible to make simultaneous 330/610 MHz observations.

(3) *Polarizer*— This device converts circular polarizations to linear for subsequent transmission. For receivers above 1 GHz, the polarizer is at cryogenic temperatures.

(4) *Pulse cal*— This system injects calibration tones based on a string of pulses at intervals of 1.0 or 0.2 microseconds. Pulses thus are generated at frequency intervals of 1 MHz or 5 MHz.

(5) *Noise cal*— This device injects switched, well calibrated, broadband noise for system temperature measurements. Synchronous detection occurs in the intermediate frequency (IF) distributors and base band converters. Switching is done at 80 Hz.

(6) *Receiver*— The receiver amplifies the signal. Most VLBA receivers are HFETs (Heterostructure Field Effect Transistors) at a physical temperature of 15 K, but the 90 cm and 50 cm receivers are GaAsFETs (Gallium Arsenide Field Effect Transistors) at room temperature. Each receiver has 2 channels, one for RCP and one for LCP. The 1 cm, 7 mm, and 3 mm receivers also perform the first frequency down conversion.

(7) *Maser*— The maser is a very stable frequency standard with two output signals, one at 100 MHz and one at 5 MHz. The 100 MHz output is the reference for the front end synthesizers and the pulse cal system. The 5 MHz output is the reference for the base band converters, the formatter, and the antenna timing.

(8) *Local oscillator transmitter and receiver*— The local oscillator (LO) transmitter and receiver multiplies the 100 MHz from the maser to 500 MHz and sends it to the antenna vertex room. A round trip phase measuring scheme monitors the length of the cable used to transmit the signal so that phase corrections can be made for temperature and pointing induced variations.

(9) *Front end synthesizer*— The front end synthesizer generates the reference signals used to convert the receiver output from RF to IF. The lock points are at $(n \times 500) \pm 100$ MHz, where n is an integer. The synthesizer output frequency is between 2.1 and 15.9 GHz. There are 3 such synthesizers, each of which is locked to the maser. One synthesizer is used for most wavelengths, but two are used at 1 cm, at 7 mm, at 3 mm, and for the wide band mode at 4 cm.

(10) *IF converter*— The IF converter mixes the receiver output signals with the first LO generated by a front end synthesizer. Two signals between 500 and 1000 MHz are output by each IF converter, one for RCP and one for LCP. The same LO signal is used for mixing with both polarizations in most cases. However, the 4 cm IF converter has a special mode that allows both output signals to be connected to the RCP output of the receiver and to use separate LO signals, thereby allowing the use of spanned bandwidths exceeding 500 MHz. Also, the 90 cm and 50 cm signals are combined and transmitted on the same IFs. The 50 cm signals are not frequency converted, while the 90 cm signals are upconverted to 827 MHz before output.

(11) *IF cables*— There are four of these, labeled A, B, C, and D. Each IF converter normally sends its output signals to A and C, or else to B and D, although switching is available for other possibilities if needed. By convention, the RCP signals are sent to A or B while the LCP signals are sent to C or D. Normally only 2 cables will be in use at a time. Certain dual frequency modes, especially 13 cm and 4 cm, can use all four cables.

(12) *IF distributors*— The IF distributors make 8 copies of each IF, one for each base band converter. They also can optionally switch in 20 db of attenuation for solar observations. There are two IF distributors, each handling two IFs. Power detectors allow the determination of total and switched power in the full IF bandwidth for system temperature determinations and for power level setting.

(13) *Base band converters*— The base band converters (BBCs) mix the IF signals to base band and provide the final analog filtering. Each of 8 BBCs generates a reference signal between 500 and 1000 MHz at any multiple of 10 kHz. Each BBC can select as input any of the four IFs. Each BBC provides the upper and lower sidebands as separate outputs, allowing for a total of 16 "BB channels", where one BB channel is one sideband from one BBC. Allowed bandwidths per BBC are 0.0625, 0.125, 0.25, 0.5, 1, 2, 4, 8, and 16 MHz. Thus the 16 possible BB channels can cover an aggregate bandwidth up to 256 MHz. The BBC signals are adjusted in amplitude. With automatic leveling turned on, the power in the signals sent to the samplers is kept nearly constant, which is important for the 2-bit (4-level) sampling mode. The

BBCs contain synchronous detectors that measure both total power and switched power in each sideband for system temperature determination.

(14) *Samplers*— Samplers convert the analog BBC outputs to digital form. There are two samplers, each of which handles signals from 4 BBCs. Either 1-bit (2-level) or 2-bit (4-level) sampling may be selected. A single sample rate applies to all BB channels; rates available are 32, 16, 8, 4, or 2 Msamples per second on each channel.

(15) *Formatter*— The formatter selects the desired bit streams from the samplers, adds time tags, and supports various other functions required to record efficiently on the VLBA original tape-based data acquisition system. Although no longer required for disk-based recording, these functions are still used in the transitional Mark 5A system. Auxiliary detection of up to 16 pulse-calibration tones and state counts also is supported in the formatter.

(16) *Recorders*— The VLBA records on Mark 5A recording systems, also in use at the VLA and the GBT. Each unit records on two removable modules, sequentially in most cases, but in parallel at the 512-Mbps data rate that is the highest currently supported. Each module comprises eight commercial disk drives. The current VLBA complement of modules is based primarily on 250 or 300 Gbyte disks, for a total of 2-2.4 Terabytes of recording capacity. Presently, a few modules with eight 500-750-Gbyte disks (4-6 Terabyte total capacity) are available. Thus, a single module lasts for approximately 17-52 hours if recorded continuously at 256 Mbps, or commensurately shorter periods for recording at 512 Mbps.

(17) *Site computer*— A VME site computer running VxWorks controls all site equipment based on commands in the current observing schedule or provided by the array operators or by the site technicians. All systems are set as requested in the current schedule for each new observation.

(18) *Monitor and control bus*— This carries commands from the site computer to all site hardware and returns data from the site hardware to the computer.

(19) *GPS receiver*— This device acquires time from the Global Positioning System (GPS). GPS time is usually used to monitor the site clock, providing critical information for data correlation. GPS time is occasionally used to set the site clock if it is disrupted for some reason. Five of the stations have co-located geodetic GPS receivers that are part of the International Global Navigation Satellite Systems network.

H.5 Recording format

The VLBA records data on Mark 5A disk-based systems in VLBA format. Although the VLBA cannot record Mark 4 format as such, there is a high degree of compatibility between Mark 4 and VLBA formats. In general, disks in either VLBA or Mark 4 formats can be played back, for the same observation if necessary, on any VLBA or Mark 4 correlator.

As part of the VLBA sensitivity upgrade, the NRAO have a goal to convert the VLBA to Mark 5C recording systems, capable of recording data at 4 Gbps, by 2010. The data then will be "format-free" data recorded as standard disk files, though there will be a compatibility mode possible to record in formats useful for earlier versions of Mark 5 hardware correlators.

H.6 Correlator

As part of the VLBA sensitivity upgrade, NRAO currently is integrating the DiFX software correlator into the operational environment of the VLBA, and performing tests to validate its results by comparison with those of the original VLBA correlator. The DiFX system was developed at Swinburne University in Melbourne, Australia (Deller et al. 2007). DiFX will become the operational VLBA correlator in 2010.

The VLBA correlator, located at the DSOC, accommodates the full range of scientific investigations for which the array was designed. The correlator supports wideband continuum, high-resolution spectroscopy, bandwidth synthesis, polarimetric, and gated observations.

The correlator is designed to process all observations involving VLBA stations. With its 20-station capacity and sub-arraying capabilities, it is designed to correlate an extended array combining the VLBA with as many

as 10 other stations. At present, the VLBA correlator has available 17 data inputs from Mark 5A recorders, so the rare observations requiring correlation of more than 17 stations including the VLBA require multiple correlator passes.

Each station input comprises 8 parallel "channels", which operate at a fixed rate of 32 Msamples per second, for either 1- or 2-bit samples. Observations at lower sample rates generally can be processed with a speed-up factor of 2 (for 16 Msamples per second) or 4 (for 8 Msamples per second or less) relative to observe time. Special modes are invoked automatically to enhance sensitivity when fewer than 8 channels are observed, or when correlating narrowband or oversampled data. The correlator accepts input data recorded in VLBA or Mark 4 longitudinal format, or on Mark 5A disk modules, and plays these data back on tape or disk drives similar to the station recorders.

Each input channel can be resolved into 1024, 512, 256, 128, 64, or 32 "spectral points", subject to a limit of 2048 points per baseline across all channels. The correlator cannot process maximally (16-fold) oversampled data at the highest spectral resolution, which effectively prohibits 1024-channel resolution at the narrowest bandwidth of 62.5 kHz. Adjacent, oppositely polarized channels can be paired to produce all four Stokes parameters; in this case correlator constraints impose a maximum spectral resolution of 128 points per polarization state.

The correlator forms cross-spectral power measurements on all relevant baselines in a given sub-array, including individual antenna "self-spectra". These can be integrated over any integral multiple of the basic integration cycle, 131.072 milliseconds (2^{17} microsec). Adjacent spectral points may be averaged while integrating to reduce spectral resolution.

Correlator output is written in a "FITS Binary Table" format, and includes editing flags plus amplitude, weather, and pulse calibration data logged at VLBA antennas at observe time (Flatters 1998; Ulvestad 1999). All results are archived on digital-audio-tape (DAT) cassettes. The output data rate is limited to 1.0 Mbytes per second (MB/s), which must be shared among all simultaneous correlator sub-arrays. Data are copied from the archive for distribution to users on a variety of media, with DAT and Exabyte currently given primary support.

Operation of the correlator is governed primarily by information obtained from the VLBA control system monitor data or from foreign stations log

files. Supervision of the correlation process is the responsibility of VLBA operations personnel, and requires no participation by the observers.

H.7 Angular resolution

Tab. H.3 gives the maximum lengths rounded to the nearest km ($B^{\rm km}_{\rm max}$) for each of the 45 VLBA internal baselines as well as the baselines to other HSA telescopes. A measure of the corresponding resolution ($\theta_{\rm HPBW}$) in milliarcseconds (mas) is

$$\theta_{\rm HPBW} \sim 2063 \times \frac{\lambda^{\rm cm}}{B^{\rm km}_{\rm max}} \ \ {\rm mas} \qquad \text{(H.1)}$$

where $\lambda^{\rm cm}$ is the receiver wavelength in cm (Wrobel 1995). A uniformly weighted image made from a long (u, v) plane track will have a synthesized beam with a slightly narrower minor axis FWHM. At the center frequencies appearing in Tab. H.2 and for the longest VLBA baseline, $\theta_{\rm HPBW}$ is 22, 12, 5, 4.3, 3.2, 1.4, 0.85, 0.47, and 0.32 mas for receivers named 90, 50, 21, 18, 13, 6, 4, 2, and 1 cm, plus 0.17 mas at 7 mm. The longest VLBA-only baseline at 3 mm is currently the one between MK and NL, which is about 30% shorter than the longest baseline at other wavelengths.

H.8 Time resolution

Time resolution is set by the VLBI correlator accumulation time. At the VLBA correlator it is about 2 seconds for most programs, although a minimum accumulation time of 131 milliseconds is available. The combination of time and spectral resolution for an observation must result in a correlator output rate of less than 1.0 Megabyte per second (MB/s). The limits on time resolution will become far more flexible when the DiFX correlator becomes operational in 2010.

H.9 Baseline sensitivity

Adequate baseline sensitivity is necessary for VLBI fringe fitting. Typical baseline sensitivities are listed in Tab. H.2. Alternatively, the following formula can be used in conjunction with the typical zenith $SEFD$s for VLBA

Table H.3. Maximum VLBI Baseline Lengths in km ($B_{\rm max}^{\rm km}$).

	SC	HN	NL	FD	LA	PT	KP	OV	BR	MK	EB	AR	GB	Y27
SC	...	2853	3645	4143	4458	4579	4839	5460	5767	8611	6822	238	2708	4532
HN	2853	...	1611	3105	3006	3226	3623	3885	3657	7502	5602	2748	829	3198
NL	3645	1611	...	1654	1432	1663	2075	2328	2300	6156	6734	3461	1064	1640
FD	4143	3105	1654	...	608	564	744	1508	2345	5134	8084	3922	2354	515
LA	4458	3006	1432	608	...	236	652	1088	1757	4970	7831	4246	2344	226
PT	4579	3226	1663	564	236	...	417	973	1806	4795	8014	4365	2551	52
KP	4839	3623	2075	744	652	417	...	845	1913	4466	8321	4623	2939	441
OV	5460	3885	2328	1508	1088	973	845	...	1214	4015	8203	5255	3323	1025
BR	5767	3657	2300	2345	1757	1806	1913	1214	...	4398	7441	5585	3326	1849
MK	8611	7502	6156	5134	4970	4795	4466	4015	4398	...	10328	8434	7028	4835
EB	6822	5602	6734	8084	7831	8014	8321	8203	7441	10328	...	6911	6335	8008
AR	238	2748	3461	3922	4246	4365	4623	5255	5585	8434	6911	...	2545	4317
GB	2708	829	1064	2354	2344	2551	2939	3323	3326	7028	6335	2545	...	2516
Y27	4532	3198	1640	515	226	52	441	1025	1849	4835	8008	4317	2516	...

antennas given in Tab. H.2 to calculate the *rms* thermal noise (ΔS) in the visibility amplitude of a single-polarization baseline between two identical antennas (Walker 1995a; Wrobel & Walker 1999):

$$\Delta S = \frac{1}{\eta_{\rm s}} \times \frac{SEFD}{\sqrt{2 \times \Delta\nu \times \tau_{\rm ff}}} \ \ {\rm Jy}. \tag{H.2}$$

In the last equation $\eta_{\rm s} \leq 1$ accounts for the VLBI system inefficiency (e.g., quantization in the data recording and correlator approximations). For the VLBA correlator $\eta_{\rm s} \approx 0.5$ for 1-bit sampling and $\eta_{\rm s} \approx 0.7$ for 2-bit sampling. For non-identical antennas 1 and 2, Eq. H.2 is modified to the following:

$$\Delta S = \frac{1}{\eta_{\rm s}} \times \frac{\sqrt{SEFD_1 SEFD_2}}{2 \times \Delta\nu \times \tau_{\rm ff}} \ {\rm Jy}. \tag{H.3}$$

The bandwidth in Hz is $\Delta\nu$. For a continuum target, use the BB channel width or the full recorded bandwidth, depending on fringe-fitting mode, and for a line target, use the BB channel width divided by the number of spectral points per BB channel. $\tau_{\rm ff}$ is the fringe-fit interval in seconds, which should be less than or about equal to the coherence time $\tau_{\rm coh}$. Eqs. H.2 and H.3 hold in the weak source limit. About the same noise can be obtained with either 1-bit (2-level) or 2-bit (4-level) quantization at a constant overall bit rate; cutting the bandwidth in half to go from 1-bit to 2-bit sampling is approximately compensated by a change in $\eta_{\rm s}$ that is very nearly equal to $\sqrt{2}$ (Moran & Dhawan 1995). The actual coherence time appropriate for a given VLBA program can be estimated using observed fringe amplitude data on an appropriately strong and compact source.

H.10 Image sensitivity

Typical image sensitivities for the VLBA are listed in Tab. H.2. Alternatively, the following formula may be used in conjunction with the typical zenith *SEFD*s for VLBA antennas given in Tab. H.2 (or a different *SEFD* for lower elevations or poor weather) to calculate the *rms* thermal noise ($\Delta I_{\rm m}$) expected in a single-polarization image, assuming natural weighting (Wrobel 1995; Wrobel & Walker 1999):

$$\Delta I_{\rm m} = \frac{1}{\eta_s} \times \frac{SEFD}{N \times (N-1) \times \Delta_\nu \times t_{\rm int}} \ \ {\rm Jy\ beam}^{-1}, \tag{H.4}$$

where N is the number of VLBA antennas available; $\Delta\nu$ is the bandwidth [Hz]; and $t_{\rm int}$ is the total integration time on source [s]. The expression for image noise becomes rather more complicated for a set of non-identical antennas such as the HSA, and may depend quite strongly on the data weighting that is chosen in imaging. The best strategy is to estimate image sensitivity using the EVN sensitivity calculator at http://www.evlbi.org/cgi-bin/EVNcalc.

If simultaneous dual polarization data are available with the above value of $\Delta I_{\rm m}$ per polarization, then for an image of Stokes I, Q, U, or V,

$$\Delta I = \Delta Q = \Delta U = \Delta V = \frac{\Delta I_{\rm m}}{\sqrt{2}}. \tag{H.5}$$

For a polarized intensity image of $P = \sqrt{Q^2 + U^2}$,

$$\Delta P = 0.655 \times \Delta Q = 0.655 \times \Delta U. \tag{H.6}$$

It is sometimes useful to express $\Delta I_{\rm m}$ in terms of an rms brightness temperature in Kelvins ($\Delta T_{\rm b}$) measured within the synthesized beam. An approximate formula for a single-polarization image is

$$\Delta T_b \sim 320 \times \Delta I_{\rm m} \times (B^{\rm km}_{\rm max})^2 \text{ K}. \tag{H.7}$$

H.11 Calibration transfer

Data necessary to perform accurate calibration for the VLBA are supplied as part of the correlator output files, and will appear within the Astronomical Image Processing System ($\mathcal{AIPS}$) as extension tables attached to the FITS files. These tables include GC (gain), TY (system temperature), and WX (weather) tables for amplitude calibration, PC (pulse-cal) tables for system phase calibration, and FG (flag) tables for editing. For non-VLBA antennas, some or all of these tables may be missing, since relevant monitor data are not available at the time of correlation. For example, for the HSA, GC and TY information are available for most antennas, except that calibration of the phased VLA requires additional information about the flux density of at least one source. Flag (FG) tables for non-VLBA antennas are absent or only partially complete, lacking information about antenna off-source times. In such cases, the "flag" input file that is output by the SCHED software

may be very useful for flagging data when antennas are not on source; this file appears to be quite good at predicting the on-source times for the GBT, Arecibo, and Effelsberg, but presently underestimates by about 10 seconds the time it takes for Y27 to change source.

H.12 Amplitude calibration

Traditional calibration of VLBI fringe amplitudes for continuum sources requires knowing the on-source system temperature in Jy ($SEFD$; Moran & Dhawan 1995). System temperatures in K ($T_{\rm sys}$) are measured "frequently" in each BB channel during observations with VLBA antennas; "frequently" means at least once per source/frequency combination or once every user-specified interval (default is 2 minutes), whichever is shorter. These $T_{\rm sys}$ values are required by fringe amplitude calibration programs such as ANTAB/APCAL in $\mathcal{AIPS}$ or CAL in the Caltech VLBI Analysis Programs. Such programs can be used to convert from $T_{\rm sys}$ to $SEFD$ by dividing by the VLBA antenna zenith gains in K Jy^{-1} provided by VLBA operations, based upon regular monitoring of all receiver and feed combinations. $T_{\rm sys}$ and gain values for VLBA antennas are delivered in TY and GC tables, respectively.

An additional loss of sensitivity may occur for data taken with 2-bit (4-level) quantization, due to non-optimal setting of the voltage thresholds for the samplers. This usually is a relatively minor, but important, adjustment to the amplitude calibration. In the VLBA, for instance, the system design leads to a systematic (5% to 10%) calibration offset of the samplers between even and odd BB channels; for dual polarization observations, this may lead to a systematic offset between RR and LL correlations that must be accounted for in the calibration. The combination of the antenna and sampler calibrations may be found and applied in $\mathcal{AIPS}$ using the procedure VLBACALA.

Post-observing amplitude adjustments might be necessary for an antenna position dependent gain (the "gain curve") and for the atmospheric opacity above an antenna, particularly at high frequencies (Moran & Dhawan 1995). The GC table described above contains gain curves for VLBA antennas. Opacity adjustments can be made with $\mathcal{AIPS}$ task APCAL if weather data are available in a WX table.

Although experience with VLBA calibration shows that it probably yields fringe amplitudes accurate to 5% or less at the standard frequencies in the

1-10 GHz range, it is recommended that users observe a few amplitude calibration check sources during their VLBA program. Such sources can be used (1) to assess the relative gains of VLBA antennas plus gain differences among base band channels at each antenna; (2) to test for non-closing amplitude and phase errors; and (3) to check the correlation coefficient adjustments, provided contemporaneous source flux densities are available independent of the VLBA observations. These calibrations are particularly important if non-VLBA antennas are included in an observation, since their a priori gains and/or measured system temperatures may be much less accurate than for the well-monitored VLBA antennas. The VLBA gains are measured at the center frequencies appearing in Tab. H.2; users observing at other frequencies may be able to improve their amplitude calibration by including brief observations, usually of their amplitude check sources, at the appropriate frequencies. Amplitude check sources should be point-like on inner VLBA baselines. Sources may be selected from the VLBI surveys available through http://www.vlba.nrao.edu/astro/obsprep/sourcelist/.

H.13 Phase calibration and imaging

(1) *Fringe finders*— VLBI fringe phases are much more difficult to deal with than fringe amplitudes. If the a priori correlator model assumed for VLBI correlation is particularly poor, then the fringe phase can wind so rapidly in both time (the fringe rate) and in frequency (the delay) that no fringes will be found within the finite fringe rate and delay windows examined during correlation. Reasons for a poor a priori correlator model include source position and antenna location errors, atmospheric (tropospheric and ionospheric) propagation effects, and the behavior of the independent clocks at each antenna. Users observing sources with poorly known positions should plan to refine the positions first on another instrument. To allow accurate location of any previously unknown antennas and to allow NRAO staff to conduct periodic monitoring of clock drifts, each user must include at least two "fringe finder" sources which are strong, compact, and have accurately known positions. Typically, a fringe finder should be observed for 5 minutes every 1-3 hours.

(2) *The pulse cal system*— VLBA observers using more than 1 BBC will

want to sum over the BBCs to reduce noise levels. This should not be done with the raw signals delivered by the BBCs: the independent local oscillators in each BBC introduce an unknown phase offset from one BBC to the next, so such a summation of the raw signals would be incoherent. A so-called "phase cal" or "pulse cal" system (Thompson 1995) is available at VLBA antennas to overcome this problem. This system, in conjunction with the LO cable length measuring system, is also used to measure changes in the delays through the cables and electronics which must be removed for accurate geodetic and astrometric observations. The pulse cal system consists of a pulse generator and a sine-wave detector. The interval between the pulses can be either 0.2 or 1 microsecond. They are injected into the signal path at the receivers and serve to define the delay reference point for astrometry. The weak pulses appear in the spectrum as a "comb" of very narrow, weak spectral lines at intervals of 1 MHz (or, optionally, 5 MHz). The detector, located at the VLBA antennas, measures the phase of one or more of these lines, and their relative offsets can be used to correct the phases of data from different BBCs. The VLBA pulse cal data are logged as a function of time and delivered in a PC table. The $\mathcal{AIPS}$ software can be used to load and apply these data. However, some VLBA observers may still want to use a strong compact source to do a "manual" pulse cal if necessary (Diamond 1995). For example, spectral line users will not want the pulse cal "comb" in their spectra, so they should ensure that their observing schedules both disable the pulse cal generators and include observations suitable for a "manual" pulse cal. Manual pulse calibration also is likely to be necessary for any non-VLBA antennas included in an observation, because they may have no tone generators, or else may not have detectors located at the antenna. In addition, it is necessary at 3 mm, where the VLBA antennas have no pulse calibration tones.

(3) *Fringe fitting*— After correlation and application of the pulse calibration, the phases on a VLBA target source still can exhibit high residual fringe rates and delays. Before imaging, these residuals should be removed to permit data averaging in time and, for a continuum source, in frequency. The process of finding these residuals is referred to as fringe fitting. Before fringe fitting, it is recommended to edit the data based on the a priori edit information provided for VLBA antennas. Such

editing data are delivered in the FG table. The old baseline-based fringe search methods have been replaced by more powerful global fringe search techniques (Cotton 1995; Diamond 1995). Global fringe fitting is simply a generalization of the phase self-calibration technique, as during a global fringe fit the difference between model phases and measured phases are minimized by solving for the antenna-based instrumental phase, its time slope (the fringe rate), and its frequency slope (the delay) for each antenna. Global fringe fitting in $\mathcal{AIPS}$ is done with the program FRING or associated procedures. If the VLBA target source is a spectral line source or is too weak to fringe fit on itself, then residual fringe rates and delays can be found on an adjacent strong continuum source and applied to the VLBA target source.

(4) *Editing*— After fringe-fitting and averaging, VLBA visibility amplitudes should be inspected and obviously discrepant points removed (Diamond 1995; Walker 1995b). Usually such editing is done interactively using tasks in $\mathcal{AIPS}$ or the Caltech program DIFMAP (Shepherd 1997). Note that VLBA correlator output data also will include a flag (FG) table derived from monitor data output, containing information such as off-source flags for the antennas during slews to another source.

(5) *Self-calibration, imaging, and deconvolution*— Even after global fringe fitting, averaging, and editing, the phases on a VLBA target source can still vary rapidly with time. Most of these variations are due to inadequate removal of antenna-based atmospheric phases, but some variations also can be caused by an inadequate model of the source structure during fringe fitting. If the VLBA target source is sufficiently strong and if absolute positional information is not needed, then it is possible to reduce these phase fluctuations by looping through cycles of Fourier transform imaging and deconvolution, combined with phase self-calibration in a time interval shorter than that used for the fringe fit (Cornwell 1995; Walker 1995b; Cornwell & Fomalont 1999). Fourier transform imaging is straightforward (Briggs et al. 1999), and done with $\mathcal{AIPS}$ task IMAGR or the Caltech program DIFMAP (Shepherd 1997). The resulting VLBI images are deconvolved to rid them of substantial sidelobes arising from relatively sparse sampling of the (u, v) plane (Cornwell et al. 1999). Such deconvolution is achieved with $\mathcal{AIPS}$ tasks based on the CLEAN or Maximum Entropy methods or

with the Caltech program DIFMAP.

Phase self-calibration just involves minimizing the difference between observed phases and model phases based on a trial image, by solving for antenna-based instrumental phases (Cornwell 1995; Walker 1995b; Cornwell & Fomalont 1999). After removal of these antenna-based phases, the improved visibilities are used to generate an improved set of model phases, usually based on a new deconvolved trial image. This process is iterated several times until the phase variations are substantially reduced. The method is then generalized to allow estimation and removal of complex instrumental antenna gains, leading to further image improvement. Both phase and complex self-calibration are accomplished with the $\mathcal{AIPS}$ task CALIB and with program DIFMAP in the Caltech VLBI Analysis Programs. Self-calibration should only be done if the VLBA target source is detected with sufficient signal-to-noise in the self-calibration time interval (otherwise, fake sources can be generated) and if absolute positional information is not needed.

The useful field of view in VLBI images can be limited by finite bandwidth, integration time, and non-coplanar baselines (Wrobel 1995; Cotton 1999; Bridle & Schwab 1999; Perley 1999).

(6) *Phase referencing*— If the VLBA target source is not sufficiently strong for self-calibration or if absolute positional information is needed but geodetic techniques are not used, then VLBA phase referenced observations must be employed (Beasley & Conway 1995). Currently, more than half of all VLBA observations employ phase referencing. A VLBA phase reference source should be observed frequently and be within a few degrees of the VLBA target region, otherwise differential atmospheric (tropospheric and ionospheric) propagation effects will prevent accurate phase transfer. VLBA users can draw candidate phase calibrators from the source catalog in use at the VLBA correlator, distributed with the NRAO program SCHED; easy searching for the nearest calibrators is available on-line through the VLBA Calibrator Survey (Beasley et al. 2002) at http://www.vlba.nrao.edu/astro/calib/. Most of these candidate phase calibrators have positional uncertainties below 1 mas.

Calibration of atmospheric effects for either imaging or astrometric experiments can be improved by the use of multiple phase calibrators that enable multi-parameter solutions for phase effects in the atmosphere.

For further information, see the $\mathcal{AIPS}$ Memos 110 (task DELZN, Mioduszewski 2004) and 111 (task ATMCA, Fomalont & Kogan 2005), available from http://www.aips.nrao.edu/aipsdoc.html

Ionospheric corrections can even be of significant benefit for frequencies as high as 5 GHz or 8 GHz. These corrections may be made with the $\mathcal{AIPS}$ task TECOR, or the procedure VLBATECR. In addition, it is strongly recommended that the most accurate Earth-Orientation values be applied to the calibration, since correlation may have taken place before final values were available; this may be done with $\mathcal{AIPS}$ task CLCOR or with the $\mathcal{AIPS}$ procedure VLBAEOPS.

The rapid motion of VLBA antennas often can lead to very short time intervals for the slew between target source and phase reference source. Some data may be associated with the wrong source, leading to visibility points of very low amplitude at the beginnings of scans. Application of the $\mathcal{AIPS}$ program QUACK using the 'TAIL' option will fix this problem.

H.14 Observing

Each VLBA program is run remotely from the DSOC by VLBA operations. No observing assistance by a VLBA user is expected, although VLBA operations should be able to reach the observer by telephone during the program. As the program progresses, the array operator monitors the state of the antennas and tape recording systems, mainly using a compact yet comprehensive display program. Various logging, calibration, and flagging data are automatically recorded by the monitor and control system running on the station computer at each VLBA site. If necessary, the array operator can request local assistance from a site technician at each VLBA antenna. Recorded media are automatically shipped from each VLBA antenna to the correlator specified by the observer.

H.15 Post-processing software

$\mathcal{AIPS}$ is a set of programs for the analysis of continuum and line VLBI observations involving one or more BB channel. These programs are available for a wide range of computer operating systems, including various flavors

of Linux and the Mac-OS/X operating system. Extensive on-line internal documentation can be accessed within $\mathcal{AIPS}$. An entire chapter in the $\mathcal{AIPS}$ *CookBook* (NRAO staff, 2007) provides useful "how-to" guidance for those reducing VLBI data. Appendix C of the $\mathcal{AIPS}$ *CookBook* provides a step-by-step guide to calibrating many types of VLBA data sets in $\mathcal{AIPS}$. A new "frozen" version of $\mathcal{AIPS}$ is produced each year, and a newer version (currently 31DEC08) is updated and made available throughout the calendar year. New capabilities such as improved astrometric calibration and simpler data-reduction procedures are implemented frequently in recently version of $\mathcal{AIPS}$.

H.16 Data archive

An archive of all output from the VLBA correlator is maintained at the DSOC. The user who proposed the observations will retain a proprietary right to the data for a fixed interval of 12 months following the end of correlation of the last observations requested in the original proposal or a direct extension of that proposal. Thereafter, archived data will be available to any user on request. An on-line data archive has been developed, and data beginning from 1998 currently are on line (https://archive.nrao.edu/archive/archiveproject.jsp). The most recent data are available either as multiple correlator output files or as large FITS files, sometimes with default calibrations attached.

Data are distributed to users on a variety of media, with DDS3 and Exabyte currently given primary support. Distribution also is possible via ftp. For the initial distribution to the user proposing the observations, this will occur automatically, soon after correlation is complete, provided a medium has been specified. Distributed data will conform to the new FITS binary table standard for interferometry data interchange (Flatters 1998), which is read by $\mathcal{AIPS}$ task FITLD.

Bibliography

[Andre et al. (1988)] Andre, P., Montmerle, T., Feigelson, E. D., Stine, P. C., & Klein, K.-L., 1988, ApJ, 335, 940

[Andre et al.(1990)] Andre, P., Montmerle, T., Feigelson, E. D., & Steppe, H., 1990, A&A, 240, 321

[Andre et al.(1991)] Andre, P., Phillips, R. B., Lestrade, J.-F., & Klein, K.-L., 1991, ApJ, 376, 630

[André et al. (1992)] Andre, P., Deeney, B. D., Phillips, R. B., & Lestrade, J.-F., 1992, ApJ, 401, 667

[Ballesteros-Paredes et al. (2009)] Ballesteros-Paredes, J., Gómez, G. C., Loinard, L., Torres, R. M., & Pichardo, B., 2009, MNRAS, 395, L81

[Baraffe et al. (1998)] Baraffe, I., Chabrier, G., Allard, F., & Hauschildt, P. H., 1998, A&A, 337, 403

[Barnard (1895)] Barnard, MNRAS, 1895, 55, 442

[Beasley & Conway (1995)] Beasley, A. J., & Conway, J. E., 1995, in ASP Conference Series, edited by J. A. Zensus, P. J. Diamond, & P. J. Napier (San Francisco: Astronomical Society of the Pacific), 82, 189

[Beasley et al. (2002)] Beasley, A. J., Gordon, D., Peck, A. B., Petrov, L., MacMillan, D. S., Fomalont, E. B., & Ma, C., 2002, ApJS, 141, 13

[Bertout et al. (1999)] Bertout, C., Robichon, N., & Arenou, F., 1999, A&A, 352, 574

[Bertout & Genova (2006)] Bertout, C., & Genova, F., 2006, A&A, 460, 499

[Bieging et al. (1984)] Bieging, J. H., Cohen, M., & Schwartz, P. R., 1984, ApJ, 282, 699

[Boden et al. (2007)] Boden, A. F., Torres, G., Sargent, A. I., Akeson, R. L., Carpenter, J. M., Boboltz, D. A., Massi, M., Ghez, A. M., Latham, D. W., Johnston, K. J., Menten, K. M., Ros, E., 2007, ApJ, 670, 1214

[Brand & Blitz (1993)] Brand, J., & Blitz, L., A&A, 1993, 275, 67

[Briceño et al. (2002)] Briceño, C., Luhman, K. L., Hartmann, L., Stauffer, J. R., & Kirkpatrick, J. D., 2002, ApJ, 580, 317

[Bridle & Schwab (1999)] Bridle, A. H., Schwab, F. R., 1999, in ASP Conference Series, edited by G. B. Taylor, C. L. Carilli, & R. A. Perley, (San Francisco: Astronomical Society of the Pacific), 180, 371

[Briggs et al. (1999)] Briggs, D. S., Schwab, F. R., Sramek, R. A., 1999, in ASP Conference Series, edited by G. B. Taylor, C. L. Carilli, & R. A. Perley, (San Francisco: Astronomical Society of the Pacific), 180, 127

[Chatterjee et al. (2004)] Chatterjee, S., Cordes, J. M., Vlemmings, W. H. T., Arzoumanian, Z., Goss, W. M., & Lazio, T. J. W., 2004, ApJ, 604, 339

[Chini (1981)] Chini, R., 1981, A&A, 99, 346

[Cohen & Kuhi (1979)] Cohen, M., & Kuhi, L. V., 1979, ApJS, 41, 743

[Cohen & Bieging (1986)] Cohen, M., & Bieging, J. H., 1986, AJ, 92, 1396

[Conway & Sault (1995)] Conway, J. E. & Sault, R. J., 1995, in ASP Conference Series, edited by J. A. Zensus, P. J. Diamond, & P. J. Napier (San Francisco: Astronomical Society of the Pacific), 82, 310

[Cornwell (1995)] Cornwell, T., 1995, in ASP Conference Series, edited by J. A. Zensus, P. J. Diamond, & P. J. Napier, (San Francisco: Astronomical Society of the Pacific), 82, 39

[Cornwell et al. (1999)] Cornwell, T., Braun, R., & Briggs, D. S., 1999, in ASP Conference Series, edited by G. B. Taylor, C. L. Carilli, & R. A. Perley, (San Francisco: Astronomical Society of the Pacific), 180, 151

[Cornwell & Formalont (1999)] Cornwell, T., & Formalont E. B., 1999, in ASP Conference Series, edited by G. B. Taylor, C. L. Carilli, & R. A. Perley, (San Francisco: Astronomical Society of the Pacific), 180, 187

[Cotton (1995)] Cotton, W. D., 1995, in ASP Conference Series, edited by J. A. Zensus, P. J. Diamond, & P. J. Napier (San Francisco: Astronomical Society of the Pacific), 82, 189

[Cotton (1999)] Cotton, W. D., 1999, in ASP Conference Series, edited by G. B. Taylor, C. L. Carilli, & R. A. Perley, (San Francisco: Astronomical Society of the Pacific), 180, 357

[Dame et al. (2001)] Dame, T. M., Hartmann, D., & Thaddeus, P., 2001, ApJ, 547, 792

[D'Antona & Mazzitelli (1996)] D'Antona, F., & Mazzitelli, I., 1996, ApJ, 456, 329

[D'Antona & Mazzitelli (1997)] D'Antona, F., & Mazzitelli, I., 1997, MmSAI, 68, 807

[Dehnen & Binney (1998)] Dehnen, W., & Binney, J. J., 1998, MNRAS, 298, 387

[Deller et al. (2007)] Deller, A. T., Tingay, S. J., Bailes, M., & West, C., 2007, PASP, 119, 318

[Demarque et al. (2004)] Demarque, P., Woo, J.-H., Kim, Y.-C., & Yi, S. K., 2004, ApJS, 155, 667

[Diamond (1995)] Diamond, P. J., 1995, in ASP Conference Series, edited by J. A. Zensus, P. J. Diamond, & P. J. Napier (San Francisco: Astronomical Society of the Pacific), 82, 227

[Duchêne et al. (2002)] Duchêne, G., Ghez, A. M., & McCabe, C., 2002, ApJ, 568, 771

[Duchêne et al. (2003)] Duchêne, G., Ghez, A. M., McCabe, C., Weinberger, A. J., 2003, ApJ, 592, 288

[Duchêne et al. (2005)] Duchêne, G., Ghez, A. M., McCabe, C., & Ceccarelli, C., 2005, ApJ, 628, 832

[Duchêne et al. (2006)] Duchêne, G., Beust, H., Adjali, F., Konopacky, Q. M., & Ghez, A. M., 2006, A&A, 457, L9

[Dulk et al. (1979)] Dulk, G. A., Melrose, D. B., & White, S. M., 1979, ApJ, 234, 1137

[Dulk & Marsh (1982)] Dulk, G. A., & Marsh, K. A., 1982, ApJ, 259, 350

[Dulk (1985)] Dulk, G. A., 1985, ARAA, 23, 169

[Dyck et al. (1982)] Dyck, H. M., Simon, T., & Zuckerman, B., 1982, ApJ, 255, L103

[Fazio et al. (1976)] Fazio, G. G., Low, F. J., Wright, E. L., & Zeilik, M., 1976, ApJ, 206, L165

[Feigelson & Montmerle (1985)] Feigelson, E. D., & Montmerle, T., 1985, ApJ, 289, L19

[Feigelson et al. (1994)] Feigelson, E. D., Welty, A. D., Imhoff, C., Hall, J. C., Etzel, P. B., Phillips, R. B., & Lonsdale, C. J., 1994, ApJ, 432, 373

[Feigelson & Montmerle (1999)] Feigelson, E. D., & Montmerle, T., 1999, ARAA, 37, 363

[Flatters (1998)] Flatters, C., 1998, in ASP Conference Series, edited by J. A. Zensus, G. B. Taylor, & J. M. Wrobel (San Francisco: Astronomical Society of the Pacific), 114, 109

[Fomalont (2005)] Fomalont, E. B., 2005, in ASP Conference Series, edited by J. Romney & M. Reid (San Francisco: Astronomical Society of the Pacific), 340, 460

[Furlan et al. (2003)] Furlan, E., Forrest, W., Watson, D. M., Uchida, K. I., Brandl, B. R., Keller, L. D., & Herter, T. L., 2003, ApJ, 596, L87

[Gahm (1970)] Gahm, G. F., 1970, ApJ, 160, 1117

[de Geus et al. (1989)] de Geus, E. J., de Zeeuw, P. T., & Lub, J., 1989, A&A, 216, 44

[Ghez et al. (1991)] Ghez, A. M., Neugebauer, G., Gorham, P. W., Haniff, C. A., Kulkarni, S. R., Matthews, K., Koresko, C., & Beckwith, S., 1991, AJ, 102, 2066

[Ghez et al. (1993)] Ghez, A. M., Neugebauer, G., & Matthews, K., 1993, AJ, 106, 2005

[Goldsmith et al. (2008)] Goldsmith, P. F., Heyer, M., Narayanan, G., Snell, R., Li, D., & Brunt, C., 2008, ApJ, 680, 428

[Gómez et al. (1993)] Gómez, M., Hartmann, L., Kenyon, S. J., & Hewett, R., 1993, AJ, 105, 1927

[Gómez et al. (2005)] Gómez, L., Rodríguez, L. F., Loinard, L., Lizano, S., Poveda, A., & Allen, C., 2005, ApJ, 635, 1166

[Grasdalen et al. (1973)] Grasdalen, G. L., Strom, K. M., & Strom, S. E., 1973, ApJ, 184, L53

[Greisen (2003)] Greisen, E. W., 2003, in Information Handling in Astronomy – Historical Vistas, edited by A. Heck (Dordrecht: Kluwer Academic Publishers)

[Güdel et al. (2007)] Güdel, M., Briggs, K. R., Arzner, K., Audard, M., Bouvier, J., Feigelson, E. D., Franciosini, E., Glauser, A., Grosso, N., Micela, G., Monin, J.-L., Montmerle, T., Padgett, D. L., Palla, F., Pillitteri, I., Rebull, L., Scelsi, L., Silva, B., Skinner, S. L., Stelzer, B., & Telleschi, A., 2007, A&A, 468, 353

[Haro & Morgan (1953)] Haro, G., & Morgan, W. W., 1953, ApJ, 118, 16

[Hartmann et al. (1986)] Hartmann, L., Hewett, R., Stahler, S., & Mathieu, R. D., 1986, ApJ, 309, 275

[Hillenbrand & White (2004)] Hillenbrand, L. A., White, R. J., 2004, ApJ, 604, 741

[Hillenbrand et al. (2008)] Hillenbrand, L. A., Bauermeister, A., & White, R. J., 2008, in ASP Conference Series, proceedings of the conference held 5-10 November, 2006, at the Spitzer Science Center and Michelson Science Center, Pasadena, California, USA. Edited by Gerard van Belle, 384, 200

[Imai et al. (2007)] Imai, H., Nakashima, K., Bushimata, T., Choi, Y. K., Hirota, T., Honma, M., Horiai, K., Inomata, N., Iwadate, K., Jike, T., Kameya, O., Kamohara, R., Kan-Ya, Y., Kawaguchi, N., Kijima, M., Kobayashi, H., Kuji, S., Kurayama, T., Manabe, S., Miyaji, T., Nagayama, T., Nakagawa, A., Oh, C. S., Omodaka, T., Oyama, T., Sakai, S., Sakakibara, S., Sato, K., Sasao, T., Shibata, K. M., Shimizu, R., Shintani, M., Sofue, Y., Sora, K., Suda, H., Tamura, Y., Tsushima, M., Ueno, Y., & Yamashita, K., 2007, PASJ, 59, 1107

[Johns-Krull et al. (2004)] Johns-Krull, C. M., Valenti, J. A., & Saar, S. H., 2004, ApJ, 617, 1204

[Johnston et al. (2003)] Johnston, K. J., Gaume, R. A., Fey, A. L., de Vegt, C., & Claussen, M. J., 2003, AJ, 125, 858

[Joy (1945)] Joy, A. H., 1945, ApJ, 102, 168

[Kemball (1999)] Kemball, A. J., 1999, in ASP Conference Series, edited by G. B. Taylor, C. L. Carilli, and R. A. Perley (San Francisco: Astronomical Society of the Pacific), 180, 499

[Kenyon et al. (1994)] Kenyon, S. J., Dobrzycka, D., & Hartmann, L. 1994, AJ, 108, 1872

[Kenyon & Hartmann (1995)] Kenyon, S. J., & Hartmann, L., 1995, ApJS, 101, 117

[Kenyon et al. (2008)] Kenyon, S. J., Gómez, M., & Whitney, B. A., 2008, in Handbook of Star Forming Regions Vol. I, edited by B. Reipurth (The Northern Sky ASP Monograph Publications), 405

[Knude & Hog (1998)] Knude, J., & Hog, E. 1998, A&A, 338, 897

[Koresko (2000)] Koresko, C. D., 2000, ApJ, 531, L147

[Köhler et al. (2008)] Köhler, R., Ratzka, T., Herbst, T. M., & Kasper, M., 2008, A&A, 482, 929

[Kuhi (1974)] Kuhi, L. V., 1974, A&AS, 15, 47

[Kutner et al. (1986)] Kutner, M. L., Rydgren, A. E., & Vrba, F. J., 1986, AJ, 92, 895

[Lada (1987)] Lada, C. J., 1987, in IAU Symposium No. 115, Star forming regions, edited by M. Peimbert & J. Jugaka (Dordrecht, D. Reidel Publishing Co.), 1

[Lada & Lada (2003)] Lada, C. J., & Lada, E. A. 2003, ARAA, 41, 57

[van Leeuwen (2007)] van Leeuwen, F., 2007, A&A, 474, 653

[Leinert et al. (1993)] Leinert, Ch., Zinnecker, H., Weitzel, N., Christou, J., Ridgway, S. T., Jameson, R., Haas, M., & Lenzen, R., 1993, A&A, 278, 129

[Lejeune et al. (1997)] Lejeune, Th., Cuisinier, F., & Buser, R., 1997 A&AS, 125, 229L

[Lestrade et al. (1999)] Lestrade, J.-F., Preston, R. A., Jones, D. L., Phillips, R. B., Rogers, A. E. E., Titus, M. A., Rioja, M. J., & Gabuzda, D. C., 1999, A&A, 344, 1014

[Leous et al. (1991)] Leous, J. A., Feigelson, E. D., Andre, P., & Montmerle, T., 1991, ApJ, 379, 683

[Loinard et al. (2003)] Loinard, L., Rodríguez, L. F., Rodríguez, M. I., 2003, ApJ, 587, L47

[Loinard et al. (2005)] Loinard, L., Mioduszewski, A. J., Rodríguez, L. F., González, R. A., Rodríguez, M. I., & Torres, R. M., 2005, ApJ, 619, L179

[Loinard et al. (2007)] Loinard, L., Torres, R. M., Mioduszewski, A. J., Rodríguez, L. F., González-Lópezlira, R. A., Lachaume, R., Vázquez, V., & González, E., 2007, ApJ, 671, 546

[Loinard et al. (2008)] Loinard, L., Torres, R. M., Mioduszewski, A. J., & Rodríguez, L. F. 2008, ApJ, 675, L29

[Lombardi et al. (2008)] Lombardi, M., Lada, C. J., & Alves, J., 2008, A&A, 489, 143

[Loren et al. (1990)] Loren, R. B., Wootten, A., & Wilking, B. A., 1990, ApJ, 365, 269

[Massi et al. (2002)] Massi, M., Menten, K., & Neidhöfer, J., 2002, A&A, 382, 152

[Massi et al. (2006)] Massi, M., Forbrich, J., Menten, K. M., Torricelli-Ciamponi, G., Neidhöfer, J., Leurini, S., & Bertoldi, F., 2006, A&A, 453, 959

[Massi et al. (2008)] Massi, M., Ros, E., Menten, K. M., Kaufman Bernadó, M., Torricelli-Ciamponi, G., Neidhöfer, J., Boden, A., Boboltz, D., Sargent, A., & Torres, G., 2008, A&A, 480, 489

[Mamajek (2008)] Mamajek, E. E., 2007, AN, 329, 10

[Mel'Nikov & Grankin (2005)] Mel'Nikov, S. Y., & Grankin, K. N., 2005, AstL, 31, 427

[Montmerle et al. (1983)] Montmerle, T., Koch-Miramond, L., Falgarone, E., & Grindlay, J. E., 1983, ApJ, 269, 182

[Moran & Dhawan (1995)] Moran, J. M., & Dhawan, V., 1995, in ASP Conference Series, edited by J. A. Zensus, P. J. Diamond, & P. J. Napier (San Francisco: Astronomical Society of the Pacific), 82, 161

[Napier (1995)] Napier, P. J., 1995, in ASP Conference Series, edited by J. A. Zensus, P. J. Diamond, & P. J. Napier (San Francisco: Astronomical Society of the Pacific), 82, 59

[O'Neal et al. (1990)] O'Neal, D., Feigelson, E. D., Mathieu, R. D., & Myers, P. C., 1990, AJ, 100, 1610

[Palla & Stahler (1999)] Palla, F., & Stahler, S. W., 1999, ApJ, 525, 772

[Phillips et al. (1991)] Phillips, R. B., Lonsdale, C. J., & Feigelson, E. D., 1991, ApJ382, 261

[Perley (1999)] Perley, R. A., 1999, in ASP Conference Series, edited by G. B. Taylor, C. L. Carilli, & R. A. Perley, (San Francisco: Astronomical Society of the Pacific), 180, 383

[Perryman et al. (1997)] Perryman, M. A. C., Lindegren, L., Kovalevsky, J., Hoeg, E., Bastian, U., Bernacca, P. L., Crézé, M., Donati, F., Grenon, M., van Leeuwen, F., van der Marel, H., Mignard, F., Murray, C. A.,

Le Poole, R. S., Schrijver, H., Turon, C., Arenou, F., Froeschlé, M., & Petersen, C. S., 1997, A&A, 323, L49

[Petrosian & McTiernan (1983)] Petrosian, V., & McTiernan, J. M., 1983, PhFl, 26, 3023

[Pradel et al. (2006)] Pradel, N., Charlot, P., & Lestrade, J.-F., 2006, A&A, 452, 1099

[Reid et al. (1999)] Reid, M. J., Readhead, A. C. S., Vermeulen, R. C., & Treuhaft, R. N., 1999, ApJ, 524, 816

[Richichi et al. (1994)] Richichi, A., Leinert, C., Jameson, R., & Zinnecker, H., 1994, A&A, 287, 145

[Ridge et al. (2006)] Ridge, N. A., Di Francesco, J., Kirk, H., Li, D., Goodman, A. A., Alves, J. F., Arce, H. G., Borkin, M. A., Caselli, P., Foster, J. B., Heyer, M. H., Johnstone, D., Kosslyn, D. A., Lombardi, M., Pineda, J. E., Schnee, S. L., & Tafalla, M., AJ, 131, 2921

[Robinson & Melrose (1984)] Robinson, P. A., & Melrose, D. B., 1984, AuJPh, 37, 675

[Rogers (1995)] Rogers, A. E. E. R., 1995, in ASP Conference Series, edited by J. A. Zensus, P. J. Diamond, & P. J. Napier (San Francisco: Astronomical Society of the Pacific), 82, 93

[Rybicki & Lightman (1986)] Rybicki, G. B., Lightman, A. P., 1986, in Radiative Processes in Astrophysics (Wiley-VCH)

[Sault & Conway (1999)] Sault, R. J., & Conway, J. E., 1999, in ASP Conference Series, edited by G. B. Taylor, C. L. Carilli, & R. A. Perley (San Francisco: Astronomical Society of the Pacific), 180, 419

[Shepherd (1997)] Shepherd M. C., 1997, in ASP Conference Series, edited by G. Hunt & H. E. Payne (San Francisco: Astronomical Society of the Pacific), 125, 77

[Schaefer et al. (2006)] Schaefer, G. H., Simon, M., Beck, T. L., Nelan, E., & Prato, L., 2006, AJ, 132, 2618

[Schaefer et al. (2008)] Schaefer, G. H., Simon, M., Prato, L., & Barman, T., 2008, AJ, 135, 1659

[Schwartz et al. (1986)] Schwartz, P. R., Simon, T., & Campbell, R., 1986, ApJ, 303, 233

[Siess et al. (2000)] Siess, L., Dufour, E., & Forestini, M., 2000 A&A, 358, 593

[Skinner (1993)] Skinner, S. L., 1993, ApJ, 408, 660

[Smith et al. (2003)] Smith, K., Pestalozzi, M., Güdel, M., Conway, J., & Benz, A. O., 2003, A&A, 406, 957

[Stark & Brand (1989)] Stark, A. A., & Brand, J., 1989, ApJ, 339, 763

[Torres et al. (2007)] Torres, R. M., Loinard, L., Mioduszewski, A. J., & Rodriguez, L. F., 2007, ApJ, 671, 1813

[Torres et al. (2009a)] Torres, R. M., Loinard, L., Mioduszewski, A. J., & Rodriguez, L. F., 2009, ApJ, 698, 242

[Torres et al. (2009b)] Torres, R. M., Loinard, L., Boden, A. F., Mioduszewski, A. J., & Rodriguez, L. F., 2009, *in preparation for ApJ*

[Thompson (1995)] Thompson, A. R., 1995, in ASP Conference Series, edited by J. A. Zensus, P. J. Diamond, & P. J. Napier, (San Francisco: Astronomical Society of the Pacific), 82, 73

[Thompson et al. (2001)] Thompson, A. R., Moran, J. M., & Swenson, G. W., Jr., 2001, in Interferometry and Synthesis in Radio Astronomy, 2nd Edition (New York: Wiley)

[Ulvestad (1999)] Ulvestad, J. S., 1999, in ASP Conference Series, edited by G. B. Taylor, C. L. Carilli, & R. A. Perley (San Francisco: Astronomical Society of the Pacific), 180, 513

[Walker (1995a)] Walker, R. C., 1995, in ASP Conference Series, edited by J. A. Zensus, P. J. Diamond, & P. J. Napier, (San Francisco: Astronomical Society of the Pacific), 82, 133

[Walker (1995b)] Walker, R. C., 1995, in ASP Conference Series, edited by J. A. Zensus, P. J. Diamond, & P. J. Napier, (San Francisco: Astronomical Society of the Pacific), 82, 247

[Walter et al. (1987)] Walter, F. M., Brown, A., Linsky, J. L., Rydgren, A. E., Vrba, F., Roth, M., Carrasco, L., Chugainov, P. F., Shakovskaya, N. I., Imhoff, C. L., 1987, ApJ, 314, 297

[Walter et al. (1988)] Walter, F. M., Brown, A., Mathieu, R. D., Myers, P. C., & Vrba, F. J., 1988, AJ, 96, 297

[Welty (1995)] Welty, A. D., 1995, AJ, 110, 776

[Wilking et al. (2008)] Wilking, B. A., Gagné, M., & Allen, L. E., 2008, in Handbook of Star Forming Regions Vol. II, edited by B. Reipurth (The Southern Sky ASP Monograph Publications), 351

[Wilson et al. (2009)] Wilson, T. L., Rohlfs, K., & Hüttemeister, S., 2009, in Tools of Radio Astronomy 5th Ed., (Berlin: Springer)

[Wrobel (1995)] Wrobel, J. M., 1995, in ASP Conference Series, edited by J. A. Zensus, P. J. Diamond, & P. J. Napier, (San Francisco: Astronomical Society of the Pacific), 82, 411

[Wrobel & Walker (1999)] Wrobel, J. M., Walker, R. C., 1999, in ASP Conference Series, edited by G. B. Taylor, C. L. Carilli, & R. A. Perley (San Francisco: Astronomical Society of the Pacific), 180, 171